On the nature of the red, 2MASS-selected AGN in the local Universe

Marvin Rose

The University Of Sheffield.

Department of Physics & Astronomy
The University of Sheffield

A dissertation submitted in candidature for the degree of Doctor of Philosophy at the University of Sheffield

September 2013

“”The most exciting phrase to hear in science, the one that heralds new discoveries, isn't ‘Eureka!’ but rather ‘hmm....that's funny.’”
Isaac Asimov

“Captain, the most elementary and valuable statement in science, the beginning of wisdom, is, ‘I do not know’. I do not know what that is, sir.”
Data, Star Trek: The Next Generation

Declaration

I declare that no part of this thesis has been accepted, or is currently being submitted, for any degree or diploma or certificate or any other qualification in this University or elsewhere.

This thesis is the result of my own work unless otherwise stated.
The following Chapters have been based on publications:

- Chapter 3 – Rose et al. 2011, MNRAS, 414, 3360
- Chapter 4 – Rose et al. 2013a, MNRAS, 432, 2150
- Chapter 5 – Rose et al. 2013b, in prep.
- Chapter 6 – Rose et al. 2013b, in prep.

Acknowledgements

There are many people I wish to thank, without whom the following work would not have been possible. I am sorry if doing this sort of thing in bullet points feels impersonal, but I am not the sentimental type. In no particular order:

- Clive Tadhunter: I am completely in your debt. Without your guidance, support, encouragement and expertise none of my work would have been possible. You have become a close friend as well as my mentor. I thank you.

- My wife, Jennifer Rose: Thank you for being my best friend and soul mate. You have given me the most special memories which I will always hold dear. Without you I surely would not have finished. You are amazing and I love you.

- Mum, my most affectionate thanks goes to you. Thank you for your unconditional love and support. Hopefully I can return the same level of commitment you have shown me.

- Dad, thank you for showing me that I must appreciate what I have, rather than just look to the next thing. Thank you.

- Dave and Christine: Thank you for taking me into your home and giving me a place to write my thesis. Your patience with me has been a great help.

- Richard 'Connman' Connaughton, Paul Munday, Mathew Lee Rose, David Adams, Tim Stewart, Martin Shipston, Marie Lever, Daniel Dewar and Ben Rush: You are the greatest friends any guy could ask for!

- Chris Savoury: Thank you for being a great friend! I miss your face.

- Emile Doran: You are an absolute legend! I will never forget how you out-danced everyone at my wedding!

- Darren White: Thank you for making the periods of procrastination fun. This was made all the better by our mutual love of great snacks!

- Paul 'Pablo' Kerry: I honestly don't think anything would get done if you were not in the department! Thank you for all of your invaluable I.T support and advice.

- In no particular order Patrica Bessiere, Cristina Ramos Almeida, Edgar Ramirez, Daniel Dicken, Javier Rodríguez Zaurín, Joanne Holt, Richard Parker, Richard Allison, Krisada Rawiraswattana, Joanne Bibby, David Hubber, Simon Goodwin, Susan Cartwright, David Sahman, Chris Rosslowe, Pavel 'You Mad Brah?' Lee, Saida Caballero, Stuart Littlefair, Paul Crowther, Vik Dhillion, Thijs Kouwenhoven, Richard de Grijs, Deepak Mahtani, Charlotte Angus, Cass Hall, Liam Hardy thank you for making my time as a grad student enjoyable and the best years of my life (so far). Thanks for all of your support, and good luck.

- I would like to thank Clive Tadhunter, Stuart Littlefair and Javier Rodríguez Zaurín for obtaining the majority of the observational data in this thesis. I would also like to thank both Joanna Holt and Javier Rodríguez Zaurín who reduced the majority of the spectroscopic data analysed in this thesis before I even started my PhD. In addition, I would also like to thank Todd Boroson, Daniel Dicken and Stefi Baum for kindly supplying the data for the PG quasars, 2Jy and 3CRR radio galaxies, and the 12μ Seyfert galaxies respectively.

Summary

A key result of the Two Micron All Sky Survey (2MASS) was the discovery of a population of AGN that appear redder than their traditional UV/optical selected counterparts at IR wavelengths. In order to investigate the nature of 2MASS-selected AGN, in this thesis I present optical spectra and near- to mid-IR photometry for a representative sample of 29 nearby (z<0.28) 2MASS-selected AGN with red near-IR colours (J-$K_S \gtrsim 2.0$), comparing my findings with those obtained for comparison samples of UV/optical selected AGN.

The spectra show a remarkable variety, including moderately reddened type 1 objects (58%), type 1 objects that appear similar to traditional UV/optically selected AGN, narrow-line Seyfert 1 AGN (14%), type 2 AGN (21%) and HII/composite objects (7%). Although the median Balmer decrement suggests significant optical reddening compared to the comparison samples, some objects show relatively little (if any) reddening in their optical spectra. In addition, the near- to mid-IR photometric results reveal that a fraction of the broad-line objects in the 2MASS sample (26%) have unusually blue 2.17-3.4μm colours when compared to the rest of the sample, suggesting that their red near-IR colours are due, at least in part, to emission by a component of hot dust with an unusually high covering factor.

Overall, a variety of mechanisms is required to explain the red near-IR colours of the 2MASS objects: although some are moderately reddened type 1 objects, or 'genuine' type 2 objects that are highly obscured by the central torus structure, others show unusually strong emission from dust close to the AGN. This is confirmed by simple modelling of the colours of the 2MASS and comparison samples However, I find no clear evidence that the 2MASS objects are young, dust enshrouded AGN.

In addition to the analysis of the full 2MASS sample, I present a detailed study of one of the red 2MASS AGN (J1131+16) which shows unusually strong forbidden high ionization lines. This study demonstrates the potential of optical spectroscopic studies of the FHILs for understanding the nature of the obscuring dust structure of AGN.

Contents

Acronyms

AGES	The AGN and Galaxy Evolution Survey
AGN	Active Galactic Nucleus
BLR	Broad Line Region
BLRG	Broad Line Radio Galaxy
BPT	Baldwin, Philips & Terlevich
CCD	Charge-Coupled Device
CFHT	Canada-France-Hawaii Telescope
ESO	European Southern Observatory
FHIL	Forbidden High Ionisation Line
FRI	Fanaroff Riley type 1
FRII	Fanaroff Riley type 2
FSRQs	Flat-Spectrum Radio Quasars
FWHM	Full Width at Half Maximum
GMOS	Gemini Multi-Object Spectrograph
HST	Hubble Space Telescope
HWHM	Half Width at Half Maximum
IPAC	Infrared Processing and Analysis Center
IR	Infrared
IRAF	Image Reduction and Analysis Facility
IRAM	Institut de Radioastronomie Millimétrique
IRAS	Infrared Astronomical Satellite
ISIS	Intermediate dispersion Spectrograph and Imaging System
ISM	Interstellar Medium
JWST	James Webb Space Telescope
LINER	Low-Ionization Nuclear Emission-line Region
LIRIS	Long-slit Intermediate Resolution Infrared Spectrograph
NDWFS	NOAO Deep Wide-Field Survey
NED	NASA/IPAC Extragalactic Database
NLR	Narrow Line Region
NLRG	Narrow Line Radio Galaxy
NLS1	Narrow Line Seyfert 1
NOAO	National Optical Astronomy Observatory
OSP	Old Stellar Population
PA	Position Angle
PAH	Polycyclic Aromatic Hydrocarbon

PFP	Profile-fit Photometry
PG	Palomar-Green
PSF	Point Spread Function
Quasar	Quasi Stellar
QSOs	Quasi Stellar Objects
RA	Right Ascension
SDSS	Sloan Digital Sky Survey
SED	Spectral Energy Distribution
SMBH	Super Massive Black Hole
SSRQs	Steep-Spectrum Radio Quasars
ULIRG	Ultraluminous Infrared Galaxy
UV	Ultraviolet
VLTI	Very Large Telescope Interferometer
WHT	William Herschel Telescope
WISE	Wide-Field Infrared Survey Explorer
WLRG	Weak Line Radio Galaxy
XRB	X-ray Background
YSP	Young Stellar Population
2MASS	2 Micron All Sky Survey
3CRR	Third Cambridge Catalogue of Radio Sources, 2nd revised edition

List of Figures

List of Tables

Chapter 1

Introduction

1.1 Active Galaxies

1.1.1 Historical background

Active galaxies are important objects that allow for detailed study of a wide range of topics in astrophysics, from understanding accretion physics, to learning how the Universe evolves over its lifetime. Active Galactic Nuclei (AGN) produce large amounts of energy from compact regions, probably with radii less than 1 pc. The luminosity is emitted over a broad range of wavelengths (from radio to gamma-rays), and can easily exceed that of the stellar populations in the host galaxies. However, much work is required in order to fully understand this important astrophysical phenomenon.

Unusually strong emission lines in galactic nuclei were first observed in 1908. Whilst investigating the nature of 'spiral nebulae', Fath (1909) noticed that most of the 'spiral nebulae' showed a continuous spectrum with several absorption lines, indicating that 'spiral nebulae' have properties that are expected for a stellar population. However, for one of the objects he observed (NGC 1068), the spectrum was a composite of unusually strong emission lines superimposed onto a continuous spectrum containing absorption lines — a signature of an AGN. But at the time the existence of galaxies other than the Milky Way was unknown.

After the 'island universe theory' of galaxies became the accepted paradigm, the first indication of the existence of extraordinary activity in the nuclei of galaxies was the discovery of broad emission lines (full width at half maximum; FWHM $>$ 2,000 km s^{-1}) in galaxies selected with high nuclear luminosity (Seyfert, 1943). If the Doppler effect dominates the broadening of the lines, then the velocities of the emission line regions

exceed the escape velocity of their galaxies. This suggests that high energy phenomena are happening in the galaxies (now referred to as Seyfert galaxies).

The study of AGN received further stimulus from the opening up of the radio window. In 1932 the Bell Telephone Laboratories commissioned Karl Jansky to investigate sources of static which had been affecting communications across the Atlantic (Jansky, 1932). By thoroughly investigating this static, Jansky found that it moved in azimuth every 24 hours. In addition, he also noted that the time and direction of the maximum intensity of the static changed throughout the year, due to the Earth's orbit around the Sun. Jansky concluded that the source of static was the Milky Way, with the intensity of the signal peaking at the Galactic centre (Jansky, 1935).

Following the work of Jansky, Grote Reber built a radio detector of his own. Using data gathered from his detector, Reber successfully published a map of the radio sky, which showed several regions of strong radio emission, including one in the constellation of Cygnus (Reber, 1944). During the 1940s several other radio surveys were conducted, some of which discovered intense discrete sources of radio emission (Hey, Parsons & Phillips 1946; Bolton & Stanley 1948; Bolton 1948), but initially no optical counterparts for these sources — required in order to understand their nature — were identified, due to limited spatial resolution. The earliest optical identifications of radio sources with galaxies were made by Bolton, Stanley & Slee (1949) and Baade & Minokowski (1954) based on the accurate positions provided by interferometry techniques, but further progress in understanding the radio sources was slow, until the observation of an optical counterpart for 3C 48. In 1960 3C 48 was identified with a blue star-like object that was described to have a 'wisp of nebulosity' associated with it. However, 3C 48 had an unusual spectrum containing broad emission lines at wavelengths which were not associated with any known atomic transitions. In addition, photometry of 3C 48 revealed that the source is in fact variable and has an excess of UV emission when compared to typical stars (Matthews & Sandage, 1963). Despite these properties, it was concluded that 3C 48 was a nearby, albeit unusual, star.

A further breakthrough came in 1962 when the radio source 3C 273 underwent 5 lunar occultations. An accurate position was determined for 3C 273, revealing two components for this radio source (see Figure 1.1). These components coincided with a star-like object (much like 3C 48) and a jet-like feature, possibly being emitted by the 'star' (Hazard, Mackey & Schmidt, 1963). Once an accurate position for the star-like object was determined, an optical spectrum was obtained. Like 3C 48, 3C 273 had an unusual spectrum containing broad emission lines at wavelengths that did not coincide with any known species (see Figure 1.2). Fortunately, Schmidt noticed that four of these

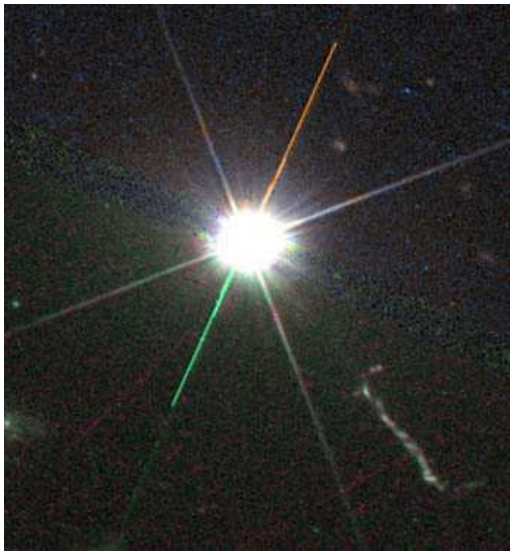

Figure 1.1: An image of 3C273, note the jet feature in the bottom right. Taken from sns.ias.edu.

emission lines followed a familiar pattern: the Balmer series of hydrogen. Realising this enabled Schmidt to determine that 3C 273 is an extragalactic source at redshift z=0.16 (Schmidt, 1963). This led to the estimation of a redshift for 3C 48: z=0.37, which was the highest redshift recorded in the Universe at the time.

By determining luminosities based on Hβ emission flux, and deducing densities from the presence of forbidden high ionization lines (FHILs), radii of 11 pc and 1.2 pc were calculated for the emission line regions of 3C 48 and 3C 273 respectively (Greenstein & Schmidt, 1964). Given their sizes, it was suggested that these objects could be contained within a galaxy (Greenstein & Schmidt, 1964). The overall interpretation given to these findings is that the radio sources are compact, and located at cosmological distances.

1.2 Classification of AGN

With the advance of technology and observational techniques, AGN have been classified according to their optical spectral and morphological properties, as well as their radio luminosities and morphologies. Details of the classifications of AGN are given in the following sub-sections.

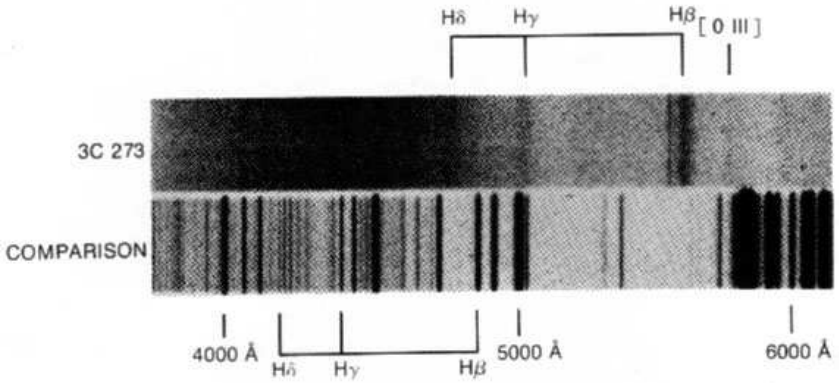

Figure 1.2: The spectrum of 3C 373 plotted with a comparison spectrum. The position of the Balmer series is indicated on both spectra and they are clearly redshifted in 3C 273 (Schmidt, 1963).

1.2.1 Radio-quiet AGN

Broadly, AGN can be separated by their radio power: strong radio emitters are classed as radio-loud; others as radio-quiet. Since there is a continuous range of radio power in the AGN population, the division between the two types is to some extent arbitrary. In this thesis I define radio-loud AGN to have radio power[1] $P_{178MHz} > 10^{25}$ W Hz^{-1}. This is lower than the conventional division between Fanaroff-Riley I and II (FRI and FRII) radio galaxies ($P_{178MHz} \sim 10^{26}$ W Hz^{-1} Fanaroff & Riley 1974, see below), but much higher than the powers of the brightest Seyfert galaxies (e.g. NGC 1068 with P_{178MHz} = 3.3 x 10^{23} W Hz^{-1} at radio wavelengths; Spinrad et al. 1985). Although radio-quiet AGN are not as powerful at radio wavelengths as radio-loud AGN, this class of objects represents ∼90% of the overall population, making them the critical to our understanding of AGN.

Seyfert galaxies

Seyfert galaxies are low-luminosity (when compared to quasars, see below), radio-quiet AGN. Seyfert galaxies appear as normal spiral galaxies, with bright resolved nuclei superimposed on their underlying galaxies; unlike quasars, the AGN do not outshine their host galaxies. The host galaxies of Seyfert galaxies are typically spiral galaxies, and the majority are early-type spirals (e.g. Sa-type, Adams 1977; Heckman 1978). However, there is a small, but significant fraction of Seyfert galaxies whose host galaxies are early-type (elliptical) galaxies, as well as S0-type (lenticular) galaxies (see Adams 1977;

[1]Throughout this thesis the following cosmological parameters are assumed: $H_0 = 70$ km s^{-1} Mpc^{-1}, $\Omega_M = 0.3$, and $\Omega_\Lambda = 0.7$.

Ferruit, Wilson & Mulchaey 2000).

The original definition of Seyfert galaxies was based on the fact that they have bright nuclei and broad optical emission lines. However spectroscopic studies of these objects have revealed unusual emission-line ratios, and therefore the definition has evolved so that Seyfert galaxies are now identified spectroscopically. Seyfert galaxies exhibit strong permitted and forbidden emission lines, which include hydrogen recombination lines (such as the Balmer series), low ionisation forbidden emission lines such as [OII]$\lambda\lambda$3726,3729, [NII]$\lambda\lambda$6548,6583 and [SII]$\lambda\lambda$6716,6731, as well as forbidden emission lines with higher ionisation potentials ($I_p > 35.1$ eV) like HeIIλ4686, [OIII]$\lambda\lambda$4959,5007, [NeV]λ3426 and [FeX]λ6375. The [NeV]λ3426 and [FeX]λ6375 unambiguously indicate the presence of an AGN, as they are not associated with starbursts.

Seyfert galaxies are divided into two sub-classes based on the presence of broad permitted emission lines in their spectra (Khachikian & Weedman, 1974). Type 1 objects have broad (FWHM >1000 km s^{-1}) permitted emission, emitted by a region of high electron density ($n_e > 10^8$ cm^{-3}), superimposed on a spectrum of narrow (FWHM <1000 km s^{-1}) permitted and forbidden emission lines, whereas type 2 objects only contain the narrow emission lines. Since many of the narrow lines are forbidden, they are produced in relatively low density regions ($n_e \sim 10^3 - 10^7$ cm^{-3}).

In addition to the emission lines, both type 1 and 2 Seyfert galaxies often show absorption lines in their spectra, and the continuum can be described using a combination of a power-law and a host galaxy component. Figure 1.3 gives examples of such spectra. Note the obvious broad emission lines in the type 1 object when compared to the type 2 object.

Quasars

Quasars are the most luminous AGN, and their nuclei outshine the stellar emission of their host galaxies. In this thesis, I have used the [OIII]λ5007 emission line luminosity to define whether an AGN is a quasar, or whether it is a Seyfert galaxy. The [OIII]λ5007 emission line luminosity has been shown to be a good indicator of AGN bolometric power (see Heckman et al. 2004; Bian et al. 2006; Dicken et al. 2009; LaMassa et al. 2010). Following Zakamska et al. (2003) I have assumed that an object is a quasar if it has an [OIII]λ5007 luminosity $L_{[OIII]} \gtrsim 10^{35}$ W, corresponding to a nuclear continuum luminosity of $M_B \lesssim$ -23 (Schmidt & Green 1983; Zakamska et al. 2003).

A small fraction of quasars are strong radio emitters, including the first two to be discovered (3C 273 and 3C 48). Quasar spectra are similar to those of Seyfert galaxies,

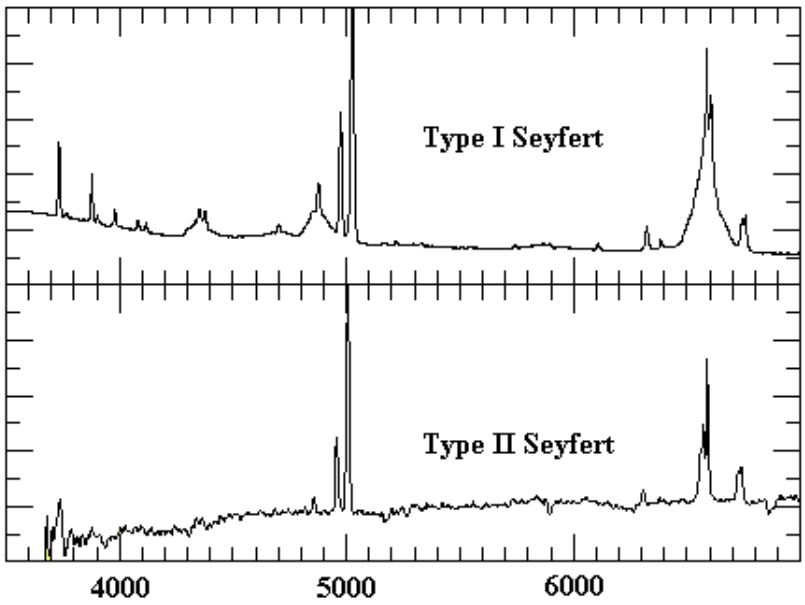

Figure 1.3: *Top.* Spectrum of a type 1 Seyfert galaxy. *Bottom.* Spectrum of a type 2 Seyfert galaxy. Taken from http://www.astr.ua.edu/keel/agn/.

except for a few key differences: any stellar absorption features are very weak because the AGN outshines the host galaxy, and the narrow emission lines have lower equivalent widths relative to the broad emission lines, when compared to those in Seyfert galaxies (Baldwin, 1977). However, these differences simply boil down to the individual luminosities of the AGN. The division between Seyfert galaxies and quasars is arbitrary.

LINERs

Low Ionisation Nuclear Emission-line Regions (LINERs) are a sub-class of galactic nuclei defined by their emission properties (see Heckman 1980). The spectra of LINERs are dominated by emission lines from neutral and low ionisation emission species such as [OI]λ6300, [OII]λ3727, [NII]$\lambda\lambda$6548,6583 and [SII]$\lambda\lambda$6716,6731, but they also have weak emission from higher ionisation species that are typical in AGN spectra (e.g. [OIII]λ5007). In general, LINERs have modest emission line luminosities — emission lines such as [OIII]λ5007 are generally weaker than in Seyfert galaxies, but similar to those of giant HII regions (Kennicutt 1978; Heckman 1980). However, unlike HII regions, low excitation forbidden emission lines, such as those of [OI]λ6300, [NII]$\lambda\lambda$6548,6583 and [SII]$\lambda\lambda$6716,6731 are strong relative to the permitted recombination emission lines (Heckman, 1980).

LINERs are common — almost 1/3 of nearby galaxies show emission from LINERs,

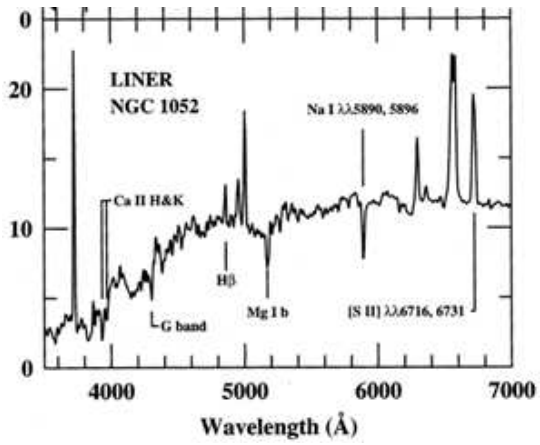

Figure 1.4: The spectrum of the LINER NGC 1052, with the key emission lines identified, take from Ho, Filippenko & Sargent (1993). Note the comparable strength of the lower ionisation emission lines and the [OIII]λ5007 emission line.

much higher than the rate of Seyfert type AGN in galaxies ($\sim$1%, Heckman 1980; Ho 1999). In addition, the velocity widths (FWHM) of the emission lines in LINER spectra are comparable to those of the narrow-lines of Seyfert galaxies (see Figure 1.4, Koski 1978; Heckman 1980; Ho, Filippenko & Sargent 1993).

The ionization mechanism for LINERs is uncertain. Some argue that LINERs are photoionized by AGN, but at lower ionization parameters than Seyfert galaxies (Heckman 1980; Ho, Filippenko & Sargent 1993). Others believe that the emission regions may be photoionized and shock heated by star forming regions (Terlevich & Melnick 1985; Shields 1992). The general consensus is that the population is heterogeneous.

1.2.2 Radio-loud AGN

Radio-loud galaxies are a subset of active galaxies which are extremely luminous at radio wavelengths: $P_{178MHz} > 10^{25}$ W Hz^{-1}. The radio emission is attributed to synchrotron emission caused by relativistic electrons spiralling in a magnetic field (Burbidge 1956; Ginzburg & Syrovatskii 1965). Radio galaxies are noted for the presence of large radio lobes, which are ellipsoidal structures positioned on either side of the active nucleus. These radio lobes are often connected to jets which originate from the nuclei of the AGN. The jets are believed to be caused spinning black holes in the nuclei of the galaxies (Scheuer 1974; Blandford & Rees 1974). Another common property of radio-loud AGN is that their host galaxies are invariably elliptical galaxies, which suggests that the host galaxy environment of the AGN plays a vital role in producing the large radio luminosities (Antonucci 1993; Urry & Padovani 1995; Wilson & Colbert 1995; Dunlop et al. 2003).

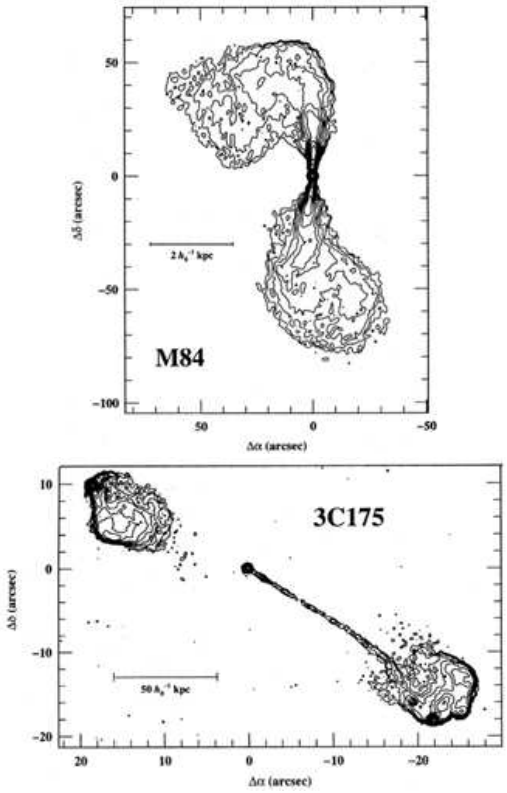

Figure 1.5: *Top.* Radio map of the FRI galaxy M84. The core and jets clearly dominate in this radio map. *Bottom.* Radio map of the FRII galaxy 3C175. Here the radio lobes are dominant. Both figures were taken from Peterson (1997).

Fanaroff-Riley classifications

Radio-loud galaxies can be divided into two main classes, based on their large scale radio structures (Fanaroff & Riley, 1974) as follows.

FRI radio galaxies are usually lower luminosity ($P_{178MHz} < 2x10^{25}$ W Hz^{-1}) objects, whose morphologies show a bright core with continuous jets joining edge darkened radio lobes (Fanaroff & Riley, 1974). An example of the morphology of an FRI is given in Figure 1.5 (top).

FRII radio galaxies are usually more luminous than FRI radio galaxies ($P_{178MHz} > 2x10^{25}$ W Hz^{-1}), with a lobe dominated morphology (rather than being dominated by the core) where the lobes are edge brightened (Fanaroff & Riley, 1974). The jets in FRII radio galaxies are more clumpy than those in FRI radio galaxies. An example of the morphology of an FRII is given in Figure 1.5 (bottom).

BL Lac objects, FSRQs and SSRQs

BL Lac objects are highly variable (days or even hours), highly linearly polarised AGN that show virtually featureless continuous spectra. While the jets in both FRI and FRII objects are orientated so that they are at a large angle to the observers line of sight, it is believed that BL Lac objects are observed face on (Stein, Odell & Strittmatter, 1976). The jet orientation results in a rapidly varying high luminosity object, with highly polarised optical emission.

In addition to BL Lac objects, flat-spectrum radio quasars (FSRQs) and steep-spectrum radio quasars (SSRQs) show variability in their optical continua. FSRQs are characterised by strong and rapid variability, high polarization, and apparent superluminal motion. This is believed to be the result of emission from a jet oriented face on. On the other hand, the properties of SSRQs are intermediate between FSRQs and radio quiet quasars because the jet is viewed more edge on (Urry & Padovani 1995; Gu & Ai 2011).

Optical spectra

Considering their optical spectral properties, radio-loud AGN are analogous to radio-quiet AGN, i.e. Seyfert galaxies. Much like Seyfert galaxies, radio-loud AGN have strong permitted and forbidden emission lines. In addition, they can also be classified according to the presence, or absence of, broad permitted emission lines: broad line radio galaxies (BLRGs) have broad permitted emission lines (> 1000 km s^{-1}) superimposed on a spectrum of narrow emission lines, whereas narrow line radio galaxies (NLRGs) show only the narrow emission lines. In addition, there is another subclass of radio galaxies — weak line radio galaxies (WLRGs) which have emission lines with low ($<$ 10Å for [OIII]λ5007; Tadhunter et al. 1998) equivalent widths. WLRGs are thought to be objects in which the activity of the central AGN is low. This is possibly due to low accretion rates leading to a low-luminosity AGN. Alternatively, the AGN may have recently switched off, resulting in weak emission from the clouds in the immediate emission regions, but the information about the change in AGN activity has not yet reached the bright radio lobes (Tadhunter et al. 1998; Capetti et al. 2011; Tadhunter et al. 2012).

1.2.3 The energy source

It is believed that AGN are powered by the accretion of material by a supermassive black hole (SMBH) with a mass in the range $10^6 < M_{BH} < 10^{10}$ $M_\odot$ (Rees, 1984). The efficiency of energy generation via accretion ($\sim$10 - 30% ; the highest efficiencies require a spinning BH) is far higher than that of nuclear fusion ($\sim$0.7%), allowing AGN to be amongst the most energetic phenomena in the Universe (Peterson, 1997). The material for accretion is provided either by secular events, such as gas flows along bars in galaxy bars, or supernova winds (see Draper & Ballantyne 2012, and references therein), or by galaxy mergers and interactions (e.g. Di Matteo, Springel & Hernquist 2005).

In the cases where AGN are triggered by galaxy mergers, during the early phase of the AGNs lifetime the SMBH is expected to be enshrouded in a cocoon of gas and dust, obscuring the AGN from view (e.g. Hopkins et al. 2006). While active, AGN produce powerful winds (e.g. Balsara & Krolik 1993), which have the potential to sweep out the enshrouding material, unveiling the central AGN (e.g. Silk & Rees 1998).

1.3 Orientation-based unified schemes

In an attempt to understand the nature of AGN, and the relationship between the different types, several orientation-based 'unified schemes' have been proposed. In these schemes, the AGN itself is assumed to be intrinsically the same in all the classes of objects being unified, however its appearance changes depending on the orientation at which we observe the system. The cause of this orientation dependence is the anisotropy of the nuclear emission, due to the obscuring effect of a dusty torus structure surrounding the nucleus and, in the case of radio-loud AGN, the beaming of radiation by the relativistic jets.

1.3.1 Emission regions and the torus

Figure 1.6 presents the unified schemes for both radio-loud and radio-quiet AGN. In the orientation-based unified scheme, the AGN is surrounded by a dusty obscuring torus. The high density broad-line region (BLR) is situated near the nucleus (r < 1 pc). This high density minimises any emission from forbidden lines, because these species are more likely to be collisionally de-excited. Surrounding the BLR is the lower-density narrow-line region (NLR) which extends to $\sim$ 0.1 – 1 kpc. This lower density allows for the emission of forbidden lines. In objects orientated face-on the BLR is directly visible,

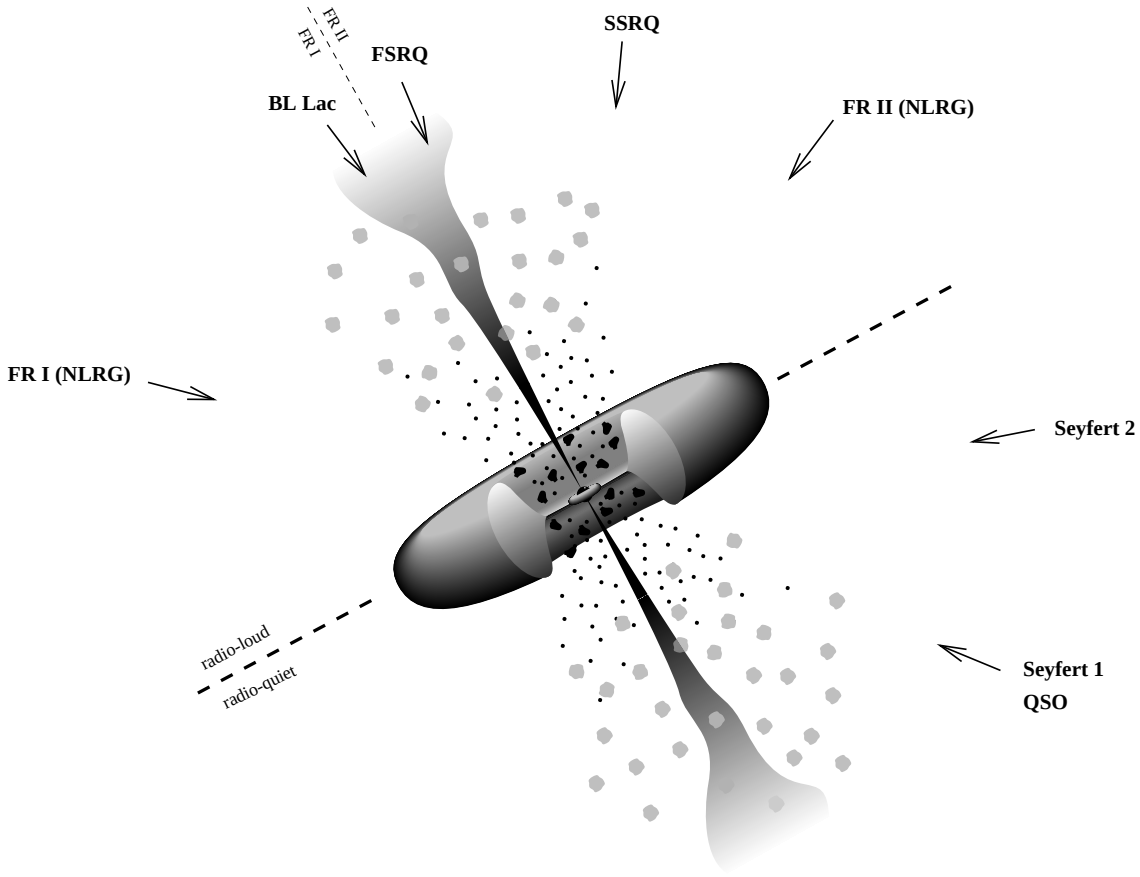

Figure 1.6: Diagram showing the unified schemes for AGN. The grey clouds represent the clouds in the NLR, black clouds are BLR clouds, the donut is the torus, the central structure within the torus is the SMBH and accretion disk, and the jets are the relativistic jets often seen in radio galaxies. The acronyms are described in the text. Note that the viewing angle required for each object is shown by the arrows next to each acronym. Taken from Torres & Anchordoqui (2004).

and therefore such objects are classified as type 1 objects. However, type 2 objects are orientated closer to edge-on, with the torus preventing our direct view of their BLR at optical wavelengths (Urry & Padovani, 1995). This scheme can be used to explain the observations of the spectral properties of both radio-loud and radio-quiet AGN.

This picture of an AGN surrounded by an obscuring torus has been supported by a number of studies: Antonucci (1984) reported differences in the polarisation properties of NLRG and BLRG; Antonucci & Miller (1985) detected broad-lines in the polarised light of the Seyfert 2 object NGC 1068; and using X-ray observations, Lawrence & Elvis (1982) found a higher column density of absorbing gas in Seyfert 2 galaxies when compared with Seyfert 1 galaxies.

There is much uncertainty surrounding the actual size and scale of the torus, with some observations suggesting a small torus (< 10 pc) and others a much larger torus ($\sim$ 1000 pc). An example of an AGN with an apparently small torus is the Circinus galaxy. Using infrared (IR) interferometric observations with the VLTI, Tristram et al. (2007b) reported a torus size of 2 pc. In contrast, to explain the mid- to far-infrared (MFIR) SEDs of AGN, Pier & Krolik (1993) concluded that the size of the torus must extend up to 100 pc. In addition, Schinnerer et al. (1999,2000) used CO molecular line observations with the IRAM millimeter interferometer in both the Seyfert 1 galaxy NGC 3227, and in the Seyfert 2 galaxy NGC 1068, to trace large scale structures ($\sim$150 pc), which are believed to be part of the torus.

However, observations with the VLTI trace the hot inner regions of the torus, whereas molecular line observations trace the outer regions, which can therefore lead to such differences in the estimation of the size of the torus. In addition, it must be noted that it is difficult to discern where the torii end, and the kpc dust lanes of host galaxies begin (Elvis, 2012). Indeed, Hubble imaging of the host galaxies of narrow-line AGN shows that there are dust lanes crossing the nuclei of AGN on large ($>$100 pc) scales (Malkan, Gorjian & Tam, 1998).

There are two main models for the dusty torus: a homogeneous, donut structure, and a clumpy ring of individual clouds. In the following sections I will describe these models.

The homogeneous torus

The homogeneous torus model consists of a continuous dust/gas structure with a donut, or toroidal shape (Pier & Krolik, 1992), and an inner radius set by the sublimation temperature of the dust grains, $\sim$ 1500K (Pier & Krolik, 1992). The inner wall of the

torus is expected to emit radiation at near-IR wavelengths, and, as the distance from the SMBH increases, the temperature of the dust grains become cooler. Therefore the outer parts of the torus are expected to emit radiation at longer MFIR wavelengths (Hill, Goodrich & Depoy, 1996).

The homogeneous torus model faces a few challenges when explaining the observed IR properties of AGN. One challenge is that the model predicts that a strong 9.7μm silicate feature should be detected in absorption in mid-IR spectra of type 2 AGN, and in emission in type 1 AGN. However, in reality, the silicate features are not always observed to be as strong as predicted (Roche, Aitken & Smith, 1991). In addition, the homogeneous torus model cannot reproduce the observed strength of the far-IR emission detected in many AGN. To solve these problems, a more extended torus structure of diffuse dust was proposed, extending the size of the torus to an outer radius of $\sim$ 100 pc (Pier & Krolik, 1993). But the model still struggled to reproduce the 9.7μm silicate features in the emission spectra of AGN.

In addition to the IR properties, the homogeneous torus model also fails to reproduce X-ray observations of AGN. For example, the X-ray absorbing column density is observed to vary on timescales of months to years (Risaliti et al., 2002, 2005), but the homogeneous torus model fails to reproduce this variability[2].

These challenges motivated the development of a more complex model for the torus.

The clumpy torus

The study of Pier & Krolik (1992) was the first to suggest that the torus could have a clumpy structure, rather than a homogeneous one. However, the clumpy torus model was not fully developed until the seminal work of Nenkova et al. (2002, 2008a,b). In this model, the dust is distributed in discrete clouds, or clumps, surrounding the central SMBH, but still with a toroidal geometry overall.

In the clumpy torus model the temperatures of the dust grains in the discrete clumps are less dependent on distance from the centre, when compared to the homogeneous models. Therefore the clouds in the clumpy torus have a range of temperatures at each distance from the inner wall of the torus. Also, it is possible for radiation from the inner (hotter) parts of the torus to pass through the outer parts of the torus without major attenuation. This results in the correct modelling of the 9.7μm silicate emission/absorption lines, and gives an outer radius for the torus which agrees better with

[2]The variability in the observed X-ray absorbing column density is not attributed to intrinsic X-ray source variability, because no correlation has been found between variations of the column density and intrinsic X-ray flux (Risaliti, Elvis & Nicastro, 2005).

observation (Nenkova et al., 2002, 2008a,b).

Although the clumpy torus model has many strengths when explaining observational data, it assumes that all the IR emission is radiated by the torus. However, IR emission is radiated by larger-scale dust located in the host galaxy, which can be heated by either the AGN, or regions of star formation (Dicken et al., 2009). For low spatial resolution mid- to far-IR observations, the large-scale dust emission can contaminate the torus emission, leading to spurious modelling results.

1.3.2 Radio-loud and radio-quiet AGN

The orientation-based unified schemes can explain many of the observed AGN properties, however they fail to explain the differences between radio-loud and radio-quiet AGN, because the torus cannot hide the extended radio lobe emission in radio-quiet AGN. Other factors, perhaps related to the physics of the central engine, may be required to explain the differences in the radio properties of AGN (e.g. Blandford & Znajek 1977; Wilson & Colbert 1995; Nipoti, Blundell & Binney 2005).

1.4 Selecting AGN

1.4.1 Radio

Historically, the first extensive studies of AGN were at radio wavelengths. Indeed, the Third Cambridge Catalogue of Radio Sources (3C) catalogued the first confirmed quasars (e.g. 3C 48, 3C 273). There have been several more recent radio surveys, such as the NRAO VLA Sky Survey (NVSS) and the NRAO Very Large Array (VLA) Faint Images of the Radio Sky at Twenty-cm (FIRST) survey, which have broadened our understanding of AGN at radio wavelengths.

However, bright radio surveys pick up the less than 10% of AGN that are radio-loud (White et al., 2000), and, at faint limits, deep radio surveys are contaminated by star-forming galaxies (Pooley 1969; Ilovaisky & Lequeux 1972; Condon 1992; Condon et al. 1998; Ivezić et al. 2002). Given these shortcomings, follow-up studies at different wavelengths are often needed to discriminate between the different phenomena. Although AGN detected in radio surveys can be confirmed spectroscopically, not all strong radio AGN show obvious AGN signatures in their optical spectra (Ivezić et al., 2002), for example, the WLRG mentioned earlier. Alternatively, the ratio of IR to radio fluxes can be used to determine whether the source of the radio emission is either a star forming

region, or an AGN: objects with low IR to radio flux ratios are AGN, conversely those with high ratios are starburst objects (Condon, Anderson & Broderick, 1995). However, some objects with high ratios have been found to be radio-quiet AGN (Mushotzky, 2004).

Given these shortcomings, and the fact that truly radio-loud AGN are relatively rare compared with radio-quiet AGN, the majority of AGN have been selected at other wavelengths.

1.4.2 UV/Optical

At UV/optical wavelengths AGN have been selected using a variety of techniques. One such technique selects AGN using a colour criterion, exploiting the fact that AGN colours, in particular the colours of quasars, are systematically different from those of quiescent galaxies. The differences are due to the AGN continuum shapes, the AGN continuum dominates more at blue/UV wavelengths than in quiescent galaxies, and therefore AGN can be selected on this basis. This technique uses multiple exposures taken through two or three filters to isolate the bluest objects, and has been used to select the quasars in the well-known Palomar-Green survey (see Schmidt & Green 1983 and Boroson & Green 1992).

The Sloan Digital Sky Survey (SDSS) was another survey which selected AGN based on their colours. However, when compared to previous surveys the SDSS used longer wavelength filters to ensure better coverage. In addition, many of the observed sources were followed up by optical spectroscopic observations. Indeed, 'The Quasar Sample' candidates were initially selected for spectroscopic follow up based on SDSS colours (Richards et al., 2002).

Another two methods employ objective prisms. One of these is known as the UV-excess technique, and was used by Markarian (1967) and Markarian, Lipovetskii & Stepanian (1981) to select galaxies with measurable, or appreciable, excess radiation in the UV part of the spectrum, many of which are AGN. It is similar to the colour selection method in that the criterion for inclusion is the presence of a very blue continuum (see above). The second, objective prism method, selects objects through the presence of emission lines in the objective-prism spectra. The idea is that high redshift AGN (and other interesting galaxies) can be distinguished from quiescent galaxies by the presence of strong emission lines such as Lyα, Hα and [OIII]λ5007. One such survey which used this method was the Tololo survey (Smith 1975; Smith, Aguirre & Zemelman 1976).

These methods are efficient at selecting high luminosity, type 1 AGN because the AGN dominates (i.e. outshines the host galaxy stars) at blue optical colours. However,

low-luminosity type 1 AGN, and type 2 AGN are less effectively selected by such methods because: (a) there is often considerable contamination from host galaxy stars at all wavelengths; (b) type 2 AGN continua are obscured by the dusty torus—therefore there is no 'blue excess' which is key to selecting AGN at these wavelengths (Zakamska et al., 2004); and (c) many AGN have large amounts of dust and gas in the line of sight of the observations, and such dust extinction can make type 1 objects appear 'redder' in their colour selection, leading to them not being selected in UV/optical colour-based AGN surveys (Mushotzky, 2004).

Clearly, UV/optical surveys are biased against objects that are subject to dust reddening/obscuration. However, the effects of reddening can be overcome by making surveys at longer wavelengths. Indeed, such surveys opened up the possibility of detecting AGN which are not 'typical' UV/optically selected AGN, hence expanding our knowledge of the field and opening up new avenues for study.

1.4.3 Obscured AGN in the local Universe

Whilst UV/optical surveys have been successful at selecting AGN, there is evidence that there also exists a red, potentially obscured, population of AGN in the local Universe, which has been missed by such surveys because it cannot match the required selection criteria. Below I discuss a few of the strands of evidence for this population.

Mid-IR and radio surveys. Mid-IR and radio surveys, which are less affected by dust extinction when compared to UV/optical surveys, suggest that >50% of AGN have been missed by short wavelength surveys. For example, the Infrared Astronomical Satellite (IRAS) found IR-luminous AGN which were not found using the typical UV/optical selection techniques, thus indicating the existence of a population of red, optically obscured AGN (Low et al., 1988). Webster et al. (1995) showed that AGN selected from radio catalogues have a wide range of optical colours. They interpret these colours as the result of varying amounts of dust along the line of sight. Webster et al. (1995) state that, if the general population of radio-quiet AGN contain as much dust as detected in radio-loud AGN (and have gone undetected at other wavelengths), then 80% of this population may have been missed by optical surveys.

The X-ray background (XRB). The origin of the XRB has been a point of interest since its discovery in the 1960s (Giaconni et al., 1962). Observations at energies below 10 keV demonstrated that a significant fraction of emission of the XRB consists of

point sources, some of which were identified with AGN (Shanks et al., 1991). But early suggestions that the XRB is the result of emission from typical, unobscured AGN could not account for the fact that such AGN have a steeper X-ray spectrum (spectral energy index of $\alpha \approx 0.7$ between energies of 2-10 keV, where $F_\nu \propto \nu^{-\alpha}$), than the XRB below 10 keV ($\alpha \approx 0.5$ between energies of 2-10 keV; Fabian & Barcons 1992). On the other hand, obscured AGN have a flatter spectrum which can account for the shape of the XRB spectrum. Indeed, the seminal work of Comastri et al. (1995) suggested that emission from an obscured population of AGN accounts for at least part of the XRB.

Given that this population of obscured AGN potentially represent a significant fraction of the AGN population, it is important that we understand how they are related to the unobscured AGN. Recently the study of obscured AGN has received considerable impetus from studies at near-IR wavelengths thanks to data available from the Two Micron All Sky Survey (2MASS). A key result of 2MASS was the discovery of a population of AGN that appear redder than their traditional optical/UV selected counterparts at near-IR wavelengths. These 2MASS AGN are described in the next section.

2MASS-selected red AGN

2MASS delivered uniform photometry and astrometry over the entire sky in the J (1.25 μm), H (1.65 μm), and K_S (2.16 μm) near-IR photometric bands. The 2MASS sensitivity specification was J = 15.8, H = 15.1, and K_S = 14.3 at a signal-to-noise ratio of S/N = 10. 2MASS produced a Point Source Catalog (PSC) that contains 470,992,970 sources, and an Extended Source Catalog (ESC) of 1,647,599 sources, covering 99.998% of the sky. These catalogs make up the 2MASS All-Sky Data Release (Skrutskie et al., 2006).

Amongst the many goals of 2MASS, one was to search for objects that are heavily obscured at optical wavelengths. In the near-IR, type 1 AGN are known to have redder colours than quiescent galaxies (Rieke, 1978). 2MASS successfully detected well known samples of UV/optically selected type 1 AGN: 100% of the PG quasars (Boroson & Green, 1992), 99% of the Hamburg/ESO QSOs (Wisotzki et al, 1996) and 75% of the Large Bright Quasar Survey (LBQS; Hewitt, Foltz & Chaffee 1995). Note that the majority of these AGN (95%; Cutri et al. 2002), while redder than stellar populations in galaxies, have NIR colours of J-K_S < 2.0.

Prior to 2MASS, surveys at mid-IR and X-ray wavelengths had indicated that UV/optical surveys had missed a significant fraction of AGN (e.g. Low et al. 1988) because their selection was biased towards unreddened, 'blue' AGN (see above). Therefore Cutri et al.

(2002) selected objects detected in all 3 2MASS bands with J-K_S > 2.0, with Galactic latitudes $|b| > 30°$ to avoid Galactic AGB stars (Cutri et al., 2002). In addition, K_S-band magnitudes in the range 11.0 < K_S < 14.9 were used. The latter criterion was chosen so that bright (K_S < 11.0) Galactic AGB and carbon stars were excluded, along with 'normal' galaxies in the redshift range 0.4 < z < 0.5 (K_S > 14.9; Cutri et al. 2002). These selection criteria produced over 17000 red AGN candidates, most of which were previously undiscovered.

However, there are a few caveats with this selection. One such caveat is that, because of host galaxy contamination, low luminosity and redshift AGN are missed. This is because the host galaxy stars contribute more flux at shorter wavelengths than at the longer wavelengths. The other caveat is that the SEDs of quiescent galaxies at redshifts between z=0.4–0.5 may also produce the red NIR colours (Cutri et al., 2002).

A spectroscopic follow up of 704 of the red AGN candidates was carried out. It was found that 55% of the objects are Type 1/Quasar objects, 14% are Type 2/LINER objects, 15% are quiescent galaxies, 10% are unusual stars such as carbon stars, and the remaining objects could not be identified due to insufficient signal-to-noise in their optical spectra (Cutri et al., 2002). The red AGN candidates selected from 2MASS represent a population of objects that have remained hidden from surveys at other wavelengths, and understanding this population is critical to our overall understanding of the entire AGN population.

1.5 Recent studies

Because the red 2MASS AGN potentially make up a large fraction of the AGN population, it is important that we understand their relationship to the unobscured population: are they young, dust obscured versions of 'typical quasars' (Hutchings et al. 2003; Georgakakis et al. 2009; Glikman et al. 2007; Glikman at al. 2012)? Or can their properties be explained by a specific viewing angle in the orientation-based unified schemes (Wilkes et al., 2002)? Are they high-redshift galaxies whose dominant emission has been shifted into the near-IR? Or do they perhaps represent a new population altogether? Are these objects all luminous quasars, or are some less luminous AGN?

There have been several studies of red 2MASS AGN in the past that have focussed on different wavelength regions (e.g. UV, optical or IR). The basic properties of the samples used for the previous studies are summarised in Table 1.1. Many of these past studies concluded that the red 2MASS quasars are young, dust-enshrouded, transitional

objects, based on the following five strands of evidence.

- **Morphological disturbance of the host galaxies.** Urrutia, Lacy & Becker (2008) followed up a representative sub-sample of 13 of the Glikman et al. (2007) sample (see Table 1.1), with $0.4 < z < 1$, using imaging observations with the ACS Wide Field Camera on the Hubble Space Telescope (HST) with the F475W and F814W filters. Their sub-sample is relatively luminous, with intrinsic AGN absolute magnitudes in the range $-26.2 \leq M_B \leq -23.5$. They found that 85% of the host galaxies in their sample show evidence for morphological disturbance, with the level of disturbance appearing to increase with the measured reddening of the AGN. Similarly, using CFHT snapshot R-band data, Hutchings et al. (2003) report a high incidence of host galaxy interaction (>70%) in their sample, based on a qualitative analysis of their images. These findings are consistent with the idea that the AGN are triggered by mergers, as gas and dust is driven into the near-nuclear regions of the merger remnant. In this scenario AGN start their lives obscured by a natal cocoon of dust, and appear in UV/optical surveys once the obscuring dust has been removed by AGN winds (e.g. Saunders et al. 1989; Hopkins et al. 2005; Narayanan et al. 2006; Hopkins et al. 2006).

- **High rate of occurrence of outflows based on absorption line studies.** Broad absorption line (BAL) quasars are defined as objects with blueshifted ($\sim$3000–25000 km s^{-1}), broad absorption features (FWHM > 2000 km s^1) associated with UV resonance lines (Weymann et al., 1991). These can be divided into objects that lack MgII absorption — high-ionization BALs (HiBALs) — and objects with MgII absorption — low-ionization BALs (LoBALs). While the overall incidence of BALs in the population of red 2MASS quasars is similar to the general population of UV/optical selected quasars (63% and 61% for Urrutia et al. (2009) and Glikman at al. (2012) respectively), for objects with redshifts that allow the detection of BALs, both Urrutia et al. (2009) and Glikman at al. (2012) find that 95% of their BAL objects are LoBALs. This is in contrast to rate of occurrence in UV/optical selected quasars where LoBALs make only 10-20% of the BAL population (Trump, Hall & Reichard, 2006). A high fraction of LoBALs is thought to be consistent with a population of objects representing a transitional stage in quasar evolution. This is because the presence of LoBALs is believed to be evidence that AGN are 'casting off' their cocoons of dust and gas (e.g. see Voit, Weymann & Korista 1993).

- **High star formation rates.** Mid- to far-IR observations of the red quasars show evidence for higher star-formation rates than measured in samples of UV/optical selected quasars. Using Spitzer photometric data, Georgakakis et al. (2009) determined that their sample of red quasars shows evidence for relatively high star formation rates, based on 60/12 μm flux ratios which are high compared to the PG quasars. Similarly, using IRS spectra, Shi et al. (2007) detect strong Polycyclic Aromatic Hydrocarbon (PAH) features in 40% of their 2MASS sample at 7.7 μm and 11.3 μm — signatures of star formation in galaxies. By comparing their results to the PG quasars and 3CR objects, Shi et al. (2007) find that the star formation rates in the red 2MASS quasars are higher than those of the UV/optical selected quasar samples.

- **High accretion rates.** Based on both broad hydrogen emission line luminosities (Balmer, Paschen etc.) and SED fitting, Urrutia et al. (2012) find that a large fraction of their sample ($\sim$54%) have relatively high Eddington ratios ($L_{BOL}/L_{EDD} > 0.3$). Higher than in UV/optical selected samples.

- **Rapid growth of Black Holes.** Canalizo et al. (2012) measured black hole masses and host galaxy properties for 29 red 2MASS AGN with $0.17 < z < 0.37$, finding that the majority of red 2MASS AGN have significantly more massive black holes than those in local AGN. Canalizo et al. (2012) believe that this indicates that the SMBH had undergone a period of rapid growth.

The majority of these previous studies of red AGN have focussed on samples covering a wide range of redshift ($0 < z < 3$). The problem with such samples is it is difficult to: (a) investigate the intrinsic diversity of the red quasar population in the face of possible evolutionary and/or luminosity-dependent effects, (b) obtain accurate estimates of the levels of dust extinction in the high redshift AGN because of the challenges faced with measuring the Balmer decrements in high redshift objects, and (c) to define appropriate comparison samples of 'typical' AGN, given such a large range of redshifts. Therefore, to limit these effects, it is important to study a sample of 2MASS-selected AGN that covers a more limited range in redshift. In this thesis, I discuss the results of observations of an RA-limited sample of 29 2MASS-selected quasars ($J\text{-}K_S \gtrsim 2.0$) with a narrow range of redshifts ($0.07 < z < 0.28$), and attempt to address the issues outlined in the next section.

Table 1.1: Basic properties of red AGN samples.

Sample	Size	Z	Data used in Study	Key Selection Criteria
This thesis	29	$0.06 < z < 0.28$	Optical Spectra	$J\text{-}K_S \gtrsim 2.0$, $11.0 < K_S < 14.9$, selected from Hutchings et al. (2003)
Hutchings et al. (2003)	76	$z < 0.3$	R-band Images	$J\text{-}K_S \gtrsim 2.0$, $11.0 < K_S < 14.9$, previously unidentified
Glikman et al. 2004, 2007, 2011 & 2012	120	$0.1 < z < 2.5$	Optical & IR Spectra	$J\text{-}K_S \geq 1.7$ & $R\text{-}K \geq 4.0$, selected by cross-correlating the 2MASS PSC with the FIRST radio catalogue
Georgakakis et al. 2009	10	$0.29 < z < 3.1$	UV-FIR SED fitting	$J\text{-}K_S \geq 1.5$ & $R\text{-}K \geq 5.0$, selected by cross-correlating the 2MASS PSC with SDSS DR3 spectra
Urrutia et al. 2008, 2009 & 2012	13	$0.1 < z < 1.0$	Optical Spectra	Selected from the Glikman et al. (2007) sample
Shi et al. 2007	25	$0.08 < z < 0.37$	IR Spectra	$J\text{-}K_S \gtrsim 2.0$, selected from Cutri et al. (2001)
Kuraszkiewicz et al. 2009a,b	44	$0.07 < z < 0.37$	X-ray-FIR SED fitting, PCA analysis	$J\text{-}K_S > 2.0$ and $B\text{-}K_S > 4.3$
Canalizo et al. 2012	9	$0.13 < z < 0.37$	Optical/NIR spectroscopy, HST images	$J\text{-}K_S > 2.0$ and $M_K \lesssim -25$
Marble et al. 2003	29	$0.13 < z < 0.6$	HST images	$J\text{-}K_S > 2.0$ and $M_K \lesssim -23$
Smith et al. 2002	20	$0.06 < z < 0.6$	Optical broadband polarimetry	$J\text{-}K_S > 2.0$ and $M_K \lesssim -23$

1.6 Outstanding questions

From the discussion above, it is clear that many questions regarding the nature of the red 2MASS AGN remain unanswered. This thesis focusses on the following issues.

Is the red 2MASS AGN population homogeneous? It is important to establish whether the red AGN population can be explained simply by one mechanism, or whether two or more are needed to explain the entire sample.

Why are their J-K_S colours red?: It is possible that the 2MASS AGN have red J-K_S colours because dust extinction reduces the J-band flux relative to the K-band flux such that the F_K/F_J flux ratio is higher than that of a typical AGN; the obscuring dust could be located in the outer layers of the torus, such that we are observing these objects at an angle where our line of sight grazes the edge of the torus, leading to the observed red colours. The large-scale dust structures in the host galaxy could also cause significant reddening.

Alternatively, rather than significant levels of dust extinction, a relatively large covering factor of hot dust (T $\sim$ 1500K) could also result in red J-K_S colours. Emission from hot dust in the torus becomes significant at wavelengths which coincide with the K_S-band. Therefore, a larger than average covering factor for this hot dust could increase the flux measured in the K_S-band relative to that of the J-band (the latter likely dominated by accretion disk emission), thus producing the red J-K_S colours measured for the red AGN.

Are the 2MASS-selected objects young, dust obscured AGN? Further evidence is needed before classifying these red AGN as young, dust enshrouded AGN. Such objects would be highly reddened when compared to typical UV/optically selected AGN. In addition, based on models for young AGN (e.g. Saunders et al. 1989; Hopkins et al. 2005; Narayanan et al. 2006; Hopkins et al. 2006), they would be expected to show greater evidence for powerful gas outflows than compared to 'typical' AGN. They would also have large quantities of gas available to the central supermassive black hole, leading to large bolometric luminosities and therefore large Eddington ratios (Hopkins et al. 2006). Also, we might expect to detect a higher incidence of Narrow-Line Seyfert 1 objects (NLSy1), which are sometimes considered to represent young AGN (Mathur, 2000).

In order to address these questions I have used deep, wide spectral coverage William Herschel Telescope (WHT) Intermediate dispersion Spectrograph and Imaging System (ISIS) spectra of a representative sample of 29 red 2MASS quasars in the local Universe (z<0.29) with NIR colours of J-$K_S \gtrsim 2.0$, and K_S-band magnitudes: $11.0 < K_S < 14.9$, taken from Hutchings et al. (2003). In addition, for most of these objects, I have analysed Wide-field Infrared Survey Explorer (WISE) observations, which are useful for investigating the nature of the IR emission/colours in greater detail. In order to adequately test whether the 2MASS-selected quasars are different from UV/optically selected quasars, the properties of the 2MASS quasars have been compared with several comparison samples of 'typical' quasars throughout the thesis.

The thesis is structured as follows. Chapter 2 describes the sample, comparison samples, observations and data reduction. Chapter 3 discusses a unique object in the sample: Q1131+16. The spectrum of this object has the richest spectrum of FHILs (e.g. [FeVII], [FeX], [FeXI] and [NeV]) yet reported for an AGN, providing a rare opportunity to investigate the physical conditions and kinematics of the region(s) emitting the FHILs. Chapter 4 discusses what can be learnt from the optical spectra of the 2MASS sample as a whole using optical emission lines and continuum observations, comparing the results to those of the comparison samples. Chapter 5 investigates the near to mid-IR photometry of the 2MASS and comparison samples. In Chapter 6, a model is developed to reproduce the near- to mid-IR colours of the 2MASS AGN, and thereby test the feasibility of the hypotheses outlined in the previous chapters. Finally, Chapter 7 discusses the results found for the 2MASS AGN and puts the sample into context of the rest of the AGN population. In addition, any necessary future work is discussed in this chapter.

Chapter 2

Samples and Observations

2.1 Introduction

As described in Chapter 1, there have been several studies of red 2MASS AGN in the past. These studies have mainly focussed on samples of AGN which cover a wide range of redshift ($0 < z < 3$: Glikman et al. 2007; Georgakakis et al. 2009; Glikman at al. 2012). The problem with such samples is that it is difficult to investigate the intrinsic diversity of the red AGN population in the face of possible evolutionary and/or luminosity-dependent effects. Therefore, it is important to study a sample of 2MASS-selected AGN that covers a more limited range in redshift. This thesis reports observations of an RA-limited sample of 29 2MASS-selected quasars (J-$K_S \gtrsim 2.0$) with a narrow range of redshifts: $0.09 < z < 0.28$. The total sample studied in this thesis consists of 29 objects, however two of these objects have redshifts z>0.2. Although I present the data for the full 29 objects, I only consider the results for the 27 objects with redshifts z<0.2 in the analysis presented in Chapters 4, 5 and 6. This is because after redshift $z = 0.2$, the nearest 2MASS AGN in the sample has a redshift of $z = 0.274$. Therefore, including these objects when making comparisons to UV/optical selected AGN over the same wavelength range will have a significant effect on the conclusions, in the sense that the comparison samples (described below) may have a greater concentration of objects with redshifts $z > 0.2$ when compared to the 2MASS sample.

In order to answer the questions raised in Chapter 1, WHT/ISIS observations for 23 of the red 2MASS AGN were taken on the nights of the 8th and 9th of February 2007 under program ID P15 (P.I. Tadhunter), a further 2 objects were observed on the night starting on the 28th of July 2006 under program ID N15 (P.I. Rodríguez Zaurín), and the final 4 objects were observed on the nights starting of the 26th and

27th of September 2011 under program ID N5 (P.I. Holt). A WHT Long-slit Intermediate Resolution Infrared Spectrograph (LIRIS) observation for one of the objects in the sample (J1131+16) was also made on the night starting the 2nd March 2010 under program ID P32 (P.I. Littlefair). Finally, a Gemini Multi-Object Spectrographs (GMOS) observation was made under program ID GS-2009B-Q-87 (P.I. Tadhunter) for the object J1131+16.

The first part of this chapter ($\oint$ 2.2) concerns the selection of both the sample of 2MASS AGN which is investigated in this thesis, and the comparison samples used to determine whether the 2MASS AGN are intrinsically different to 'typical' UV/optical selected AGN. I outline how the samples were selected and comment on their near-IR (J-K_S) colours.

The second part of this chapter ($\oint$ 2.3) discusses the details of the observations and the data that I have reduced myself. In this section, I also discuss the methods used to reduce the data in order to extract accurate spectral flux measurements for the analysis in the remainder of the thesis. The data reduction discussion covers WHT ISIS spectra, a WHT LIRIS spectrum, and a GMOS spectrum.

In the final part of this chapter I discuss both the 2MASS (Skrutskie et al., 2006) and WISE (Wright et al. 2010) surveys, which are used extensively in this thesis. In addition, in $\oint$ 2.5, I outline how the photometric data were estimated from these surveys.

2.2 Selecting the samples

2.2.1 Red 2MASS AGN

The full sample for this thesis comprises a RA-limited ($2 < \mathrm{RA} < 15$ hr) sub-sample of 27 objects with red near-IR colours (J-$K_S \gtrsim 2$), K_S-band magnitudes $11.0 < K_S < 14.9$ mag, and redshifts $z < 0.28$, selected from the list of Hutchings et al. (2003), which is itself representative of the population of red, 2MASS-selected AGN[1]. There are also a further 2 objects from Hutchings et al. (2003) that fall outside the original RA range: J1637+25 (z=0.277), and J2124-17 (z=0.111). These latter objects are included for completeness, but their inclusion does not affect the main results of the thesis. In Tables 2.1&2.2 I present the basic information relating to the 2MASS AGN in this thesis.

[1]The work of Hutchings et al. (2003) presents optical imaging obtained from the Canada-France-Hawaii Telescope (CFHT) of 76 AGN that are representative of the 2MASS sample for z < 0.3.

Table 2.1: The basic information relating to the 2MASS AGN studied in this thesis. Presented are the right ascensions (R.A), declinations (δ), redshifts measured using the spectra, the 2MASS photometric magnitudes, the J-K_S colours and the 'photometric quality' flags of each object. A quality flag of 'A' indicates that the S/N ratio of the detected flux in the band is greater than 10, and the uncertainty of the measurement is less than 0.109, 'B' indicates S/N > 7 and an uncertainty less than 0.1551, and finally 'C' indicates S/N > 5 and an uncertainty less than 0.2171.

Object ID	R.A. (J2000.0)	δ (J2000.0)	z	J (mag)	H (mag)	K_S (mag)	J-K_S (mag)	Quality Flags JHK
J0221+13	02:21:50.60	13:27:41.0	0.1402 ± 0.0002	15.65 ± 0.08	14.53 ± 0.08	13.28 ± 0.05	2.37	AAA
J0248+14	02:48:07.37	14:59:57.7	0.0718 ± 0.0002	14.80 ± 0.07	13.71 ± 0.07	12.67 ± 0.04	2.13	AAA
J0306-05	03:06:52.43	-05:31:56.4	0.1261 ± 0.0009	15.19 ± 0.07	14.14 ± 0.06	12.95 ± 0.04	2.24	AAA
J0312+07	03:12:31.03	07:06:55.0	0.1455 ± 0.0003	15.38 ± 0.07	14.58 ± 0.09	13.40 ± 0.05	1.98	AAA
J0400+05	04:00:19.77	05:02:14.6	0.1876 ± 0.0001	14.77 ± 0.06	13.79 ± 0.06	12.77 ± 0.04	2.00	AAA
J0409+07	04:09:24.86	07:58:56.1	0.0914 ± 0.0002	14.84 ± 0.05	13.83 ± 0.05	12.68 ± 0.03	2.17	AAA
J0411-01	04:11:26.47	-01:18:05.6	0.1395 ± 0.0035	16.70 ± 0.15	15.68 ± 0.12	14.48 ± 0.09	2.22	BBA
J0422-18	04:22:56.57	-18:54:42.1	0.0646 ± 0.0002	13.81 ± 0.04	12.72 ± 0.04	11.61 ± 0.03	2.21	AAA
J0435-06	04:35:22.56	-06:35:26.1	0.1846 ± 0.0007	15.27 ± 0.06	14.36 ± 0.06	13.29 ± 0.05	1.98	AAA
J0447-16	04:47:47.62	-16:49:34.7	0.1985 ± 0.0009	15.78 ± 0.09	14.75 ± 0.08	13.69 ± 0.05	2.10	AAA
J0504-19	05:04:25.68	-19:09:25.4	0.1376 ± 0.0009	15.53 ± 0.08	14.57 ± 0.09	13.48 ± 0.06	2.04	AAA
J0910+33	09:10:00.75	33:48:09.2	0.1779 ± 0.0002	16.62 ± 0.17	15.35 ± 0.13	14.29 ± 0.08	2.33	CBA
J1001+41	10:01:18.15	41:04:13.2	0.1427 ± 0.0021	16.15 ± 0.11	15.21 ± 0.09	14.23 ± 0.07	1.92	BAA
J1006+41	10:06:57.84	41:04:06.6	0.0890 ± 0.0003	15.75 ± 0.07	14.79 ± 0.07	13.83 ± 0.06	1.92	AAA
J1014+19	10:14:00.48	19:46:14.4	0.1112 ± 0.0002	14.41 ± 0.04	13.39 ± 0.05	12.38 ± 0.03	2.04	AAA
J1040+59	10:40:43.66	59:34:09.2	0.1476 ± 0.0008	14.84 ± 0.06	13.46 ± 0.05	11.82 ± 0.02	3.02	AAA
J1057-13	10:57:28.63	-13:53:59.5	0.1633 ± 0.0002	16.06 ± 0.09	14.91 ± 0.07	13.56 ± 0.05	2.50	AAA

J1127+24	11:27:51.14	24:32:08.1	0.1366 ± 0.0002	14.93 ± 0.05	13.95 ± 0.05	12.96 ± 0.04	1.97	AAA
J1131+16	11:31:11.05	16:27:39.5	0.1732 ± 0.0001	16.22 ± 0.11	15.17 ± 0.10	14.07 ± 0.06	2.15	BAA
J1158-30	11:58:24.61	-30:03:34.9	0.1352 ± 0.0006	15.01 ± 0.07	14.02 ± 0.06	12.99 ± 0.04	2.02	AAA
J1212-14	12:12:14.49	-14:22:16.1	0.1481 ± 0.0006	15.73 ± 0.08	14.66 ± 0.07	13.67 ± 0.06	2.06	AAA
J1307+23	13:07:00.66	23:38:05.0	0.2741 ± 0.0012	16.79 ± 0.16	15.09 ± 0.07	13.47 ± 0.04	3.31	CAA
J1321+13	13:21:39.08	13:42:30.4	0.1990 ± 0.0003	17.05 ± 0.17	15.57 ± 0.12	14.90 ± 0.10	2.15	CBA
J1323-02	13:23:14.70	-02:19:02.0	0.1606 ± 0.0003	15.07 ± 0.05	14.10 ± 0.04	12.82 ± 0.03	2.25	AAA
J1338-04	13:38:45.30	-04:38:53.0	0.1625 ± 0.0009	15.57 ± 0.07	14.57 ± 0.05	13.59 ± 0.04	1.99	AAA
J1407+42	14:07:37.48	42:56:16.3	0.1183 ± 0.0001	15.32 ± 0.07	14.25 ± 0.06	13.16 ± 0.04	2.16	AAA
J1448+44	14:48:19.38	44:32:32.7	0.0795 ± 0.0003	14.20 ± 0.05	13.11 ± 0.04	12.17 ± 0.03	2.03	AAA
J1637+25	16:37:36.52	25:43:02.8	0.2769 ± 0.0001	16.52 ± 0.14	15.33 ± 0.12	14.19 ± 0.06	2.33	BBA
J2124-17	21:24:41.63	-17:44:45.8	0.1110 ± 0.0006	13.79 ± 0.04	12.64 ± 0.04	11.42 ± 0.03	2.37	AAA

In Figure 2.1 I plot the J-K_S colours against the J-band magnitude for the 2MASS sample and the comparison samples used in this thesis. Figure 2.1 clearly illustrates that the red 2MASS AGN have redder near-IR colours (median J-K_S = 2.15±0.08) when compared with the comparison samples (see below). Nevertheless, it is clear that there are a few objects in the comparison samples that also have red J-K_S colours (J-K_S > 2.0), implying that some of the objects in the comparison samples could be similar to the red 2MASS AGN.

2.2.2 Comparison samples

In attempting to understand the nature of the red 2MASS AGN, some of the key questions we are trying to address are: if one takes a sample of AGN selected on the basis of their red colours at near-IR wavelengths (J-K_S>2.0), how do the optical spectroscopic properties of such a sample differ from those of samples of typical type 1 AGN selected using their optical/UV colours, and can any differences between the samples be explained in terms of reddening effects? Therefore, it is important to compare the results for the 2MASS sample with those of comparison samples of 'typical' quasars. For any comparisons that are made, the samples I use are limited to redshifts z < 0.2, so that they are consistent with the 2MASS AGN sample.

2.2.3 PG quasars

One of the comparison samples used throughout this thesis is the PG quasar sample of Boroson & Green (1992). The PG quasars comprise a complete sample of 87 UV-selected objects from the Palomar bright quasar survey (Schmidt & Green, 1983), selected to have redshifts z < 0.5, and UV/optical colours U-B < -0.44 to ensure an excess of flux in the UV. This sample is also selected to have quasar-like luminosities, with total luminosities of M_B < -23 for the AGN and host galaxies together[2], and broad permitted emission lines clearly present in the optical spectra (Boroson & Green, 1992). The PG quasars provide a useful comparison with the 2MASS sample because they represent 'typical' blue selected quasars at their redshifts (z < 0.5). Limiting the redshift range of the sample to z < 0.2, there are 61 PG quasars suitable for comparison with the red 2MASS sample. Spectra of the Boroson & Green (1992) sample were kindly supplied by T. Boroson, and remeasured by myself. The data cover an observed spectral range of λλ4300–5700 and

[2]Note that in reality, many PG quasars do not have AGN of true quasar luminosity because of significant host galaxy contamination.

Table 2.2: WISE magnitude values for the 2MASS AGN studied in this thesis. Also indicated are the W1, W2, W3 and W4 'photometric quality' flags for each object. A quality flag of A indicates that the detected flux for the object had a S/N greater than 10, 'B' indicates $3 < S/N < 10$, and finally 'U' indicates that the given magnitude is an upper limit ($S/N < 2$). Note that J1321+13 was not detected in the WISE survey.

Object ID	3.4μm (mag)	4.6μm (mag)	12μm (mag)	22μm (mag)	Quality Flags 1234
J0221+13	11.84 ± 0.02	10.67 ± 0.02	7.36 ± 0.02	4.62 ± 0.02	AAAA
J0248+14	10.91 ± 0.03	10.02 ± 0.02	7.25 ± 0.02	5.01 ± 0.03	AAAA
J0306-05	11.54 ± 0.02	10.46 ± 0.02	7.57 ± 0.02	4.90 ± 0.03	AAAA
J0312+07	12.00 ± 0.02	11.12 ± 0.02	8.26 ± 0.02	6.17 ± 0.05	AAAA
J0400+05	11.25 ± 0.02	10.25 ± 0.02	7.73 ± 0.02	5.07 ± 0.03	AAAA
J0409+07	11.78 ± 0.02	10.87 ± 0.02	8.06 ± 0.02	5.63 ± 0.04	AAAA
J0411-01	14.62 ± 0.04	14.33 ± 0.07	10.99 ± 0.12	8.45 ± null	AABU
J0422-18	9.95 ± 0.02	8.94 ± 0.02	6.37 ± 0.01	4.28 ± 0.03	AAAA
J0435-06	12.10 ± 0.02	11.03 ± 0.02	8.08 ± 0.02	5.81 ± 0.04	AAAA
J0447-16	12.27 ± 0.02	11.23 ± 0.02	8.53 ± 0.02	6.09 ± 0.04	AAAA
J0504-19	11.53 ± 0.02	10.29 ± 0.02	7.27 ± 0.02	5.25 ± 0.03	AAAA
J0910+33	12.71 ± 0.02	11.45 ± 0.02	7.73 ± 0.02	4.90 ± 0.03	AAAA
J1001+41	13.59 ± 0.03	13.00 ± 0.03	8.57 ± 0.02	5.93 ± 0.04	AAAA
J1006+41	12.40 ± 0.02	11.45 ± 0.02	8.41 ± 0.02	5.81 ± 0.04	AAAA
J1014+19	11.59 ± 0.02	10.58 ± 0.02	7.51 ± 0.02	4.95 ± 0.03	AAAA
J1040+59	9.90 ± 0.02	8.80 ± 0.02	6.42 ± 0.01	4.10 ± 0.02	AAAA
J1057-13	11.87 ± 0.02	10.61 ± 0.02	7.63 ± 0.02	5.28 ± 0.04	AAAA
J1127+24	12.05 ± 0.02	10.98 ± 0.02	8.11 ± 0.02	5.81 ± 0.04	AAAA
J1131+16	12.42 ± 0.02	11.09 ± 0.02	7.94 ± 0.02	5.79 ± 0.04	AAAA
J1158-30	11.54 ± 0.02	10.56 ± 0.02	8.33 ± 0.02	5.85 ± 0.04	AAAA
J1212-14	12.55 ± 0.03	11.54 ± 0.02	8.52 ± 0.02	6.17 ± 0.05	AAAA
J1307+23	11.34 ± 0.02	10.11 ± 0.02	7.67 ± 0.02	5.09 ± 0.03	AAAA
J1321+13	-	-	-	-	-
J1323-02	11.40 ± 0.02	10.39 ± 0.02	7.79 ± 0.02	5.60 ± 0.03	AAAA
J1338-04	11.91 ± 0.02	10.76 ± 0.02	7.68 ± 0.02	5.34 ± 0.03	AAAA
J1407+42	11.53 ± 0.02	10.32 ± 0.02	7.25 ± 0.01	4.51 ± 0.02	AAAA
J1448+44	11.11 ± 0.02	10.21 ± 0.02	7.50 ± 0.02	5.15 ± 0.03	AAAA
J1637+25	12.35 ± 0.02	11.20 ± 0.02	8.35 ± 0.02	5.78 ± 0.04	AAAA
J2124-17	9.96 ± 0.02	8.92 ± 0.02	5.85 ± 0.01	3.35 ± 0.02	AAAA

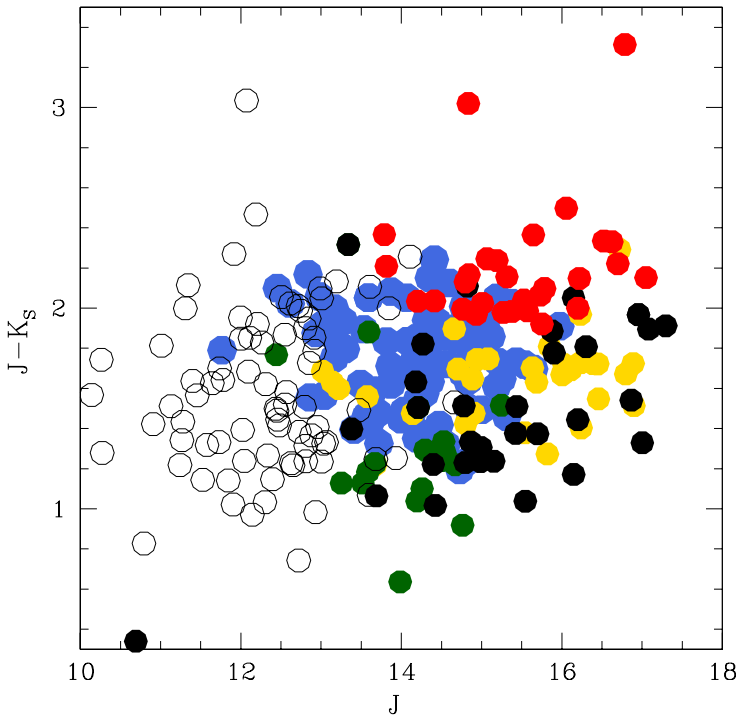

Figure 2.1: J-K$_S$ versus J 2MASS magnitude plot. Throughout this thesis, with the exception of Chapter 6, red 2MASS AGN will be represented by red circles, PG quasars by blue circles, the unobscured type 1 AGN population in gold, 2Jy sample in black, the 3CRR sample in green and the 12μ Seyfert galaxies by unfilled circles. In Chapter 6 the PG quasars and unobscured type 1 AGN population are represented by open blue and gold circles respectively.

have spectral resolutions in the range 6.5–7.0 Å. Detailed properties of the sample and the FeII subtraction procedure are outlined in Boroson & Green (1992).

A sub-sample of these quasars (24) have high quality Sloan Digital Sky Survey (SDSS) spectra available, which cover a wider wavelength range than the spectra from the Boroson & Green (1992) study. I will refer to this as the PG/SDSS sample. Where possible, these spectra have been used as part of the comparison with the 2MASS sample.

As shown in Figure 2.1, which plots the J magnitude against the J-K_S colours, the PG quasars are comparatively 'bluer' than the 2MASS sample at near-IR wavelengths (PG median: J-K_S=1.79±0.03; 2MASS median: J-K_S=2.15±0.08), with some overlap in J-K_S colours between the samples: 20% of the PG sample have J-K_S > 2.0.

2.2.4 Unobscured type 1 AGN

The second comparison sample comprises the 51 relatively nearby (z < 0.38), unobscured type 1 AGN selected by Jin et al. (2012a,b,c) on the basis of low optical reddening, and low gas columns as indicated by their X-ray spectra. The optical properties of this sample were obtained from high quality SDSS DR7 spectra (Jin et al., 2012a,b,c). The SDSS DR7 spectra cover a wavelength range of 3800-9200Å and have a spectral resolution of ∼3Å. The analysis techniques are outlined in the work of Jin et al. (2012a,b,c). There are 14 PG quasars in this sample, which I have removed these from any comparison that includes the PG quasar sample to avoid overlap. However, when the 2MASS sample is compared to the unobscured type 1 AGN alone, I use the complete unobscured sample. When considering the objects with redshifts z < 0.2, there are 21 unobscured type 1 AGN suitable for comparison with the 2MASS AGN sample. As these objects comprise unobscured AGN, I consider this a suitable sample to compare to the red 2MASS quasars.

As shown in Figure 2.1, like the PG quasars, the unobscured type 1 AGN are also relatively 'blue' compared with the 2MASS sample at near-IR wavelengths (median J-K_S=1.60±0.04), with no overlap in J-K_S colours between the samples. However, unlike the PG quasars, the unobscured type 1 objects have comparable J-band magnitudes to the 2MASS sample. This suggests that, given the redshifts of the objects in the sample (median z = 0.08±0.05), this sample has similar luminosities to the 2MASS objects.

2.2.5 12μ Seyfert galaxies

Another radio-quiet sample used for comparison in this thesis is the 12μ galaxy sample (Rush, Malkan & Spinoglio, 1993). The 12μ galaxies were selected from the IRAS Faint

Source Catalogue, Version 2 (FSC-2) with the criteria that their 12μm flux densities exceed 0.15 Jy, their far-IR fluxes are relatively strong when compared to the mid-IR fluxes ($F_{60\mu m} \geq 1/2\ F_{12\mu m}$, or $F_{100\mu m} \geq F_{12\mu m}$), and they have Galactic latitudes $|b| \geq 25°$. A total of 118 Seyfert galaxies and quasars fulfil these criteria. In this thesis I use the sub-sample of 83 12μ Seyfert galaxies with redshifts $z < 0.036$ presented in the work of Baum et al. (2010). This sub-sample is restricted to include only the objects categorised by Rush et al. (1993) as Seyfert galaxies or LINERs, and only the sources with $cz < 10000$ km s^{-1} (Gallimore et al., 2010). Given that the 12μ Seyfert galaxy sample is considered to be an unbiased sample of Seyfert galaxies with a high level of completeness (Rush, Malkan & Spinoglio, 1993), I consider this a suitable sample of 'typical' AGN for comparison with the 2MASS-selected AGN.

It is clear from Figure 2.1 that the objects in the 12μ Seyfert sample span a wide range of J-K$_S$ colours (median J-K$_S$=1.52±0.05), with considerable overlap in the colours of the 12μ Seyfert galaxies and the 2MASS AGN: 17% of the 12μ Seyfert galaxies have J-K$_S$ > 2.0.

2.2.6 2Jy radio galaxies

In addition to making comparisons with radio-quiet AGN, I also compare the red 2MASS AGN with radio-loud AGN. One of the radio-loud comparison samples used in this thesis is the southern 2Jy sample (Tadhunter et al., 1993). The 2Jy sample is a complete subset of the Wall & Peacock (1985) 2.7 GHz sample, selected with declinations $\delta < 10°$, redshifts $0.05 < z < 0.7$, flux densities $S_{2.7GHz} > 2.0$ Jy (Tadhunter et al., 1993), and a steep-spectrum selection of $\alpha_{2.7}^{4.8} > 0.5$ ($F_\nu \propto \nu^{-\alpha}$; Dicken et al. 2008). In total there are 47 objects, all of which have spectroscopy that covers the [OIII]λ5007 emission line. The analysis techniques are outlined in the work of Dicken et al. (2008). While the PG quasars and unobscured type 1 AGN of Jin et al. (2012a,b,c) are more useful for comparison with the 2MASS AGN because they represent 'typical' blue selected quasars, the 2Jy sample can provide a useful comparison with the 2MASS AGN in terms of comparing host galaxy emission in these objects. This is because the flux from the host galaxy can dominate the observations when compared to the AGN component in the 2Jy radio galaxies objects. Indeed, 66% of the 2Jy radio galaxies objects are WLRG/NLRGs which will have a large host galaxy contribution.

In Figure 2.1 the J-K$_S$ colours of the 2Jy radio galaxies are much bluer (median J-K$_S$=1.44±0.07) than those of the red 2MASS objects and the rest of the radio-quiet AGN, with minimal overlap in J-K$_S$ colours between the 2Jy sample and the red 2MASS

objects: only 9%[3] of the 2Jy sample have J-K_S > 2.0. This reflects the dominant host galaxy emission in many of the 2Jy radio galaxies objects at near-IR wavelengths.

2.2.7 3CRR radio galaxies

The other sample of radio galaxies used for comparison in this thesis is a subset of the 3CRR sample of Laing, Riley & Longair (1983). The 3CRR sample consists of radio galaxies selected to have radio fluxes of $S_{178MHz} > 10.9$ Jy, and declinations of $\delta > 10°$. 3CRR is an improvement on the 3CR sample of Bennett (1962) because it includes galaxies which were not detected in the 3CR catalogue due to source confusion, and partial resolution of the data. The 3CR sample itself is a revised version of the 3C catalogue (Edge et al., 1959). The subset of the 3CRR catalogue I use for comparison was that used in the work of Dicken et al. (2010), comprising objects with FRII morphologies and redshifts $z \leq 0.1$. The result is a complete sample of 19 radio galaxies with spectroscopy that covers the [OIII]λ5007 emission line.

As shown in Figure 2.1, like the 2Jy sample, the 3CRR objects are much bluer (median J-K_S=1.23±0.09) than the red 2MASS objects and the rest of the radio-quiet AGN, with no overlap in J-K_S colours between the samples. Like the 2Jy sample, this reflects the dominant host galaxy emission in the 3CRR radio galaxies objects at near-IR wavelengths.

2.3 New observational data

2.3.1 Observations

Details of the observations

The observations for the entire sample were split over three runs. Additional observations of J1131+16 were carried out over a further two runs.

WHT ISIS. Low resolution optical spectroscopic observations of the sample were taken with the ISIS dual-arm spectrograph on the 4.2-m WHT on La Palma in three runs: 28th of July 2006 (ID N15), 8th and 9th of February 2007 (ID P15), and the 26th and 27th of September 2011 (ID N5). The data were taken with the ISIS Dual arm spectrograph on the WHT. On the red arm, the R158R and R316R gratings were used with the RED-

[3]Note that only 77% of the 2Jy sample is covered in 2MASS.

PLUS Charge-Coupled Device (CCD)[4], the dispersions of these gratings are 1.81 and 0.93 Å/pixel respectively. On the blue arm, the R300B grating was used with the EEV12 CCD, this grating has a dispersion of 0.86 Å/pixel. A dichroic cutting at 5300Å was employed to obtain spectra simultaneously in the blue (∼3250-5250Å), and in the red (∼5200-9500Å). To reduce the effects of differential refraction, all exposures were taken when the objects were at low airmass (sec $z < 1.1$) and/or with the slit aligned close to the [5] angle. The seeing for the nights of the observations varied over the range $0.8 <$ FWHM < 1.3 arcseconds[6]. The spatial pixel scales of the 2D spectra are 0.4 arcseconds in the blue and 0.44 arcseconds in the red. The details of the observations for this data set are given in Table 2.3. Note that the resolutions presented in Table 2.3 vary considerably. This is likely due to a combination of the varying observing conditions (due to changing temperatures, air currents, weather fronts etc.) and changes in the focus of the telescope through the night.

Sets of three exposures were taken on both arms simultaneously for each object using a 1.5 arcsecond slit. An additional wider slit (5 arcseconds) exposure was taken on both arms for 23 of the objects[7]. This was to assess the effect of possible slit losses on the emission line fluxes. To eliminate contamination from second order emission, a GG495 blocking filter was introduced into the ISIS red arm. Details of the observations for each object are given in Table 2.3.

The wide to narrow slit [OIII] flux ratios are shown in Figure 2.2. The majority of objects have wide and narrow slit fluxes that agree within ±40%, suggesting that the narrower slits captured the majority of the flux from the emission regions: the median wide to narrow flux ratio is 1.14, showing that the wide slit captured slightly more flux than the narrow slit, as expected. There are some outliers: J0435-06, J1001+41 and J1307+23 all have ratios above 1.5. However, the wide to narrow flux ratios for all these objects agree within $\sim 2\sigma$ of the median ratio. In the cases of J0435-06 and J1001+41 the [OIII]λ5007 emission lines have a low equivalent widths, whereas in J1307+23, even

[4]The R158R grating was used on the nights of the 28th of July, and the 8th and 9th of February. The R316R grating was used on the nights of the 26th and 27th of September 2011.

[5]The parallactic angle is defined as the angle at which the slit is aligned with the direction from the target to the zenith. When targets are observed away from the zenith, atmospheric refraction disperses the light in the vertical direction. If the slit is not aligned vertically, some of the light will fall outside the slit, and therefore some of the light from the target is lost.

[6]Unfortunately, due to a lack of suitable imaging observations, an accurate seeing estimate does not exist for the exact time for each object in the WHT observations. The quoted range is based on measurements with the DIMM seeing monitor at the ING observatory.

[7]Wide slit exposures were not taken for 6 of the objects in the sample: J0221+13, J0248+14, J0306-05, J0312+07, J1637+25 and J2124-17. These objects were observed on separate runs to the rest of the sample.

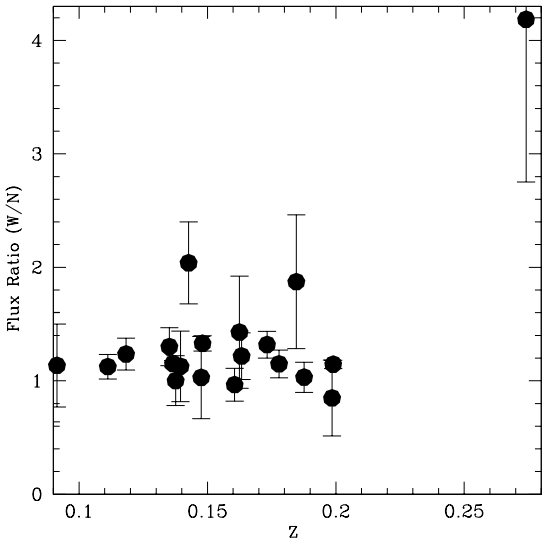

Figure 2.2: Wide to narrow [OIII] flux ratio plotted against redshift for the 2MASS sample.

the narrow slit data have a relatively low S/N. Therefore the large wide to narrow flux ratios reflect the large uncertainties in [OIII] fluxes, as measured from the noisy wide slit data, rather than uncertainties in the narrow slit fluxes. The similarity between the flux captured in the wide and narrow slit observations gives confidence that the spectra for the 6 objects without wide slit data (runs 'b' and 'c' in Table 2.3) give an accurate indication (within ∼40%) of $L_{[OIII]}$ for these objects.

J1131+16 LIRIS. On the night starting the 2nd March 2010, Stuart Littlefair obtained a 1.388 – 2.419μm spectrum of J1131+16 using the HK grism in LIRIS (Manchado et al., 1998) on the 4.2-m William Herschel Telescope on La Palma. The spectrum has a dispersion of 9.7Å per pixel, and a 1 arcsecond slit was used, giving a spectral resolution of ∼40Å. The seeing was approximately 2 arcseconds, and the night suffered from heavy cirrus. A total exposure time of 88 minutes was obtained over airmasses ranging from 1.0 to 2.2. The total exposure was divided into 240 second sub-exposures, and the telescope was nodded in the standard ABBA nodding pattern to aid sky subtraction. A random jitter of 10 arcseconds was added to the default nod positions to limit the impact of bad pixels. Observations of the A5V star BD+16 2325 were also taken to correct for the effects of telluric absorption and to provide a relative flux calibration. Both objects were observed with a slit position angle of zero degrees.

J1131+16 GMOS. Spectroscopic and imaging observations using GMOS were taken on the 21st February 2010 during Gemini queue observation time as part of the program GS-2009B-Q-87. The spectral observations comprised three 600 second exposures using a central wavelength 5000Å at an airmass of 1.46, and a 1.5 arcseconds slit aligned along position angle PA163° — close to the parallactic angle for the centre of the observations. The spectrum has a dispersion of 1.83 Å/pixel. This resulted in a spectrum with a useful wavelength range ∼3700-6450Å. The observations of the flux standard star, Feige56, had the same set-up but with an exposure time of 10 seconds, taken at an airmass of 1.61 and with a 5 arcsecond slit. Deep GMOS images were also taken using an r' filter at an airmass of 1.56. Each exposure of the imaging observations had an exposure time of 250 seconds, and the data were taken in a 4 point dither pattern, resulting in a total exposure time of 1000s. The seeing was estimated to be 0.75±0.02 arcseconds (FWHM), based on measurements of stars in the GMOS image. The spatial pixel scale is 0.147 arcseconds per pixel.

2.3.2 Data reduction

Whilst data for 25 of the objects in the sample were already reduced by J. Holt and J. Rodríguez Zaurín when I started my PhD, I obtained WHT ISIS spectroscopy for a further 4 objects, and additional LIRIS spectroscopy for J1131+16. An r'-band image of J1131+16 (presented in Figure 3.9 in Chapter 3) was also taken as part of this thesis work (see above), however the GMOS image was reduced using the standard Gemini pipeline reduction software, and the photometric calibration used the zero point magnitude for the r' filter advertised on the GMOS south website, taking full account of the airmass and exposure time of the observations, therefore the reduction steps are not described below. The majority of the data reduction was done in IRAF (Image Reduction and Analysis Facility) and using the STARLINK package FIGARO, using the standard packages and procedures for optical and IR spectroscopy. Here I describe the standard steps that were used by Joanna Holt, Javier Rodríguez Zaurín and myself to reduce the optical spectroscopy.

Optical spectroscopy

Mosaicing the Data. GMOS spectra are taken over 3 CCDs and need to be mosaiced before any further reduction steps can be carried out[8]. In the case of the J1131+16 Gemini GMOS spectra, all 2D images were mosaiced using the IRAF GEMINI package before

[8]Note that this step is not required for the WHT/ISIS spectra.

Table 2.3: Basic observational details for the 2MASS sample, including spectral resolutions and extracted apertures. The key for the 'Run' column is: a – observed on 8-9th of February 2007, b – 28th of July 2006 , c – 26-27th of September 2011 and d – 21st February 2010. 'EXP' indicates the exposure time. Column 'PA' gives the position angle of the slit in degrees. Columns 'Blue' and 'Red' give the instrumental widths measured from the sky lines in the 2-dimensional frames of the observations. Note that, in the case of the GMOS spectrum of J1131+16, there is only one instrumental width for the spectrum, I have placed this in the 'Red' column. The 'Aperture' column refers to the extraction aperture size for the 1-dimensional spectra.

Object ID	Run	EXP (s)	PA (Deg)	Blue (Å)	Red (Å)	Aperture (arcsec^2)
J0221+13	c	600	298	6.8	6.1	2.2x1.5
J0248+14	c	300	298	6.9	6.4	2.2x1.5
J0306-05	c	600	326	6.2	6.4	2.2x1.5
J0312+07	c	600	307	6.6	6.5	1.8x1.5
J0400+05	a	600	12	5.0	10.5	2.2x1.5
J0409+07	a	600	10	5.3	10.1	1.8x1.5
J0411-01	a	600	50	5.2	10.4	2.2x1.5
J0422-18	a	300	20	5.6	10.6	2.2x1.5
J0435-06	a	600	20	5.6	10.4	2.2x1.5
J0447-16	a	600	30	5.6	10.8	2.2x1.5
J0504-19	a	450	25	5.5	10.2	2.2x1.5
J0910+33	a	600	85	5.3	10.2	1.8x1.5
J1001+41	a	450	230	5.7	10.9	1.8x1.5
J1006+41	a	600	68	5.2	10.5	1.8x1.5
J1014+19	a	300	125	5.6	10.8	2.2x1.5
J1040+59	a	600	190	5.3	10.2	2.2x1.5
J1057-13	a	600	345	5.7	10.5	2.2x1.5
J1127+24	a	500	135	5.5	10.1	2.6x1.5
J1131+16$_{ISIS}$	a	600	315	6.1	11.4	1.8x1.5
J1131+16$_{GMOS}$	d	600	163	-	7.1	1.5x1.5
J1158-30	a	450	180	5.5	9.8	2.8x1.5
J1212-14	a	600	180	5.3	10.2	2.2x1.5
J1307+23	a	600	310	5.5	10.6	2.2x1.5
J1321+13	a	600	350	5.3	10.6	1.8x1.5
J1323-02	a	600	180	5.3	10.7	2.2x1.5
J1338-04	a	450	185	5.6	11.0	2.2x1.5
J1407+42	a	600	190	5.3	10.0	2.2x1.5
J1448+44	a	300	40	5.6	9.9	1.8x1.5
J1637+25	b	900	70	6.5	5.2	1.6x1.5
J2124-17	b	300	8	6.5	6.0	2.0x1.5

any further reduction was performed. I did not interpolate the images, meaning that I left gaps in the spectra corresponding to the chip gaps. I did this so not to introduce any spurious features in the spectrum.

Image Combining. There were 3 sets of spectra for any given object in the sample. These spectra were median combined to both increase the signal-to-noise ratio of the data, and to remove the bulk of the cosmic rays from the images (see below).

Bias subtraction. A bias is added to every pixel on a CCD before the image is read out. This is because the analogue-to-digital converter cannot read out negative counts, and therefore the bias is added to ensure that the counts of each pixel on the CCD are positive, thus preventing a systematic error that would result when reading out low counts. This bias should be constant, however, because there are imperfections on CCDs, the value of the bias varies between pixels. For both the ISIS and GMOS data, the overscan regions of the CCD chips (a number of rows/columns on a CCD which are not exposed to the captured photons) were used for the bias subtraction.

Flat Fielding. The sensitivity of a CCD to incoming photons is not uniform across the surface of the chip: the sensitivity can vary from pixel-to-pixel. These variations can be caused by manufacturing imperfections, geometric variations between pixels or mechanical stresses. In addition, slightly non-parallel slit edges can induce larger scale gradients across the image. Also, fringing (an interference effect) may occur on the red arm of ISIS. Fringing begins at about 7500Å, and increases considerably in amplitude redward of 9000Å. To remove these variations, it is common practice to obtain a series of flat field frames at both the beginning and end of an observing night, or following a change in the instrumental setup. The individual flat field frames were bias subtracted, median combined and normalised to produce a master flat field. All the spectral images were then divided by the master flat field to remove the variations.

Cosmic Ray Removal. During any exposure, CCDs are affected by cosmic rays. Cosmic rays, and the secondary particles caused by cosmic rays, are detected by CCDs, resulting in unwanted artifacts on the 2-dimensional images. The bulk of the cosmic rays were removed when the spectra images were median combined. Any remaining cosmic rays were then removed by hand using the CLEAN algorithm in FIGARO.

Wavelength Calibration. An accurate wavelength calibration is crucial for any work

involving the kinematics of the emission regions of AGN. Because ISIS is a heavy instrument, it suffers from flexure as the telescope slews to different positions. To minimise this effects, arcs were taken at the position of each object on the sky. For GMOS, a flexure model has been derived to incorporate the effects of both temperature and inclination. For the ISIS data, CuNe+CuAr calibration lamps were observed. For the GMOS data, a CuAr calibration lamp was observed.

Initially, the arc lines were identified using IRAF and the arc maps for the particular instruments (ISIS: Garcia-Lorenzo & Holt 2001, Holt & Garcia-Lorenzo 2001; GMOS: Gemini 2001). The emission lines were first identified on a 1-dimensional arc spectrum taken at the exact position of the object on the CCD. These identifications were then applied to the 2-dimensional frame to correct for any curvature in the spatial direction. Then the wavelength calibration was applied to the 2D AGN spectra. The calibration accuracies were checked by comparing the measured sky lines (see below) with those measured in published work such as Osterbrock et al. (1996). If there were any systematic shifts in the wavelength accuracy, they were then corrected. Based on measurements of the night sky lines, the wavelength calibration uncertainties are 0.1 Å on both the blue and red arms of the ISIS spectra, and the analysis of the night sky lines of the GMOS spectrum of J1131+16 implies a wavelength calibration uncertainty of 0.50±0.06 Å for the spectrum.

Sky Subtraction. In addition to the spectrum of the target object, emission from the atmosphere also produces a spectrum on the CCD. This emission is a combination of airglow emission lines, and the solar spectrum from scattered moonlight. To subtract the sky emission from each spectrum, I extracted portions of the 2-dimensional image from both above and below the continuum of each object. I then averaged these and subtracted the resultant image from the target spectrum.

In addition to removing the sky emission features from the AGN spectra, the sky lines were also used to determine the instrumental width of each spectrum. The instrumental width is the measured spectral resolution of the spectrograph. Knowledge of the instrumental width of the observations is necessary for the analysis of the kinematics of the emission lines in the spectra, because the observed widths of emission lines are a convolution of the intrinsic widths caused by gas motions in the host galaxy, and the instrumental profile that results from the slit and spectrograph optics. The instrumental widths for each object are given in Table 2.3.

Flux Calibration. Before the spectra can be used to provide useful results, the photon

counts on the CCD must be converted into an absolute flux scale, i.e. flux calibrated. To achieve accurate relative flux calibrations for the observations, several spectrophotometric standard stars were observed during the observing runs. For the WHT ISIS run on the nights of the 26th and 27th of September 2011, 7 standard stars were observed, and for the Gemini GMOS run only one star standard star was observed. The standard stars were observed with the same grating/grism, central wavelength and CCD positions of the observed AGN, however the slits used for the observations were wider (5 arcseconds) to ensure no flux was lost.

For each run, the flux calibrations were normalised with respect to an average sensitivity function. To be included in the overall average for each observing run, the relative flux of each sensitivity function is required to be consistent within 10% of the other sensitivity function at all wavelengths. 2 of the sensitivity functions on the blue ISIS arm were not used because they were not consistent. Note that this step was not taken for the GMOS observation of J1131+16 because only one flux standard was observed. During the flux calibration, the sensitivity functions were corrected for the effects of atmospheric extinction due to the airmass of the observation; the observatories provide their own extinction curves for this step. The relative flux calibration uncertainty – based on the comparison of observations of the flux standard stars taken throughout the runs – is estimated to be $\pm 5\%$.

Image Straightening. In most cases, the continua of the spectra were not straight on the CCD image. To ensure that the extraction apertures extracted the entire continuum of the AGN, these images were 'straightened' in IRAF.

Telluric Correction. In addition to observing the flux standard stars, early type stars such as A or F type (stars with virtually featureless continua at wavelengths 6600-8000Å) were observed in order to correct the spectra for atmospheric absorption features, particularly the A band at ∼7600 Å, the B band at ∼6800 Å and other telluric features redward of 6000 Å. It was crucial to correct for the telluric features because they often coincide with important emission lines (mainly the Hα+[NII] blend) in the AGN spectra. The telluric standard stars were reduced in the standard way (bias subtraction, flat fielding, cosmic ray removal and wavelength calibration), before they were extracted. The stellar features of the continua of these standard stars were fitted, so once the spectrum was normalised only the telluric absorption features remained in the spectrum. In addition, I cut the spectra such that only the wavelength range between 6000 to 8500 Å remained, this was to ensure that any possible left-over features in the rest of the standard stars

spectrum were not introduced into the AGN spectrum. The AGN spectra were then divided by the telluric spectra to remove the features. Note that the observations of the telluric standard stars were taken close in time and airmass to the observations of the AGN, in order to minimise any differences between the airmass and therefore strength of the absorption features. The telluric corrections were only required for the WHT ISIS spectra, because the wavelength range of the Gemini GMOS spectrum for J1131+16 did not encompass any atmospheric absorption bands. No telluric standards were taken for J1637+25 and J2124-17, and therefore the atmospheric features were not removed for those objects.

Correction for Galactic Extinction. For the final step, all the spectra were corrected for Galactic extinction using the Galactic extinction maps of Schlegel, Finkbeiner & Davis (1998), and the extinction laws of Seaton (1979) for UV wavelengths, and Howarth (1983) for optical/IR wavelengths.

Aperture Selection. Once the 2-dimensional images of the spectra were reduced, extraction apertures were selected based on a visual inspection of the 2-dimensional spectra. The sizes of the apertures were chosen so that they contained as much emission from the AGN as possible, while minimising any emission from the extended host galaxy. The aperture sizes are presented in Table 2.3.

The extracted ISIS spectra for the 2MASS AGN sample are presented in Chapter 4, and the GMOS spectrum for J1131+16 is shown in Chapter 3.

Infrared spectroscopy

The steps involved when reducing IR spectroscopy are subtly different from those required to reduce optical spectra. As discussed in § 2.3.1, the telescope was nodded in an ABBA nodding pattern to aid sky subtraction. Both J1131+16 and the A5V star BD+16 2325 were observed in this manner. Consecutive pairs of AB 2-dimensional spectra were subtracted to remove the sky background for both the target and standard star. The resulting frames were then wavelength-calibrated. The wavelength calibration was provided by observations of Ar+Xe lamps available in the calibration unit at the A&G box of the telescope. Once the frames were wavelength calibrated they were co-added to produce master spectra for J1131+16 and the standard star, and extracted to produce a 1-dimensional spectrum. The master spectrum of J1131+16 was then divided by the

standard star master spectrum to both flat field the data, and to attempt to remove the telluric features in the data. However, there were considerable differences between the strengths of telluric features between the spectrum of J1131+16 and that of the standard star. This was likely due to the mismatch in the air masses of the observations, and variations in the atmospheric conditions between the observations. Instead, the telluric absorption was modelled by Jose Antonio Acosta Pulido using an atmospheric model, and consequently removed from both the spectrum of J1131+16 and that of the standard star. In order to flux calibrate the data, the telluric corrected spectrum of the target was then multiplied by a blackbody emitter with the effective temperature of a A5V type star. The reduced H and K band spectra are presented in Chapter 3.

2.4 2MASS and WISE data

The work in this thesis makes use of data in both the 2MASS and WISE catalogues. In this section I will briefly outline both surveys, and discuss how the fluxes and magnitudes were derived from the survey data.

2.4.1 2MASS

2MASS used two automated 1.3-m telescopes, one at Mt. Hopkins, AZ, and one at CTIO, Chile. Each telescope was equipped with a three-channel camera, capable of observing the sky simultaneously in the J (1.25 μm), H (1.65 μm), and K_S (2.16 μm) bands. 2MASS produced a Point Source Catalog (PSC) containing 470,992,970 sources and an Extended Source Catalog (ESC) of 1,647,599 sources, along with 4,121,439 FITS images covering 99.998% of the sky. 2MASS achieved an effective spatial resolution of approximately 5-6 arcseconds. The PSC is >99% complete for $J < 15.8$, $H < 15.1$ and $K_S < 14.3$ magnitudes across the sky, except in regions of high source density (Skrutskie et al., 2006). The basic properties of the 2MASS band passes are given in Table 2.4.

The main goals of 2MASS were to detect galaxies in the "Zone of Avoidance" (a strip of sky obscured in visible light by the Milky Way), detect brown dwarfs, survey low mass stars, and catalog all detected stars and galaxies in the survey.

2.4.2 WISE

WISE was a space-based IR-sensitive telescope, launched in December 2009 with the aim of mapping the entire sky at 3.4 μm, 4.6 μm, 12 μm, and 22 μm with an angular resolution

Table 2.4: Basic details for the 2MASS and WISE point source catalogs. Note that the column 'ZP flux' presents the zero point fluxes for the bands.

Survey	Band	λ (μm)	Bandwidth (μm)	ZP Flux (Jy)
2MASS	J	1.235±0.006	0.162±.001	1594±27.8
Skrutskie et al. (2006)	H	1.662±0.009	0.251±.002	1024±20.0
	K_S	2.159±0.011	0.262±0.002	666.7±2.6
WISE	W1	3.353±0.013	0.663±0.001	306.7±4.6
Wright et al. (2010)	W2	4.603±0.017	1.042±0.001	170.7±2.6
	W3	11.561±0.045	5.507±0.017	29.05±0.44
	W4	22.088±0.118	4.101±0.045	8.284±0.290

of 6.1, 6.4, 6.5 and 12.0 arcseconds, and achieving 5σ point source sensitivities better than 0.08, 0.11, 1 and 6 mJy respectively (Wright et al., 2010). The basic properties of the WISE band passes are given in Table 2.4.

The main goals of WISE were to find the most luminous galaxies in the Universe, detect asteroids larger than 3 km in the asteroid belt, contribute to a wide variety of studies in astronomy, and to provide a source catalog for the James Webb Space Telescope (JWST).

2.5 Photometry

In this section I will outline the techniques used by both 2MASS and WISE to calculate their photometric magnitudes. This section is presented for the purpose of background reading, and is not my own work.

2.5.1 Profile-fit photometry

One of the primary methods to determine the photometric magnitudes used by both 2MASS and WISE is profile-fit photometry (PFP). PFP relies on fitting a point spread function (PSF) to the point source in question. PSP gives reliable estimations for the photometry of faint sources and objects in dense environments (i.e. multiple point sources within a short distance of each other). Below I outline the main steps used by 2MASS and WISE in their PFP techniques.

Point spread function

The PSF describes the 2-dimensional distribution of photons of a point source in a telescopes focal plane. A typical PSF will be peaked in the centre with the detected falling off with increasing distance from the centre. PSF are normally described by a 2-dimensional function. Both 2MASS and WISE estimate PSFs from observations of bright stars, and both compile a library of PSFs for use when estimating the PFP of point sources. However, given that 2MASS used ground based observations, the PSF library of 2MASS is indexed by the seeing for each band, and therefore the appropriated PSF shape is chosen based on the seeing of the observation in question. However, being a space based mission, WISE indexed its PSF shapes by the position in the focal plane of the telescope.

In PFP, the expected shape of the PSF, $H_\lambda(r)$, is described by:

$$H_\lambda(r_{\lambda i} - s_n), \tag{2.1}$$

where $r_{\lambda i}$ is sky location in the given waveband (λ), and s_n is a 2-dimensional vector which describes the location of the n^{th} blend component, if the PSF of the target overlaps with PSFs of any nearby sources. Blends arise when the PSFs of nearby objects overlap.

Local background and statistical noise

Sources of noise in the local background vary in scale from point sources such as faint stars, to large extended scales such as IR cirrus. The local background level, b_λ, is determined from the pixel value distribution within a circular annulus (2MASS: 14-20 arcseconds; WISE: 50-70 arcseconds) centred on the source position. The annulus must be large enough to avoid the influence of the PSF of the point source, and to minimise the Poisson component of the sky pixels. However, the annulus must remain small enough to be representative of the local sky background. b_λ is estimated from the trimmed average of the pixel value distribution, where the trimming is driven by the emission contained within the peak (50%) of the background emission distribution, and 1-σ (16%), measured in the background annulus.

In addition to any local background source contamination, the statistical noise ($\nu_{\lambda i}$) – unexplained variation in the detected flux – must also be accounted for. $\nu_{\lambda i}$ includes the uncertainty in the pixel value due to instrumental effects (including the effects of Poisson noise, read noise, and flat-fielding error), and the uncertainty in the PSF.

Determining the flux

To determine the flux emitted by a point source, a measurement model which describes the observed pixel value, ρ_i corresponding to the ith pixel within the profile of the point source, is needed. For an isolated object, i.e., where the PSF does not overlap with the PSF of a separate object, the flux can be determined using the integrated pixel values of the PFP, and taking into account the local background noise. However, if the PSF of any candidate overlaps with a PSF of another object[9], then the profiles will be fit to both detections simultaneously. The number of sources being solved for simultaneously is referred to as the blend number (NB).

The measurement model used in PFP is described by:

$$\rho_i = \sum_{n=1}^{N_B} (f_\lambda)_n H_\lambda (r_{\lambda i} - s_n) + b_\lambda + \nu_{\lambda i}, \tag{2.2}$$

where $(f_\lambda)_n$ is the flux in the given waveband, and the other symbols are described above. Using this, the emission from the separate point sources can be determined by combining the emission for the PSF describing the point source over all the required pixels.

2.5.2 Standard aperture photometry

Where there is no source confusion, aperture photometry provides better photometry for brighter sources (e.g. $K_S < 13$ mag) than PFP. Both 2MASS and WISE perform aperture photometry in addition to PFP for point sources in their catalogues.

Multiple aperture photometry is performed using a set of circular apertures centred on the source. The 2MASS apertures have a range of sizes from 3 to 14 arcseconds, and use a 'standard aperture' of 4 arcseconds for point sources, while the WISE apertures have a range of aperture sizes from 5.5 to 24.75 arcseconds for the 3.4μm, 4.6μm and 12μm bands, and 11.0 to 49.50 arcseconds for the 22μm band, using 'standard apertures' of 8.25 and 16.5 arcseconds respectively. Aperture measurements from each of the frames are combined using an unweighted mean taking into account non-detections in frames to avoid flux overestimation. Fluxes are determined by summing pixels entirely within the aperture and interpolating pixels partially within the aperture.

The 'standard apertures' may not capture all of the flux, because the PSF may be sufficiently broad such that the light from the wings of the point source is not completely

[9]Note that for 2MASS this is closer than approximately 5 arcseconds, this varies with the seeing of the observation. For WISE the distance for blending is driven by the size of the PSF in the 22μm band: twice the FWHM.

captured within the 'standard aperture'. This is a particular problem for the 2MASS catalogue because it is a ground-based survey and therefore is affected strongly by the seeing conditions of the observations. To correct for these losses, a curve-of-growth correction is required.

The curve-of-growth correction is a constant which is subtracted from the magnitude measured by the 'standard aperture'. This makes the resulting magnitude equivalent to that measured in an infinite sized aperture. This correction factor is the difference between the 'standard aperture' magnitude and the magnitude in the aperture at which the magnitude differentials tend to zero. The benefits of using a curve-of-growth correction over using a large aperture are: (a) it avoids the decrease in the signal-to-noise due to the increase in the sky photon noise which comes with larger apertures, and (b) it avoids confusion with possible nearby sources. However, the curve-of-growth correction assumes that the targets are unresolved, and have profiles which are consistent with a PSF combined with the effects of seeing. Therefore, magnitudes measured using aperture photometry for resolved or multiple sources may not be accurately estimated.

For 2MASS, curve-of-growth corrections were drawn from tables indexed by seeing, where the corrections were derived from multi-aperture photometry of bright sources in density environments. For WISE, the curve-of-growth corrections were constructed for each PSF in their PSF library (see $\oint$ 2.5.1).

The local background estimations for the standard aperture photometry measurements are determined in the same manner as in the PFP method, this is outlined in $\oint$ 2.5.1.

It must be noted that both the 2MASS and WISE catalogues prefer to present the magnitudes determined from the PFP method, and the aperture photometry measurements are used for a sanity check. However, in cases where the profile of the target is not characterised by a PSF, the standard aperture measurements are more suitable. In this thesis I use the magnitudes determined from the PFP method for all the 2MASS objects, and the objects in the comparison samples. This is to minimise the affects of source confusion.

2.5.3 Summary

The main sections of this chapter are summarised as follows.

- I have defined a representative sub-sample of 29 red 2MASS AGN with red near-IR colours (J-$K_S \gtrsim 2$), K_S-band magnitudes $11.0 < Ks < 14.9$ mag, and redshifts

$z < 0.2$ selected from the list of Hutchings et al. (2003), which is itself representative of the population of red, 2MASS-selected AGN.

- I have described the basic properties and selection criteria for 5 comparison samples of AGN.
- The observations and data reduction for the WHT/ISIS and Gemini/GMOS spectra of the red 2MASS AGN have been described. In addition, the observations and data reduction for the WHT/LIRIS spectrum for J1131+16 has also been described
- I have discussed both the 2MASS and WISE catalogues, describing the methods that these surveys used to determine the magnitudes of the detected objects.

In the following chapters in this thesis I will discuss the analysis of the red 2MASS AGN, starting with a detailed investigation of the object J1131+16.

Chapter 3

J1131+16: a clear view of the inner face of the torus?

A version of the work presented in this chapter has been published in the Monthly Notices of the Royal Astronomical Society as part of Rose et al. (2011). The analysis and text presented below are my own work.

3.1 Introduction

During the analysis of the optical spectra of the 2MASS AGN sample, I found that one of the objects (J1131+16) has the richest spectrum of FHILs (e.g. [FeVII], [FeX], [FeXI] and [NeV]) yet reported for an AGN. This object provides a rare opportunity to investigate the physical conditions and kinematics of the region(s) emitting the FHILs. In this chapter, I use a combination of optical and near-IR spectra, as well as an optical image, to determine the physical conditions and the kinematics of the FHILs emission region(s).

3.2 Forbidden high ionisation lines and their relationship to the torus

Most Seyfert galaxies show some spectral lines from forbidden transitions of highly ionised ions in their spectra, e.g. [FeVII] , [FeX], [FeXI] and even [FeXIV] (Penston et al., 1984). These emission lines are often blueshifted with respect to the rest frame of the AGN and have velocity widths which are between those of the NLR, and BLR

(Penston et al. 1984, Appenzeller & Wagner 1991, Mullaney et al. 2009). In some rare cases many FHILs of relatively high equivalent width have been detected. Examples include III Zw 77 (Osterbrock, 1981), Tololo 0109-383 (Fosbury & Sansom, 1983) and ESO 138 G1 (Alloin et al., 1992).

The physical mechanisms and conditions that allow strong FHILs to be produced have been debated for some time: whether there is a continuity from the photoionisation processes which produce the lower ionisation lines in the NLR (Korista & Ferland 1989, Ferguson, Korista & Ferland 1997), or there is an entirely different mechanism for their formation (e.g. collisional excitation in a high temperature gas; Nussbaumer & Osterbrock 1970).

Given that the transitions associated with many of the FHILs have high critical densities (n_c>10^5 cm^{-3}), it has been suggested that they may originate in the innermost torus wall facing the illuminating source. Studies of the high critical density [FeVII]λ6086 emission line across Seyfert galaxies from types 1-2, including intermediate types, find that its strength increases relative to the low ionisation lines from type 2 to type 1. This can be interpreted in terms of the orientation-based division between Seyfert types (e.g. Antonucci 1993): as the Seyfert type gets closer to a Seyfert 1, more of the emission from the inner torus becomes visible to the observer (see Murayama & Taniguchi 1998, Nagao et al. 2001). Therefore the high critical density lines that are preferentially emitted by the torus are likely to be stronger in type 1 objects, as observed. However, to date the idea that the [FeVII] emission lines are associated with the torus has not been thoroughly tested using detailed emission line ratios that measure physical conditions accurately.

Although it seems plausible that at least some of the FHIL emission arises in the torus, the causes of the diversity in both the relative strength and kinematics of the FHILs remain uncertain. One possibility is that the unusually strong FHILs observed in some objects are symptomatic of a recent energetic occurrence which is able to illuminate the region that produces these lines (Komossa et al., 2009); suggestions for such events include the rapid accretion of material from the interstellar medium (ISM), the tidal disruption of a stars by the SMBH, gamma-ray bursts and supernovae (Komossa et al., 2009).

The unusual strength of the FHILs in objects such as III Zw 77, Tololo 0109-383 and ESO 138 G1 provides us with a rare opportunity to study the nature of the region of the AGN which emits them, and thus helps us to better understand the structure of AGN in general.

This chapter reports an investigation of the object J1131+16, which has the richest spectrum of FHILs yet reported for an AGN. J1131+16 was discovered in the 2MASS

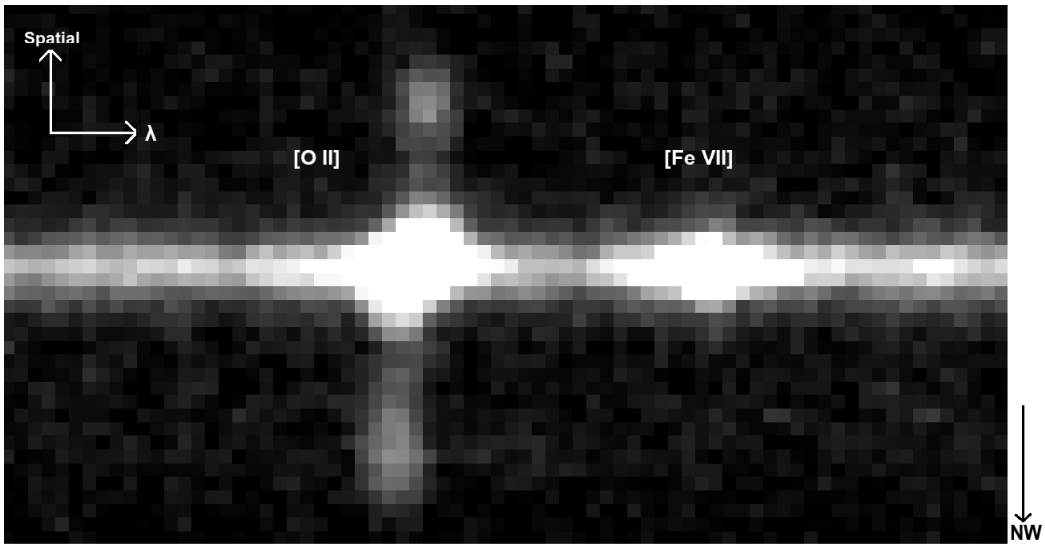

Figure 3.1: A section of the 2D WHT spectrum along PA315 showing [OII]λ3727 and [FeVII]λ3759. Note that the [OII] is extended 6.9 arcseconds above and 8.1 arseconds below, the continuum of J1131+16 and is well resolved. The spatial scale for the assumed cosmology for these observations is 3.46 kpc arcsec^{-1}. The spatial direction of the slit is indicated along side the plot. In addition, a nuclear velocity gradient in the [OII] can be seen from the fact that its profile is slanted when compared to that of [FeVII]

.

survey and was classified as a Seyfert 2 galaxy with a redshift of 0.174. It belongs to sample of quasar-like objects identified on the basis of their red near-IR colours (J-K>2.0) in the 2MASS survey (Cutri et al., 1995). In this chapter I present deep optical and IR spectra of J1131+16, and use these to deduce the physical conditions and kinematics of the FHIL emission lines, with the aim of investigating their origin. The cosmological parameters used throughout this chapter are adopted from WMAP: $H_\circ = 71$ km s^{-1}, $\Omega_M = 0.27$ and $\Omega_\Lambda = 0.73$ (Spergel et al., 2003), resulting in a spatial scale of 3.46 kpc arcsec^{-1} (obtained from the NED).

3.3 Results

3.3.1 Spatial distribution of the emission lines

While the 2D spectra show that all the emission lines are strongly concentrated on the nucleus of the host galaxy, I detect spatially extended line emission in [OII]λ3727 (see Figure 3.1), Hβ, [OIII]$\lambda\lambda$5007,4959 and the Hα+[NII] blend. The emission lines have a maximum extent of 9 arcseconds in the north–south direction (31kpc) in the Gemini

Table 3.1: Centroid positions and spatial extents of selected emission lines and the continuum at different wavelength intervals, as measured from the 2D WHT spectrum. The centroids (measured in pixels) and the FWHM (measured in arc seconds) were determined using single Gaussian fits to the bright cores of the spatial distributions of the emission lines along the slit.

λ_{Rest} Å	Range Å	Centroid	±	FWHM (arc seconds)	±
Blue Arm					
[NeV] 3425	35	98.34	0.01	1.35	0.01
cont. 3392	35	98.23	0.04	1.71	0.04
[OII] 3727	45	98.39	0.08	1.56	0.06
cont. 3690	45	98.21	0.07	1.78	0.06
[FeVII] 3759	45	98.32	0.07	1.28	0.05
[NeIII] 3868	45	98.32	0.01	1.24	0.01
cont. 3923	45	98.33	0.06	1.81	0.07
Hδ	50	98.49	0.05	1.04	0.05
cont. 4147	50	98.25	0.06	1.74	0.06
Hγ	35	98.33	0.04	1.09	0.04
[OIII] 4363	35	98.35	0.05	1.14	0.02
cont. 4466	35	98.38	0.05	1.73	0.07
Red Arm					
He II 4686	50	89.82	0.12	1.25	0.15
cont. 5545	50	89.84	0.04	1.74	0.05
Hβ	50	89.74	0.04	1.09	0.04
[OIII] 4959&5007	130	89.75	0.01	1.18	0.01
cont. 5093	130	89.85	0.04	1.74	0.05
[FeVII] 6086	65	89.83	0.02	1.19	0.02
cont. 6139	65	89.80	0.04	1.87	0.05
Hα	145	89.81	0.01	1.09	0.02
cont. 6435	145	89.81	0.04	1.71	0.05
[FeXI] 7892	40	89.76	0.10	1.18	0.11
cont. 7927	40	89.84	0.06	1.80	0.07

spectrum (PA163), and 15 arcseconds in the north west–south east direction (52kpc) in the WHT spectra (PA315), corresponding to the spatial extent of the galaxy disk visible in the Gemini r' image (see ∮ 3.3.5).

To determine the spatial distributions of both the emission lines and continuum along the slit, spatial slices were extracted from the 2D WHT spectrum over the wavelength ranges given in Table 3.1. The continuum slices were extracted with similar wavelength ranges to their nearby emission lines so that the continuum could be accurately subtracted from the slices containing the emission lines. The DIPSO STARLINK package was then used to measure the centroid and spatial FWHM of the flux distribution of each slice, by fitting a single Gaussian profile to the central cores of the emission.

Overall, the centroids measured for each emission line and continuum slice in Table 3.1 are all consistent within their uncertainties, implying no spatial offset between any of the emission lines individually, nor between the emission lines and the continuum.

The spatial FWHM of all the emission lines — with the exception of [OII]λ3727 — are consistent with the seeing on the night of the observations (see Chapter 2), suggesting that their spatial distributions are unresolved in the observations. Therefore the spatial distributions of the high ionisation lines provide an indication of the true seeing of the WHT observations ($1.1 < \mathrm{FWHM} < 1.35$ arcseconds). As expected, there is evidence that the seeing degrades towards shorter wavelengths, since the two shortest wavelength FHIL have significantly larger spatial FWHM than their longer wavelength counterparts. Moreover, the fact that the spatial FWHM measured for all continuum slices significantly exceeds the estimated seeing, demonstrates that the continuum emission is spatially resolved in the nuclear regions.

The spatial FWHM of the [OII]λ3727 emission line is significantly broader than the other FHILs at similar wavelengths in Table 3.1, and this line is clearly resolved in the 2D spectrum (see Figure 3.1). The combination of the large spatial extent and spatially resolved nuclear emission of [OII] makes this emission line ideal for the study of the emission line kinematics across the host galaxy J1131+16 presented in ∮ 3.3.6.

3.3.2 Line identifications

The optical spectra of J1131+16 are shown in Figures 3.2-3.5. What makes the spectrum of J1131+16 special is not only the large number of emission lines, but also their rich variety. In particular, the detected FHILs include [FeV]$\lambda\lambda\lambda$3839,3891&4181, [FeVI]$\lambda\lambda\lambda$5146,5176&5335, [FeVII]$\lambda\lambda\lambda\lambda\lambda\lambda$3759,4893,5159,5276,5720&6086, [FeX]λ6375,

[FeXI]λ7891 and [NeV]$\lambda\lambda$3346&3426[1]. As well as the FHILs, lower ionisation species which are not typically detected in quasar spectra are found in the spectrum, including [FeIV]$\lambda\lambda\lambda\lambda$2829,2836,4903&5236, along with Bowen resonance fluorescence lines of OIII, such as OIII λ3133. Also detected are more typical AGN emission lines such as Hα, Hβ, HeII λ4686, [OII]$\lambda\lambda$3726,3729, [OIII]$\lambda\lambda\lambda$4363,4959&5007. However, the FHILs are unusually strong with respect to these latter lines, with [NeV]λ3426 comfortably exceeding the strength of the [OII]λ3727 doublet, and [FeVII]λ6086 of comparable strength to Hβ. Also notable is the unusual strength of [OIII]λ4363 compared to Hγ and [OIII]λ5007 ([OIII]5007/4363 = 5.86$\pm$0.21 in the WHT spectrum), as well as the relatively modest ratio of [OIII]λ5007 to Hβ ([OIII]/Hβ=5.27$\pm$0.16), given the strength of the other high ionisation lines.

The strongest emission lines in this object have relatively large equivalent widths (EWs), including a large number of FHILs with EWs comparable to other typical lower ionisation emission lines. Indeed, the EWs of the FHILs in J1131+16 are larger than those of any other AGN with published spectra, including other objects with unusually strong FHILs such as III Zw 77 (Osterbrock, 1981) and Tololo 0109-383 (Fosbury & Sansom, 1983). Moreover the [OIII] emission line luminosity of J1131+16 (4.6$\pm$0.1x10^8 $L_\odot$) would lead to its classification as a quasar 2 object according to the criterion of Zakamska et al. (2003). Overall, the rich variety of emission lines, and their relatively large EWs, allow for a thorough investigation of the physical conditions of the FHIL emission region.

A full list of line identifications made from these spectra is presented in Tables 3.3 & 3.4. All the line identifications have been determined by fitting single Gaussians to the emission features in both the WHT and Gemini spectra. The rest-frame wavelength ranges that were fitted for J1131+16 are 2700-4600 Å and 4400-8000 Å in the WHT spectra, and 3100-5450 Å in the Gemini spectrum. Tables 3.3 & 3.4 give the line flux ratios relative to Hβ for both spectra. The fluxes of the emission lines have not been corrected for intrinsic reddening for reasons that will become clear in $\oint$ 3.3.8. In addition, it appears that there is no need of a Galactic extinction correction, since the IRSA extinction tool in the NASA/IPAC Extragalactic Database (NED) gives a reddening of only E(B-V)= 0.0306 (Schlegel, Finkbeiner & Davis, 1998).

The majority of line identifications have been confirmed in other astrophysical objects such as AGN and planetary nebula (e.g. Osterbrock 1981, Fosbury & Sansom 1983, Alloin et al. 1992, Kaler 1976). However, there are several emission lines on Tables 3.3 &

[1]In this study I define a FHIL as an emission species with an ionisation potential greater than or equal to 54.4 eV (that of HeII).

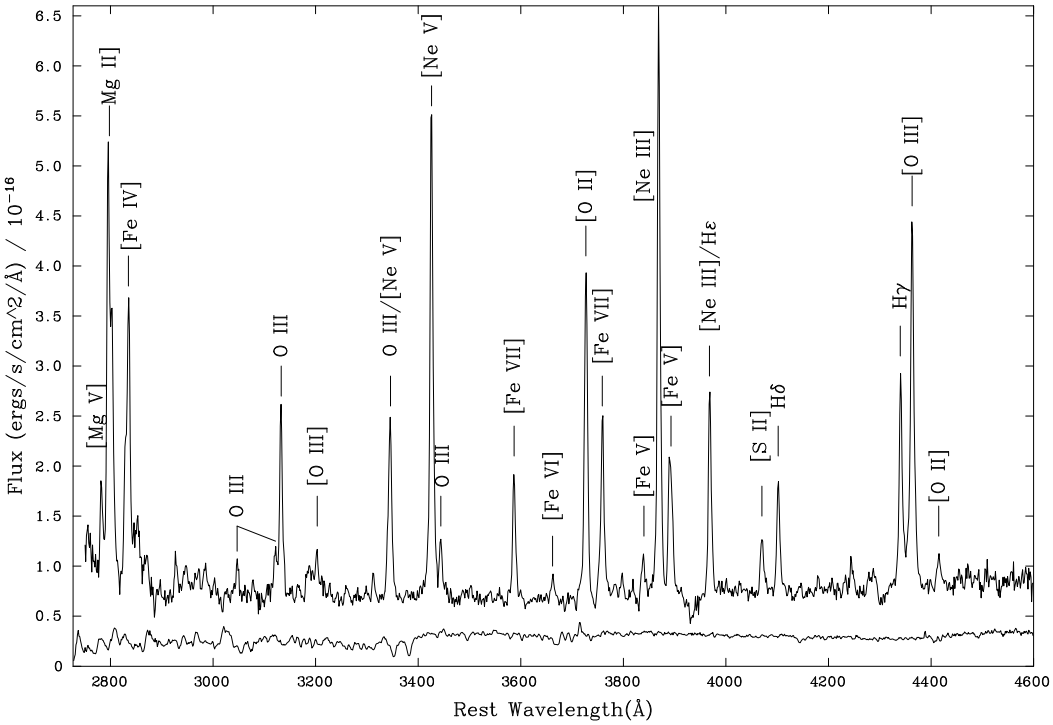

Figure 3.2: WHT nuclear spectrum of J1131+16 taken on the ISIS blue arm. Double lines which are labelled with an '&' indicates that both components are resolvable, those labelled with a '/' indicates that both components are not resolvable. The flux scale is measured in units of 10^{-16} ergs s^{-1} $Å^{-1}$ cm^{-2}. Note the strength of high ionisation lines such as [NeV] and [FeVII] relative to [OII], and of [OIII]λ4363 relative to Hδ. For reference I also show a scaled version of the night sky spectrum extracted from the 2D frames at the bottom of the plot.

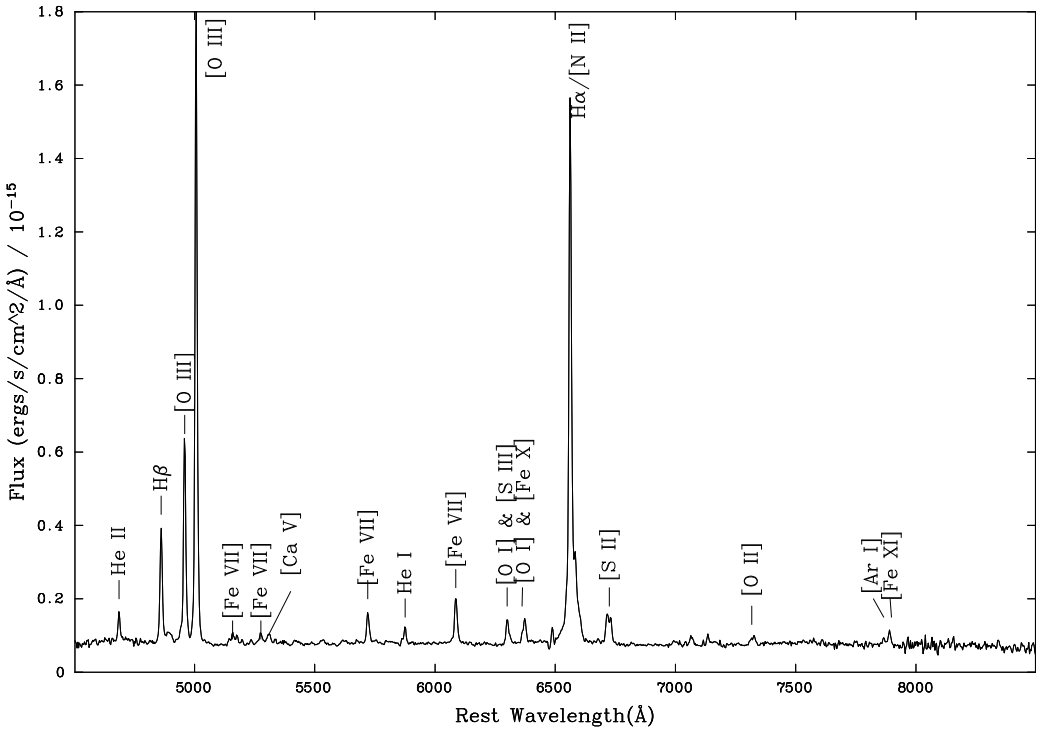

Figure 3.3: WHT nuclear spectrum of J1131+16 taken on the ISIS red arm. Double lines which are labelled with an '&' indicates that both components are resolvable, those labelled with a '/' indicates that both components are not resolvable. The flux scale is measured in units of 10^{-15} ergs s^{-1} $Å^{-1}$ cm^{-2}.

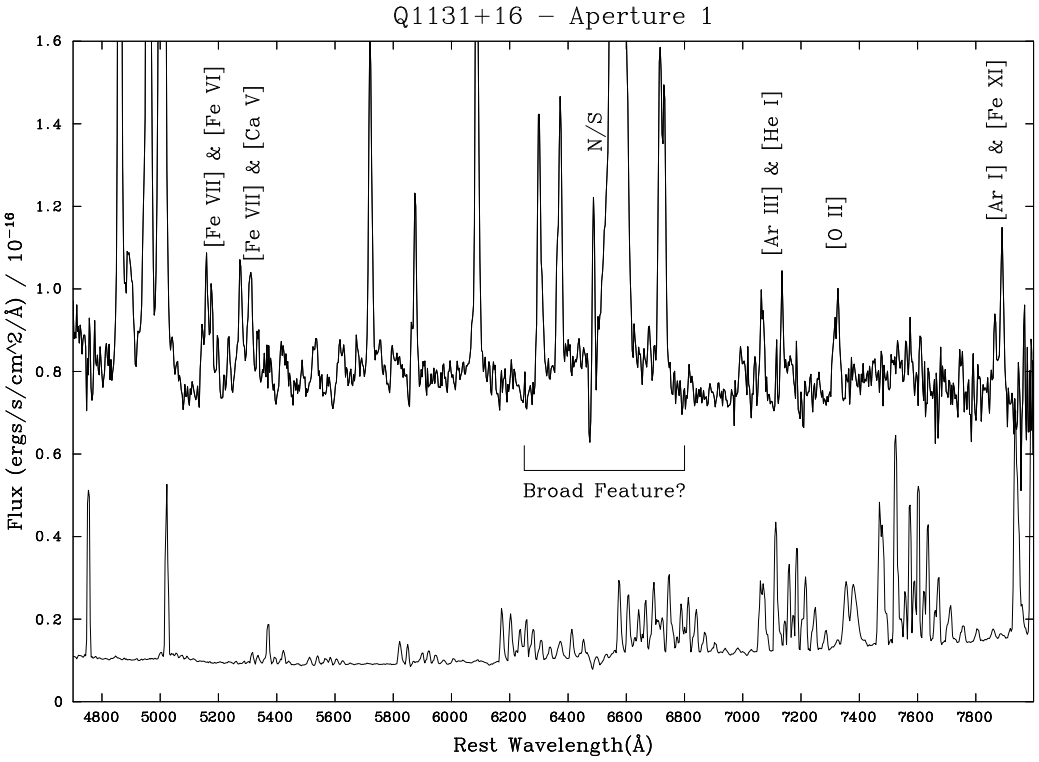

Figure 3.4: An expanded plot of the J1131+16 ISIS red arm spectrum. This has been presented to highlight the weaker features in the red spectrum. The flux scale is measured in units of 10^{-16} ergs s^{-1} $Å^{-1}$ cm^{-2}. As well as the multitude of high ionisation lines, note the broad base to the Hα+[NII] blend. For reference I also show a scaled version of the night sky spectrum extracted from the 2D frames at the bottom of the plot.

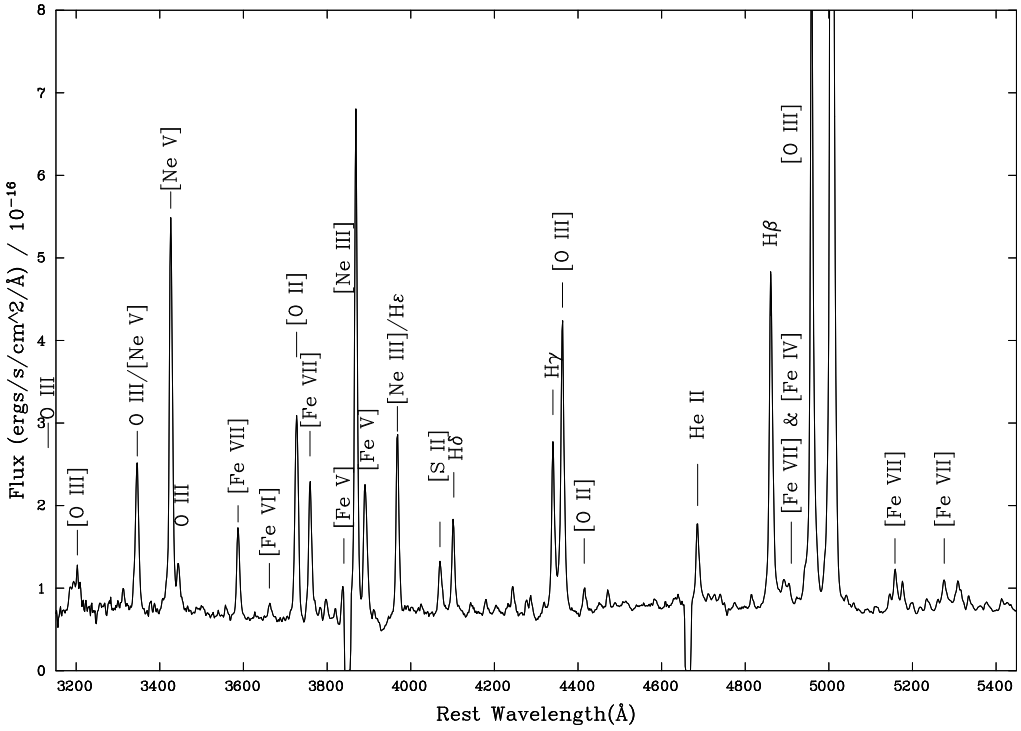

Figure 3.5: Nuclear spectrum of J1131+16 taken using GMOS on the Gemini South telescope. The flux scale has been narrowed here to highlight how rich the spectrum is in emission lines. The flux scale is measured in units of 10^{-16} ergs s^{-1} $Å^{-1}$ cm^{-2}. The gaps in the spectrum are due to the gaps between the CCD chips in the GMOS instrument.

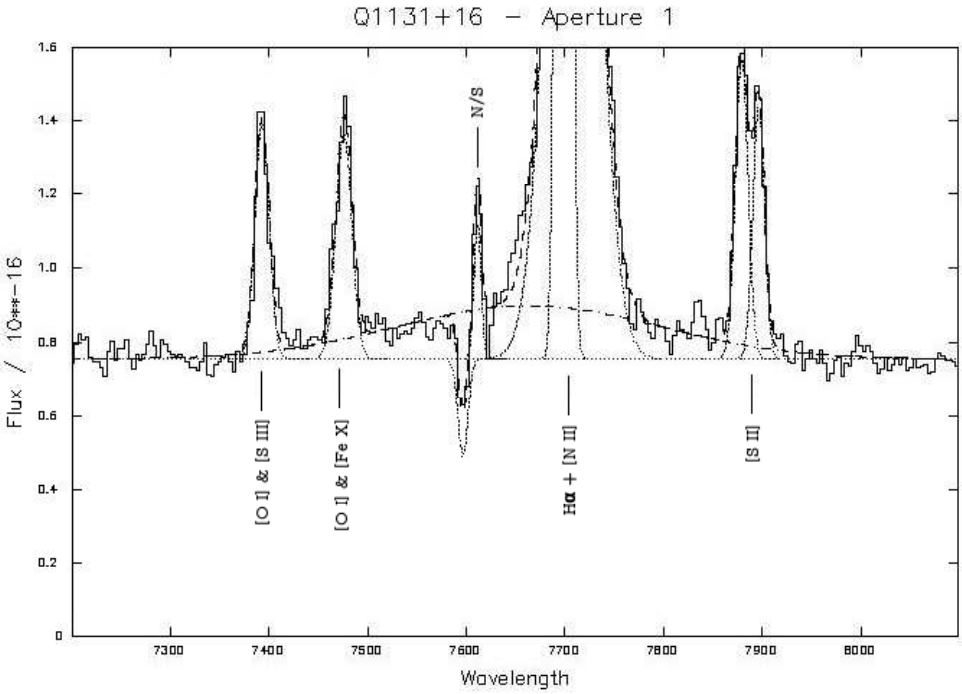

Figure 3.6: The broad component centered on the Hα+[NII] emission blend. The telluric feature is fitted as well as the various emission components from J1131+16.

3.4 which have been identified using the National Institute of Standards and Technology (NIST) spectral line database (see ref. 4 in Tables 3.3 & 3.4). An emission line was only regarded as a secure ID if its line centre was within 1.5 sigma of the wavelength predicted for that particular emission line based on the mean redshift, and if its S/N ratio exceeded 3.0. As well as the 66 identified emission lines, there are 37 emission lines which remain unidentified (see Table 3.5), in the sense that there are no IDs for them in the NIST spectral line database that give redshifts within 1.5 sigma of the mean redshift, yet their S/N exceeds 3. Note that, due to its higher S/N, the Gemini spectrum reveals a large number of faint lines that were not detected in the original WHT spectrum (see Tables 3.3, 3.4 and 3.5).

Interestingly, although there are many iron FHILs in the spectrum of J1131+16, there is no clear evidence for the [FeXIV]λ5303 emission line. The identification of this emission feature at $\sim$5300 Å has been controversial in the past: it has been debated whether it is [FeXIV]λ5303 or [CaV]λ5309 (e.g. Oke & Sargent 1968, Weedman 1971). When this feature is fitted in the WHT spectrum, if only the [CaV]λ5309 identification is considered, the individual redshift of the emission line (0.17319$\pm$0.00011 for the WHT spectrum) agrees within the uncertainties with the average redshift of all the lines (0.17325$\pm$0.00001,

Table 3.2: Observed wavelength, line widths and fluxes of the Paschen emission lines in the LIRIS spectra.

Line ID	λ (Å)	Line Width (Å)	Flux ($10^{(}-15$) erg s^{-1} Å^{-1} cm^{-3})
Pα	21997.6±2.4	68±7.2	3.4±0.3
Pβ	15027.3±2.0	39±5.0	1.6±0.2

see § 3.3.6). However, if the feature is identified with [FeXIV]λ5303, the individual redshift becomes 0.17455±0.00011, which is significantly higher (>10σ) than the mean redshift.

A further interesting feature of the spectrum is that the Hα+[NII] emission blend shows tentative evidence for a broad base of rest-frame width 11,500±2200 km s^{-1} (FWHM, see Figures 3.4 & 3.6). This is consistent with the presence of a scattered (Antonucci & Miller, 1985), or directly observed, BLR component. Spectropolarimetry observations will be required to confirm the scattered BLR possibility.

3.3.3 Infrared spectrum

In order to further understand the nature of this object I made spectroscopic observations of J1131+16 at near-IR wavelengths. The observed wavelength range (1.4 to 2.4μm) was selected in order to simultaneously detect both Paα and Paβ.

The H and K-band NIR spectra of J1131+16 taken using LIRIS are presented in Figure 3.7, and the properties of the emission lines as measured by DIPSO are given in Table 3.2. Due to its relatively low S/N, this spectrum does not show the abundance of emission lines seen at optical wavelengths. Although weak narrow Paα and Paβ[2] emission lines are detected, there is no sign of any broad Paα and Paβ components, implying the BLR is enshrouded by dust. A single Gaussian fit to the Paα line shows that it is unresolved within the uncertainties for the resolution of the observations, and its redshift (z=0.17314±0.00011) is consistent with those of the optical emission lines.

Any quasar nucleus component present in this system must be highly extinguished; the relatively red near-IR colours of this source measured by 2MASS do not appear to be due to a moderately extinguished quasar component that becomes visible at the longer near-IR wavelengths. Therefore this object cannot truly be described as a 'red quasar'.

[2]The Paβ emission line is on the blue edge of the H-band NIR spectrum, because of this any measured emission line data is questionable.

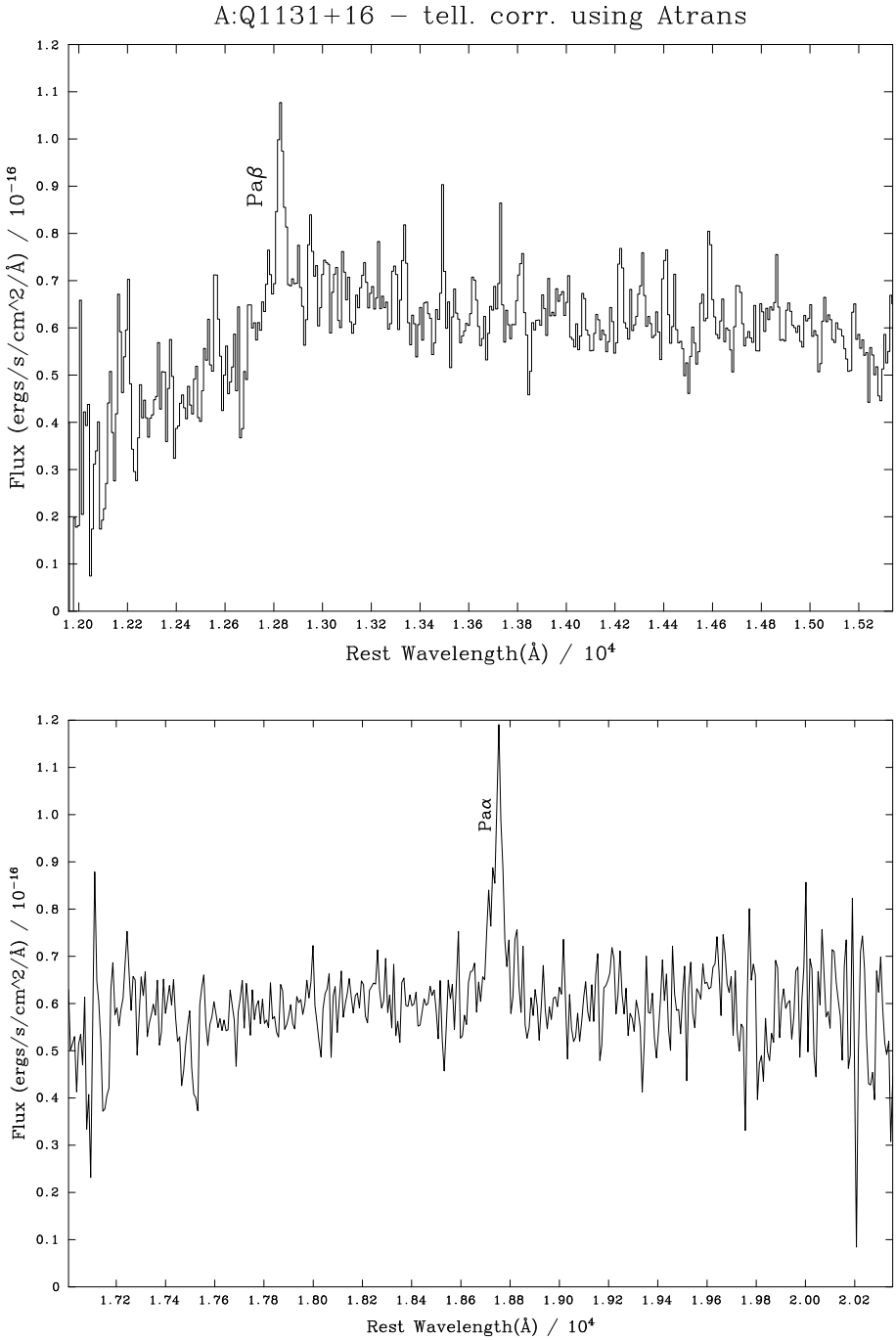

Figure 3.7: *Top.* The H-band LIRIS spectrum of J1131+16. The rest wavelength range shown here is 12000-15400 Å. The only significant feature is the Paβ emission line, however due to being on the blue edge of the H-band, any measured emission line data for Paβ is questionable. *Bottom.* The K-band LIRIS spectrum of J1131+16. The rest wavelength range shown here is 17000-20500 Å. The only significant feature is the Paα emission line.

3.3.4 Spectral fitting model

The emission lines in the spectrum of J1131+16 were initially fitted with single Gaussian profiles, but such fits did not provide an entirely adequate fit to the wings of the stronger lines (see Figure 3.8). To overcome this, a double Gaussian model was fitted to the spectral lines. This model is based on the fit of the [OIII]$\lambda\lambda$5007,4959 lines, because they are particularly strong emission features. To produce the model, both broad and narrow Gaussians were fitted to the Gemini [OIII] line profiles, where the centres, widths and intensities of each Gaussian were free parameters. The widths (FWHM) of the narrow components for the [OIII] emission lines were found to be consistent with the instrumental width of the Gemini spectra (7.1 Å) at 6.9±0.2 Å. I therefore use the instrumental width to fit the narrow components in the model fit to other lines, varying this to take into account the resolution of the different spectra. The measured FWHM of the broad component (14.1±0.6 Å(FWHM), corresponding to a rest-frame velocity width of 720±30 km s^{-1}) was used to obtain an intrinsic velocity width for the broader component by correcting its FWHM in quadrature using the instrumental width. In addition, the broad component is redshifted by 1.8±0.1 Å from the narrow component, corresponding to a velocity shift of 92±6 km s^{-1} in the galaxy rest frame. The double Gaussian [OIII] model was then fitted to all other emission lines, in order to derive the line fluxes listed in Tables 3.3, 3.4 and 3.5.

Figure 3.8 shows the spectral fit to the [OIII]λ5007 emission line used to determine the spectral fitting model. The overall fit in the bottom panel of Figure 3.8 is significantly better than that shown in the top panel, where the emission lines are fitted with a single component free fit. The parameters from the double Gaussian [OIII] fits were used to fit the emission lines throughout the spectrum. In general these fits were extremely successful. There is, however, a minority of lines — indicated by notes 1 and 2 in Tables 3.3, 3.4 and 3.5 — which are not fitted well by both components of the [OIII] model. These lines are generally weak, and many are in blends with other emission lines.

The [NII]$\lambda\lambda$6548,6584 doublet is blended with the Hα emission line and therefore was modelled using constraints provided by atomic physics (i.e. same FWHM, 1:3 intensity ratio, and line centre of λ6548 fixed to the centre of λ6583). This is true of other doublet blends, for example the [OI]$\lambda\lambda$6300,6364 (blended with [SIII]λ6312 and [FeX]λ6375).

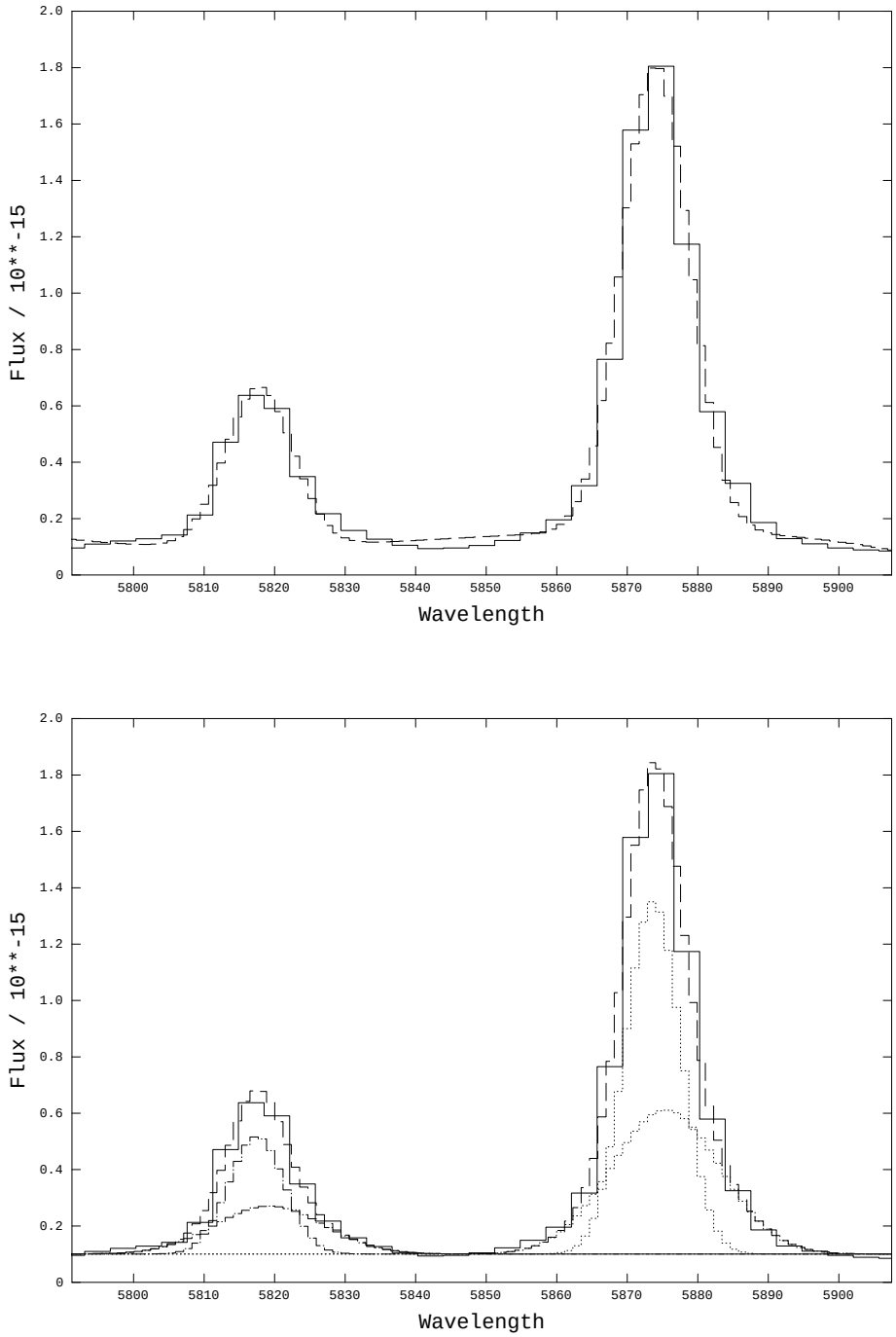

Figure 3.8: Fits to the [OIII]$\lambda\lambda$5007,4959 emission lines. *Top.* Single Gaussian fit to both [OIII]λ5007 and λ4959. The overall fit does not fit the wings of the emission lines well. *Bottom.* The double Gaussian fit to the [OIII]λ5007 and λ4959 emission lines from the Gemini data. Here the model has had more success in fitting the wings of the emission lines when compared to that above. The individual components of the fit are included on the plot; the components of λ5007 are drawn with a dotted line and the components of λ4959 are fitted with a dashed and dotted line. The overall line profile is fit with a dashed line. The model throughout this investigation is based on the [OIII]λ5007 emission line. The flux is measured in 10^{-15} ergs s^{-1} Å^{-1} cm^{-2} and the wavelength is in units of Å.

Table 3.3: Line identifications for the nuclear spectra of J1131+16 from the WHT spectrum. Flux ratios relative to Hβ are not corrected for reddening. Line IDs and redshifts are determined via fitting a single Gaussian to the emission lines. Errors for the measured wavelengths and redshifts include calibration errors as well as errors due to the measurement techniques. The total flux of the Hβ emission line is (4.38±0.11)x10^{-15} ergs s^{-1} $Å^{-1}$ cm^{-3}. Reference key for Table 3.3: (1)Osterbrock (1981), (2) Siegel et al. (1998), (3) Identified Using the FIVEL program, (4) Identified using NIST database, (5) Meinel et al. (1975), (6) Kaler (1976) & (7) Tran et al. (1998). Notes key for Table 3.3: (1) The broad line components were not modelled for these emission features to avoid negative flux results for their line fluxes. (2) The narrow line components were not modelled for these emission features to avoid negative flux results for their line fluxes.

[-2ex] **Line ID**	λ **(Å)**	λwht **(Å)**	**F/F**$H\beta wht$	**z**wht	**Ref.**	**notes**
[MgV]	2782.7	3264.7 ± 0.36	0.158 ± 0.024	0.1732 ± 0.00011	7	-
MgII]	2795.5	3279.7 ± 0.6	0.63 ± 0.126	0.1732 ± 0.00015	2	-
MgII]	2802.7	3287.9 ± 0.71	0.549 ± 0.129	0.1731 ± 0.00015	4	-
[FeIV]	2829.3	3319.6 ± 0.6	0.199 ± 0.021	0.1733 ± 0.00013	4	1
[FeIV]	2835.7	3326.9 ± 0.52	0.419 ± 0.021	0.1732 ± 0.0001	4	1
OIII	3132.9	3675.2 ± 0.52	0.358 ± 0.027	0.1731 ± 0.00014	1	-
HeI	3187.7	3740.1 ± 0.61	0.081 ± 0.01	0.1733 ± 0.00026	4	2
HeII	3202.7	3757.2 ± 0.97	0.095 ± 0.024	0.1731 ± 0.00026	6	-
[OIII]	3312.3	3886.6 ± 0.64	0.037 ± 0.004	0.1734 ± 0.00018	4	1
[NeV]	3425.9	4019.5 ± 0.5	1.01 ± 0.085	0.1733 ± 0.00012	1	-
[FeVI]	3662.5	4297.2 ± 0.51	0.051 ± 0.011	0.1733 ± 0.00014	1	-
[OII]	3726	4371.9 ± 0.61	0.597 ± 0.028	0.1733 ± 0.00011	1	-
[OII]	3728.8	4375.1 ± 0.63	0.156 ± 0.049	0.1733 ± 0.00011	1	-
[FeVII]	3758.9	4410.5 ± 0.51	0.421 ± 0.028	0.1733 ± 0.00012	1	-

Continued on Next Page...

Table 3.3 – Continued

Line ID	λ **(Å)**	λwht **(Å)**	$\mathbf{F/F}H\beta wht$	$\mathbf{z}wht$	**Ref.**	**notes**
[FeV]	3839.3	4504.1 ± 0.91	0.084 ± 0.035	0.1731 ± 0.0002	1	-
[NeIII]	3868.8	4539.4 ± 0.5	1.103 ± 0.05	0.1733 ± 0.00012	1	-
[FeV]	3891.3	4565.6 ± 0.56	0.363 ± 0.051	0.1733 ± 0.00012	1	-
[NeIII]	3967.5	4655.3 ± 0.51	0.449 ± 0.038	0.1733 ± 0.00011	1	-
[SII]	4068.6	4773.5 ± 0.5	0.098 ± 0.012	0.1733 ± 0.00012	1	-
[SII]	4076.3	4782.5 ± 0.5	0.021 ± 0.004	0.1733 ± 0.0001	3	2
Hδ	4101.7	4812.7 ± 0.51	0.24 ± 0.016	0.1733 ± 0.00011	1	-
Hγ	4340.5	5092.6 ± 0.5	0.438 ± 0.024	0.1733 ± 0.0001	1	-
[OIII]	4363.2	5119.2 ± 0.5	0.899 ± 0.019	0.1733 ± 0.0001	1	-
[OII]	4414.9	5180.1 ± 0.78	0.067 ± 0.023	0.1733 ± 0.0001	4	-
HeII	4685.7	5497.5 ± 0.63	0.207 ± 0.05	0.1733 ± 0.00011	1	-
Hβ	4861.3	5703.5 ± 0.5	1 ± 0	0.1733 ± 0.0001	1	-
[FeVII]	4893.4	5740.8 ± 0.51	0.055 ± 0.018	0.1732 ± 0.0001	4	-
[FeIV]	4903.1	5753 ± 0.52	0.012 ± 0.004	0.1733 ± 0.00012	4	1
[OIII]	4958.9	5817.7 ± 0.5	1.757 ± 0.085	0.1732 ± 0.0001	1	-
[OIII]	5006.8	5874 ± 0.5	5.27 ± 0.155	0.1732 ± 0.0001	1	-
[FeVI]	5145.8	6036.9 ± 0.52	0.053 ± 0.005	0.1732 ± 0.0001	1	-
[FeVII]	5159	6052.7 ± 0.81	0.103 ± 0.03	0.1732 ± 0.00012	1	-
[FeVI]	5176.4	6073.4 ± 0.66	0.097 ± 0.024	0.1733 ± 0.00012	1	-
[FeIV]	5236.1	6142.3 ± 1.21	0.035 ± 0.005	0.1731 ± 0.00021	4	1
[FeVII]	5276.4	6189.6 ± 0.65	0.121 ± 0.021	0.1731 ± 0.00011	4	-
[CaV]	5309.1	6228.6 ± 0.7	0.135 ± 0.016	0.1732 ± 0.00011	1	-

Continued on Next Page...

Table 3.3 – Continued

Line ID	λ **(Å)**	λwht **(Å)**	**F/F**$H\beta wht$	**z**wht	**Ref.**	**notes**
[FeVI]	5335.2	6259.9 ± 2.25	0.032 ± 0.005	0.1733 ± 0.0003	4	-
[FeVII]	5720.7	6712 ± 0.56	0.318 ± 0.027	0.1733 ± 0.0001	1	-
HeI	5875.6	6893.1 ± 0.66	0.141 ± 0.026	0.1732 ± 0.0001	1	-
[FeVII]	6086.9	7141.1 ± 0.52	0.495 ± 0.028	0.1732 ± 0.0001	1	-
[OI]	6300.3	7391.5 ± 0.55	0.196 ± 0.017	0.1732 ± 0.0001	1	-
[SIII]	6312.1	7405.7 ± 0.55	0.06 ± 0.016	0.1733 ± 0.0001	1	-
[OI]	6363.8	7466.5 ± 0.55	0.063 ± 0.006	0.1733 ± 0.0001	1	-
[FeX]	6374.6	7479.2 ± 0.55	0.234 ± 0.034	0.1733 ± 0.0001	1	-
[NII]	6548.1	7682.2 ± 0.61	0.262 ± 0.02	0.1732 ± 0.00018	1	-
Hα	6562.8	7699.5 ± 0.7	4.997 ± 0.173	0.1732 ± 0.00019	1	-
Hα_{broad}	6562.8	7663.4 ± 16.06	1.088 ± 0.188	0.1677 ± 0.0021	1	-
[NII]	6583.4	7723.6 ± 0.62	0.786 ± 0.059	0.1732 ± 0.00018	1	-
[SII]	6716.4	7879.7 ± 0.65	0.332 ± 0.039	0.1732 ± 0.0001	1	-
[SII]	6730.8	7896.1 ± 0.65	0.219 ± 0.039	0.1732 ± 0.0001	1	-
HeI	7065.7	8290 ± 1.06	0.111 ± 0.024	0.1733 ± 0.00013	4	-
[ArIII]	7135.8	8371 ± 0.69	0.091 ± 0.031	0.1731 ± 0.0001	5	-
[OII]	7319.9	8586.3 ± 0.99	0.096 ± 0.028	0.173 ± 0.00013	1	-
[OII]	7330.2	8598.3 ± 0.99	0.037 ± 0.011	0.173 ± 0.00013	1	-
[ArI]	7868.2	9228.6 ± 1.03	0.09 ± 0.022	0.173 ± 0.00013	4	-
[FeXI]	7891.8	9256.8 ± 0.67	0.157 ± 0.021	0.173 ± 0.0001	1	-

Table 3.4: Line identifications for the nuclear spectra of J1131+16 from the Gemini spectrum. Flux ratios relative to Hβ are not corrected for reddening. Line IDs and redshifts are determined via fitting a single Gaussian to the emission lines. Errors for the measured wavelengths and redshifts include calibration errors as well as errors due to the measurement techniques. The total flux of the Hβ emission line is (4.74±0.11)x10^{-15} ergs s^{-1} $Å^{-1}$ cm^{-3}. Reference key for Table 3.4: (1)Osterbrock (1981), (2) Siegel et al. (1998), (3) Identified Using the FIVEL program, (4) Identified using NIST database, (5) Meinel et al. (1975), (6) Kaler (1976) & (7) Tran et al. (1998). Notes key for Table 3.4: (1) The broad line components were not modelled for these emission features to avoid negative flux results for their line fluxes. (2) The narrow line components were not modelled for these emission features to avoid negative flux results for their line fluxes.

[-2ex] **Line ID**	λ **(Å)**	λgem **(Å)**	**F/F**$H\beta gem$	**z**gem	**Ref.**	**notes**
OIII	3132.9	3675.8 ± 0.51	0.382 ± 0.041	0.1733 ± 0.00014	1	-
HeI	3187.7	3738.7 ± 0.7	0.074 ± 0.006	0.1729 ± 0.00019	4	2
HeII	3202.7	3757.6 ± 0.55	0.079 ± 0.006	0.1733 ± 0.00015	6	-
[OIII]	3312.3	3885 ± 2.1	0.034 ± 0.003	0.1729 ± 0.00054	4	1
[NeV]	3425.9	4020.2 ± 0.52	1.051 ± 0.035	0.1735 ± 0.00013	1	-
[NI]	3466	4067 ± 1.8	0.026 ± 0.003	0.1734 ± 0.00044	6	1
HeI	3487.6	4092.3 ± 1.7	0.023 ± 0.003	0.1734 ± 0.00042	6	-
[FeVI]	3662.5	4298 ± 1.1	0.042 ± 0.006	0.1735 ± 0.00026	1	-
HI	3704.9	4346.7 ± 0.52	0.011 ± 0.002	0.1732 ± 0.00012	6	2
[OII]	3726	4371.6 ± 0.59	0.513 ± 0.039	0.1733 ± 0.00013	1	-
[OII]	3728.8	4374.7 ± 0.6	0.131 ± 0.025	0.1732 ± 0.00011	1	-
[FeVII]	3758.9	4410.9 ± 0.51	0.395 ± 0.018	0.1735 ± 0.00012	1	-
HI	3797.9	4455.6 ± 0.8	0.036 ± 0.004	0.1732 ± 0.00018	6	-

Continued on Next Page...

Table 3.4 – Continued

Line ID	λ **(Å)**	λgem **(Å)**	$\mathbf{F/F}H\beta gem$	$\mathbf{z}gem$	**Ref.**	**notes**
HeI	3819.3	4480.4 ± 0.8	0.023 ± 0.003	0.1731 ± 0.00018	6	2
[FeV]	3839.3	4502.6 ± 0.52	0.069 ± 0.003	0.1728 ± 0.00012	1	2
[NeIII]	3868.8	4539.3 ± 0.79	1.359 ± 0.102	0.1733 ± 0.00017	1	-
[FeV]	3891.3	4565.4 ± 0.6	0.533 ± 0.003	0.1732 ± 0.00013	1	-
[NeIII]	3967.5	4655.7 ± 0.59	0.466 ± 0.02	0.1735 ± 0.00013	1	-
HeI	4026.2	4722.6 ± 1.1	0.013 ± 0.002	0.173 ± 0.00023	6	2
[SII]	4068.6	4774.1 ± 0.58	0.142 ± 0.012	0.1734 ± 0.00012	1	-
[SII]	4076.3	4785.4 ± 0.58	0.019 ± 0.006	0.174 ± 0.00012	3	-
Hδ	4101.7	4812.3 ± 0.5	0.24 ± 0.013	0.1732 ± 0.0001	1	-
[FeV]	4180.9	4904.1 ± 0.52	0.04 ± 0.006	0.173 ± 0.00011	6	-
[OII]	4317.2	5066.6 ± 0.5	0.056 ± 0.007	0.1736 ± 9.9E-05	6	-
Hγ	4340.5	5092.7 ± 0.61	0.454 ± 0.029	0.1733 ± 0.00012	1	-
[OIII]	4363.2	5118.8 ± 0.59	0.839 ± 0.031	0.1732 ± 0.00012	1	-
[OII]	4414.9	5180.5 ± 0.55	0.075 ± 0.011	0.1734 ± 0.00011	4	-
HeI	4471.4	5246.4 ± 0.5	0.044 ± 0.011	0.1733 ± 9.5E-05	6	-
HeII	4685.7	5497.9 ± 0.51	0.234 ± 0.012	0.1733 ± 9.3E-05	1	-
[ArIV]	4712.6	5528.6 ± 0.67	0.055 ± 0.01	0.1732 ± 0.00012	6	-
Hβ	4861.3	5703.8 ± 0.52	1 ± 0	0.1733 ± 9.1E-05	1	-
[FeVII]	4893.4	5740.6 ± 0.52	0.057 ± 0.016	0.1731 ± 0.00012	4	-
[FeIV]	4903.1	5753.1 ± 0.51	0.038 ± 0.011	0.1734 ± 0.00012	4	1
[OIII]	4958.9	5818.1 ± 0.55	1.914 ± 0.053	0.1733 ± 9.5E-05	1	-
[OIII]	5006.8	5874.3 ± 0.55	5.74 ± 0.158	0.1733 ± 9.4E-05	1	-

Continued on Next Page...

Table 3.4 – Continued

Line ID	λ **(Å)**	λgem **(Å)**	$\mathbf{F/F}H\beta gem$	$\mathbf{z}gem$	**Ref.**	**notes**
[FeVI]	5145.8	6036.7 ± 0.65	0.047 ± 0.005	0.1731 ± 0.00011	1	-
[FeVII]	5159	6052.7 ± 0.51	0.123 ± 0.004	0.1732 ± 8.4E-05	1	-
[FeVI]	5176.4	6072.9 ± 0.6	0.094 ± 0.004	0.1732 ± 9.9E-05	1	-
[FeIV]	5236.1	6143.3 ± 0.62	0.051 ± 0.006	0.1733 ± 0.0001	4	-
[FeVII]	5276.4	6189.3 ± 0.52	0.113 ± 0.006	0.173 ± 8.4E-05	4	-
[CaV]	5309.1	6227.4 ± 2.1	0.105 ± 0.009	0.173 ± 0.00034	1	-
[FeVI]	5335.2	6259.7 ± 0.64	0.046 ± 0.007	0.1733 ± 0.0001	4	-
[FeVI]	5425.7	6366.4 ± 0.64	0.03 ± 0.004	0.1734 ± 0.0001	6	-

Table 3.5: Unidentified emission lines across both spectra. The flux ratios are relative to Hβ. All wavelengths are measured in the observed frame. A notes key is included in Table 3.3.

λwht	$\lambda gemini$ **(Å)**	**F/F**$H\beta wht$	**F/F**$H\beta gem$	**notes**	**Suggested ID**
3344.0±1.09	-	0.141 ± 0.034	-	2	[ArIV]
3488.9 ± 0.91	-	0.055 ± 0.008	-	2	[NeV]
3661.9 ± 0.52	3662.9 ± 0.61	0.072 ± 0.027	0.091 ± 0.007	2	[OIII]
-	3747.9 ± 1.10	-	0.079 ± 0.009	-	?
3924.7 ± 0.51	3925.1 ± 0.52	0.420 ± 0.016	0.434 ± 0.034	-	OIII/[NeV]
-	3963.2 ± 0.56	-	0.023 ± 0.004	2	?
4040.4 ± 0.66	4039.4 ± 1.50	0.122 ± 0.033	0.099 ± 0.036	-	OIII
-	4108.1 ± 1.50	-	0.029 ± 0.004	1	?
-	4174.6 ± 0.60	-	0.017 ± 0.002	2	?
4208.3 ± 0.51	4208.9 ± 0.58	0.164 ± 0.017	0.242 ± 0.012	-	[FeVII]
-	4326.5 ± 0.52	-	0.006 ± 0.002	2	HI
-	4336.2 ± 0.52	-	0.008 ± 0.002	2	HI
4426.3 ± 1.24	4425.3 ± 1.45	0.010 ± 0.002	0.008 ± 0.001	-	HI
-	4438.4 ± 1.40	-	0.017 ± 0.004	2	?
-	4863.6 ± 0.60	-	0.034 ± 0.006	-	HeI
-	4904.1 ± 0.52	-	0.040 ± 0.006	-	[FeV]
-	4933.8 ± 0.70	-	0.030 ± 0.006	-	?
4979.8 ± 0.57	4979.7 ± 0.55	0.091 ± 0.022	0.080 ± 0.009	-	?
5030.2 ± 1.13	5029.6 ± 0.66	0.072 ± 0.027	0.047 ± 0.014	-	?
-	5066.6 ± 0.50	-	0.056 ± 0.007	-	[OII]
-	5291.0 ± 2.40	-	0.009 ± 0.002	-	[NIII]
5301.8 ± 0.59	5302.1 ± 1.60	0.056 ± 0.027	0.030 ± 0.004	1	?
-	5443.5 ± 1.10	-	0.024 ± 0.006	-	[NIII]
-	5544.5 ± 0.76	-	0.048 ± 0.009	-	?
-	5561.1 ± 0.63	-	0.045 ± 0.009	-	?
-	5649.8 ± 0.52	-	0.034 ± 0.006	-	?
-	5915.6 ± 0.60	-	0.025 ± 0.006	1	[SiII]
-	6122.5 ± 0.60	-	0.010 ± 0.002	2	?
-	6171.4 ± 0.81	-	0.018 ± 0.004	-	?
-	6238.3 ± 5.90	-	0.025 ± 0.007	-	?
-	6309.3 ± 0.78	-	0.029 ± 0.006	-	?

Continued on Next Page...

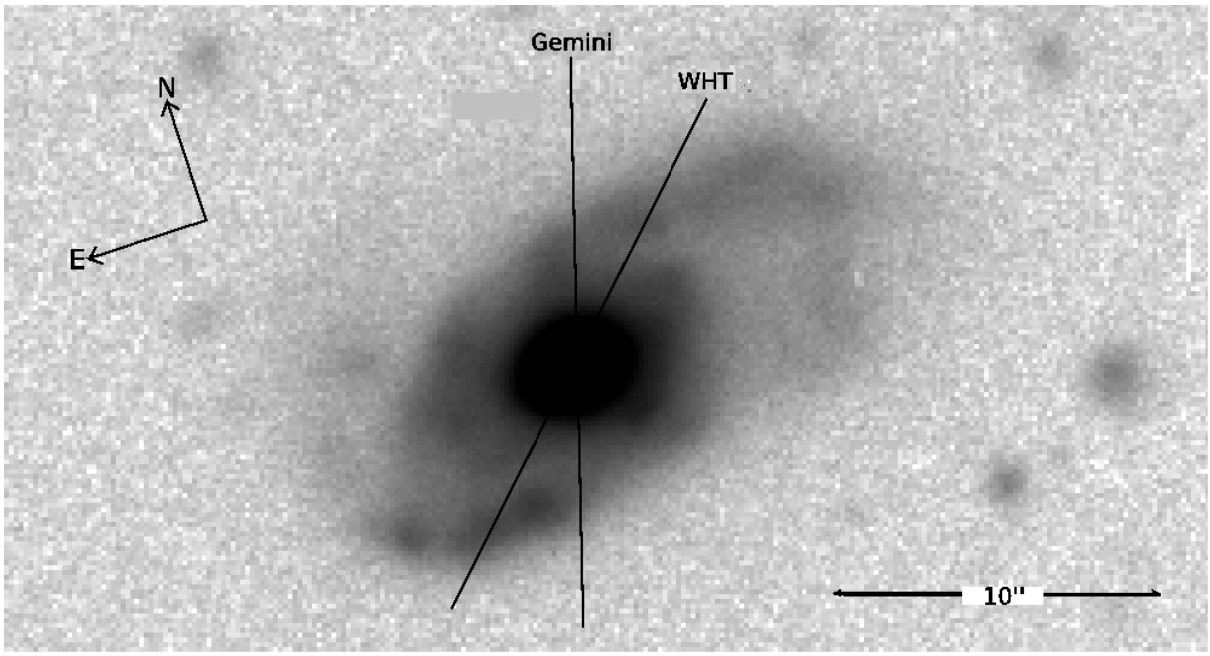

Figure 3.9: GMOS r' image of the host galaxy J1131+16. Indicated are the North and East axes as well as the slit PA of each spectroscopic data set.

Table 3.5 – Continued

λwht	$\lambda gemini$ (Å)	**F/F**$H\beta wht$	**F/F**$H\beta gem$	**notes**	**Suggested ID**
-	6350.1 ± 0.52	-	0.036 ± 0.004	-	HeII
6481.8 ± 1.42	-	0.023 ± 0.003	-	-	?
6495.8 ± 1.15	-	0.044 ± 0.019	-	-	?
6588.3 ± 2.17	-	0.024 ± 0.008	-	-	?
6605.3 ± 2.18	-	0.239 ± 0.016	-	-	[FeVI]
6748.5 ± 2.94	-	0.046 ± 0.010	-	2	[NII]
8403.8 ± 3.14	-	0.062 ± 0.013	-	-	?

3.3.5 Host galaxy morphology

Figure 3.9 presents the Gemini r'-band image of J1131+16. The galaxy morphology appears consistent with a late type spiral classification (Sb or Sc), with a moderate degree of asymmetry in the sense that the spiral arms are more extended to the west than the east of the nucleus. However, I do not find evidence for the "large scale and clear tidal disturbance" reported by Hutchings et al. (2003). Clearly, a more detailed

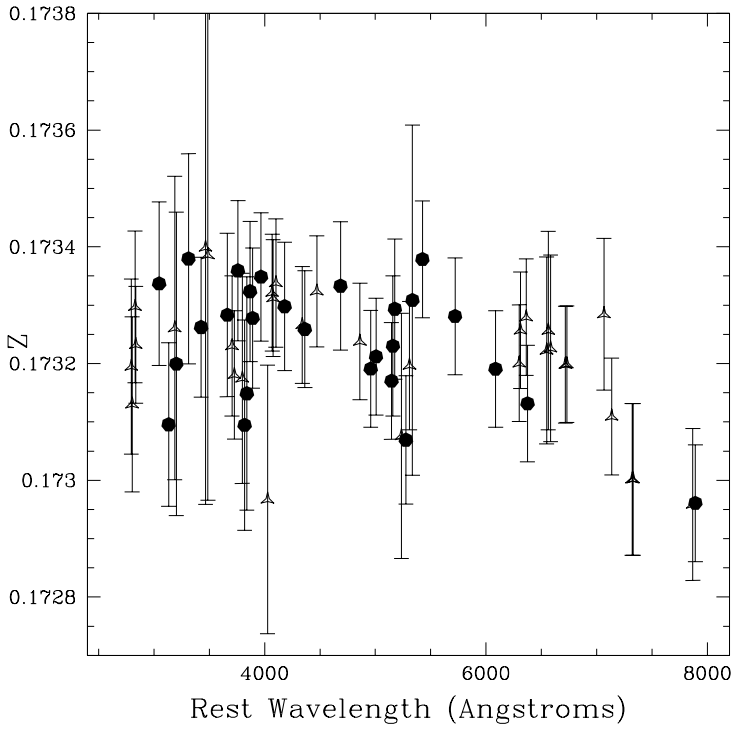

Figure 3.10: Individual redshifts of the emission lines of J1131+16 as measured for the WHT data. The triangles indicate the low ionisation emission lines and neutral species emission, the black circles indicate the FHILs. All points lie within 1.5 σ of the mean redshift, however the longer wavelength emission lines ([OII]$\lambda\lambda$7320&7330, [ArIV]λ7868 and [FeXI]λ 7892) do not. This is likely due to larger wavelength calibration errors at the long wavelength end of the spectrum.

analysis of the morphology and kinematics of the host galaxy is required in order to determine the true interaction status of this system.

Based on aperture photometry, the total magnitude of the host galaxy was estimated using a circular aperture of diameter 23 arcseconds (57 kpc), giving an r'-band magnitude of 17.11±0.26 — consistent with the Petrosian r-band magnitude for this object listed on the SDSS web site. Note that this estimate represents an upper limit on the brightness of the stellar component of the host galaxy since no correction has been made for AGN components such as emission lines and scattered light.

3.3.6 Emission line kinematics and redshift

The median redshift determined using all of the securely identified emission lines is z=0.17325±0.00001. From only the securely identified FHILs (IP $\geq$ 54.4 eV) the redshift

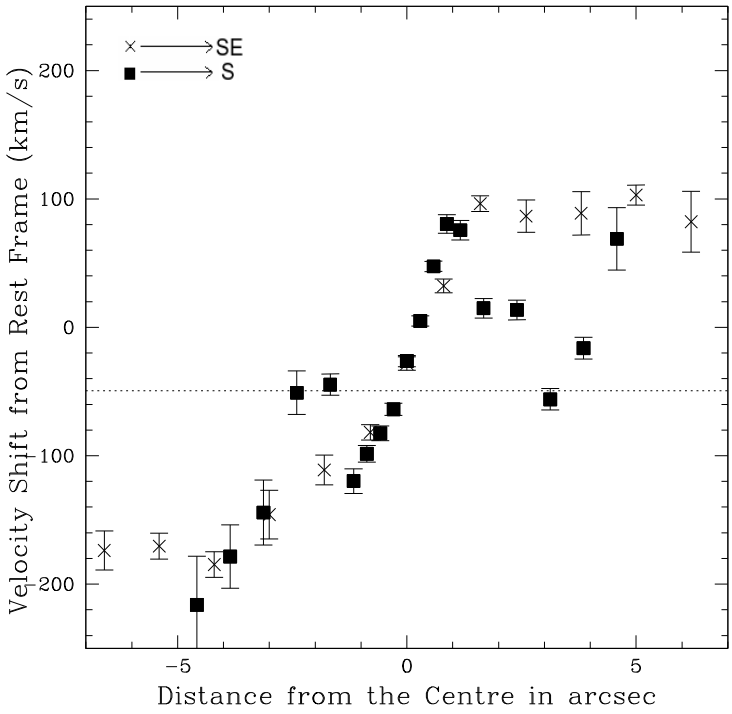

Figure 3.11: The rotation curves for J1131+16. The crosses (WHT, PA315) and filled squares (Gemini, PA163) are the measured velocity shifts determined at different spatial locations along the slit of the long slit spectrum. The directions of the slits are indicated in the upper left-hand corner. Velocity shifts are determined by the difference between the measured redshift of [OII] on each pixel and the average redshift of the emission lines. The horizontal line indicates the bisector of the flat parts of the rotation curves at large radii along PA315.

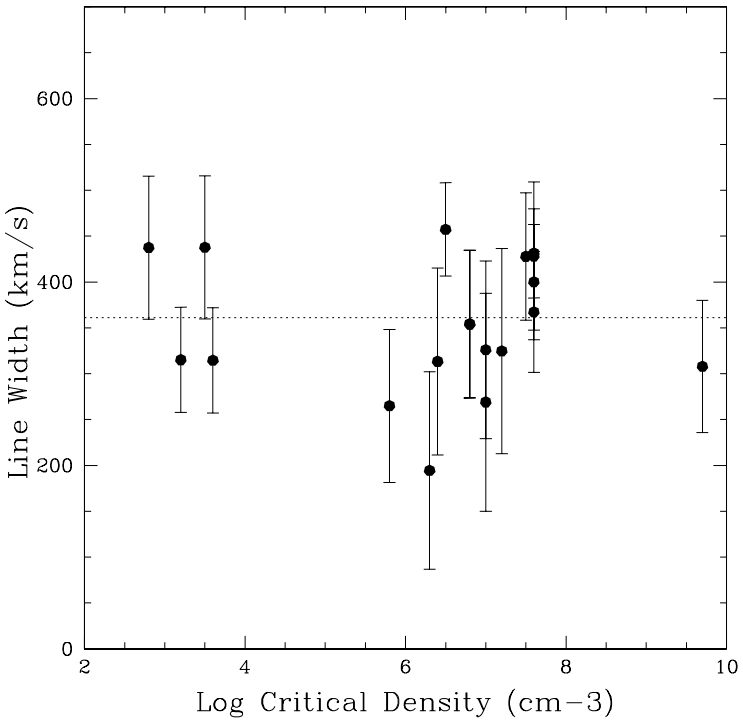

Figure 3.12: Rest-frame line width (FWHM) versus critical density for the emission lines of J1131+16. The line widths have been determined from single Gaussian free fits to the emission lines, and have been corrected for the instrumental profile.

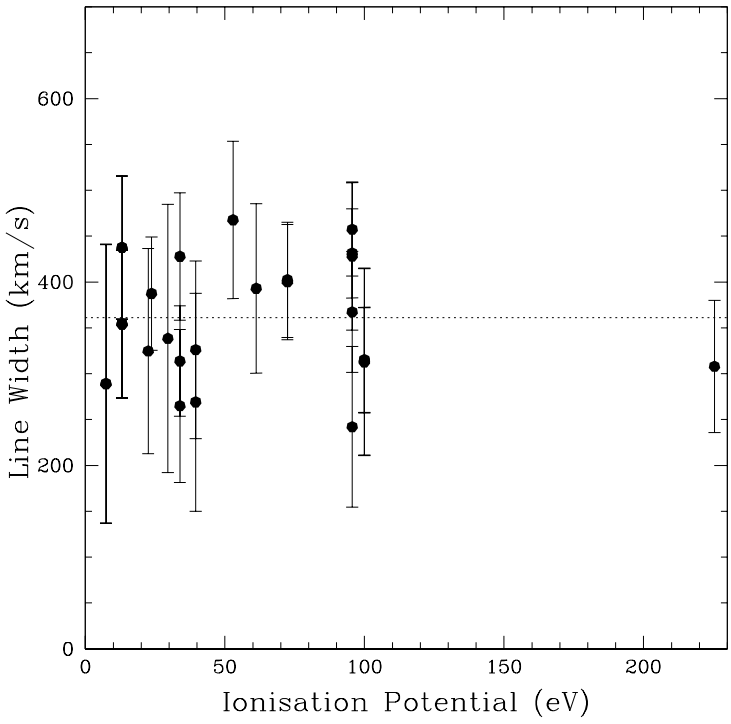

Figure 3.13: Rest-frame line width (FWHM) versus ionisation potential for the emission lines of J1131+16. The line widths have been determined from single Gaussian free fits to the emission lines, and have been corrected for the instrumental width.

is z=0.17323±0.00002, while for the low ionisation lines I find z=0.17326±0.00001. These values are consistent within their uncertainties, as emphasised by Figure 3.10, where estimated redshifts of all the lines are plotted.

In order to check whether the mean emission line redshift represents that of the host, the [OII]λ3727 emission line blend was fitted as a function of position across the galaxy for both Gemini and WHT spectra. Figure 3.11 presents the results. The velocities were determined relative to the median redshift of all the emission lines of the system (z=0.17325±0.00001), assuming a rest-frame wavelength of 3727.4 Å for the blend — representing the flux weighted wavelength of the [OII]$\lambda\lambda$3726,3729 blend for a density of 10^3 cm^{-3}. For both position angles, the central region (±1.2 arcseconds, ±4kpc) shows a velocity field that resembles a rotation curve; the velocity gradient of the [OII]λ3727 emission in the nucleus can also clearly be seen in Figure 3.1. This component of emission may correspond to an inner disk of the galaxy, implying that the [OII]λ3727 emission component in J1131+16 is resolved in the nucleus. However, the two datasets differ significantly at larger radii; such differences are likely due to the different slit PAs, given that each slit intersects different regions of J1131+16 see Figure 3.11): whereas the slit for the Gemini data is within $\sim$ 20 degrees of the minor axis of the host galaxy, that for the WHT is offset for the minor axis by $\sim$ 50 degrees.

The rotation curve derived from the PA315 WHT data appears flat at large radii. However, the velocities of the flat parts of the velocity curves are asymmetric about the host redshift measured from the nuclear spectrum: the rotation velocity ranges from +90±5 km/s for the region moving away from the observer to -176±5 km/s for the region moving towards the observer in the WHT spectrum. This asymmetry can be explained by either the uncertainty in the electron density assumed in determining the rest wavelength of the [OII] blend (n_e is likely to differ between the nucleus and the disk of J1131+16), or the uncertainty in the wavelength calibration of the spectrum. Both of these aspects can systematically shift the curve in Figure 3.11, leading to an asymmetric appearance. However, despite the apparent asymmetry, the bisector of the two flat parts of the rotation curve is within 50 km s^{-1} of the rest frame of the host galaxy estimated on the basis of the median redshift derived from the nuclear spectrum. Thus the data provide no evidence for high velocity outflows in the nuclear emission line regions.

On the other hand, the rotation curve derived from the PA163 Gemini data appears more complex: outside the inner rapidly rotating region, the velocities drop significantly at intermediate radii (1.2<r<2.5 arcseconds) on either side of the nucleus, before rising again at larger radii. It is possible that the inner rapid rotation along PA163 samples the seeing disk of the same inner disk component detected in the WHT data along PA315.

In this case, the initial drop in the velocities (1.2<r<2.5 arcseconds) may be due to the slit sampling the outer disk close to the minor axis where the (projected) rotation velocity amplitude is likely to be small. However, given the complexity of the rotation curve along PA163, non-circular gas motions cannot be ruled out.

The double Gaussian [OIII] model fits the majority of the lines well in the nuclear spectrum, suggesting that the velocity widths of the FHIL and low ionisation emission lines are similar. The median rest-frame velocity width of the emission lines, based on single Gaussian fits, is found to be 361±29 km s^{-1} (FWHM).

Figures 3.12 and 3.13 also show that there is no correlation between the widths of the emission lines as measured by single Gaussian fits, and their critical densities and ionisation potentials. Again this suggests the kinematics of the FHILs and the low ionisation lines are similar.

3.3.7 FHILs in 'typical' Seyfert galaxies

FHILs are detected in the spectra of all types of Seyfert galaxies (Penston et al., 1984). These emission lines have been studied rigorously in the past (e.g. Penston et al. 1984, Nagao et al. 2000, Mullaney & Ward 2008), and several common properties have been identified. It is therefore important to highlight the differences between the spectrum of J1131+16 and the spectra of 'typical' Seyfert galaxies.

Possibly the most notable property of the FHILs in typical AGN is that the velocity widths (FWHM as measured by single Gaussian fits) tend to be intermediate between the NLR and BLR (in the range of 500 < FWHM < 1000 km s^{-1}, Appenzeller & Östreicher 1988). However the FHILs in J1131+16 and other similar objects (e.g. III Zw 77 and Tololo 0109-383 etc.) do not share this property. In the case of J1131+16, Figures 3.12 and 3.13 show no significant variation in the velocity width (FWHM) with the critical density, and ionisation potential.

For typical AGN it is also found that FHILs are blueshifted with respect to the host galaxy rest-frames. In fact, the blueshift correlates with the observed velocity FWHM (Mullaney et al., 2009). There is no evidence for this in the spectrum of J1131+16. The individual redshifts from single Gaussian fits of each emission line are plotted in Figure 3.10. From this it is clear that there is no tendency for the FHILs to be blueshifted with respect to the average redshift of the low ionisation lines; the points representing the FHIL redshifts are scattered about the average redshift of the low ionisation species.

Finally, the FHILs of J1131+16 and similar objects have larger equivalent widths when compared to those of other 'typical' Seyfert galaxies.

Table 3.6: Line flux ratios for Balmer recombination emission lines for both the WHT and Gemini observations. Ratios are relative to Hβ. The last two columns on the table are the expected ratios for case B recombination at different temperatures at a typical NLR density (10^4 cm^{-3}, Osterbrock 1978).

Species	WHT	Gemini	10000K	20000K
Hα	4.99±0.17	-	2.85	2.74
Hγ	0.44±0.02	0.45±0.03	0.47	0.48
Hδ	0.24±0.02	0.24±0.01	0.26	0.26
Paα	0.78±0.07	0.71±0.06	0.33	0.28
Paα/Paβ[a]	2.14±0.32	-	2.05	2.05

[a] This ratio is based on LIRIS data.

3.3.8 Balmer decrements

In order to derive accurate physical conditions, it is crucial to correct for any intrinsic dust extinction. The most common way to achieve this for optical spectra is to use Balmer line recombination ratios.

Table 3.6 presents flux ratios for the Balmer and Paschen recombination lines measured from the Gemini and WHT spectra. The Hγ/Hβ, Hδ/Hβ and Paα/Paβ ratios all agree with their theoretical Case B values within the uncertainties, assuming conditions typical of the NLR. This suggests that there is no need for an extinction correction for the spectrum of J1131+16. Note that, because of the large equivalent widths of the Balmer lines, uncertainties due to underlying Balmer absorption lines from young stellar populations in the host galaxy are not a serious issue for J1131+16.

Another interesting feature of the spectrum of J1131+16 is that its Hα flux is high when compared to other Balmer lines in the series. The Hα/Hβ ratio is not consistent with Case B recombination (Hα/Hβ=4.99±0.17), see § 3.4.2 for a detailed discussion. Given the potential for collisional excitation of the Hα line (see § 3.4.2) (Gaskell & Ferland, 1984), I ignore the Hα/Hβ ratio when assessing the level of extinction in J1131+16. To further test for evidence of collisional excitation in Hα, I present the Paα/Hβ ratio in Table 3.6. This is because the Paα/Hβ ratio is not significantly altered by collisional excitation (Gaskell & Ferland, 1984). The ratio exceeds that expected of case B recombination supporting the idea that the high Hα/Hβ ratio is due to extinction rather than collisional excitation of the Hα line. However, it must be noted that the other recombination ratios presented in Table 3.6 suggest that there is no evidence for dust extinction in this object. In addition, the LIRIS observation was not taken in ideal (i.e. photometric) conditions, meaning that the observing conditions were not entirely consistent between

Table 3.7: Diagnostic line intensity ratios measured for the nuclear regions J1131+16, as derived from the WHT data. Values in brackets are the ratios given by the Gemini data. Potentially, the [FeVII]λ6086 line may suffer from some contamination by [CaV]λ6087. However, the fact that the [FeVII] (5720/6086) ratio is within 1 σ of the value predicted by atomic physics ([FeVII] (5720/6086) = 0.617: Nussbaumer & Storey 1982) indicates that any such contamination is modest.

Species	Ratio	$\pm$
[OII](3726+3729)/(7317+7330)	5.02	1.19
[OIII](5007/4363)	5.86(6.84)	0.21(0.32)
[OIII](5007/Hβ)	5.27(5.74)	0.16(0.16)
[SII](6717+6731)/(4069+4076)	7.51	1.46
[FeVI](5176)/[FeV](3891)	0.267(0.176)	0.076(0.008)
[FeVII](6086/3759)	1.18	0.076
[FeVII](5159/6086)	0.208	0.067
[FeVII](5720/6086)	0.667	0.067
[FeX](6375)/[FeVII](6086)	0.473	0.074
[FeXI](7892)/[FeVII](6086)	0.317	0.046
[NeV](3426)/[FeVII](6086)	2.04	0.207

the observations of J1131+16 and the flux standard. Therefore the flux calibration is not likely to be representative of the actual flux observed from J1131+16.

Since the high order Balmer line ratios for this source do not provide any significant evidence for reddening, I make no reddening correction of the line ratios.

3.4 Discussion

3.4.1 Physical conditions implied by the FHILs

To investigate the physical conditions implied by both the low ionisation and high ionisation species, the photoionisation model code CLOUDY[4] (Ferland et al., 1998) was used to create single slab photoionisation models for the emission lines of J1131+16. The ionisation parameter was varied over the range -3.0 $\leq$ log[U] $\leq$ 0, in steps of log[U]=0.5, and the hydrogen density was varied over the range 3.0 $\leq$ log(n_H cm^{-3}) $\leq$ 8.0 in steps of log(n_H cm^{-3}) =0.5. The rest of the properties of the model were kept constant: an ionising power-law index of -1.2 was assumed[5], and I only considered radiation-bounded

[4]The version of CLOUDY used in this investigation is c08.00.

[5]Testing power-laws between -1.5 and -0.8, this power-law was the most successful at modelling the observed HeIIλ4686/Hβ ratio compared to the FHIL ratios.

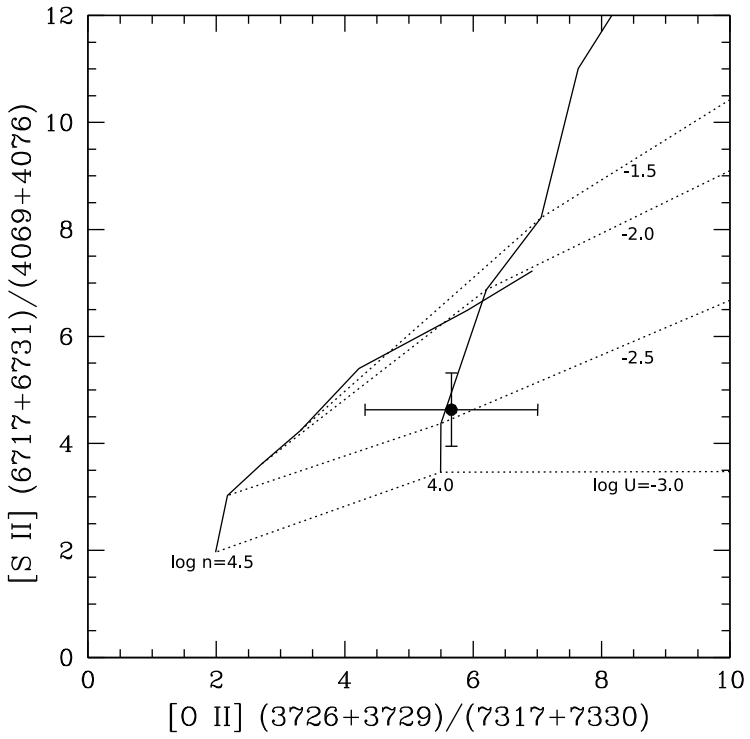

Figure 3.14: Diagnostic plot showing the measured [SII](6717+6731)/(4069+4076) and [OII](3726+3729)/(7317+7330) trans-auroral ratios (filled point), compared with photoionisation model results for different densities and ionisation parameters[3]. Equal densities are connected by the solid lines (as labelled), and the ionisation parameters are connected by the dotted lines (also labelled).

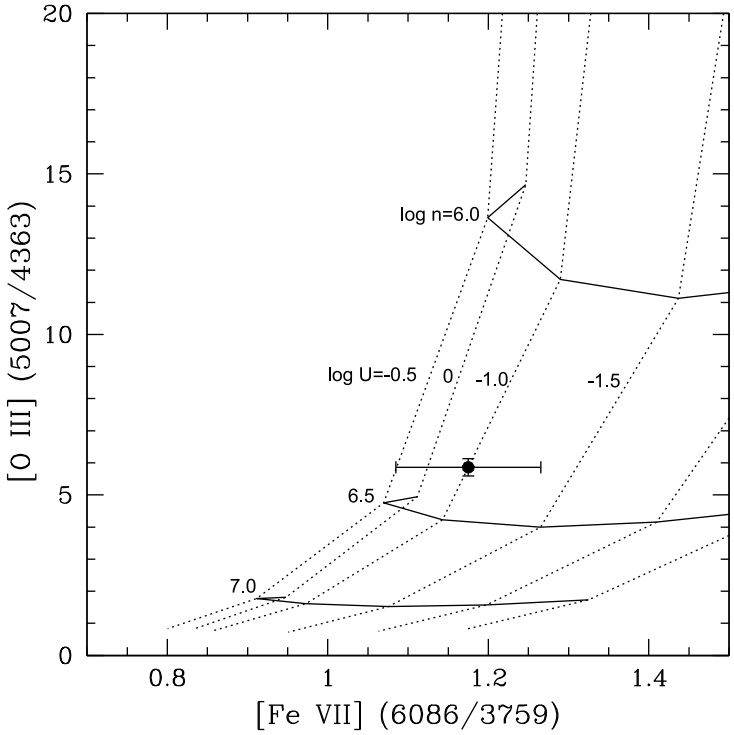

Figure 3.15: Diagnostic plot showing the measured [OIII](5007/4363) and [Fe-VII](6086/3759) ratios (filled point), compared with photoionisation model results for different densities and ionisation parameters. Equal densities are connected by the solid lines (as labelled), and the ionisation parameters are connected by the dotted lines (also labelled).

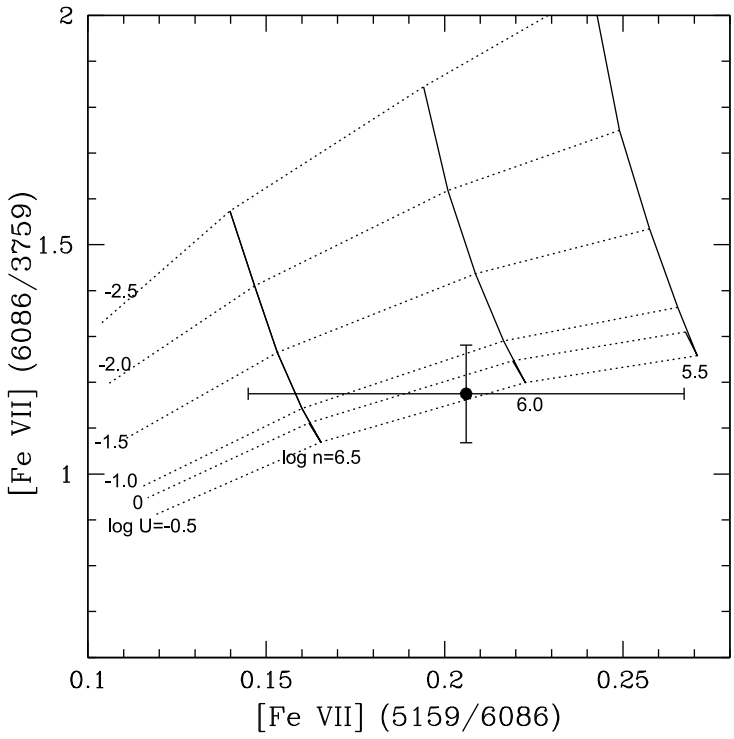

Figure 3.16: Diagnostic plot showing the measured [FeVII](6086/3759) and [Fe-VII](5159/6086) ratios (filled point), compared with photoionisation model results for different densities and ionisation parameters. Equal densities are connected by the solid lines (as labelled), and the ionisation parameters are connected by the dotted lines (also labelled).

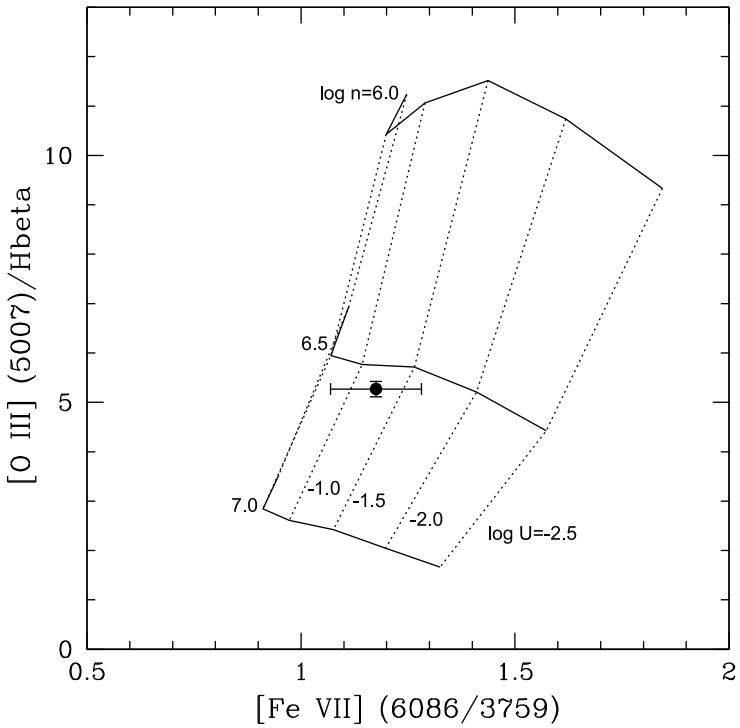

Figure 3.17: Diagnostic plot showing the measured [OIII]λ5007/Hβ and [Fe-VII](6086/3759) ratios (filled point), compared with photoionisation model results for different densities and ionisation parameters. Equal densities are connected by the solid lines (as labelled), and the ionisation parameters are connected by the dotted lines (also labelled).

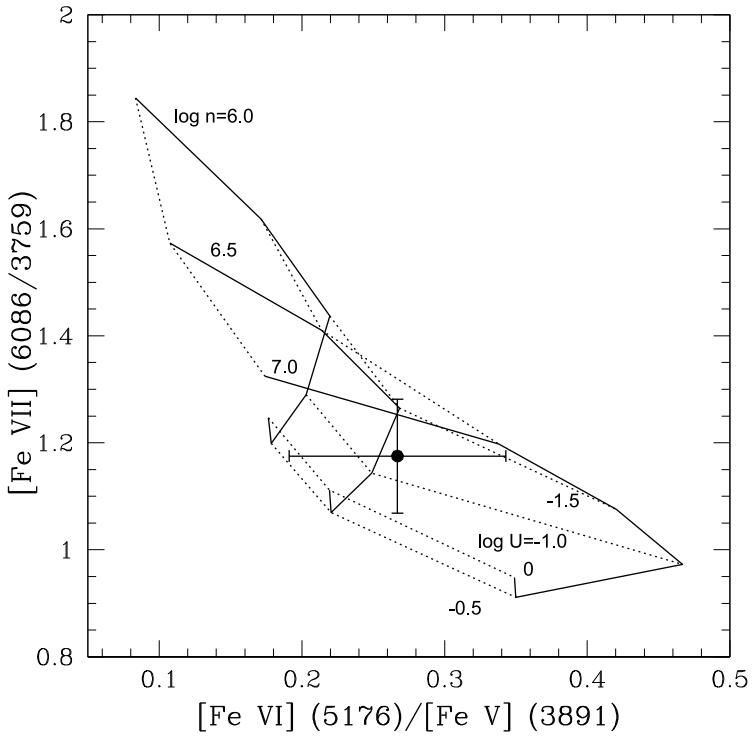

Figure 3.18: Diagnostic plot showing the measured [FeVII](6086/3759) and [FeVI]λ5176/[FeV]λ3891 ratios (filled point), compared with photoionisation model results for different densities and ionisation parameters. Equal densities are connected by the solid lines (as labelled), and the ionisation parameters are connected by the dotted lines (also labelled).

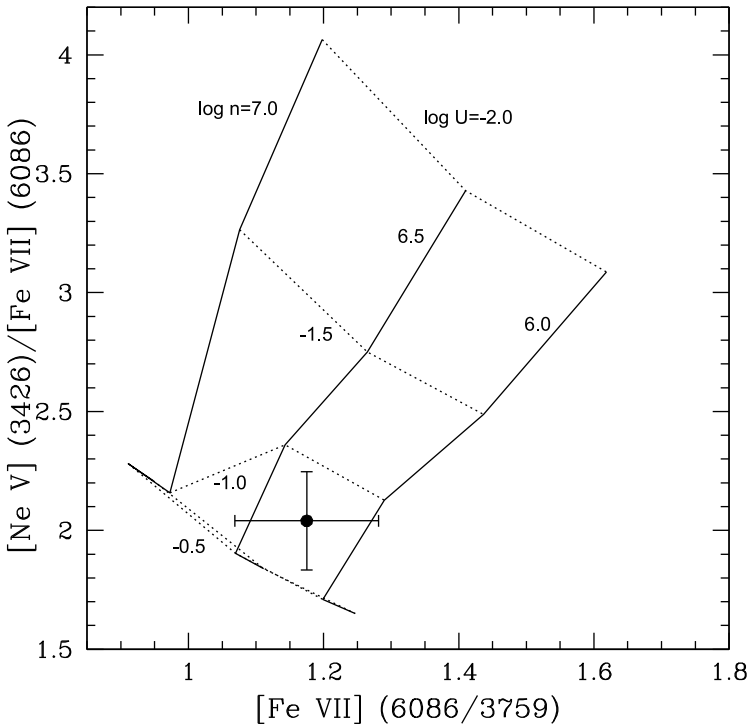

Figure 3.19: Diagnostic plot showing the measured [NeV]λ3426/Hβ and [Fe-VII](6086/3759) ratios (filled point), compared with photoionisation model results for different densities and ionisation parameters. Equal densities are connected by the solid lines (as labelled), and the ionisation parameters are connected by the dotted lines (also labelled).

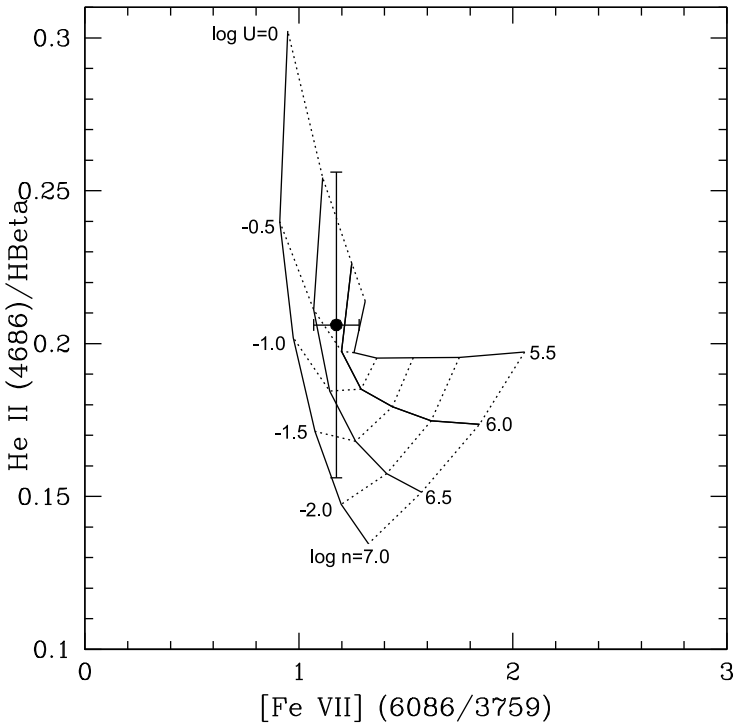

Figure 3.20: Diagnostic plot showing the measured HeIIλ4686/Hβ and [Fe-VII](6086/3759) ratios (filled point), compared with photoionisation model results for different densities and ionisation parameters. Equal densities are connected by the solid lines (as labelled), and the ionisation parameters are connected by the dotted lines (also labelled).

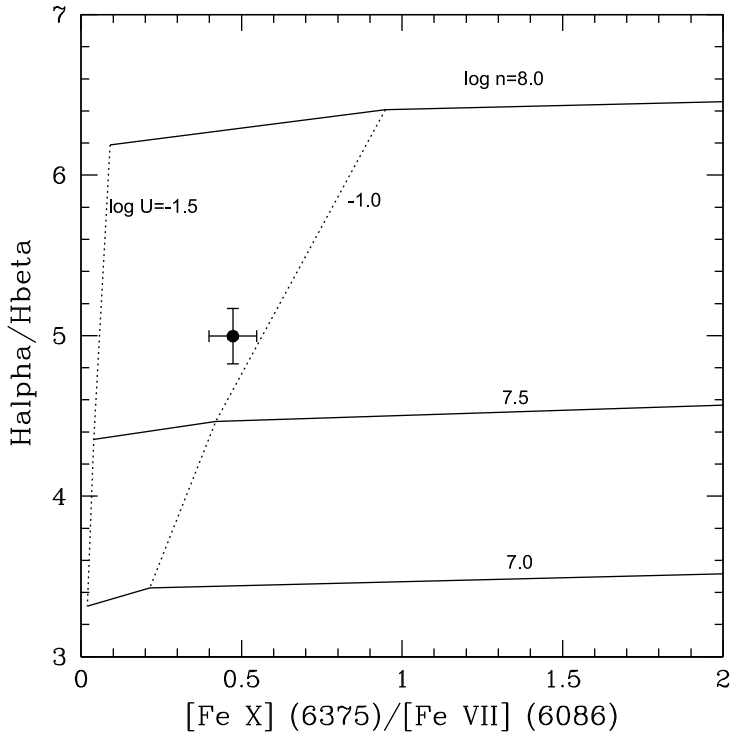

Figure 3.21: Diagnostic plot showing the measured Hα/Hβ and [FeX]λ6374/[FeVII]6086 ratios (filled point), compared with photoionisation model results for different densities and ionisation parameters. Equal densities are connected by the solid lines (as labelled), and the ionisation parameters are connected by the dotted lines (also labelled).

models that are optically thick to the ionising continuum. In terms of abundances, Solar 84 was used (see Grevesse & Anders 1989, Grevesse & Noels 1993). Also no grains were included. This was so that the CLOUDY results were not affected by depletion of iron due to condensation onto dust grains. Nagao et al. (2003) have demonstrated for a large sample of AGN that the observed FHIL ratios[6] cannot be reproduced in CLOUDY models that contain grains, but can be successfully reproduced with models not containing grains.

The ratios measured for each of the main diagnostic ratios used in this study are given in Table 3.7. The WHT ratios are used in this investigation because the WHT spectrum has the greatest wavelength range.

Considering first the low ionisation lines, I plot the trans-auroral [OII](3726+3729)/(7317+7330) and [SII](6717+6731)/(4069+4076) ratios against each other in Figure 3.14. By comparison with the models, the ratios are consistent with hydrogen densities of $\log(n_H$ cm$^{-3}) \approx 4.0$ at an ionisation parameter of $\log[U] \approx -2.5$. The densities and ionisation parameters found for these low ionisation ratios are typical of these found for the NLR of AGN in general (e.g. see Peterson 1997, Osterbrock & Ferland 2006).

On the other hand, the high ionisation species show markedly different results. In Figure 3.15 the [FeVII](6086/3759) ratio is plotted against the [OIII](5007/4363) ratio. These ratios consistent with a hydrogen densitie of $\log(n_H$ cm$^{-3}) \approx 6.5$ at ionisation parameters in the range $-1.5 < \log[U] < 0$. Similarly Figure 3.16 shows the results found by comparing the [FeVII] ratios of (6086/3759) and (5159/6086). These ratios consistent with hydrogen densities $5.5 < \log(n_H$ cm$^{-3}) < 6.5$ and ionisation parameters $-1.0 < \log[U] < 0$. The densities and ionisation parameters indicated by the latter ratios are much higher than those implied by the low ionisation emission lines.

As mentioned previously, the [OIII]λ5007 emission line intensity is surprisingly low relative to Hβ for an AGN with a high ionisation emission line spectrum. Figure 3.17 illustrates that such a low ratio is possible at high densities. The [OIII]λ5007/Hβ emission ratio is consistent with a hydrogen densitie of $\log(n_H$ cm$^{-3}) \approx 6.5$ at ionisation parameters in the range $-1.5 < \log[U] < -1.0$. At such densities, above the critical densities of the [OIII]$\lambda\lambda$5007,4959 transitions, the [OIII] emission lines are suppressed relative to Hβ; this explains the relatively low [OIII]λ5007/Hβ ratio.

FHILs with lower ionisation potentials, such as [FeVI]λ5176, are also consistent with the results found using the [FeVII] ratios. In Figure 3.18 the [FeVII] (6086/3759) ratio is plotted against the [FeVI]λ5176/[FeV]λ3891 ratio. These ratios are consistent with

[6]The ratio used in Nagao et al. (2003) was [FeVII]λ6086/[NeV]λ3426.

hydrogen densities $6.5 < \log(n_H \text{ cm}^{-3}) < 7.0$ at ionisation parameters in the range -1.5 $< \log[U] <$ 0.

Similarly, FHILs which are not from iron ions are consistent with the results found using the [FeVII] ratios. Figure 3.19 shows the [NeV]λ3426/[FeVII]λ6086 ratio plotted against the [FeVII](6086/3759) ratio. This diagram is consistent with hydrogen densities $6.0 < \log(n_H \text{ cm}^{-3}) < 6.5$ and ionisation parameters -1.0 $< \log[U] <$ -0.5. Therefore the high densities and ionisation parameters found for the FHILs are not limited to iron ions.

The HeIIλ4686/Hβ ratio is relatively insensitive to the density of the emission region, but more sensitive to the shape of the ionising continuum spectrum (e.g. Penston & Fosbury 1978), and whether the emitting regions are matter bounded (Robinson et al., 1987). Therefore, this ratio can be used to check whether the emission clouds are radiation bounded, and also whether the assumed ionising continuum shape is appropriate. The measured HeIIλ4686/Hβ ratio is found to be 0.21$\pm$0.05 and 0.23$\pm$0.01 for the WHT and Gemini spectra respectively. Figure 3.20 shows this ratio plotted against the [FeVII](6086/3759) ratio. The densities and ionisation parameters implied by this diagram are consistent with those deduced from the other diagnostic diagrams involving the FHILs ($5.5 < \log(n_H \text{ cm}^{-3}) < 7.0$, -1.5 $< \log[U] <$ 0). In this case, the consistency between the data and the models, as well as the results for other high ionisation line ratios, support the assumption of optically thick models with an ionising continuum spectral index of -1.2.

Although the models can successfully reproduce the FHIL line ratios in Table 3.7, the emission line ratios involving lines with the highest critical densities (e.g. Hα/Hβ, [FeX]/[FeVII]) cannot be successfully modelled using the range of physical conditions and ionisation parameters that successfully reproduce the [FeVII] and [OIII] line ratios. Indeed the higher critical density line ratios can only be reproduced at higher densities ($n_H > 10^7$ cm^{-3}) using CLOUDY. Figure 3.21 shows Hα/Hβ ratio plotted against the [FeX]λ6374/[FeVII]λ6086 ratio. In this case, hydrogen densities of $7.5 < \log(n_H \text{ cm}^{-3})$ < 8.0 and an ionisation parameter pf log[U] $\approx$ -1.5 are required to reproduce the data. This suggests that some regions in J1131+16 have even higher densities than implied by the [FeVII], [FeVI] and [OIII] diagnostic ratios.

To summarise, most of the key high and low ionisation diagnostic ratios are consistent with the radiation-bounded photoionisation models. While the low ionisation lines require low densities ($3.5 < \log(n_H \text{ cm}^{-3}) < 4.5$) and ionisation parameters (-3.0 $< \log[U] <$ -2.0), the higher ionisation lines imply much higher densities ($6.0 < \log(n_H$ cm$^{-3}) < 8.0$) and ionisation parameters (-1.5 $< \log[U] <$ 0). However, it is important to

emphasise that my approach assumes that the lines contributing to a particular ratio are emitted by a single cloud with a single density and ionisation parameter; the reality is likely to be more complex. In particular, some of the low ionisation lines (e.g. [SII]λ4072, [OII]λ7330) may have contributions from the high density/high ionisation regions, while some of the higher ionisation lines (e.g. [OIII]λ5007, Hβ) will have contributions from the low density/low ionisation region. Therefore the differences deduced between the conditions in the high and low density regions may be even more extreme than implied by my simple analysis.

3.4.2 Explaining the high Hα/Hβ ratio

The Hα/Hβ ratio gives an unusual result in J1131+16. This may be due to the high density of the FHIL region in this object coupled with an extended partially ionised zone (Gaskell & Ferland, 1984). Such high densities can lead to significant collisional excitation of the neutral hydrogen atoms in the partially ionised zones of clouds in the FHIL region. This results in an enhanced Hα emission, but no further enhancement in the other Balmer series emission lines, which have lower cross-sections for collision, as well as higher excitation temperatures (Gaskell & Ferland 1984, Osterbrock & Ferland 2006). Such a process could explain the high Hα/Hβ ratio measured in the spectrum of J1131+16, since there is likely to be be a major contribution from the FHIL region to the line flux of Hα.

The Hα/Hβ flux ratio was investigated using CLOUDY, as described in $\oint$ 3.4.1 The ratio indicated by the WHT data could only be reached at the highest densities (n_H $> 10^7$ cm^{-3}: see Figure 3.21) and is not consistent with the conditions implied by the [FeVII] and lower iron species ratios. Note that high Hα/Hβ would also be favoured by lower metal abundances and a harder ionising continuum than I have assumed in the modelling (Gaskell & Ferland, 1984).

3.4.3 Location of the FHIL region

The presence of FHILs in the spectra of the majority of active galaxies has led to a number of studies on their nature, kinematics and location in AGN (e.g. see Mullaney et al. 2009). One of the most credible suggestions for the origin of the FHIL emission is the inner torus wall (see Murayama & Taniguchi 1998 and Nagao et al. 2001). The FHIL emission is rich in iron lines, which can be enhanced (relative to the classical NLR) by the evaporation of dust grains in the inner torus wall, releasing the iron locked up

in the grains (Pier & Voit, 1995). Moreover, studies of molecular emission from the circum-nuclear molecular clouds of the centres of the Milky Way and other galaxies (hypothetically the torus) reveal densities in the range $n_{H2} \sim 10^{5-6}$ cm^{-3} (e.g. Paglione et al. 1998), similar to the densities deduced for the FHILs.

In the case of J1131+16, the results are consistent with the idea that the FHILs are emitted by the *far wall* of the torus, observed with our line of sight at a relatively large angle to the torus axis. I emphasise that such a geometry is consistent with the relatively narrow line widths and small velocity shifts of the FHIL, since the circular velocities associated with the torus and any out-of-the-plane gas motions would then be directed close to perpendicular to the line of sight. In this case, the results imply that the torus is dynamically cold, with velocity dispersion that is small relative to its circular velocity.

It is difficult to entirely rule out the idea that the FHILs are emitted by an infalling molecular cloud, or a clump of the torus which has broken off from the rest of the torus and is falling towards the AGN. However, in such cases we might expect to see a larger velocity shift between the FHIL emission lines and the host galaxy rest-frame, unless the cloud happens to be falling perpendicular to the line of sight.

Therefore the FHIL emission is most likely to originate from the inner torus wall of the AGN, supporting the original suggestion of Murayama & Taniguchi (1998) and Nagao et al. (2001).

3.4.4 The radial distance to the FHIL region

The idea that the FHIL region is located in the torus can be further investigated by determining its radial distance from the AGN (r_H).

First I estimate r_H based on the spatial information given in ∮ 3.3.1, and the parameters determined in ∮ 3.4.1. The ionising luminosity (L_{ION}) of the illuminating source is related to the radial distance of the emission region from the ionising source (r) and the ionisation parameter (U), by:

$$L_{ION} = 4\pi r^2 U n_H c \{h\nu\}_{ion}; \tag{3.1}$$

where n_H is the hydrogen density, $\langle h\nu \rangle_{ion}$ is the mean ionising photon energy[7], and c is the speed of light. Then, solving for the radial distance of the low ionisation/density

[7]I assume a value of 56 eV for $\langle h\nu \rangle_{ion}$, which is based on an ionising power-law of -1.2, with photon energy limits of 13.6 eV and 5 keV.

region, we get:

$$r_L{}^2 = \frac{L_{ION}}{4\pi\ U_L n_H^L c \left\langle h\nu \right\rangle_{ion}} \tag{3.2}$$

and similarly for the high ionisation/density emission region:

$$r_H{}^2 = \frac{L_{ION}}{4\pi\ U_H n_H^H c \left\langle h\nu \right\rangle_{ion}}. \tag{3.3}$$

By combining equations 3.2 and 3.3, we obtain an equation which allows us to determine the relative radial distances of the high and low density regions from the AGN:

$$\left[\frac{r_H}{r_L}\right]^2 = \frac{U_L n_H^L}{U_H n_H^H}. \tag{3.4}$$

Using the densities and ionisation parameters estimated in § 3.4.1, I find that the radial distance of the FHIL emission region ranges from 0.0002 to 0.03 of that of the low ionisation region. As mentioned in § 3.3.6, the [OII] λ3727 emission is resolved in the 2D spectrum of J1131+16, and the half width at half maximum (HWHM) measured for the central peak of this emission line is found to be 0.53±0.05 arcseconds (corrected for the seeing). This corresponds to r_L=1.7±0.2 kpc, implying that the radial distance of the FHIL region from the AGN is in the range $0.30 < r_H < 50$ pc — consistent with recent observational estimates of the size of the torus in nearby AGN, based on IR interferometry and high resolution molecular line observations (e.g. Haschick et al. 1994, Chou et al. 2007, Tristram et al. 2007a). However, I emphasise that this argument assumes that the [OII] emission line region is solely ionised by the AGN, which may not be true if stellar photoionisation is significant at a kpc scale. Also, if the contrast between the conditions in the low and high ionisation regions is larger than assumed here (see discussion in § 3.4.1), the radial distance of the FHIL region from the AGN will be correspondingly lower. Overall it is likely that this analysis, based on estimates of U and n_H, overestimates the true radial distance of the FHIL region.

If the ionising luminosity (L_{ION}) is known it is also possible to estimate the radial distance of the FHIL region from the AGN using equation 3.1 directly. L_{ION} can be estimated from the bolometric luminosity (L_{BOL}), which itself can be determined from the [OIII]λ5007 emission line luminosity ($L_{[OIII]}$). This assumes that, based on simple recombination theory, the total narrow emission line luminosity (e.g. $L_{[OIII]}$) generated in the NLR of an AGN, is related to L_{ION}, which itself can be related to L_{BOL} using $L_{BOL} \approx 3.1 L_{ION}$ based on the results of Elvis et al. (1994). By manipulating equation 1

from Dicken et al. (2009)[8] L_{BOL} can be determined:

$$L_{BOL} = \frac{100}{C_{nlr}} L_{[OIII]}, \tag{3.5}$$

where C_{nlr} is the NLR covering factor. Assuming typical NLR covering factors in the range $0.02 < C_{NLR} < 0.08$ (Netzer & Laor, 1993), I estimate a bolometric luminosity in the range $3\text{x}10^{38} < L_{BOL} < 10^{39}$ W.

Alternatively, we can use our knowledge of the likely geometry of the FHIL to estimate an upper limit on the covering factor of the FHIL region and a lower limit on L_{BOL}. Assuming that the FHILs are emitted by the inner wall of the torus on the far side of the AGN (see § 3.4.3), we see a maximum of 25% of the total area of the inner wall of the torus (with the rest obscured). A typical torus with an opening angle of 45° has a *total* covering factor of C_{torus}=0.7. Therefore, for my assumed geometry, an upper limit on the covering factor of the FHIL region is C_{FHIL}=0.7x0.25=0.175. Substituting this into equation 3.5, we obtain the following lower limit on the bolometric luminosity: $L_{BOL} > 10^{38}$ W.

I convert L_{BOL} to L_{ION} using the relationship given in Elvis et al. 1994 ($L_{BOL} \approx 3.1\ L_{ION}$), which leads to $3\text{x}10^{37} < L_{ION} < 3\text{x}10^{38}$ W. Then, using equation 3.1 and the model parameters in § 3.4.1, I estimate the radial distance of the FHIL region from the AGN to be in the range $0.3 < r_H < 30$ pc. For comparison, based on the estimates of the AGN bolometric luminosity, the sublimation radius of the dust grains in the torus[9] is $0.26 < r_{sub} < 0.52$ pc — consistent with the lower end of the range of the estimates of r_H. This consistency supports the idea that the FHILs are emitted by the inner torus wall.

3.4.5 The unusual strength of the FHIL

It is also important to consider why the FHILs are so much stronger in J1131+16 and other similar objects than in more typical AGN.

First we must consider the possibility that, rather than an AGN, the spectrum of J1131+16 is the result of a supernova, in particular a type IIn supernova. A type IIn supernova is a subclass of supernova for which it is believed that the supernova progenitor has undergone mass stripping of its outer layers in the late stages of its life. This process introduces a dense hydrogen gas in the circumstellar medium surrounding the progenitor.

[8] Assuming $L_{[OIII]}$=5.5$L_{H\beta}$ rather than $L_{[OIII]}$=12$L_{H\beta}$.

[9] I calculate the sublimation radius using the expression for AGN sublimation radius given in Elitzur 2008.

The shockwave from the supernova interacts with the material, heating it. This results in a rich spectrum of narrow emission lines, which has some similar characteristics of the spectrum of J1131+16 (Smith et al., 2009). It is notable that early observations of the [FeVII] emission lines in one such supernovae, SN 2005ip (see Smith et al. 2009), indicate electron densities of 10^8 cm^{-3} and higher (Smith et al., 2009).

One argument against this suggestion is that the [OIII]λ5007 luminosity of J1131+16 exceeds that of the hottest known type IIn supernova by 3 orders of magnitude (Smith et al., 2009). Also the line emission from a supernova is expected to be variable. In the case of the type IIn supernova considered by Smith et al. (2009), the [OIII]λ5007 increased 8-fold after 100 days and then faded to half this intensity after 3 years. The [FeVII]λ5720 emission line decreased 4-fold in intensity after 100 days, but after 3 years this intensity had increased to half its original intensity. As for the [FeVII]λ6086 emission line, this decreased in intensity by half after 100 days and then varied over 3 years around half its original intensity. However, in J1131+16 there is no evidence for emission lines fading in the 3 years between the WHT and Gemini spectra. This lack of variability rules out any supernova component.

The lack of variability in the emission lines of J1131+16, also provides strong evidence against the the idea that its unusual FHILs are due to an illumination flare caused by the tidal disruption of a star by the SMBH (Komossa et al., 2008). In the well-studied case of SDSSJ095209.56+214313.3 (Komossa et al., 2009), FHILs such as [FeVII]$\lambda\lambda$3759&5159, are seen to dramatically vary over a timescale of 3 years: the [FeVII]λ3759 line[10] by 36% in intensity over 3 years, the [FeVII]λ5159 line by 79%, and HeIIλ4686 by 65%. In contrast, the same lines in J1131+16 did not vary significant over a similar 3 year timescale. Moreover, the Balmer lines in J1131+16 lack the variable, multi-peaked profiles observed in SDSSJ095209.56+214313.3 (Komossa et al. 2008 & Komossa et al. 2009).

Rather than an illumination event, an explanation for the unusual strength of the FHILs may by provided by the inner torus wall being viewed at a specific orientation, at which the inner wall on the far side of the torus can be seen by the observer, but the quasar itself remains hidden, because the torus is being viewed at a relatively large angle to its axis (see $\oint$ 3.4.3). In this case, the visible area of the torus wall is high enough that the FHILs are strong, but the direct quasar continuum emission does not dilute the torus line emission (see Figure 3.22). Therefore the FHILs are observed with large equivalent widths. Viewed at smaller angles to the axis of the torus, the luminous quasar nuclear

[10]Here all ratios are relative to [OIII]λ5007. In SDSSJ095209.56+214313.3 the [OIII] flux varies very little between the spectra (see Komossa et al. 2009).

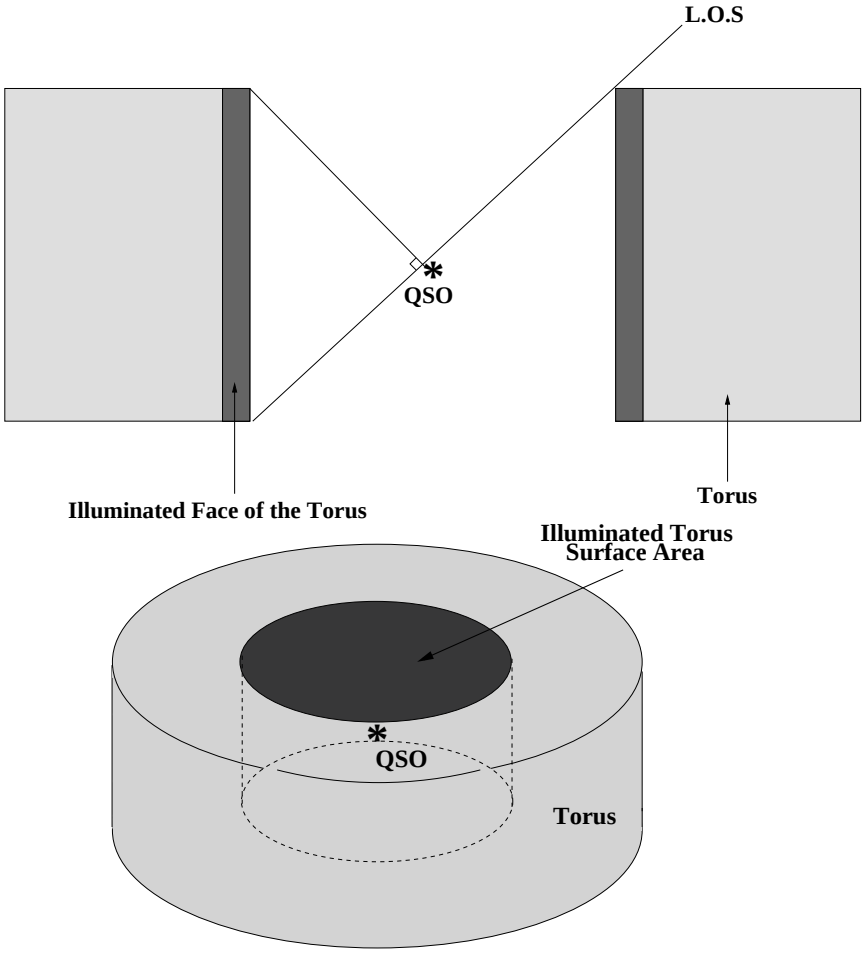

Figure 3.22: *Top.* Schematic displaying an edge-on view of the possible observed orientation of the AGN of J1131+16. *Bottom.* Schematic displaying the visible area of the inner torus wall of J1131+16 as viewed by the observer. This special geometry will maximise the observed emission line flux of the inner wall of the torus yet still obscure the central quasar, thus lowering the underlying continuum, and hence resulting in FHILs with large equivalent widths.

Table 3.8: Table comparing key properties determined for the FHIL regions in of J1131+16, III Zw 77 (Osterbrock, 1981), Tololo 0109-383 (Fosbury & Sansom 1983, Murayama & Taniguchi 1998) and ESO 138 G1 (Alloin et al., 1992).

Object	Density (cm^{-3})	Velocity Width (FWHM, km s^{-1})	[OIII](5007/4363)
J1131+16	$10^8 > n_H > 10^5$	361±29	5.86±0.21 (WHT)
III Zw 77	$n_e > 10^5$	∼400*	11.48±0.02
Tololo 0109-383	$n_e > 10^6$	∼330	21.50±0.46
ESO 138 G1	$n_e > 10^5$	∼1000	30±2

* Shows systematic increase from low to high ionisation lines.

emission would become directly visible, substantially reducing the equivalent widths of the FHILs.

In this context I note that, despite the unusually large equivalent widths of its FHILs, the measured ratios of the FHILs to lower ionization lines (e.g. [FeVII]/[OIII], [FeVII]/[SII], [FeVII]/[OI] and [FeX]/[OI]) for J1131+16 fall well within the ranges measured for typical broad line AGN (Sy1, Sy1.5, NLSy1) in the sample compiled by Nagao et al. (2000). Therefore, viewed from a direction closer to the torus axis, we would expect J1131+16 to display a normal quasar/Seyfert 1 spectrum, but the multitude of fainter FHIL would be difficult to detect because of the dilution by the bright quasar continuum and broad line emission.

However, it is more challenging to explain why the FHIL are significantly stronger relative to the low ionization lines in J1131+16 than in typical Type 2 AGN (Nagao et al., 2000). Given the geometry in Figure 3.22, we would expect to observe significant FHIL emission over a range of viewing angles, even if the quasar nucleus itself is obscured; rather than a sharp cut-off, for this simple geometry, the strength of the FHIL would gradually diminish as the orientation of the axis of the torus to the line of sight increased (i.e. the torus became more edge-on). Therefore, although the particular geometry shown in Figure 3.22 would maximise the FHIL emission, it is unlikely that a specific geometry alone can explain the rarity of objects like J1131+16. I now discuss three further factors that might lead to the FHIL appearing relatively strong compared with the general population of Type 2 AGN.

- **A lack of conventional NLR emission.** If the emission from a "conventional" NLR on a scale of ∼100 pc — 1 kpc were strong, this would dilute the FHIL emission, and the overall spectrum would not appear unusual relative to other Type 2 AGN. Therefore, the conventional NLR emission must be relatively weak

in the case of J1131+16 and other similar objects. Weak NLR emission can arise if the covering factor of the NLR is relatively small, or if the illuminating AGN has only recently been triggered (within the last 100 – 1000 yr), so that the ionising radiation has not had time to traverse the scale of the NLR. However, while the lack of a conventional NLR might help to explain the unusual emission line ratios, it would not explain the unusually high equivalent widths measured for many of the emission lines in J1131+16. Indeed, if this was the dominant factor we would expect the emission lines in J1131+16 to have *lower* equivalent widths than most other Type 2 AGN, which is clearly not the case.

- **A lack of obscuration by large-scale dust structures that are not coplanar with the torus.** Along with a compact torus on a scale of 1 – 100 pc, many active galaxies show evidence for larger dust lane structures on a scale of 100 pc – 5 kpc. If the dust lanes are not exactly co-planar with the torus structures (e.g. thicker or different orientation), they will make it more difficult to observe the inner face of the torus, thus reducing the strength of the optical FHIL emission, and narrowing the range of angles over which the FHIL would appear strong. While the lack such large-scale dust structures would certainly increase the chance of observing unusually strong FHIL, their presence would in any case reduce the range of viewing angles over which the FHIL would be visible.

- **A recently triggered AGN.** If the AGN has only recently been triggered then, not only might this result in reduced emission from the conventional NLR (see above), but the inner wall of the torus itself might not yet have reached an equilibrium radius set by dust sublimation. In this case, the clouds close to the AGN are likely to be in the process of evaporation by the strong AGN radiation field (Pier & Voit, 1995) and, depending on the density gradient, might have a higher ionisation parameter than clouds at the sublimation radius, leading to relatively strong FHIL. The problem with this explanation for J1131+16 is that the radius of the FHIL emission line region is similar to the estimated sublimation radius of the torus (see § 3.4.4), suggesting an equilibrium situation. However, it is possible that future refinement of the physical conditions of the FHIL in J1131+16 and the bolometric luminosity of its AGN might lead to a revision of this picture.

Overall, while a specific viewing angle is likely to provide an important part of the explanation for the unusual spectrum of J1131+16, one or more of the other factors discussed above may also be significant.

3.4.6 J1131+16 in relation to other similar objects

As mentioned previously, there are a few similar objects in which the FHILs are unusually strong (III Zw 77, Tololo 0109-383 and ESO 138 G1). The key properties of these objects, as derived from their FHILs, are presented in Table 3.8. In particular, I note that the densities derived from the FHILs are consistently high. Also all the objects show a particularly low [O III](5007/4363) line ratio when compared to 'typical' Seyfert galaxies (although in this respect J1131+16 is the most extreme). Finally, all the objects show relatively modest FHIL line widths (FWHM), with the exception of ESO 138 G1 whose line widths are larger.

Because there are relatively few objects with such unusual features, it is entirely plausible that the properties of all these objects can be explained in a similar way e.g. with a specific viewing angle of the torus that maximises the observed emission area of the torus whilst still obscuring the central engine, consistent with the scheme described by Murayama & Taniguchi (1998), Nagao et al. (2001) and Nagao et al. (2000).

3.5 Conclusions

J1131+16 has a remarkable spectrum which displays a multitude of FHILs of relatively high equivalent width, as well as the more common emission lines expected of an AGN spectrum.

An in-depth study of the spectrum of J1131+16 has revealed:

- emission line ratios for the FHIL region that are consistent with high densities ($10^{5.5} < n_H < 10^{8.0}$ cm^{-3}) and ionisation parameters (-1.5 < log[U] < 0);
- similar velocity widths (FWHM) for the low and high ionisation lines, and a lack of evidence for substantial velocity shifts of the FHILs relative to the galaxy rest frame;
- a small radial distance from the AGN for the region emitting the FHILs ($0.30 < r_{FHIL} < 50$ pc).

Based on the high densities and relatively quiescent kinematics implied by the observations, it is likely that the FHILs in J1131+16 are emitted by the torus wall, with the inner wall on the far side of the torus viewed directly by the observer, but the quasar itself remaining hidden. This geometry is also consistent with the relatively small radial distance found for the FHIL region.

These results demonstrate the potential of the FHILs for probing the circum-nuclear obscuring regions in AGN.

Further analysis of J1131+16 is outlined in Chapters 4, 5 and 6. In Chapter 5 in particular I will highlight the interesting properties of this object at IR wavelengths and will compare the findings with III Zw 77, Tololo 0109-383 and ESO-138-G1.

Chapter 4

An optical spectroscopic study of the red, 2MASS-selected AGN in the local Universe

A version of the work presented in this chapter has been published in the Monthly Notices of the Royal Astronomical Society as part of Rose et al. (2013). The analysis and text presented below are my own work.

4.1 Introduction

A key result of 2MASS was the discovery of a population of AGN that appear redder than their traditional optical/UV selected counterparts at IR wavelengths. The red 2MASS AGN were selected to have J-$K_S \gtrsim 2.0$, distinguishing them from most optical/UV selected AGN that have bluer near-IR colours (J-$K_S < 2.0$; Cutri et al. 2002), and K_S-band magnitudes in the range $11.0 < K_S < 14.9$ mag. The latter criterion was chosen so that bright ($K_S < 11.0$) Galactic AGB and carbon stars were excluded, along with 'normal' galaxies in the redshift range $0.4 < z < 0.5$ ($K_S > 14.9$; Cutri et al. 2002). Spectroscopic follow up of the objects which fulfill these criteria revealed that the majority of the candidates have spectra resembling AGN (Cutri et al., 2002). More recent surveys have determined that these 'red quasars' do indeed represent a large fraction of the overall population of quasars in the local Universe (∼15–60%; Glikman et al. 2007; Glikman at al. 2012).

Because the red quasars potentially make up a large fraction of the AGN population, it is important that we understand their relationship to the unobscured population:

are they young, dust obscured versions of 'typical quasars' (Hutchings et al. 2003; Georgakakis et al. 2009; Glikman et al. 2007; Glikman at al. 2012)? Or can their properties be explained by a specific viewing angle in the orientation-based unified schemes (Wilkes et al., 2002)? Or do they perhaps represent a new population altogether? Are these objects all luminous quasars, or are some less luminous AGN?

Past studies of red 2MASS quasars have found reddenings in the range $0.1 < E(B\text{-}V) < 3.2$ magnitudes based on Balmer decrements and fits to the continuum shape (e.g. Glikman et al. 2007; Georgakakis et al. 2009; Kuraszkiewicz et al. 2009a,b; Glikman at al. 2012; Canalizo et al. 2012), although it is important to recognise that some have negligible reddening (Glikman et al., 2007). In addition, imaging studies of the host galaxies find evidence for disturbed morphologies in up to 70% of cases (Hutchings et al. 2003; Marble et al. 2003; Urrutia, Lacy & Becker 2008), which may support the idea that host galaxies have undergone recent interactions with other galaxies. Such interactions could drive material into the central region of the galaxies, enshrouding the SMBH in a cocoons of dust (Hopkins et al., 2006a), making them difficult to detect in traditional UV/optical surveys (Cutri et al., 2002).

This thesis reports observations of an RA-limited sample of 29 2MASS-selected quasars ($J\text{-}K_S \gtrsim 2.0$) with a narrow range of redshifts: $0.09 < z < 0.28$. I aim to determine how the red 2MASS AGN fit into our picture of active galaxies in general, and how important they are to our understanding of AGN. In this chapter I report a spectroscopic study of this sample, focussing on the AGN properties, emission line outflows and dust extinction. The spectral properties are compared to control samples of optical/UV selected quasars and AGN. The next 2 chapters will focus on the near- and mid-IR properties of the sample, and will include a comprehensive comparison with several complete samples of active galaxies.

4.2 Continuum subtraction and emission line modelling

Fitting emission features in AGN spectra is often complicated by the presence of the host galaxy continuum in the spectrum. Subtle features such as weak broad components can often be overlooked, and the presence of underlying Balmer absorption from the stellar continuum can lead to underestimation of the intensity of the Balmer and other emission line strengths (e.g. Sarzi et al. 2006).

For the purposes of studying the emission regions, the underlying continuum was

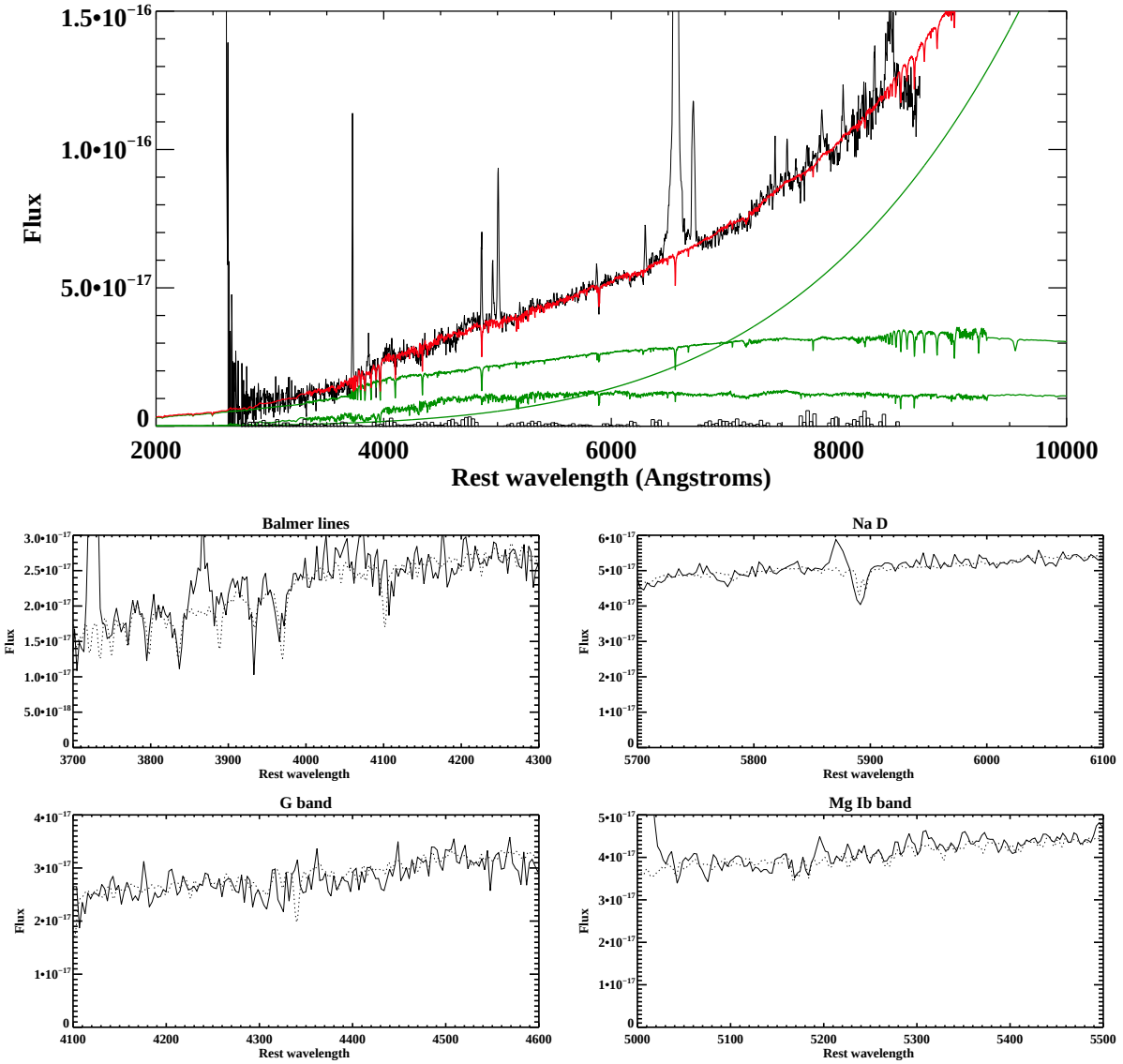

Figure 4.1: A best-fit CONFIT model for J10404364+5934092 (χ^2=0.54) plotting F_λ against λ. The smaller plots show how the combined stellar populations fit the detailed features. The object requires an OSP, a YSP, and a power-law component for an adequate fit. The YSP has an age of 0.005 Gyr, an extinction of E(B-V)=1.0 and represents 58.7% of the flux in the normalising bin. The power-law component has α=5.11 and represents 16.4% of the flux in the normalising bin. Finally, the OSP represents 24.8% of the flux in the normalising bin. The flux is in units of erg s^{-1} cm^{-2} $Å^{-1}$, and wavelength is in units of Å.

modelled and subtracted in all objects in which the stellar continuum is significant — mainly LINER/Seyfert 2 type objects (e.g. J0221+13) and objects with weak broad lines (e.g. J0422-18). These steps required the use of the STARLINK package DIPSO (Howarth et al., 2004) and a customised IDL minimum χ^2 fitting program called CONFIT (Robinson et al. 2000; Tadhunter et al. 2005; Holt et al. 2007; Rodríguez Zaurín, Tadhunter & González Delgado 2009).

I started by experimenting with subtracting a nebular continuum component, which might be significant at near-UV wavelengths (Dickson et al., 1995). The contribution of the nebular continuum was estimated using the narrow Hβ emission line flux. However, its strength is sensitive to the reddening of the NLR, which is not accurately known in most cases. Indeed, I found that in all cases I obtained better fits if I did not subtract a nebular continuum. Therefore the results below refer to models without nebular continuum subtraction.

Once the spectra had been prepared, the continua were modelled using the customised IDL procedure CONFIT (Robinson et al. 2000; Holt et al. 2007). To minimise degeneracy when fitting the spectra, I fit the smallest number of stellar and/or power-law components to the continuum as possible. For each object I ran 3 sets of models. In the first run I fit an unreddened old stellar population (OSP, 12.5 Gyr) and a young stellar population (YSP), with ages in the range 0.001–5 Gyr, and reddening: $0 < \mathrm{E(B\text{-}V)} < 2.0$[1]. The inclusion of a YSP is justified on the basis that many of the objects with significant stellar continua show higher order Balmer lines in absorption (e.g. J1001+41). The stellar population templates were taken from the instantaneous burst spectral synthesis results of Bruzal & Charlot (2003) for a Salpeter IMF and solar metallicities. For the second run a power-law component, which represents either the direct or scattered AGN component, was also included in the model fitting. Finally, an OSP with and without a power-law was fitted to each spectrum, independent of a YSP.

The spectra were fitted using fluxes measured in 30Å bins, chosen to have as even a distribution in wavelength as possible, and avoiding the brighter atmospheric emission and stronger atmospheric absorption, and AGN emission, features in the spectra. The entire useful wavelength ranges of the spectra were fitted: observed wavelengths 3200–9000Å. In addition, a normalising bin was chosen which is also free of any emission/absorption features (∼5050–5200 Å for all objects in the rest frame).

Fits to the overall continuum shape were chosen with low reduced $\chi^2 < 1$ (see discussion in Tadhunter et al. 2005). Then a visual inspection of fits to individual absorption

[1]I used the Calzetti et al. (2000) reddening law to redden the YSP spectra.

Table 4.1: The [OIII] model parameters used when fitting the emission lines of the spectra. The second and third columns present the rest-frame widths of the narrow and broad kinematic components respectively. The final column gives the rest-frame velocity separation of the broad relative to the narrow kinematic components, negative velocity separations indicate that the broad component is blueshifted with respect to the narrow component.

Object	$FWHM_N$ (km s^{-1})	$FWHM_B$ (km s^{-1})	Separation (km s^{-1})
J0221+13	Inst.	799 ± 36	-217 ± 27
J0248+14	448 ± 39	945 ± 61	-168 ± 44
J0306-05	Inst.	826 ± 148	-426 ± 152
J0312+07	Inst.	718 ± 95	-227 ± 72
J0400+05	326 ± 13	1197 ± 51	-36 ± 11
J0409+07	620 ± 22	1842 ± 340	-44 ± 68
J0411-011[a]	544 ± 150	-	-
J0422-18[b]	Inst.	1700 ± 56	-298 ± 31
J0435-06	256 ± 19	376 ± 84	-655 ± 93
J0447-16	194 ± 7	1072 ± 165	-569 ± 187
J0504-19[b]	Inst.	1778 ± 40	191 ± 32
J0910+33	715 ± 21	1652 ± 48	-276 ± 33
J1001+41[a]	418 ± 76	-	-
J1006+41[b]	Inst.	554 ± 159	-353 ± 152
J1014+19	428 ± 13	1637 ± 63	127 ± 23
J1040+59	181 ± 22	993 ± 84	214 ± 62
J1057-13	707 ± 14	1477 ± 139	-855 ± 116
J1127+24	267 ± 7	-	-
J1131+16[c]	Inst.	720 ± 31	-92 ± 5
J1158-30	693 ± 27	1177 ± 139	-1195 ± 66
J1212-14[a]	455 ± 25	-	-
J1321+13[a]	390 ± 14	-	-
J1323-02	366 ± 16	1512 ± 108	-488 ± 94
J1338-04[b]	Inst.	780 ± 24	-224 ± 34
J1407+42	584 ± 8	1316 ± 48	190 ± 28
J1448+44[a]	441 ± 15	-	-
J2124-17[a]	753 ± 22	-	-

[a] The model for this object requires just one component.
[b] The narrow component of the model can be modelled with the instrumental width.
[c] This object was studied in detail in Chapter 3.

Table 4.2: Best fit CONFIT model results for the 2MASS sample. The simple stellar population models were taken from Bruzal & Charlot (2003). The subscripts 'U' and 'L' refer to the upper and lower cases of the model parameters that provide a good fit to the continuum. For the cases where the best fits include power laws I use the form $F_\nu \propto \nu^{-\alpha}$, where α represents the power law index.

Object	YSP_U (Gyr)	YSP_L (Gyr)	$E(B\text{-}V)_U$	$E(B\text{-}V)_L$	α_U	α_L
J0221+13	1.0	0.7	0.5	0.3	2.18	0.457
J0306-05	2.0	0.8	0.5	0.3	3.95	1.40
J0411-01	0.006	0.005	1.1	0.6	-	-
J0422-18	0.005	0.004	1.1	0.9	2.35	0.32
J0447-16	1.2	0.8	0.3	0.2	1.31	1.28
J0504-19	0.01	0.006	0.9	0.7	-	-
J0910+33	0.9	0.3	0.3	0.1	-0.347	-0.818
J1001+41	0.2	0.1	0.7	0.6	-	-
J1040+59	0.005	0.004	1.1	0.8	5.97	5.11
J1057-13	2.0	0.2	0.6	0.0	-0.30	-1.33
J1158-30	0.4	0.2	0.5	0.2	2.86	1.74
J1212-14	1.2	0.8	0.4	0.2	1.07	0.627
J1321+13	0.05	0.005	0.7	0.4	-	-
J1407+42	0.06	0.04	0.6	0.5	-	-

lines, including CaII K (3934Å), MgI (5175 Å), Balmer and NaI D (5890-5896 Å), was used to select the best overall fits. Note that not all objects were successfully fitted. For example, I could not produce an adequate fit to the type 2 object J1131+16 because there are relatively few genuine continuum bins suitable to model the spectrum of this object. It should be noted that this object has an unusual spectrum, which contains a large number of FHILs (see Chapter 3). Figure 4.1 shows an example of a successful CONFIT fit to a 2MASS object. Details of the models chosen for the continuum subtraction in individual objects are given in Table 4.2.

Once the continuum had been subtracted from the spectra (where applicable), the emission lines were fitted using the STARLINK DIPSO package (Howarth et al., 2004).

The emission lines in the spectra of the 2MASS and PG comparison sample AGN were initially fitted with single Gaussian profiles, starting with [OIII]$\lambda\lambda$5007,4959 doublet. I used the [OIII]$\lambda\lambda$5007,4959 emission lines because they are often the strongest unblended lines emitted by the NLR. To produce the models, Gaussian profiles were fitted to the [OIII] doublet, with the separation and intensity ratio set by atomic physics for each kinematic component (as defined by the velocity shifts and line widths). While single Gaussian fits were sufficient in some objects, such fits did not adequately model the wings of the emission lines of most of the objects; in such objects double Gaussian model were fitted to the spectral lines. When a second Gaussian was added, the line ratios, wavelength separations and FWHM were fixed for the two doublet components as before, however the shift and FWHM were allowed to vary relative to the first component, and the widths were allowed to vary. In all cases, one or two Gaussian components proved sufficient, and in all cases where two Gaussian profiles were required, the width of one Gaussian was significantly broader than the other. In some cases, the widths of the narrow components for the [OIII] emission lines were found to be consistent with the instrumental width of their spectra. In such cases, the narrow components of the models that were fitted to the other lines were fixed to the instrumental width. However, in the other (resolved) cases, the measured FWHM was used to obtain an intrinsic velocity width for the narrow component by correcting its FWHM in quadrature using the instrumental width. The same technique was applied to the broader components of the model. Also, the broad component is often shifted with respect to the narrow component; this is accounted for in the models.

Once the model parameters had been determined from the fits to [OIII], they were used to fit the other lines in the spectra. The [OIII] model parameters for each object are presented in Table 4.1. Known blends (e.g. Hα & [NII]$\lambda\lambda$6548,6583) and doublets (e.g. [SII]$\lambda\lambda$6716,6731 and [OII]$\lambda\lambda$3726,3729) were modelled with the [OIII] model using

constraints provided by atomic physics (i.e. fixed FWHM, line separation and, where appropriate, the intensity ratios set by atomic physics). In most cases, the [OIII] model successfully fit all the emission lines/blends in the spectra. However, in a few cases where emission lines have a low equivalent width (e.g. weaker lines such as [OI] or [FeX]), one of the components in the 2 component [OIII] model provides a better fit to the emission line. This happened in some objects with strong broad Balmer emission lines.

The broad permitted lines emitted by many of the objects (mainly Hα and Hβ) were initially fitted with a single Gaussian component, where the intrinsic velocity widths (FWHM) were kept the same for all the BLR emission lines in each object. The NLR emission components of the Balmer emission were still fitted with the [OIII] model. However, for 11 objects in the 2MASS sample, the broad and narrow line components of the Balmer lines could not be confidently separated because, at the resolution of the spectra, they merge seamlessly together, leading to degeneracies in fits that attempt to model the lines as single narrow and broad Gaussians (see Figure 4.2). In addition, for the PG/SDSS sample, I could only confidently separate the broad and narrow emission in 6 objects. Figure 4.2 highlights the problem of degeneracy in the blending of the NLR with BLR in the Balmer lines, using the example of J0422-18. Although the overall fit to the Hβ feature is adequate, the narrow line Gaussian fitted to the Hβ emission line may be over- or underestimating the flux of the NLR Hβ emission. In such cases, I only consider the total fluxes of the combined broad and narrow emission components of the Balmer lines.

The Hβ and [OIII]$\lambda\lambda$5007,4959 emission may also be strongly blended with broad permitted FeII emission. In cases where broad permitted FeII emission is prominent in the spectra (e.g. J0248+14), the FeII emission was fitted separately from the affected emission lines as follows: the FeII emission lines in the same multiplets (F, S or G) were fitted with the same intrinsic velocity widths as the broad Hβ emission line, and their expected intensity ratios were used to constrain the fits, as outlined in Kovačević, Popović & Dimitrijević (2010). This approach provided a good fit to the FeII emission blends in all objects where they are significant.

Examples of model fits are given in Figures 4.3 and 4.4. Figure 4.3 shows an example of a multi-component Gaussian fit to the Hβ and [OIII]$\lambda\lambda$5007,4959, where the broad and narrow components of Hβ were easy to separate. In contrast, Figure 4.4 shows a case where the broad and narrow emission could not be easily separated, and where FeII emission is prominent. Interestingly, the BLR of this object is substantially blueshifted relative to the NLR in this object (by -2870$\pm$160 km s^{-1}; see $\oint$ 4.5).

The results for the NLR [OIII] model fits to the other lines are presented in Tables 4.3

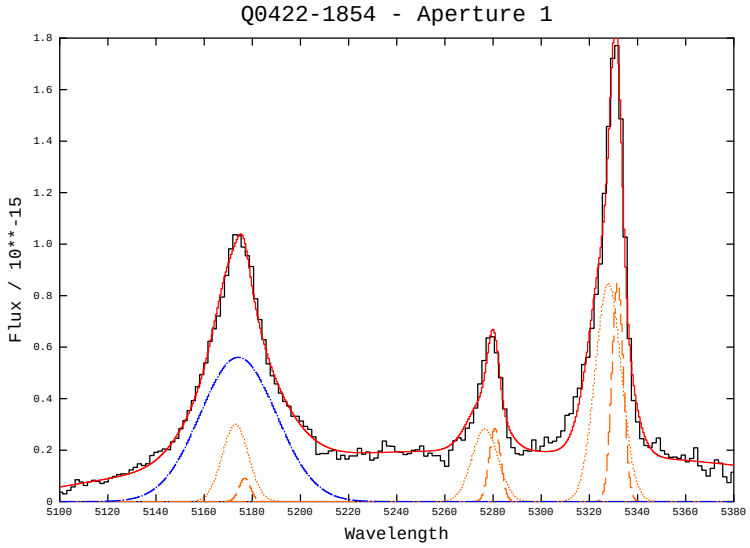

Figure 4.2: Gaussian fits to the Hβ and [OIII]$\lambda\lambda$5007,4959 emission lines of J0422-18. The overall fit is represented by a red line. Both the NLR [OIII] model (orange lines; the narrow component is represented by a dashed line and the broad component is presented by a dotted line) and BLR components (represented by a blue dashed and dotted line) are displayed. The NLR model fit to the Hβ blend highlights the degeneracy issues with blended emission from the BLR and the NLR (this is described in more detail in $\oint$ 4.2).

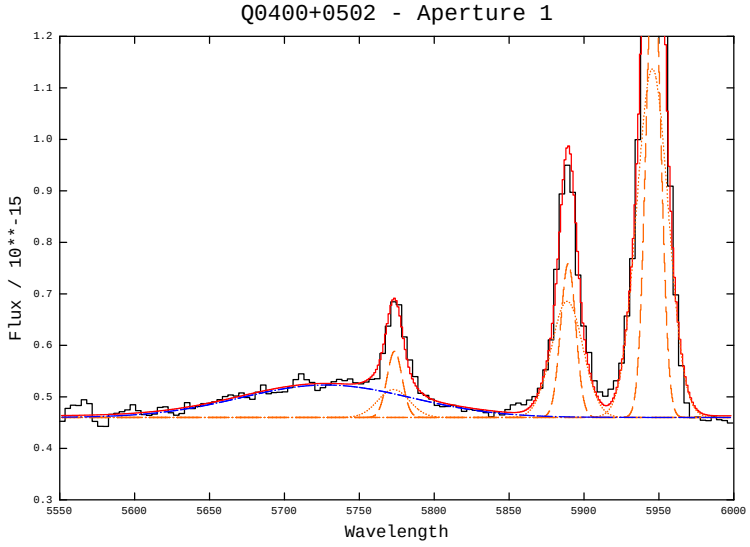

Figure 4.3: Gaussian fits to the Hβ and [OIII]$\lambda\lambda$5007,4959 emission lines of J0400+05. Both the NLR [OIII] model and BLR components are displayed. In this case the BLR and NLR components of Hβ could be clearly separated. Interestingly, the BLR is substantially blueshifted relative to the NLR in this object (by -2870$\pm$160 km s^{-1}).

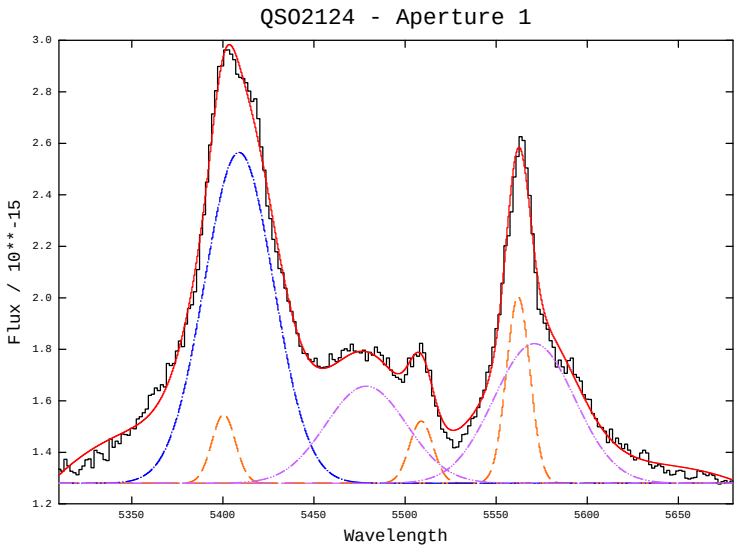

Figure 4.4: Gaussian fits to the Hβ and [OIII]$\lambda\lambda$5007,4959 emission lines of J2121-17. The NLR [OIII] model, BLR component and FeII emission (represented by a violet dashed and dotted line) are displayed. The overall fit is far better than when the emission lines are modelled without the FeII emission.

& 4.4; all the emission line ratios are presented relative to [OIII]λ5007, and the narrow and broad line region Balmer components are presented separately.

4.3 Results

The optical spectra of the 2MASS sample, shown in Figure 4.5, reveal a remarkable variety, ranging from Seyfert 2 galaxies that lack broad emission lines (e.g. J0504-19 & J1057-13), through highly reddened broad line objects (e.g. J1040+59 & J1127+24), to objects that show optical spectra similar to 'normal' blue quasars (e.g. J1338-04 & J2124-17) and even LINER/HII region-like objects (e.g. J0411-01 & J1001+41). I now describe the results obtained from the detailed analysis of the spectra.

4.3.1 Quasars, AGN or starbursts?

Quasars?

Previous studies of red 2MASS AGN have shown that most red 2MASS AGN in the local Universe are not quasars, but have luminosities more consistent with those of Seyfert galaxies (Smith et al. 2002; Marble et al. 2003; Kuraszkiewicz et al. 2009a,b).

Table 4.3: Emission line fluxes of the key emission lines in the 2MASS sample, given as a ratio to the flux of the [OIII]λ5007 emission line (in units of erg s^{-1} cm^{-2}, presented in column 2), for emission lines blueward of Hβ. In general, the uncertainties associated with the emission line fluxes do not exceed $\pm$10%.

Object	$F_{[OIII]}$	[NeV] 3425	[OII] 3727	[NeIII] 3868	Hδ	Hγ	[OIII] 4363
J0221+13	1.8E-15	0.226	0.264	3.971	-	-	-
J0248+14	2E-15	0.208	0.446	0.323	0.495	0.789	0.179
J0306-05	2.1E-15	-	0.285	-	-	-	-
J0312+07	7.6E-16	0.023	0.065	0.024	-	0.111	-
J0400+05	3E-14	0.027	0.151	0.059	0.013	0.046	-
J0409+08	2.1E-14	0.052	0.125	0.07	0.009	0.026	0.015
J0411-01	1.5E-16	-	1.044	-	-	0.487	-
J0422-18	2.8E-14	0.049	0.056	0.075	0.07	0.181	0.108
J0435-06	2.3E-15	-	0.338	-	0.362	1.059	-
J0447-16	1.2E-15	-	0.504	-	-	-	-
J0504-19	8.4E-15	0.166	0.191	0.219	-	0.088	0.105
J0910+33	1.3E-14	0.132	0.112	0.173	0.022	0.03	0.036
J1001+41	2.4E-16	-	2.532	4.897	-	0.812	0.128
J1006+41	1.2E-14	0.114	0.158	0.266	0.045	0.161	0.055
J1014+19	3.6E-14	0.045	0.076	-	0.011	0.02	0.047
J1040+59	2.1E-15	-	1.073	0.157	-	0.083	-
J1057-13	8.9E-15	0.123	0.078	0.071	0.021	0.035	0.014
J1127+24	5.1E-15	0.084	0.147	0.132	0.057	0.094	-
J1131+16	2.3E-14	0.192	0.138	0.209	0.046	0.083	0.171
J1158-30	9.2E-15	-	0.345	0.118	-	0.106	-
J1212-14	4.5E-15	0.104	0.415	-	-	-	-
J1307+23	9.4E-16	-	0.045	-	-	0.121	0.019
J1321+13	6.8E-16	0.089	0.417	0.156	-	-	-
J1323-02	1.4E-14	0.173	0.082	0.13	-	0.011	0.021
J1338-04	1.4E-14	0.233	0.14	0.124	0.011	0.015	0.042
J1407+42	1.6E-14	0.014	0.319	0.069	0.032	0.063	0.01
J1448+44	1.4E-14	0.046	0.203	0.077	-	-	-
J1637+25	2.3E-15	0.042	0.371	0.087	0.03	0.054	0.125
J2121-17	2.7E-14	0.113	0.112	-	-	0.434	0.913

Table 4.4: Same as Table 4.3, however the emission lines presented here have wavelengths redward of [OIII]λ4363. The broad and narrow line region emission is indicated separately for the Hα and Hβ emission lines. For [SII], *blend* refers to 6716&6731.

Object	Hβ_{NLR}	Hβ_{BLR}	[FeVII] 6086	[OI] 6300	[FeX] 6374	Hα_{NLR}	Hα_{BLR}	[NII] 6583	[SII] *blend*
J0221+13	0.203	-	0.128	0.03	-	0.61	-	1.139	0.42
J0248+14	2.19	1.052	-	0.106	-	17.841	5.535	4.395	0.476
J0306-05	0.761	-	-	0.163	-	6.751	-	3.578	0.95
J0312+07	0.818	2.721	0.038	0.082	-	3.586	14.832	1.442	1.041
J0400+05	0.095	0.391	-	0.025	0.061	0.668	3.157	0.42	0.259
J0409+08	0.185	0.675	0.024	0.031	0.017	0.926	1.124	0.173	0.138
J0411-01	1.639	-	-	0.139	-	7.031	-	3.224	1.578
J0422-18	0.854	0.522	-	0.01	-	0.464	5.357	0.916	0.069
J0435-06	2.42	3.752	-	0.035	-	12.498	8.809	0.97	0.496
J0447-16	0.169	1.224	0.072	0.15	-	0.508	11.667	3.362	0.544
J0504-19	0.179	-	-	0.038	-	0.686	-	0.736	0.275
J0910+33	0.098	-	0.022	0.04	0.016	0.211	-	0.367	0.121
J1001+41	2.102	-	-	1.204	-	16.816	-	9.636	5.907
J1006+41	0.52	-	-	0.037	0.014	1.707	1.393	0.315	0.171
J1014+19	0.385	0.517	0.008	0.035	0.046	2.141	2.881	0.303	0.128
J1040+59	0.516	-	-	0.248	-	1.118	5.143	0.434	1.573
J1057-13	0.052	-	0.081	0.055	-	0.368	-	0.105	0.105
J1127+24	0.264	0.909	0.079	0.077	-	0.857	4.886	0.376	0.203
J1131+16	0.19	-	0.094	0.037	0.044	0.948	-	0.149	0.103
J1158-30	0.121	-	-	0.162	-	1.328	-	0.658	0.365
J1212-14	0.325	1.182	-	0.005	-	1.646	5.565	1.593	0.507
J1307+23	0.084	-	-	0.011	-	0.254	-	0.283	0.048
J1321+13	0.254	-	-	0.105	-	1.444	-	0.9	0.491
J1323-02	0.049	1.827	0.074	0.025	-	1.264	7.657	1.98	0.132
J1338-04	0.092	1.461	0.08	0.074	0.045	0.426	5.397	0.222	0.108
J1407+42	0.139	-	0.029	0.124	-	0.947	-	0.685	0.481
J1448+44	0.074	0.722	-	0.046	-	0.473	3.422	0.461	0.26
J1637+25	0.264	-	-	-	-	-	-	-	-
J2121-17	0.498	2.685	-	0.089	-	5.152	1.680	3.141	0.083

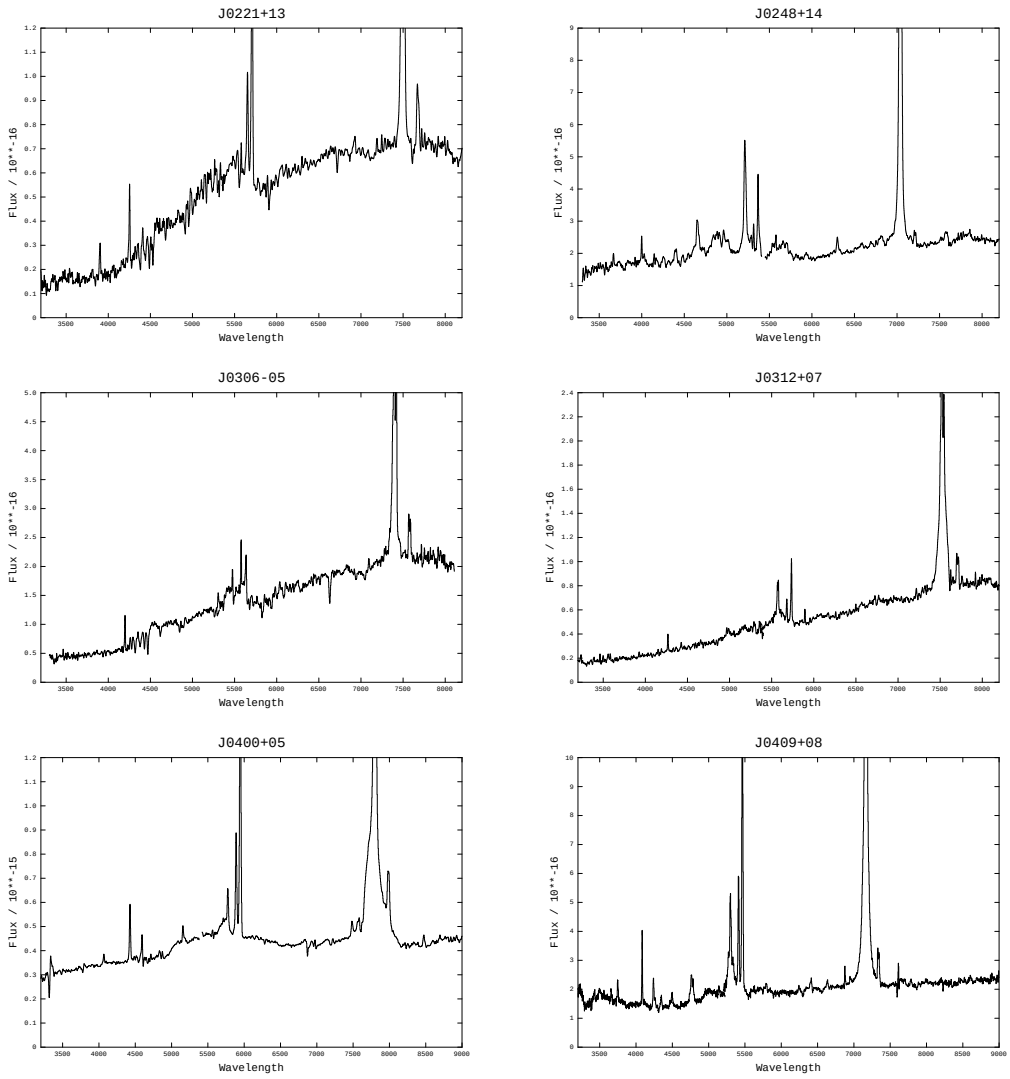

Figure 4.5: The combined (blue and red arm), reduced spectra of the 2MASS sample discussed in this thesis. The flux is plotted as Fλ. Note that J1637+25 and J2124-17 have not had the telluric absorption features removed, because no telluric standard stars were observed during the particular run in which they were measured. Continued on next page.

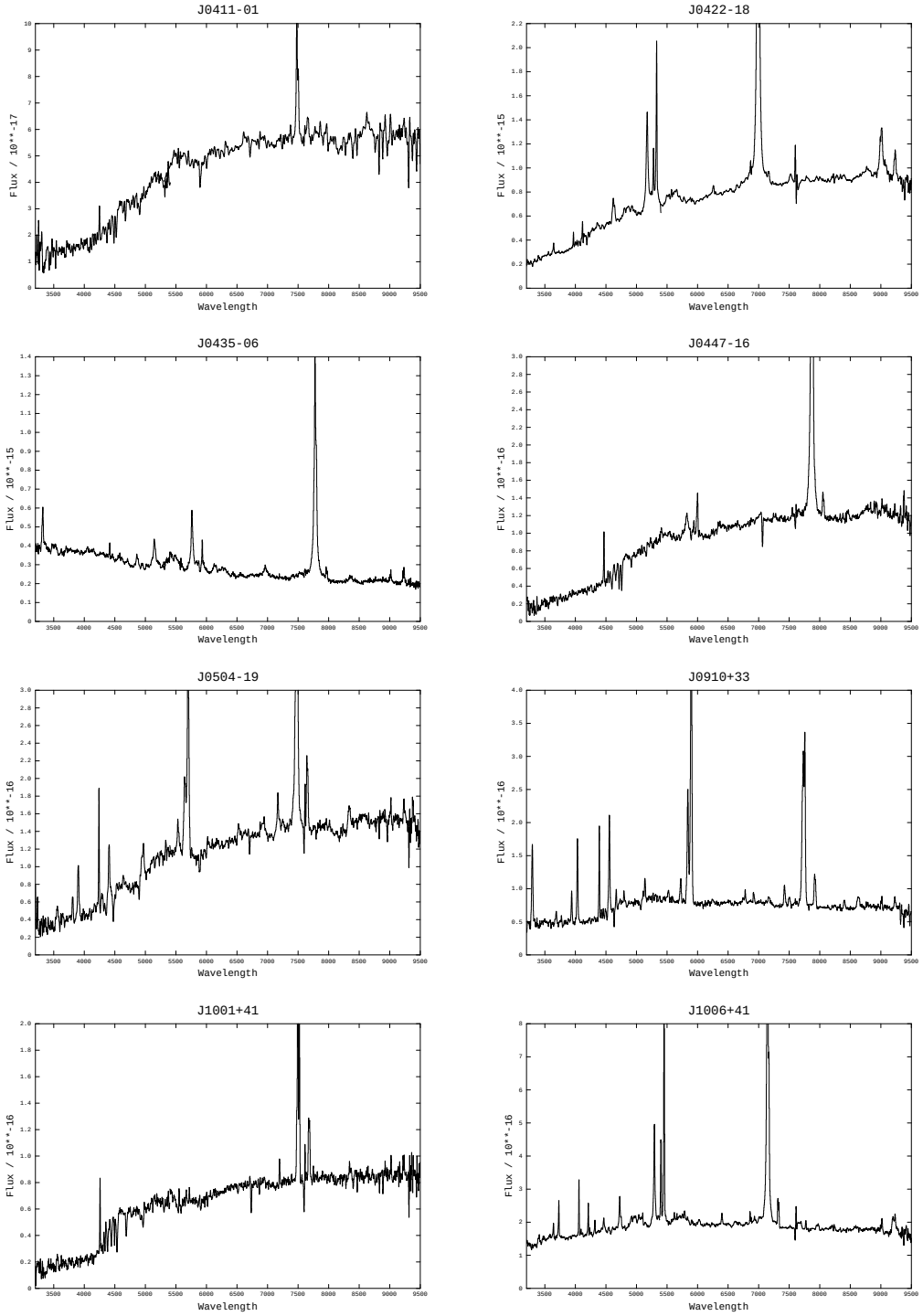
J0411-01
Flux / 10**-17
Wavelength
J0422-18
Flux / 10**-15
Wavelength
J0435-06
Flux / 10**-15
Wavelength
J0447-16
Flux / 10**-16
Wavelength
J0504-19
Flux / 10**-16
Wavelength
J0910+33
Flux / 10**-16
Wavelength
J1001+41
Flux / 10**-16
Wavelength
J1006+41
Flux / 10**-16
Wavelength

Figure 4.5

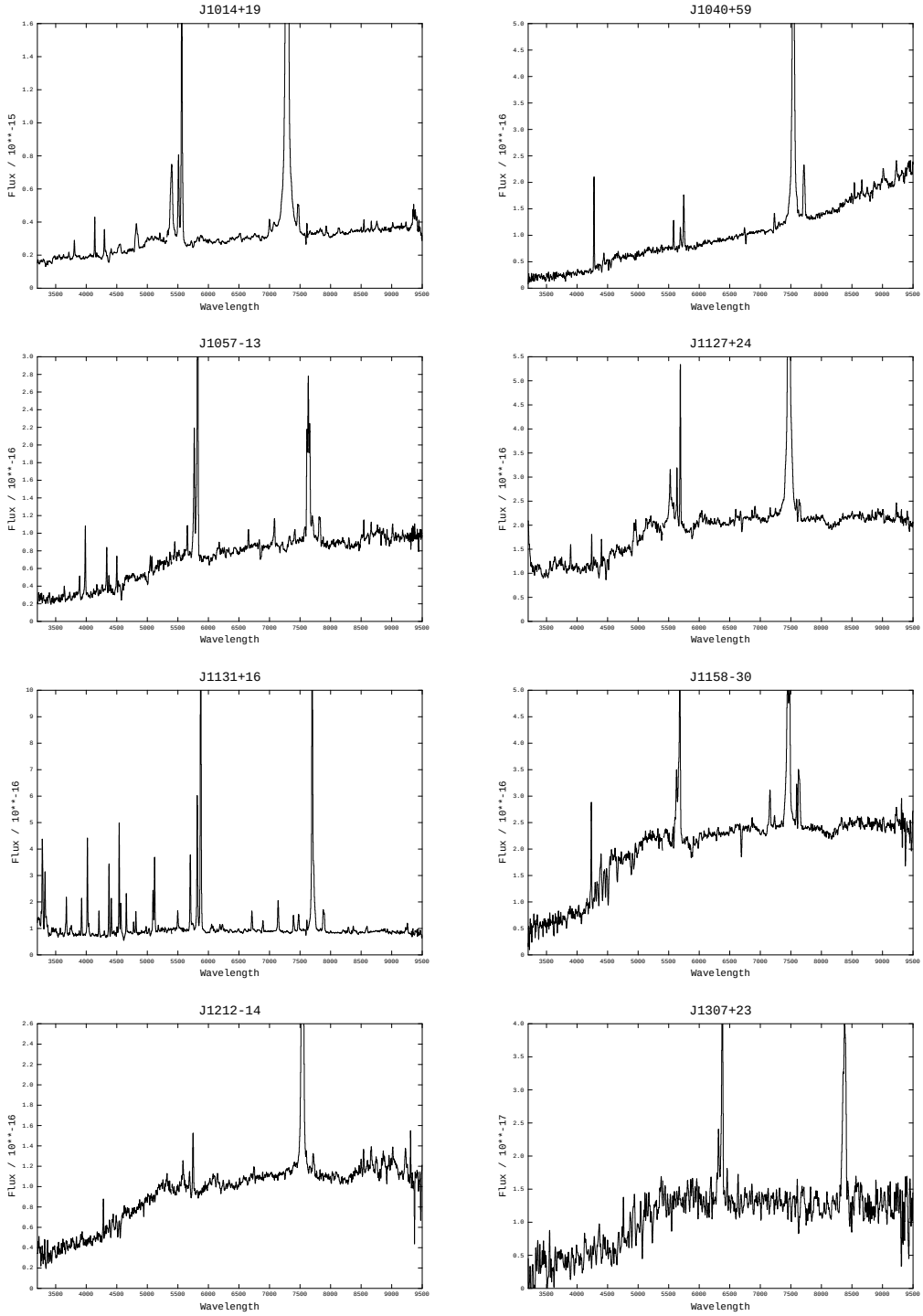
J1014+19
Flux / 10**-15
Wavelength
J1040+59
Flux / 10**-16
Wavelength
J1057-13
Flux / 10**-16
Wavelength
J1127+24
Flux / 10**-16
Wavelength
J1131+16
Flux / 10**-16
Wavelength
J1158-30
Flux / 10**-16
Wavelength
J1212-14
Flux / 10**-16
Wavelength
J1307+23
Flux / 10**-17
Wavelength

Figure 4.5

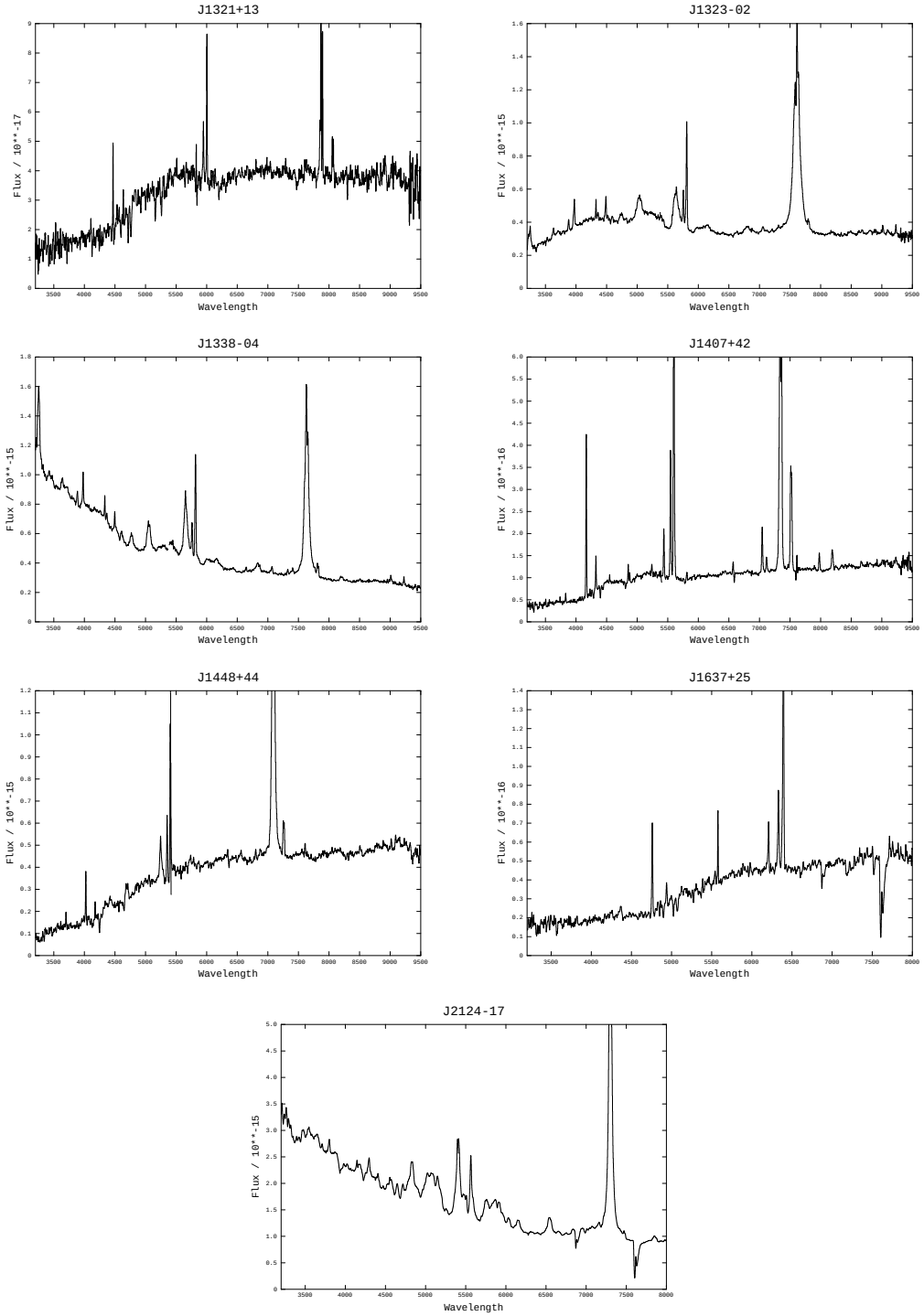
J1321+13
Flux / 10**-17
Wavelength
J1323-02
Flux / 10**-15
Wavelength
J1338-04
Flux / 10**-15
Wavelength
J1407+42
Flux / 10**-16
Wavelength
J1448+44
Flux / 10**-15
Wavelength
J1637+25
Flux / 10**-16
Wavelength
J2124-17
Flux / 10**-15
Wavelength

Figure 4.5

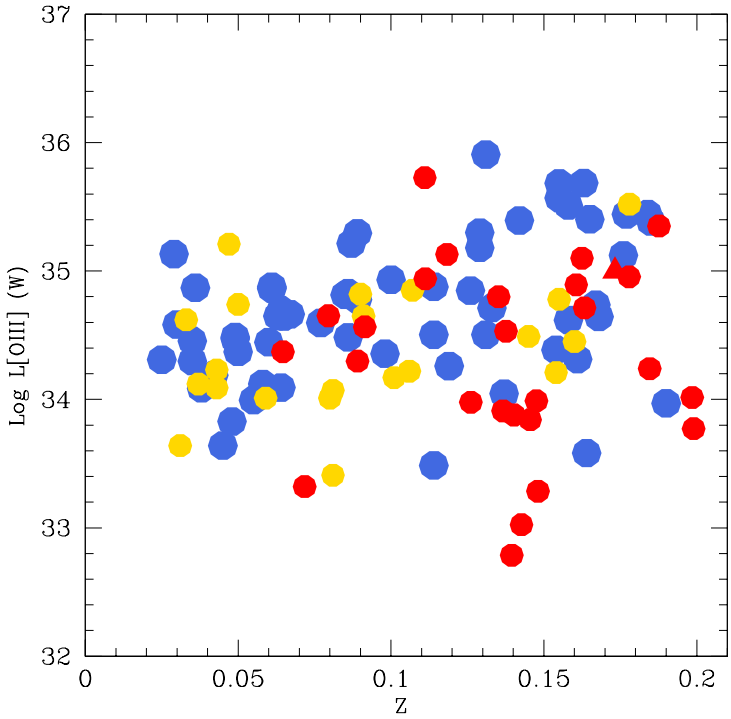

Figure 4.6: [OIII] emission line luminosity ($L_{[OIII]}$) plotted against redshift for the 2MASS objects and the comparison samples. The 2MASS objects are represented by red circles with the exception of J1131+16 which is represented by a red triangle, the PG quasars are represented by blue circles, and the unobscured type 1 AGN are represented by gold circles. Objects with $L_{[OIII]}$ greater than 10^{35} W are likely to have quasar-like bolometric luminosities.

To test the incidence of quasars in the low-z 2MASS sample, I used the [OIII]λ5007 emission line luminosity, which has been shown to be a good indicator of AGN bolometric power (see Heckman et al. 2004; Bian et al. 2006; Dicken et al. 2009; LaMassa et al. 2010). Other luminosity indicators, such as the L_{5100} optical continuum luminosity, cannot be accurately calculated in most of the 2MASS objects because of a combination of reddening of the AGN continuum and host galaxy contamination. Following Zakamska et al. (2003) I assume that an object is a quasar if it has an [OIII]λ5007 luminosity $L_{[OIII]} \gtrsim 10^{35}$ W, corresponding to a nuclear continuum luminosity of $M_B \lesssim$ -23 (Schmidt & Green 1983; Zakamska et al. 2003).

Figure 4.6 shows $L_{[OIII]}$ plotted against redshift for the 2MASS objects and the comparison samples. Note that the luminosities have been determined using the observed frame [OIII]λ5007 fluxes and the luminosity distances appropriate for the assumed cosmology, but have not been corrected for intrinsic reddening. Where possible I use the wide slit (5 arcseconds) data to ensure that the AGN [OIII] luminosity measurements are not affected by slit losses; for the 5 objects for which there are no wide slit data, I use the available 1.5 arcsecond data. I find that 5 objects in the sample (19%) qualify as quasars according to the [OIII] emission line luminosity criterion: J0400+05, J1131+16, J1338-04, J1407+42 and J2124-17. Note that the latter object was previously identified as a ULIRG by Kim & Sanders (1998).

The rate of quasars for the 2MASS sample (red) is comparable to that of the rate of quasars in the comparison samples: 28% of the PG quasars (blue) and 10% of the unobscured type 1 AGN (gold) have quasar-like luminosities based on the $L_{[OIII]}$ luminosity. Therefore the rate of occurrence of quasars in the PG and unobscured type I samples is not significantly different from that of the 2MASS sample. However, I note that 4 objects in the 2MASS sample have lower [OIII] emission line luminosities than any of the objects in the PG quasar and unobscured type 1 AGN samples.

I can only be confident that 5 of the objects in the sample are genuine quasars. The remaining sample has [OIII] luminosities in the range $32.5 < L_{[OIII]} < 35$ W — more typical of Seyfert galaxies. If the 4 objects with low [OIII] luminosities are ignored, the 2MASS AGN have a similar range of luminosities as the PG quasars and the unobscured type 1 AGN. Note that I have not corrected the [OIII] emission line luminosities for intrinsic dust extinction. If I correct the emission line luminosities using the NLR reddening estimates available for 16 objects ($\oint$ 4.3.2), I find that the rate of occurrence of quasars in the 2MASS sample increases to 27% (8 objects). However, I emphasise that I can only accurately correct the narrow line fluxes for reddening in 55% of the objects.

AGN or starbursts?

Both starbursts and AGN activity can potentially ionise the narrow emission regions in the nuclei of galaxies (Baldwin, Phillips & Terlevich 1981). It is therefore important to establish whether the NLR in the 2MASS objects are indeed photoionized by AGN, or whether recent starburst activity provides the photons needed to ionize the emission line regions. Therefore I have categorised the spectra based on the emission line ratios using Baldwin, Phillips & Terlevich (BPT) diagnostic diagrams (e.g. see Baldwin, Phillips & Terlevich 1981; Kewley et al. 2006).

Figures 4.7 - 4.9 show the results for the 2MASS sample. The divisions between the different classes of objects in these figures are taken from Kewley et al. (2006). Note that only ∼50% of the 2MASS sample could be plotted on the BPT diagrams because of the difficulty of measuring accurate narrow Hβ emission line fluxes in many of the objects, related to the de-blending of the emission of the BLR and the NLR (see discussion in § 4.2).

Based on the diagnostic diagrams, all of the objects that could be plotted fall in the AGN part of the diagrams with the exceptions of J0411-01 and J1001+41, which fall in the composite/HII region part of the diagrams, suggesting a major contribution from stellar photoionization. I therefore exclude the latter two objects from any subsequent analysis involving AGN properties.

In addition to emission line diagnostic ratios plotted in Figures 4.7 - 4.9, the presence of FHILs in the spectra can indicate unambiguously the presence of an AGN. These lines include [NeV]$\lambda\lambda$3345,3426, [FeVII]λ6086 and [FeX]λ6374 which, due to their high ionisation potentials (>97 eV), are not generally associated with LINER nuclei or starbursts. I find that 23 of the objects in the sample (85%) show evidence for at least one FHIL, suggesting significant AGN activity.

Another indicator of the presence of an AGN is the detection of broad line emission from the BLR. Table 4.5 indicates whether broad emission lines are detected for each of the 2MASS objects. I assume that the BLR is detected if the Balmer recombination lines show significant (i.e. well above the noise) broad wings that cannot be accounted for by the [OIII] model, and have FWHM > 1000 km s^{-1}. 16 out of 27 objects in the sample (59%) show the presence of definite BLR emission. In addition, tentative evidence for weak Hα broad line emission in J1131+16 was presented in Chapter 3. The broad line component in J1131+16 is consistent with the presence of a scattered (Antonucci & Miller, 1985), or a directly observed, but weak, BLR component. The rest of the type 2 objects had no such emission. Figure 4.10 presents the velocity widths (FWHM) of

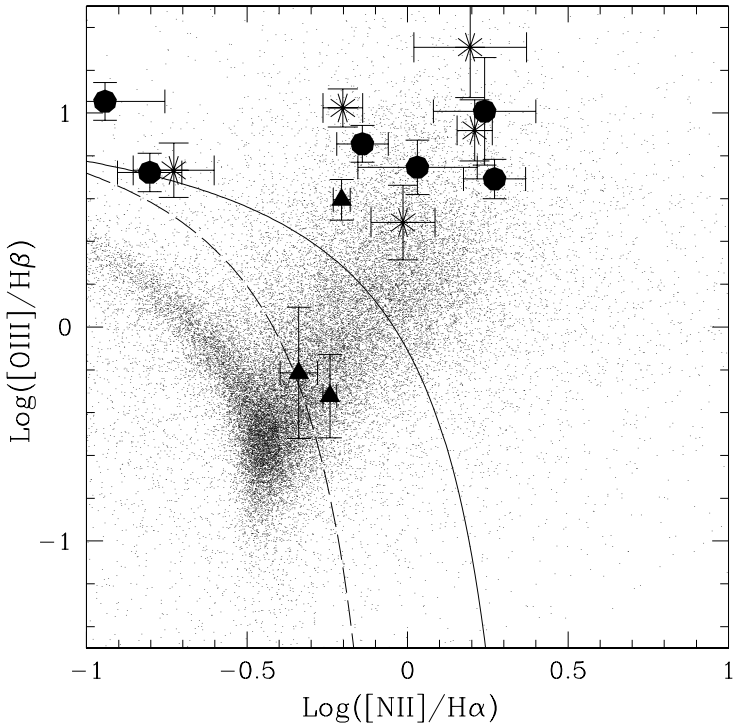

Figure 4.7: Diagnostic plot of $\mathrm{Log}_{10}([\mathrm{OIII}]/\mathrm{H}\beta)$ vs $\mathrm{Log}_{10}([\mathrm{NII}]/\mathrm{H}\alpha)$. AGN are defined to lie above the solid line, HII-region like galaxies below the dashed line, and composite galaxies between these boundaries. The filled circles indicate the emission line measurements for type 2 objects in the 2MASS sample, the stars represent narrow-line emission from the type 1–1.9 objects, the triangles represent the objects in the 2MASS sample, which have fainter emission than the rest of the sample, and the small points are from SDSS-DR 8 data.

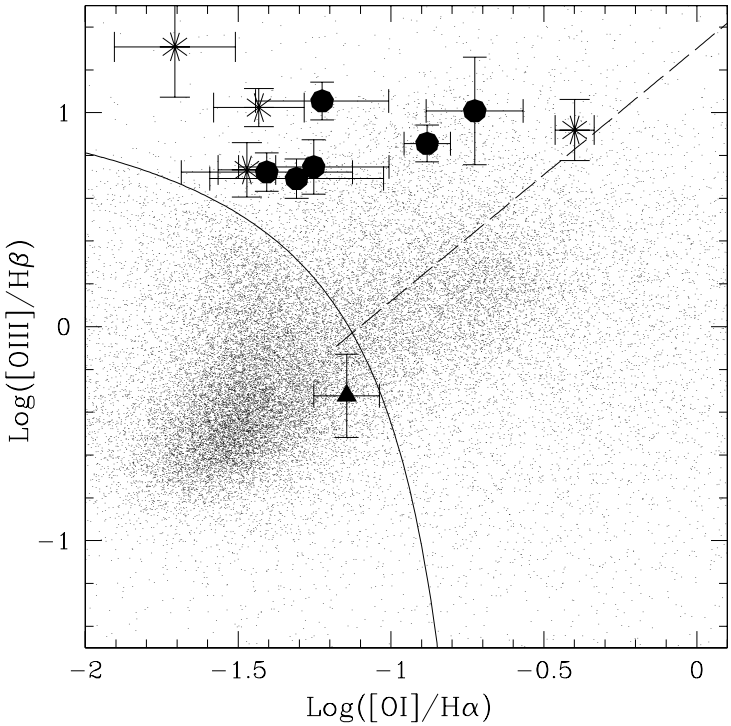

Figure 4.8: Diagnostic plot of $\mathrm{Log}_{10}([\mathrm{OIII}]/\mathrm{H}\beta)$ vs $\mathrm{Log}_{10}([\mathrm{OI}]/\mathrm{H}\alpha)$. AGN are defined to lie above the solid line, with the dashed line separating Seyfert-type objects (above the line), and LINER-type objects (below). HII-region like galaxies fall below the solid line. The symbols are the same as Figure 4.7.

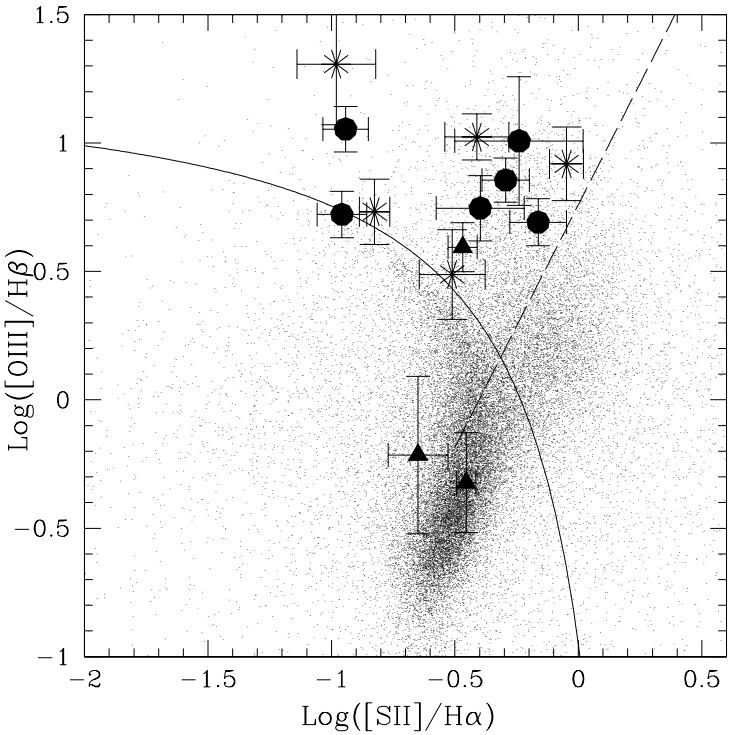

Figure 4.9: Diagnostic plot of $\mathrm{Log}_{10}([\mathrm{OIII}]/\mathrm{H}\beta)$ vs $\mathrm{Log}_{10}([\mathrm{SII}]/\mathrm{H}\alpha)$. AGN are defined to lie above the solid line, with the dashed line separating Seyfert-type objects (above the line), and LINER-type objects (below). HII-region like galaxies fall below the solid line. The symbols are the same as Figure 4.7.

the BLR components as measured from single Gaussian fits to the broad Balmer lines[2], plotted against $L_{[OIII]}$ for both the 2MASS sample and PG sample. Where possible, the broad and narrow-line emission were fitted separately in order to obtain the BLR FWHM; such cases are indicated by the red circles. Where the broad and narrow components could not be confidently separated I use the velocity widths of single Gaussian fits to the whole profiles; these cases are indicated by the red squares. The median BLR velocity width (FWHM) for the 2MASS sample is 2100±400 km s^{-1}, which is lower than that of the PG sample (4500±300 km s^{-1}). However, the 2MASS median may be affected by the inclusion of NLR emission in the objects for which I could not confidently separate the emission from the BLR and the NLR. The median velocity width for the 2MASS objects in which the broad and narrow components could be confidently separated is 4400±1100 km s^{-1} — comparable with the PG quasars.

All the results from this section are summarised in the truth table of Table 4.5. Overall, 25/27 (∼93%) objects show some sign of AGN activity; and only 2 objects — J0411-01 and J1001+41 — show no clear evidence of AGN activity. Given that it is not clear whether the latter two objects are powered by AGN activity, I do not include them in the analysis in the rest of the chapter. In terms of a more detailed classification of the spectra of the 2MASS objects for which I detect significant AGN activity, 59% qualify as Seyfert 1 galaxies, 30% as Seyfert 2 galaxies, and 4% have weak broad lines placing them between the Seyfert 1 and Seyfert 2 classification.

Narrow-line Seyfert 1 galaxies

Narrow-line Seyfert 1 galaxies (NLS1) are a sub-class of Seyfert galaxies with BLR Balmer emission lines that are relatively narrow ($FWHM_{H\beta} < 2000$ km s^{-1}: Osterbrock & Pogge 1985; Vron-Cetty, Vron & Gonçalves 2001). There are several hypotheses surrounding the nature of these objects. One prevailing idea is that NLS1 are AGN with lower than typical black hole masses that are undergoing a phase of rapid accretion (Pounds, Done & Osbourne, 1995). In this scenario the NLS1 fall below, but are growing towards, the M-σ correlation (Ferrarese & Merritt, 2000); eventually, as they accrete more mass, they will appear as typical Seyfert galaxies (Mathur, 2000).

If the red 2MASS objects are young, recently triggered AGN, then I might expect there to be a relatively large fraction of NLS1 objects in the sample. I checked the sample for NLS1 based on single Gaussian fits to their Hβ lines, to find objects with

[2]Note that the FWHM of the Balmer lines are based on fits to the Hβ in all cases except of J1006+41 and J1040+59, which do not have any detectable broad emission in the Hβ emission line, but clear BLR Hα components.

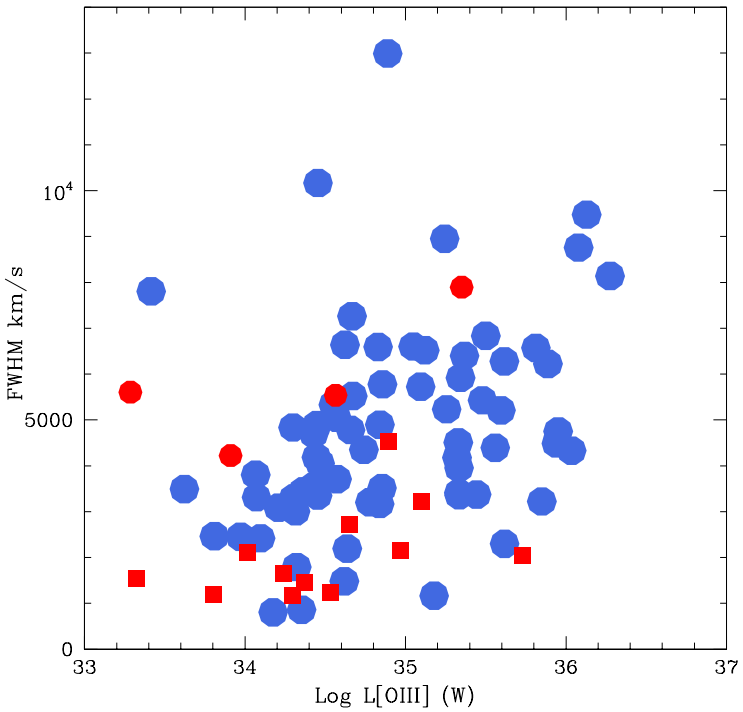

Figure 4.10: Velocity width (FWHM) of the BLR components plotted against $L_{[OIII]}$. The 2MASS objects for which broad emission can be confidently separated from the narrow line emission are indicated by the red circles, whereas the 2MASS objects for which the broad and narrow emission could not be confidently separated are indicated by the red squares. The PG quasar population are indicated by the blue circles. All the line measurements are based on single Gaussian fits.

Table 4.5: Truth table presenting the evidence for AGN activity in the 2MASS sample objects. A true result for BLR indicates the detection of a broad component for either/both Hα and Hβ. A true result for the FHIL indicates the positive detection of a high ionisation species (>54.4 eV). The [NII] column shows the results from Figure 4.7, the [OI] column shows Figure 4.8 and the [SII] column shows Figure 4.9. T=true, F=false, P=tentative evidence for a BLR, A=AGN, S=Seyfert type, H=starburst galaxy, C=composite galaxy, D=unmeasured due to the degeneracy between the broad and narrow Balmer emission, and X=unmeasured because an appropriate emission line has not been detected.

Name	quasar	BLR	FHIL	[NII]	[OI]	[SII]
0221+13	F	F	T	A	S	S
0248+14	F	T	T	D	D	D
0306-05	F	F	T	D	D	D
0312+07	F	T	T	D	D	D
0400+05	T	T	T	A	S	S
0409+08	F	T	T	A	S	S
0411-01	F	F	F	C	X	H
0422-18	F	T	T	D	D	D
0435-06	F	T	F	D	D	D
0447-16	F	T	T	D	D	D
0504-19	F	F	T	A	S	S
0910+33	F	F	T	A	S	S
1001+41	F	F	F	C	H	H
1006+41	F	T	T	D	D	D
1014+19	F	T	T	D	D	D
1040+59	F	T	F	D	D	D
1057-13	F	F	T	A	S	S
1127+24	F	T	T	D	D	D
1131+16	T	P[a]	T	A	S	S
1158-30	F	F	T	A	S	S
1212-14	F	T	T	A	X	S
1321+13	F	F	T	A	X	S
1323-02	F	T	T	A	S	S
1338-04	T	T	T	D	D	D
1407+42	T	F	T	A	S	S
1448+44	F	T	T	D	D	D
2121-17	T	T	T	D	D	D

[a] See Chapter 3 for full description.

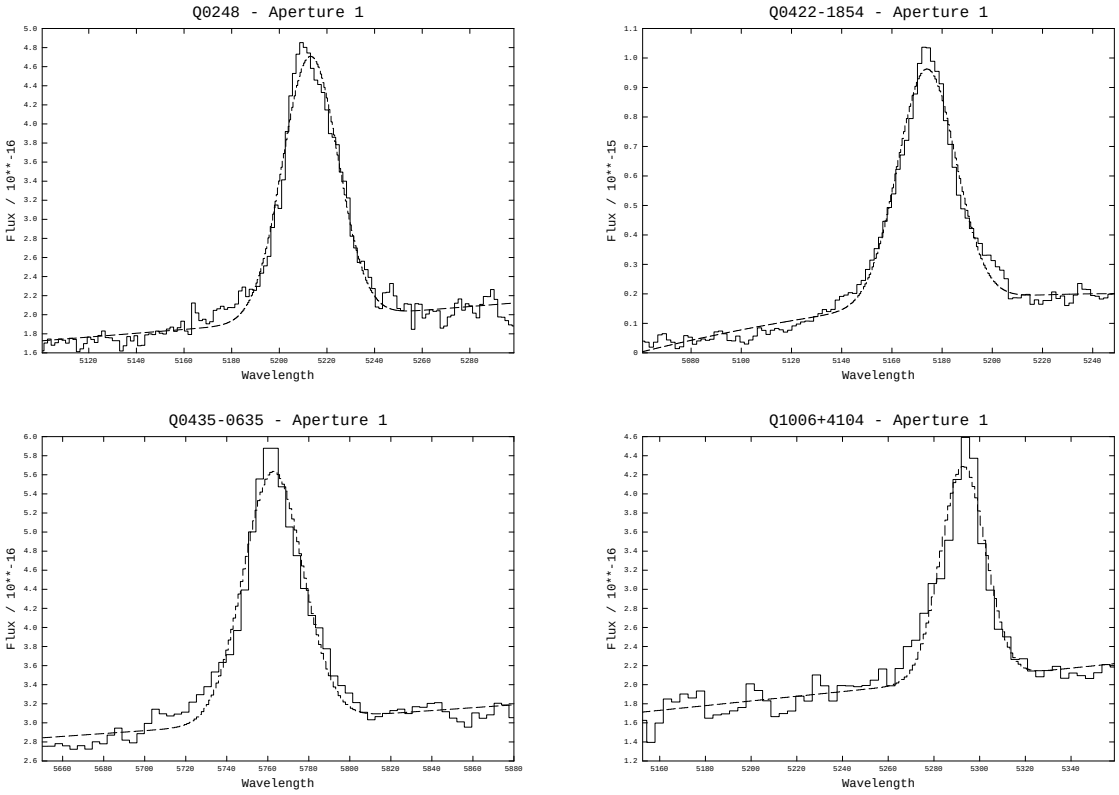

Figure 4.11: Gaussian fits to the Hβ emission lines of the NLS1 candidates in the 2MASS sample. From top to bottom: J0248+14, J0422-18, J0435-06 and J1006+41. The overall fits to the emission lines are adequate and therefore I use the velocity widths (FWHM) to characterise these objects.

Hβ or Hα emission line widths that are below the NLS1 limit (FWHM $<$ 2000 km s^{-1}), but greater than the widths of the [OIII] lines. This is consistent with the fitting procedures of Osterbrock & Pogge (1985) and Goodrich (1989). I found that 4 objects with adequate single Gaussian fits to Hβ have velocity widths consistent with them being NLS1: J0248+14, J0422-18, J0435-06 and J1006+41. These objects have Hβ velocity widths (FWHM) of 1550±20 km s^{-1}, 1450±120 km s^{-1}, 1780±70 km s^{-1} and 1170±70 km s^{-1} respectively.

Figure 4.11 shows the single Gaussian fits to the Hβ emission lines in these objects. Apart from the line widths, there are two other key properties that are found to be associated with NLS1: [OIII] emission lines that are weak relative to the broad Hβ lines ([OIII]/Hβ_{total}<3) and the presence of strong FeII emission (FeII$_{4570}$/Hβ_{total}>0.5: Osterbrock & Pogge 1985; Goodrich 1989; Vron-Cetty, Vron & Gonçalves 2001). I find that all 4 objects with FWHM$_{H\beta}$<2000 km s^{-1} in the sample also possess these typical NLS1 properties.

Of the AGN in the 2MASS sample, only ∼16% are NLS1 objects, or ∼24% as a fraction of all the broad emission-line objects in the 2MASS sample. This is similar to the fraction of NLS1s found in other samples of broad-line AGN: ∼24% for the unobscured type 1 AGN (Jin et al., 2012a); 11% for the PG quasars (Hao et al., 2005); and ∼15% of all QSOs in SDSS DR3 AGN catalogue (Zhou et al. 2006). Therefore I conclude that the 2MASS sample does not contain an unusually high proportion of NLS1 objects.

4.3.2 Balmer decrements and reddening

One possible explanation for the red colours of the 2MASS objects at near-IR wavelengths is that their AGN suffer an unusual amount of dust extinction compared with other samples of AGN (e.g. Glikman et al. 2004). In order to investigate this possibility, I have calculated Balmer recombination line decrements for the 2MASS, PG/SDSS and Jin et al. 2012a,b,c samples to determine whether the 2MASS objects have higher levels of dust extinction than 'typical' blue quasars.

Ideally, Balmer decrements (F$_{H\alpha}$/F$_{H\beta}$) would be determined for the narrow and broad line components of each object separately. However, some objects with a detectable BLR have relatively narrow broad lines (e.g. J1006+41), which makes it difficult to separate the components at the resolution of the spectra (see § 4.2). Therefore I have taken two approaches. For the first approach I used the measured total (broad and narrow) fluxes of the Balmer emission lines. The second approach was to separate the broad and narrow emission components of the blends, where the components could be confidently

separated. I only used the total (broad + narrow) Balmer flux measurements for the Jin et al. (2012a) sample, because I was uncertain whether the broad and narrow emission components could be confidently separated in that sample. In addition, when I consider Balmer decrements for the total flux of the Balmer lines, I only use the data for the objects with a detectable BLR, and do not consider the Balmer decrements for the type 2 objects. Balmer decrements for the 2MASS objects are given in Table 4.6.

Figure 4.12 shows histograms of the Balmer decrements ($F_{H\alpha}/F_{H\beta}$) for the combined broad and narrow Balmer emission of the 2MASS sample (broad line objects only), the PG/SDSS sample and the unobscured type 1 AGN.

It is clear from this figure that, on average, the 2MASS sample objects have higher $F_{H\alpha}/F_{H\beta}$ ratios than the PG quasars and unobscured type 1 AGN, implying that there is more dust extinction in the 2MASS sample. There is also a significant fraction of objects (5/19) with Balmer decrements that are higher than the most reddened PG quasars. This is reflected in the median $F_{H\alpha}/F_{H\beta}$ ratios: $F_{H\alpha}/F_{H\beta}$=4.9±0.5, 3.2±0.4, and 2.8±0.1 for the 2MASS, PG/SDSS and unobscured type 1 objects respectively.

To put this in context, the Balmer decrements for the 2MASS sample suggest reddening in the range $0.0 \leq$ E(B-V) ≤ 1.3, with a median E(B-V)=0.52±0.05, assuming a Case B Hα/Hβ ratio of 3.1 (Gaskell & Ferland 1984). However, although the 2MASS sample displays a significant degree of dust reddening, there are several objects ($\sim$25% of all the broad line objects) which show very little (if any) significant BLR reddening. These objects include J0312+07, J0409+08, J0435-06, J1338-04 and J2121-17. This is interesting, because it highlights the diverse nature of the 2MASS sample. I further note that three of the objects with low Balmer decrements — J0312+07, J0435-06 and J1338-04 — have J-K_S colours just below the J-K_S=2.0 limit. Also, J1040+59, an object with one of the highest Balmer decrements, has one of the reddest J-K_S colours in the sample (J-K_S=3.02). However, overall I do not find a statistically significant correlation between J-K_S colours and Balmer decrements for the 2MASS sample.

I have performed K-S tests (Peacock 1983; Fasano & Franceschini 1987) to check the significance of any differences in the distribution of the Balmer decrements between the samples. I find that I can reject the null hypothesis that the 2MASS sample is drawn from the same parent population as the PG quasars and unobscured type 1 AGN at the 2σ and $>3\sigma$ levels of significance respectively (the corresponding p values are 0.007 and $<$0.001).

In the cases where it was possible to clearly separate the BLR and NLR components, I find that the Balmer decrements obtained for the BLR components alone are not significantly different from those derived from the total (BLR + NLR) fluxes (see Table

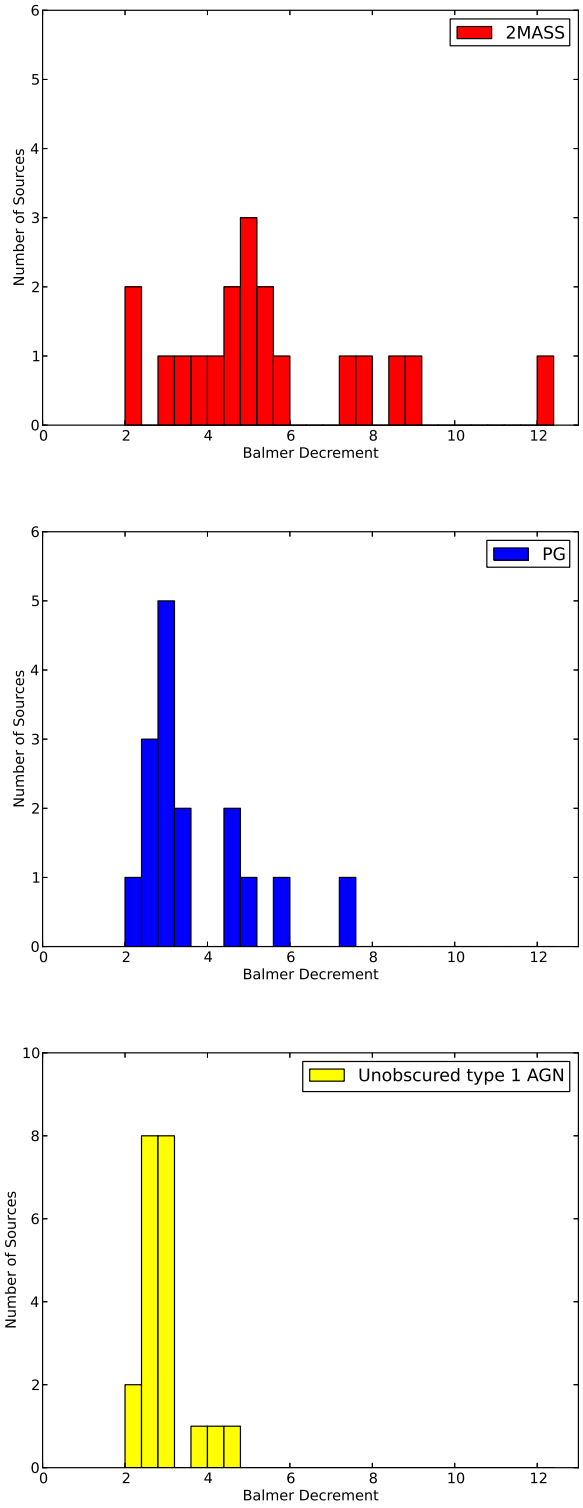

Figure 4.12: Comparison of the total flux Balmer decrements ($F_{H\alpha}/F_{H\beta}$). The 2MASS population measurements (broad line objects only) are indicated in red (top), the PG quasar population are shown in blue (middle) and the unobscured type 1 AGN are given in yellow (bottom). Note that the Balmer decrements are only presented for those objects with broad Balmer emission.

4.6). Therefore I do not consider the pure BLR Balmer decrements further in this chapter.

When considering the range of reddening found for the 2MASS AGN, the results are consistent with the idea that dust reddening plays a significant role in causing the red near-IR colours of the 2MASS objects (see § 4.6.1).

Reddening in the NLR

It is also interesting to consider the NLR Balmer decrements for the red 2MASS AGN in which the NLR and BLR components could be clearly separated. The results are presented in Figure 4.13. I find that the NLR Balmer decrements cover a similar range to those measured for the BLR (and BLR + NLR combined), with some objects showing evidence for a high degree of reddening, but others showing no significant reddening. I have compared the distributions of the narrow emission line Balmer decrements for the 2MASS objects and unobscured type 1 AGN using a K-S test and find that I cannot reject the null hypothesis that these samples are drawn from the same parent population, because the test gives a high p value: 0.099. Note that small number statistics preclude a detailed comparison of the NLR Balmer decrements between the 2MASS and PG/SDSS samples. Also, in the case of the NLR it may not be valid to assume Case B recombination for the intrinsic reddened Balmer decrement: the detailed analysis of J1131+16 (see Chapter 3) demonstrates that collisional excitation of the Hα emission line in the partially ionised zone can significantly enhance the Hα/Hβ ratio if the gas densities are high (e.g. if part of the NLR emission originates in the circum-nuclear torus).

4.3.3 Outflows

If the red 2MASS objects truly represent young AGN enshrouded in a cocoon of dust and gas, then I might expect them to show strong evidence for outflows in their spectra, when compared to other types of active galaxies. For example, in models of major galaxy mergers the AGN are triggered as gas and dust is driven by the tidal torques associated with the mergers into the nuclear regions of the galaxies; the AGN accrete at high Eddington rates, and then drive powerful outflows, blowing away the enshrouding dust and gas (Hopkins et al. 2005; Narayanan et al. 2006; Hopkins et al. 2006a).

Figure 4.14 shows a histogram of the rest-frame velocity shifts of the broad [OIII] components (where detected) relative to those of the narrower components, as calculated from the parameters given in Table 4.1. The 2MASS objects are plotted along with

Table 4.6: The Hα/Hβ Balmer decrements measured for the 2MASS sample. The second column presents the Balmer decrements for the total (BLR + NLR) fluxes. The third and fourth columns present the NLR and BLR Balmer decrements respectively. The fifth and sixth columns present the extinction estimates using the total and BLR Balmer decrements respectively. To calculate the extinction estimates I use the standard stellar extinction curve of Osterbrock & Ferland (2006), and assume the case B recombination ratio of Hα/Hβ has the value 3.1. Note that I do not give the extinction estimates for Balmer decrements below 3.1 because this will lead to negative extinction values.

	$F_{H\alpha}/F_{H\beta}$			E(B-V)	
Name	Total	NLR	BLR	Total	BLR
J0221+13	-	3 ± 0.34	-	-	-
J0248+14	7.21 ± 0.64	-	-	0.81 ± 0.08	-
J0306-05[a]	-	8.87 ± 2.2	-	-	-
J0312+07	5.2 ± 0.45	-	-	0.50 ± 0.08	-
J0400+05	7.87 ± 0.51	7.03 ± 0.51	8.07 ± 0.79	0.89 ± 0.06	0.92 ± 0.09
J0409+07	2.38 ± 0.46	5 ± 0.46	1.67 ± 0.08	-	-
J0422-18	4.3 ± 0.35	-	-	0.31 ± 0.08	-
J0435-06	3.45 ± 0.43	-	-	0.10 ± 0.11	-
J0447-16	8.74 ± 1.48	-	-	0.99 ± 0.15	-
J0504-19	-	3.83 ± 0.82	-	-	-
J0910+33	-	2.15 ± 0.62	-	-	-
J1006+41[b]	5.96 ± 0.28	-	**>5.00**	0.63 ± 0.04	0.46
J1014+19	5.57 ± 0.79	-	-	0.56 ± 0.13	-
J1040+59[b]	12.14 ± 0.57	-	**>6.67**	1.31 ± 0.04	0.74
J1057-13	-	8.05 ± 0.67	-	-	-
J1127+24	4.89 ± 0.46	3.25 ± 0.46	5.38 ± 0.6	0.44 ± 0.09	0.53 ± 0.10
J1131+16[c]	-	5 ± 0.17	-	-	-
J1158-30	-	10.98 ± 0.48	-	-	-
J1212-14	4.79 ± 0.93	5.07 ± 0.93	4.71 ± 0.75	0.42 ± 0.17	0.40 ± 0.14
J1321+13	-	5.67 ± 0.52	-	-	-
J1323-02	4.75 ± 0.87	-	-	0.41 ± 0.16	-
J1338-04	3.75 ± 0.69	-	-	0.18 ± 0.16	-
J1407+42	-	6.79 ± 0.68	-	-	-
J1448+44	4.9 ± 1.21	-	-	0.44 ± 0.21	-
J2124-17	2.15 ± 1.19	-	-	-	-

[a] Sky line features cut through the region of the Hβ emission line. Results are based on an upper limit measurements for the Hβ emission line, but are presented as a lower limit on the Balmer decrement.

[b] BLR Balmer decrement is based on an upper limit of the Hβ flux and therefore is a lower limit of the Balmer decrement.

[c] The emission flux from Hα is boosted by collisional excitation in this object (see Chapter 3).

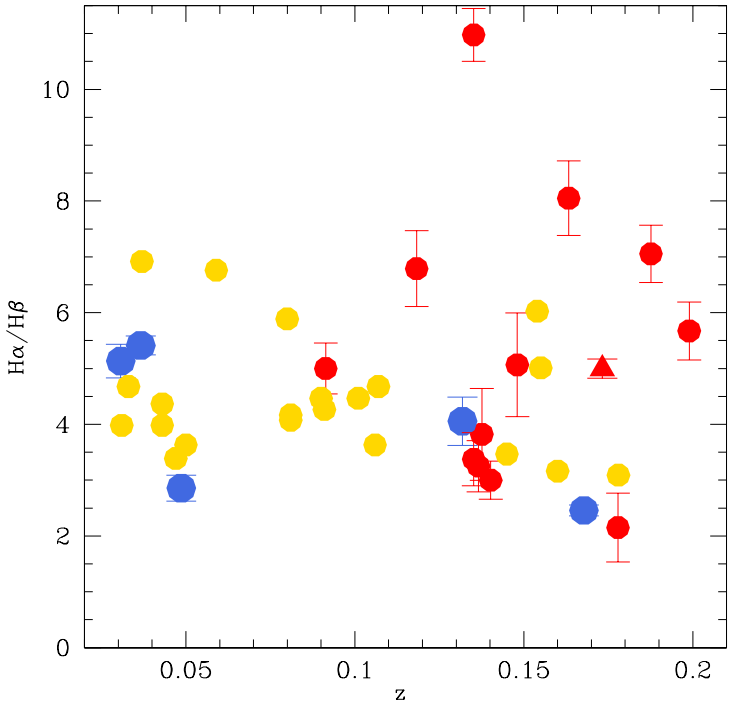

Figure 4.13: The Balmer decrement ($F_{H\alpha}/F_{H\beta}$) versus redshift, z, for the NLRs of the 2MASS sample. The 2MASS objects are represented by red circles with the exception of J1131+16 which is represented by a red triangle, the PG/SDSS quasars are indicated by blue circles and the unobscured type 1 objects are indicated by gold circles.

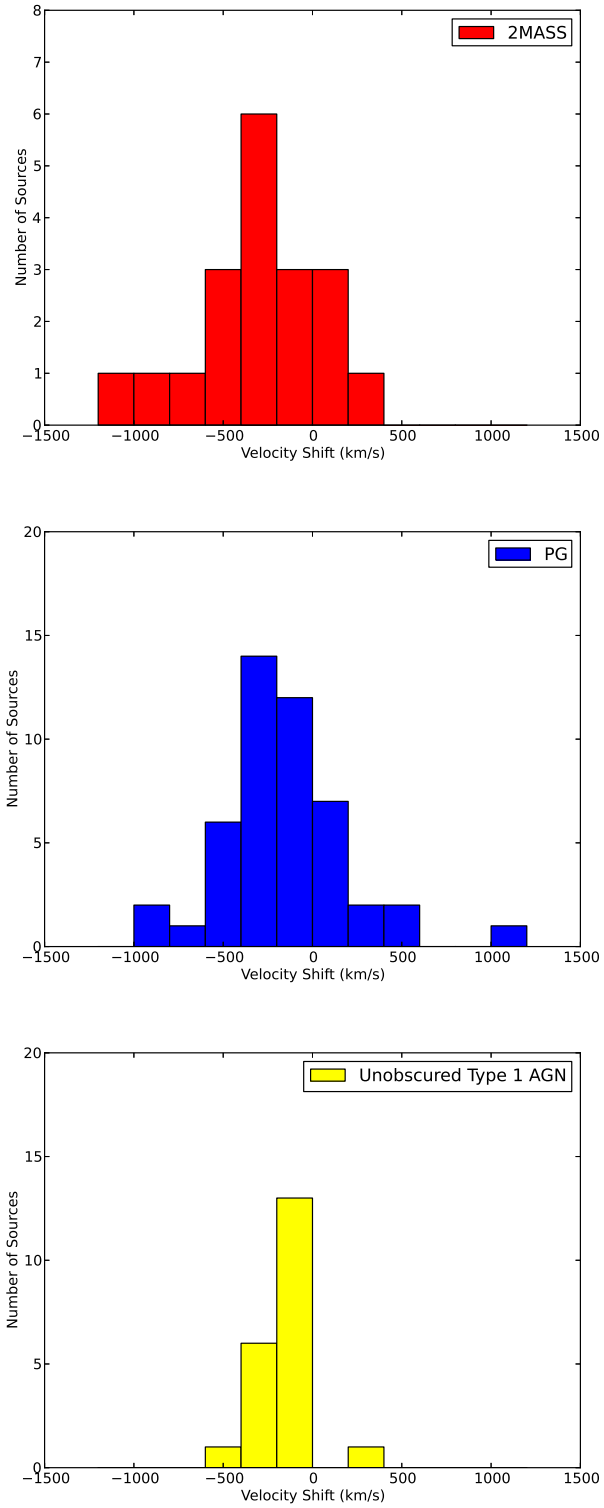

Figure 4.14: Histogram of the shift of the broad [OIII]λ5007 components relative to the narrow components, as measured using DIPSO. The 2MASS measurements are indicated by the red bars (top), the PG quasar population by the blue bars (middle) and the unobscured type 1 AGN by the yellow bars (bottom).

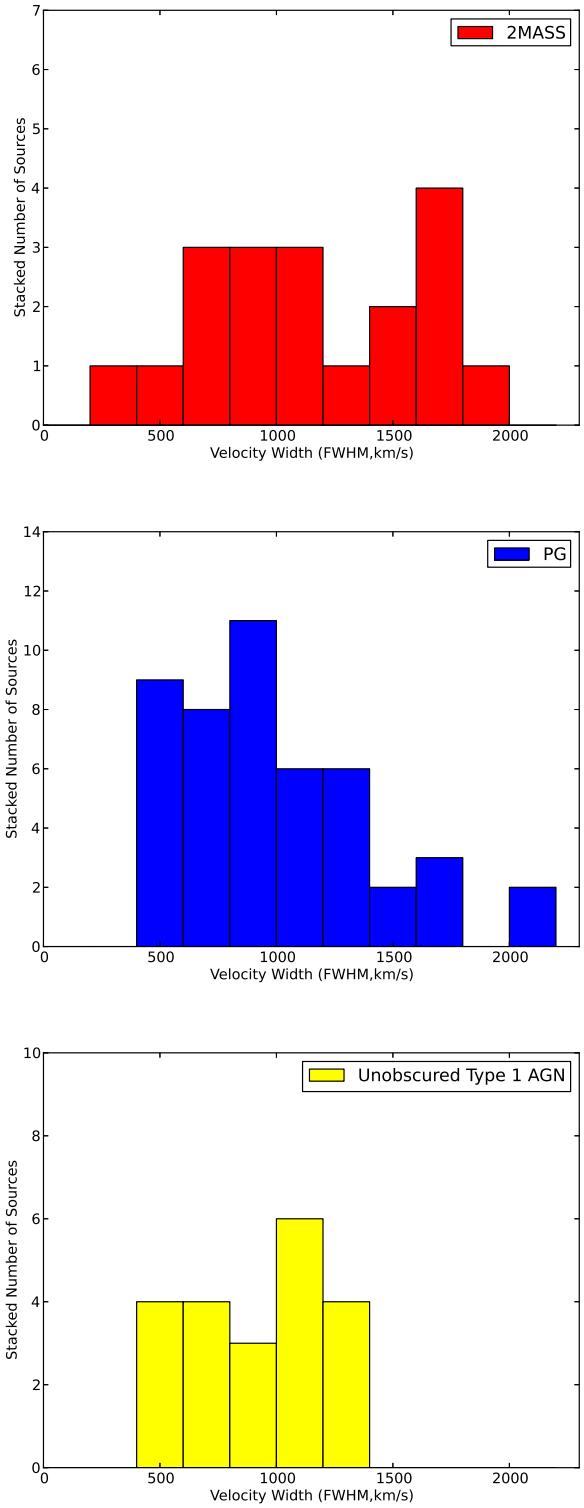

Figure 4.15: Histogram of the instrumentally corrected velocity widths (FWHM, km s^{-1}) of the broad [OIII]λ5007 component, as measured using DIPSO. The 2MASS measurements are indicated by the red bars (top), the PG quasar population by the blue bars (middle) and the unobscured type 1 AGN by the yellow bars (bottom).

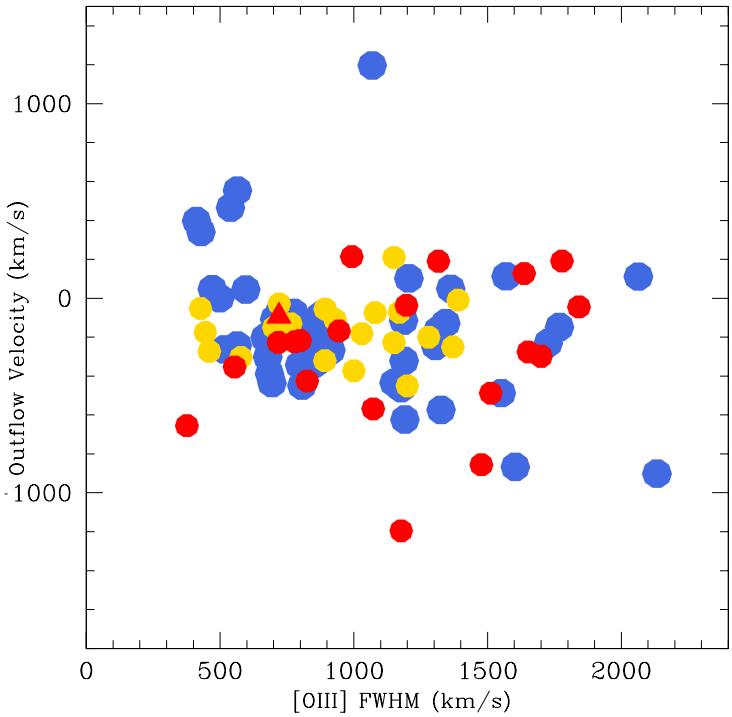

Figure 4.16: Outflow velocity (km s^{-1}) plotted against the velocity width at FWHM (km s^{-1}) of the broad [OIII]λ5007 components as measured by DIPSO. The 2MASS objects are represented by red circles with the exception of J1131+16 which is represented by a red triangle, the PG quasar population are indicated by the blue circles and the unobscured type 1 AGN are indicated by gold circles.

the PG quasars and the unobscured type 1 AGN for comparison. For the unobscured type 1 AGN, I used the online data tables from Jin et al. (2012a) to determine the outflow properties. For the 2MASS objects, PG quasars and unobscured type 1 AGN, I assume that the narrow component of the [OIII] emission represents the host galaxy rest frame emission, and the broader-line emission component the outflow (Holt, Tadhunter & Morganti, 2008).

From Figure 4.14 it is clear that there are no significant differences between the distributions of the velocity shifts of the samples and, the broad components are predominantly blue-shifted in all three samples, with only a few exceptions. I find the median velocity shifts of -240±80 km s^{-1}, -230±50 km s^{-1}, and -160±30 km s^{-1} for the 2MASS, PG and unobscured type I samples respectively. I have tested the significance of any difference between the distribution of velocity shifts of the samples using a 1D K-S test. Between the 2MASS objects and PG quasars I find a p value= 0.731, and between the 2MASS objects and unobscured type 1 objects I find p value= 0.230. Therefore I cannot confidently reject the null hypothesis that these samples are drawn from the same parent population. Note that, although there are no significant differences between the three samples, the most extreme object in all three samples in terms of its shift is a red 2MASS object: J1158-30. This object might be a good candidate for a young AGN.

In addition, in Figure 4.15 I plot a histogram of the rest-frame velocity widths (FWHM) of the broad [OIII] components. As with the velocity shifts, the widths (FWHM) of all three samples have a comparable range. Again, I have tested for any significant differences between the distribution of velocity widths (FWHM) of the samples using a 1D K-S test. Between the 2MASS objects and PG quasars I find a p value= 0.385, and a p value=0.089 for the unobscured type 1 AGN. Therefore I cannot reject the null hypothesis that the samples are drawn from the same parent population when comparing the line widths of the PG quasars and unobscured type 1 AGN with the 2MASS sample.

Figure 4.16 shows the outflow velocity plotted against the velocity width (FWHM) of the broad [OIII]λ5007 component. I present this Figure to further illustrate that there are no significant differences between the [OIII] emission line kinematics of the samples. I have also tested for any significant difference between the populations using a 2D K-S test (Peacock 1983; Fasano & Franceschini 1987). Again, I find no evidence for significant differences between the samples ($p > 0.05$).

One important caveat when considering these results is that the emission line kinematics may be affected by the orientation of the AGN. One possibility is that our line of sight to the type 2 AGN is at a larger angle to the torus axis than type 1 AGN (as

suggested by the orientation-based unified schemes). Therefore due to projection effects the measured blueshifts of the broad components might be lower in the type 2 than the type 1 objects. Alternatively, it is possible that the torus obscures the narrow line outflows from our direct line of sight in the type 2 objects. However, comparisons between the NLR kinematics of type 1 and 2 AGN show no clear differences (e.g. Whittle 1985; Nelson & Whittle 1995).

4.4 Black hole and accretion properties

Further insights into the nature of the red 2MASS objects can be obtained by studying the SMBH and accretion properties of the sample. Young, dust enshrouded objects are expected to have higher than average accretion rates, because there is more gas available for accretion (e.g. see Di Matteo, Springel & Hernquist 2005).

To determine the accretion properties, I must first determine the black hole masses of the objects. In this section I use the broad Balmer emission line properties to determine virial black hole masses and Eddington ratios for the 2MASS sample, the PG sample, and the unobscured type 1 AGN[3]. Any significant differences in the Eddington ratios between the samples could indicate differences in their evolutionary stage.

To determine virial black hole masses, I have used the relationships between the Balmer emission and black hole mass from Greene & Ho (2005). These relationships were obtained using both the observed correlations between the intrinsic luminosity of an AGN and its emission lines, and the correlation between the intrinsic luminosity of the AGN and SMBH mass as estimated from reverberation mapping. Equation 6 from Greene & Ho (2005) is the relationship which determines the BH mass using the broad Hα emission line, and is given as:

$$M_{\rm BH} = (2.0^{+0.4}_{-0.3}) \times 10^6 \left(\frac{L_{\rm H\alpha}}{10^{42}\ {\rm erg\ s^{-1}}}\right)^{0.55\pm0.02} \left(\frac{\rm FWHM_{H\alpha}}{10^3\ {\rm kms^{-1}}}\right)^{2.06\pm0.06} M_\odot.$$

Similarly, equation 7 from Greene & Ho (2005) is the relationship which determines the BH mass using the broad Hβ emission line:

[3]For consistency, I use the Hβ luminosities and velocity widths (FWHM) provided in Jin et al. 2012a to determine the black hole masses, bolometric and Eddington luminosities of the unobscured type 1 AGN sample ($L_{H\beta}$ and $FWHM_{H\beta}$ are flux weighted means of the intermediate and broad components of the Hβ emission lines). Note that, the data used from Jin et al. 2012a is not corrected for extinction. This is reasonable as the sample is selected to be unreddened.

$$M_{\rm BH} = (3.6 \pm 0.2) \times 10^6 \left(\frac{L_{\rm H\beta}}{10^{42}\ {\rm erg\ s^{-1}}} \right)^{0.56\pm0.02} \left(\frac{\rm FWHM_{H\beta}}{10^3\ {\rm kms^{-1}}} \right)^2 M_\odot.$$

I use equation 7 for most cases where I can use the broad Hβ emission lines, minimising any degeneracies due to blending with other emission lines (e.g. [NII] with Hα). In cases where the Hβ broad emission is not detectable, I used the Hα broad emission with equation 6 instead.

I fitted the broad Hβ emission with the minimum number of Gaussian components required to obtain an adequate fit to the emission from the BLR, and took a flux weighted mean of the FWHM, consistent with the method of Greene & Ho (2005). Where possible, I corrected the BLR fluxes for extinction, and in cases where I could not confidently separate the broad and narrow emission, I used the total Balmer decrement measurements for the extinction correction. Note that, while this approach is consistent with that outlined in Greene & Ho (2005) when measuring the broad Hβ emission, problems with the separation of the broad and narrow emission in the objects where I could not separate the components may potentially have an affect on the line width measurements. Also, for the cases where I estimated an upper limit on the broad Hβ flux, I used the lower limiting estimate of the extinction to find a lower limit on the SMBH mass, and therefore an upper limit on the Eddington ratio. The 2MASS objects have virial SMBH masses in the range 7.2$<\log_{10}[{\rm M}_{BH}]<$9.2 M$_\odot$.

As well as making virial SMBH estimates based on the broad emission line properties, for comparison I have also used the absolute R-band magnitudes (M$_R$) of the host galaxies of the 2MASS sample taken from Hutchings et al. (2003). These estimates have the advantage of being free from any degeneracies caused by the blending of the emission lines from the BLR and the NLRs of the sample. In addition, masses can be estimated for all the sources, rather than just the sources with an observable BLR. To make these estimates I used the relation given in McLure & Dunlop (2001), which takes advantage of the correlation between black hole mass and host galaxy bulge luminosity, to determine the SMBH masses.

Figure 4.17 shows the SMBH mass estimates from the R-band magnitudes plotted against the masses calculated using the properties of the BLR. In addition, I have plotted a line showing a one-to-one relationship between the black hole masses. While some objects show good agreement between the two estimates, there is a large scatter which is reflected in the uncertainty of the median ratio ($\rm M^{SMBH}_{Virial}/M^{SMBH}_{R-band}$): 0.81$\pm$0.81. In cases where the virial mass estimates are lower than the R-band estimates, orientation/geometric and/or reddening effects could potentially lead to the Balmer fluxes,

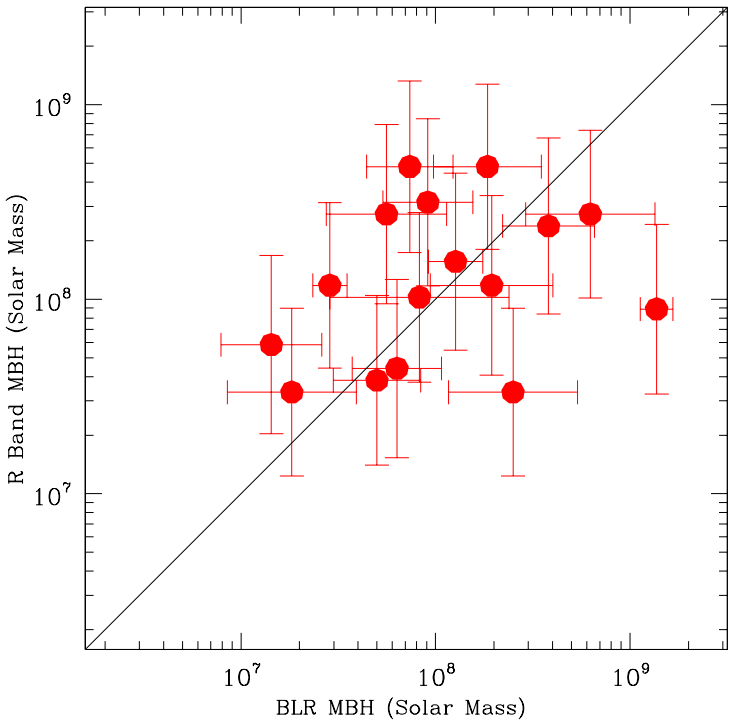

Figure 4.17: A comparison of the SMBH mass estimates for the 2MASS AGN. I plot the mass estimates based on the the R-band magnitudes against the virial mass estimates based on the broad Balmer emission lines. In addition, I have plotted a line showing a one to one relationship for the black hole masses. The mass estimates obtained from the R-band magnitudes are higher on average than those obtained from the BLR measurements.

velocity widths and SMBH masses being underestimated. Alternatively the R-band measurements may be contaminated by light from the disks of the host galaxies, leading to over-estimates of the SMBH masses. Certainly, at least one object in the sample – J1131+16 – has a strong disk component (see Chapter 3). However, in cases where the virial masses are higher, the flux of the BLR may be overestimated because of an inaccurate measurement in the broad Hα flux due to blending with the narrow Hα+[NII] lines, which could lead to an overestimation of the level of extinction.

Figure 4.18 shows the virial black hole masses plotted against $L_{[OIII]}$ for the 2MASS and comparison samples, where the uncertainties are only plotted for the 2MASS objects for clarity. I do not plot the R-band black hole mass estimates because I do not have R-band magnitudes for the comparison samples, and I want to present the comparisons between mass estimates which have been determined via the same method. In addition, Table 4.7 shows the individual SMBH masses of the 2MASS sample. Overall, from this figure it is clear that the black hole masses of the PG quasars (blue) and unobscured

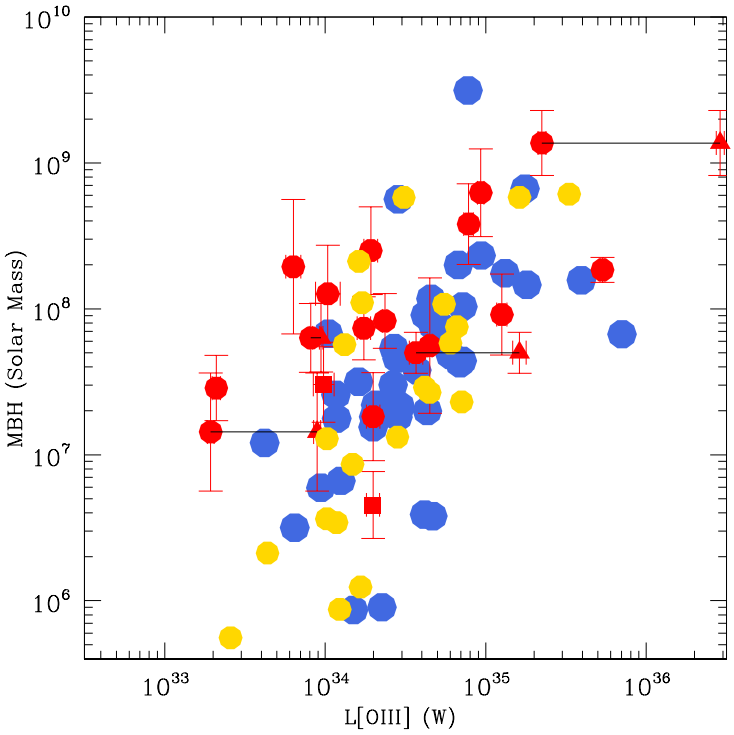

Figure 4.18: Virial black hole mass ($M_\odot$) plotted against $L_{[OIII]}$ (W). The red circles and triangles represent the 2MASS sample. Circles represent black hole masses estimated using Hβ emission and red squares are based on the Hα emission. Where possible, I correct $L_{[OIII]}$ for reddening, these estimates are represented by red triangles and are joined to their uncorrected counterparts by a straight line. The blue circles represent the black hole mass estimates of the PG sample and the gold circles indicate the type 1 AGN estimates.

Table 4.7: Virial SMBH masses and Eddington ratio results for the 2MASS sample. Values presented in brackets are for those objects where L_{BOL} has been corrected for dust extinction.

Name	M_R $Log_{10}[M_{SMBH}]$ ($M\odot$)	Virial $Log_{10}[M_{SMBH}]$ ($M\odot$)	(L_{BOL} /L_{EDD})
J0221+13[c]	8.19 ± 0.43	-	-
J0248+14	8.07 ± 0.44	7.46 ± 0.09	0.020 ± 0.005
J0306-05	8.25 ± 0.43	-	-
J0312+07	8.07 ± 0.44	8.29 ± 0.32	0.009 ± 0.001
J0400+05[a]	7.95 ± 0.44	9.14 ± 0.08	0.056(0.585) ± 0.009(0.125)
J0409+07[a]	7.58 ± 0.46	7.70 ± 0.05	0.204(0.901) ± 0.025(0.112)
J0422-18	8.01 ± 0.44	7.92 ± 0.11	0.079 ± 0.024
J0435-06	8.68 ± 0.41	7.87 ± 0.26	0.065 ± 0.003
J0447-16	8.19 ± 0.43	8.10 ± 0.11	0.023 ± 0.007
J0504-19	8.01 ± 0.44	-	-
J0910+33	7.83 ± 0.45	-	-
J1006+41[b]	7.52 ± 0.46	7.26 ± 0.10	0.302 ± 0.105
J1014+19	8.44 ± 0.42	8.80 ± 0.13	0.041 ± 0.014
J1040+59[b]	7.52 ± 0.46	8.40 ± 0.11	0.021 ± 0.007
J1057-13	7.77 ± 0.45	-	-
J1127+24[a]	7.64 ± 0.45	7.80 ± 0.10	0.036(0.041) ± 0.019(0.0010)
J1131+16	8.31 ± 0.43	-	-
J1158-30	8.25 ± 0.43	-	-
J1212-14[a]	7.77 ± 0.45	7.16 ± 0.18	0.037(0.172) ± 0.020(0.090)
J1321+13	7.52 ± 0.46	-	-
J1323-02	8.38 ± 0.42	8.58 ± 0.16	0.057 ± 0.026
J1338-04	8.50 ± 0.42	7.96 ± 0.26	0.383 ± 0.025
J1407+42	7.95 ± 0.44	-	-
J1448+44	8.44 ± 0.42	7.75 ± 0.21	0.222 ± 0.137
J1637+25[c]	8.13 ± 0.42	-	-
J2124-17	8.68 ± 0.41	8.27 ± 0.04	0.802 ± 0.068

[a] The NLR of this object has been corrected for dust extinction.
[b] M_{SMBH} and therefore L_{EDD} are calculated using broad Hα emission as opposed to Hβ.
[c] Note that the SMBH mass estimates for these objects based on the M_R magnitudes are comparable (within 2σ) twith the virial mass estimates presented in Canalizo et al. (2012) (the SMBH mass for J0221+13 is given as $Log_{10}[M_{SMBH}/M\odot] = 8.42$, and the SMBH mass for J1637+25 is given as $Log_{10}[M_{SMBH}/M\odot] = 8.62$).

type 1 AGN (gold) are generally lower than the 2MASS objects (red) of equivalent [OIII] luminosity. Potentially, this difference can be explained in terms of extinction effects: in the cases of the few objects with virial mass estimates for which I have been able to correct $L_{[OIII]}$ for extinction in the NLR, the extinction correction moves the points onto the main correlation defined by the PG quasars and unobscured type 1 objects.

Alternatively, the black hole masses of the 2MASS objects could be genuinely higher than those of the PG quasars and unobscured type 1 AGN of similar intrinsic power. In this context I note that the recent study of Canalizo et al. (2012) measured black hole masses and host galaxy properties for 29 red 2MASS AGN with $0.17 < z < 0.37$, finding that the majority of red 2MASS AGN also have significantly more massive black hole masses than the masses of black holes in local AGN. However, I remain cautious in the interpretation of the derived black hole masses for the 2MASS sample because of the uncertainty surrounding the extinction corrections.

In terms of estimating the Eddington ratio (L_{BOL}/L_{EDD}), I used $L_{[OIII]}$ to calculate the bolometric luminosities of the AGN, rather than the AGN continuum, because the [OIII] emission line is well detected in all the objects, whereas the AGN continuum emission is subject to reddening effects and potential contamination by the host stellar continuum. L_{BOL} was determined from $L_{[OIII]}$ using the relationship L_{BOL}=3500$L_{[OIII]}$ (Heckman et al., 2004). This relationship was determined by relating the mean ratio of the optical continuum and [OIII] luminosities of a large sample of type 1 AGN, to the mean ratio of the bolometric and continuum luminosities for type 1 AGN as determined in studies such as Elvis et al. (1994) and Marconi et al. (2004).

Figure 4.19 shows the Eddington ratios plotted against L_{BOL}. Once again the uncertainties are only plotted for the 2MASS objects for clarity. I present Eddington ratios for all possible objects in the 2MASS sample without correcting [OIII] for dust extinction (red circles) and, where possible, I also show the Eddington ratios following the correction of the [OIII] luminosity for dust extinction (red triangles), connecting both sets of estimates with a straight line. It is clear that, for the 4 objects in which I can measure reddening accurately, reddening has a significant effect on the Eddington ratio. There is an obvious, large scatter in Eddington ratios for all the samples: the 2MASS objects have ratios in the range: $0.009 < L_{BOL}/L_{EDD} < 0.91$. The median ratio for the 2MASS sample is 0.05±0.05, without correcting [OIII] for reddening and 0.08±0.04 in the reddening corrected case. In comparison, the PG quasar sample (blue) and the unobscured type 1 AGN sample (gold) have median ratios of 0.22±0.12 and 0.23±0.14 respectively; the large uncertainties reflect the large scatter in Eddington ratio. These ratios are all consistent within 2σ of the uncertainties. Note that, if I could correct for

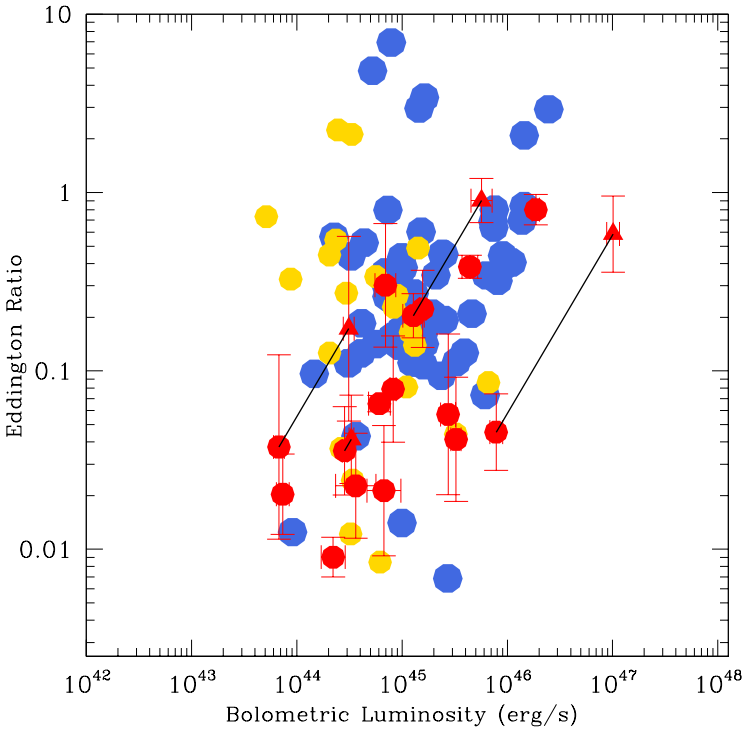

Figure 4.19: Eddington ratio plotted against L_{BOL} (erg s^{-1}) based on measurements of $L_{[OIII]}$ and virial black hole mass estimates. Red circles represent the 2MASS objects where $L_{[OIII]}$ has not been corrected for dust extinction. For objects which could be corrected for dust extinction, I represent them with red triangles and join them to their respective estimates where no correction has been made. The blue circles represent the PG quasars and the gold circles represent the unobscured type 1 objects.

NLR reddening in *all* the objects, the median ratio for the 2MASS objects would likely increase to a value closer to that measured for the PG quasar and unobscured type 1 AGN samples. Clearly, there is no evidence that the 2MASS objects have Eddington ratios that are significantly higher than those of the comparison samples.

4.5 J0400+05: a black hole recoil candidate?

The continuum of J0400+05 has an unusual shape which includes an unidentified, broad emission feature between 4200 and 5200 Å in the rest-frame (see Figure 4.5). In addition, the BLR Balmer emission in J0400+05 is significantly blue shifted by -2870±160 km s^{-1} relative to the NLR emission. Such shifts in the BLR are predicted for the recoils ('kicks') that result from the merger of two black holes (Shields & Bonning, 2008). The magnitude of the kick can be large: Dain, Lousto & Zlochower (2008) have computed kicks of up to 3300 km s^{-1}, but the most extreme kicks require black hole binaries of equal mass and spin, where the spins are extremely high. I further note that J0400+05 has the highest virial black hole mass calculated for the 2MASS sample. I note that Hutchings et al. (2003) does not detect the presence of the shifted broad line emission in J0400+05; they classify this object as a type 2 AGN.

To confirm whether J0400+05 belongs to this interesting class of objects, further observations are needed. I discuss this in Chapter 7.

4.6 Discussion

4.6.1 Moderately reddened objects

A key result from this study is that many of the red 2MASS AGN have moderate amounts of dust extinction when compared to the comparison samples ($0.2 < E(B\text{-}V) < 1.2$); the reddening values I measure are consistent with those determined for other samples of red 2MASS AGN ($0.1 < E(B\text{-}V) < 3.2$: Glikman et al. 2004, 2007, 2011 & 2012; Shi et al. 2007; Urrutia et al. 2008, 2009 & 2012; Georgakakis et al. 2009; Kuraszkiewicz et al. 2009a,b; Canalizo et al. 2012). Therefore it is possible that the 2MASS AGN have red J-K_S colours because dust extinction reduces the J-band flux relative to the K-band flux such that the F_K/F_J flux ratio is higher than a typical AGN. In Chapter 6 I show that for an AGN with intrinsic near-IR colours that are typical of the PG quasars and the unobscured type 1 AGN (J-K_S∼1.70), I require only a moderate level of reddening

of E(B-V) > 0.8 in order to give J-$K_S > 2.0$ — this level of extinction is measured for 29% of the 2MASS AGN with broad Balmer emission lines.

Rather than the red near-IR colours being a result of dust extinction from a natal cocoon of dust, it is possible that the obscuring dust is located in the outer layers of the torus, and that I am observing these objects at an angle where our line of sight grazes the edge of the torus, leading to the observed red colours. However, such modest levels of reddening could also be produced by dust on a kpc-scale in the disks of the host galaxies.

Alternatively, rather than moderately extinguished AGN, it is possible that some of these objects are genuine type 2 objects in which the torus completely extinguishes the broad-line AGN in the optical and shorter wavelength near-IR bands. In this case, the level of extinction is expected to be much higher ($A_V > 10$) than that indicated by the Balmer decrements in the NLR because, while the SMBH and BLR are completely obscured at optical wavelengths by the torus, the NLR extends beyond the scale of the torus and is therefore relatively unaffected. In this case, due to the much higher levels of extinction caused by the torus, their J-K_S colours should be much redder than is observed. Indeed, I find that $A_v > 5$ would produce J-$K_S > 3.00$, a level only found for the type 2 2MASS object J1307+23 (excluded from the main study of this chapter), but not for any of the other type 2 objects in the sample. However, the integrated near-IR colours of the heavily extinguished type 2 objects could be made bluer if the host galaxies make a significant contribution in the near-IR, because the colours of typical unreddened stellar populations are relatively blue at such wavelengths.

Finally, I note that dust extinction is not the only explanation for the red near-IR colours of the 2MASS objects. Some objects in the sample show relatively modest levels of extinction based on their BLR Balmer decrements, and have optical continuum shapes that appear similar to UV/optical selected AGN (e.g. J2124-17). Rather than moderate levels of dust extinction in such cases, a relatively large covering factor for the hot dust ($T \sim 1500$K) could also result in red J-K_S colours. Emission from hot dust in the torus becomes significant at wavelengths which coincide with the K-band. Therefore, a larger than average covering factor for this hot dust could increase the flux measured in the K-band relative to that of the J-band (likely dominated by accretion disk emission), thus producing the red J-K_S colours measured for the 2MASS sample.

All of these possibilities will be explored further in the next two chapters, where I will model the near- to mid-IR SEDs of the 2MASS objects with varying the level of extinction, dust covering factors and host galaxy contributions.

4.6.2 Young, dust enshrouded objects

As discussed in Chapter 1, there have been several studies of red 2MASS AGN in the past that have focussed on different wavelength regions of the SEDs of the population (e.g. X-ray, UV, optical or IR). In this section I outline the basic results and conclusions of these studies, and compare them with the results obtained in this chapter, in order to determine the nature of the red, low-z, 2MASS AGN sample. The basic properties of the samples used for the previous studies are summarised in Table 1.1 in Chapter 1.

Many of these past studies conclude that the red 2MASS quasars are young, dust-enshrouded, transitional objects. This conclusion is based on several lines of evidence, including a high rate of morphological disturbance of the host galaxies (Urrutia, Lacy & Becker, 2008), a relatively high rate of occurrence low ionization broad absorption lines (LoBALs; Urrutia et al. 2009), evidence for enhanced star formation rates compared to typical UV/optical selected AGN (Shi et al. 2007; Georgakakis et al. 2009), and high Eddington ratios for the gas being accreted by the central super-massive black holes (Urrutia et al., 2012).

In contrast, although the results from the local 2MASS AGN sample agree with the these previous studies in the sense that I determine the same moderate levels of reddening, I find no strong evidence that these are young quasars based on their [OIII] outflow properties, the incidence of NLS1, and the distribution of Eddington ratios. Indeed, the properties the 2MASS sample appear similar to those of the samples of UV/optical selected quasars in the local Universe.

The apparent discrepancy between the conclusions of the study and the previous studies that identify the red 2MASS objects as young, transition objects may be due to different selection criteria. In particular, the Glikman et al. (2004, 2007, 2011, 2012), Georgakakis (2009) and Urrutia et al. (2008, 2009, 2012) samples extend up to much higher redshifts than the local sample, include optical colour selection criteria as well as near-IR colour selection, and some require the objects to have broad lines; in addition, Glikman et al. (2004, 2007, 2011, 2012) require detection of the objects in the FIRST radio survey. Such selection criteria favour more extreme objects that are more likely to be genuinely young and dust enshrouded.

In this context it is notable that other studies of 2MASS AGN which are based on lower redshift samples and/or samples selected without additional optical colour criteria (the bottom four entries in Table 1.1), agree with with the conclusions of this investigation, albeit using different analysis techniques:

- Kuraszkiewicz et al. (2009a) study the SEDs (from X-ray to FIR), and find that

the 2MASS AGN colours are strongly affected by reddening, host galaxy emission, the redshift of the AGN and scattered AGN light;

- using Principle Component Analysis (PCA) Kuraszkiewicz et al. (2009b) find that the first four eigenvectors (which explain 70% of the variance in the sample) correlate with ratios of the intrinsic X-ray flux to the observed optical/IR fluxes (i.e. the intrinsic absorption), the optical/IR colours and optical spectral type, X-ray and optical reddening indicators, and the degree of polarization of the dust respectively;

- using I-band HST images to study the host galaxies of red 2MASS AGN, and comparing their findings to the PG quasars and a sample of Ultraluminous Infrared Galaxies (ULIRGs), Marble et al. (2003) find no indication that red 2MASS AGN represent young, dust enshrouded, transitional objects based on the similarities of the variety of morphologies, luminosities, and dynamical states of the host galaxies between their sample and the PG quasars;

- by comparing optical broad-band polarimetry results of red 2MASS AGN, PG quasars and BAL AGN, Smith et al. (2002) find that overall 2MASS AGN show relatively high levels of polarization (P $>$ 3%), consistent with the idea that orientation/obscuration effects are responsible for the red NIR colours.

These comparisons between the previous studies of the red 2MASS AGN emphasise the sensitivity of the conclusions to the precise selection criteria employed for the particular samples. However, it is seems unlikely that the majority of low redshift 2MASS AGN that are selected solely on the basis of near-IR colour [$(J - K) \geq 2$] are young, transitional objects.

4.7 Conclusion

In this chapter I have presented a study of the optical spectra of the red 2MASS-selected AGN. I compare the results from this sample with those obtained for comparison samples of PG quasars and unobscured type 1 AGN. I find the following.

- Overall the local 2MASS AGN population show significantly higher reddening than samples of UV/optical selected AGN. However, while some objects are highly reddened (E(B-V)=1.2), others show relatively little (if any) reddening.

- The velocity shifts and widths of the [OIII] lines of the red 2MASS AGN are not significantly larger than those of the comparison samples.

- The Eddington ratios of the 2MASS AGN and the incidence of NLS1 type objects are comparable with those of 'typical' AGN.

These results do not support the view that the local red 2MASS AGN represent young quasars in a transitional phase, where the AGN are emerging from their natal cocoons of gas and dust. However, they are consistent with the idea that these objects are reddened either by obscuring dust in the outer layers of the circum-nuclear torii, or by dust in the kpc-scale disks of the host galaxies.

In the next two chapters I will focus on the near-IR properties of this sample of red 2MASS AGN, and investigate the origin of their red J-K_S colours.

Chapter 5

An infrared photometric study of red, 2MASS-selected AGN in the local Universe

5.1 Introduction

The infrared is one of the most beneficial wavelength ranges for investigating AGNs and starbursts. This is primarily because of the reduced effects of dust extinction at these wavelengths. In addition, the thermal IR emission represents the emission that is absorbed and then re-radiated by dust, indirectly sampling the radiative power of the active core, and any starburst component that may be present. Therefore, studying the 2MASS AGN at IR wavelengths allows detailed investigation of the intrinsic properties of the AGN, and good comparisons with UV/optical selected AGN.

In Chapter 4, I showed that, based on their optical spectra, many of the red 2MASS AGN are moderately reddened when compared to the optical spectra of the AGN in the comparison samples ($0.2 < \mathrm{E(B\text{-}V)} < 1.2$). In such cases, dust extinction reduces the J-band flux relative to the K_S-band flux such that the F_K/F_J flux ratio is higher than a typical AGN. However, dust extinction is not the only explanation for the red near-IR colours of the 2MASS objects. Some objects in the sample show relatively modest levels of extinction based on their BLR Balmer decrements (e.g. J0221+13), and/or have optical continuum shapes that appear similar to UV/optical selected AGN (e.g. J2124-17).

Rather than moderate levels of dust extinction, a relatively large covering factor for the hot, circum-nuclear dust ($T \sim 1500$K) could also result in red J-K_S colours. Emission

from hot dust in the torus becomes significant at wavelengths which coincide with the K_S-band, and is also strong at mid-IR wavelengths. Therefore, a larger than average covering factor for this hot dust could increase the flux measured in the K_S-band relative to that of the J-band (likely dominated by accretion disk emission), thus producing the red J-K_S colours measured for the 2MASS sample. Note that, although emission from the circum-nuclear dust structures is likely to make a contribution to the continuum of AGN in the longer near-IR wavelengths, and the mid-IR, dust heated by stars may make a significant contribution, especially at the longer mid-IR wavelengths.

In this chapter I present the analysis of the near- to mid-IR properties of the 2MASS AGN and the comparison samples, using data from both 2MASS and WISE. I first investigate the near- to mid-IR colours of the samples and determine how important dust extinction is in producing these colours. I also determine whether AGN type has a significant effect on the near-IR colours. In addition, I plot the mid-IR luminosities of each object against their [OIII] emission line luminosities. This is to investigate whether the mid-IR emission of the 2MASS sample can be explained by an unusually high torus dust covering factor. Finally, I plot the near- to mid-IR SEDs of the 2MASS sample to investigate whether the full SEDs of these objects provide more detailed information, which may help to explain any observed trends in the proceeding sections.

5.2 Colour plots

The red 2MASS AGN were selected with colours J-$K_S > 2.0$ and $K_S < 15.0$, distinguishing them from most optical/UV selected AGN which have near-IR colours J-$K_S < 2.0$ (Cutri et al., 2002). In Figure 2.1 in Chapter 2 I plotted the J-K_S colours against the J-band magnitude for the 2MASS sample and the comparison samples. It is clear from Figure 2.1 that there are a few objects in the comparison samples that also have J-K_S colours greater than 2.0, implying that some of the objects in the comparison samples could be similar to the red 2MASS AGN. This suggests that there may be similar processes taking place in some UV/optical selected AGN which result in red J-K_S colours in these objects. I give the survey coverage and median J-K_S colours for each sample in Table 5.1.

There are various factors which may affect the near-IR colours of AGN. These include the following.

- **Dust extinction.** It is possible that the AGN have red J-K_S colours because dust extinction reduces the J-band flux relative to the K_S-band flux, such that the

Table 5.1: 2MASS and WISE coverage, and J-K_S colours of the 2MASS AGN and comparison samples. The 'Reference' column gives the key paper for the samples.

Sample	J-K_S(Median) z < 0.2	2MASS Coverage	WISE Coverage	Reference
2MASS	2.13±0.07	100%	96%	Chapter 4
PG Quasars	1.79±0.03	100%	100%	Boroson & Green (1992)
Unobscured Type 1	1.60±0.04	92%	98%	Jin et al. (2012a)
12 Micron	1.52±0.05	94%	94%	Rush et al. 1993
2Jy	1.38±0.09	78%	91%	Dicken et al. (2008)
3CRR	1.23±0.09	95%	95%	Dicken et al. (2010)

F_K/F_J flux ratio is higher than in a typical AGN.

- **Covering factor of dust radiating at mid-IR wavelengths.** A relatively large covering factor for the hot dust (T $\sim$ 1500K) could also result in red J-K_S colours. Emission from hot dust in the torus becomes significant at wavelengths which coincide with the K_S-band. Therefore, a larger than average covering factor for this hot dust could increase the flux measured in the K_S-band relative to that of the J-band, that is likely to be dominated by accretion disk emission.

- **Host galaxy contamination.** In addition to the intrinsic AGN properties, emission from the host galaxy may also be important in determining the observed J-K_S colours of AGN. If the AGN does not dominate the emission at near-IR wavelengths, then the host galaxy will make a significant contribution to the observed flux, affecting the J-K_S colours.

- **Redshift.** An important feature of the SED of an AGN is found at near-IR wavelengths: the point of inflection. The point of inflection marks the boundary between the wavelength regions in which the accretion disk and thermal dust emission dominate (Neugebauer et al. 1987; Saunders et al. 1989). At low redshifts the accretion disk dominates the J-band flux of the AGN, whereas emission from hot dust in the torus dominates in the K_S-band. At higher redshifts the point of inflection will be shifted towards longer wavelengths, and therefore the emission from the accretion disk will be shifted into the K_S-band, having an impact on the observed J-K_S colours.

So far, the approach used in this thesis to determine the nature of the red 2MASS AGN, has focussed on their optical spectra. However, the recent availability of data from

the WISE catalogue (see Tables 2.1&2.2 in Chapter 2), coupled with the data obtained from 2MASS, makes it possible to study the red 2MASS AGN at longer wavelengths (near- to mid-IR). It is important to establish whether the red colours extend to longer wavelengths for the 2MASS AGN, or whether this is only observed in the 2MASS bands, where the near-IR point of inflection is located. In addition, it is necessary to compare the mid-IR colours of the red 2MASS AGN to those of the comparison samples, in order to determine whether the 2MASS AGN simple represent 'typical' UV/optical selected AGN seen through a higher column of dust.

To determine whether the unusual colours of the 2MASS sample are reflected at longer wavelengths, I plot longer wavelength colours (e.g. 2.17-3.4μm etc.) against J-K_S for each sample in Figures 5.1(a)-(d). Note, I do not present a H-K_S colour plot, because the H-K_S colours correlate with the J-K_S colours too closely for there to be any noticeable differences from the trends visible in Figure 5.1. Also, I only plot objects in the 2MASS and comparison samples which have redshifts < 0.2, in the interest of completeness. The HII composite objects of the 2MASS sample identified in Chapter 4 are indicated separately (red crosses), this is because my aim is to concentrate on the AGN objects in the 2MASS sample. Finally, as a follow up to the analysis of J1131+16 in Chapter 3, I distinguish J1131+16 and the AGN with strong FHILs from the rest of the AGN (using triangles instead of circles).

In addition to the AGN samples, I plot a reddening line to demonstrate how reddening can effect the near- to mid-IR colours of a typical UV/optical selected AGN. This line has been shifted away from the data points to make the plots clearer. Conversions in extinction curve between the V band to the near-IR bands are based on the work of Flaherty et al. (2007) and Nishiyama et al. (2008).

I also plot the colours of both an elliptical galaxy (red square) and a late-type (Sbc) spiral galaxy (blue square) at the median redshift of the 2MASS sample. This is to demonstrate how the host galaxy can have an effect on the IR colours of AGN. The colours of the quiescent galaxies were calculated using the galaxy templates of Assef et al. (2010), presented in Figure 5.2, and the modelling technique that is described in Chapter 6.

In addition, I plot the colours of an accretion disk (violet square) whose flux is described by $F(\nu)_{ACC} \propto \nu^{1/3}$, in order to demonstrate the colours of an AGN that lacks any emission from a host galaxy, as well as dust radiating at mid-IR wavelengths. The accretion disk is also modelled at the median redshift of the 2MASS sample. Finally, I also plot the colours produced by black-body emitters at temperatures of 1200K (blue asterisk), 1500K (green asterisk) and 1800K (red asterisk), to represent dust heated to

these temperatures. Black-body emitters at higher temperatures produced colours which were too blue to be plotted within the axes ranges on Figures 5.1(a)-(d). In addition, for the range of temperatures used in this study, the 4.2-12 and 12-22μm colours were too blue to be plotted on Figures 5.1(c)&(d). Once again, these emitters are modelled at the median redshift of the 2MASS sample.

Comparison with the PG quasars and Unobscured type 1 AGN

2.17-3.4μm, Figure 5.1(a). In general, in this figure the 2MASS AGN are only significantly redder than the comparisons samples in J-K_S colour space. When their 2.17-3.4μm colours are compared to those of the UV/optical selected AGN, there are no significant differences. This is reflected in the median values for the 2.17-3.4μm colours presented in Table 5.2. It is possible that the lack of difference in the 2.17-3.4μm colours could be due to the mid-IR flux contribution from the host galaxies of the 2MASS AGN making the AGN colours bluer. It is clear from the reddening line that high levels of dust extinction will make the J-K_S colours of an AGN redder than when compared to their effect on the 2.17-3.4μm colours. Therefore reddening, coupled with the emission from the host galaxy, could result in these colours of the 2MASS AGN.

Despite the similarity in the median 2.17-3.4μm colours between the 2MASS and comparison samples, it is notable that a significant fraction of the 2MASS objects (25% out of the 28 objects with available WISE magnitudes) are bluer in their 2.17-3.4μm colours when compared to the rest of the 2MASS sample (2.17-3.4μm < 1.3 magnitudes), yet have similar red J-K_S colours. These objects are J0409+08, J0435-06, J1014+19, J1127+24, J1212-14, J1323-02 and J1448+44; they are all type 1 objects, together comprising 44% of the type 1 objects in the 2MASS sample. Note that there is nothing unusual about the optical spectra of these objects as a group when compared to the spectra of the other red 2MASS AGN (e.g. there is no higher incidence of FeII emission). This combination of red J-K_S and blue 2.17-3.4μm colours cannot be explained in terms of reddening of the SED of a 'typical' UV/optical selected AGN, or by host galaxy contamination, but must relate to the intrinsic SEDs of the AGN. It is possible that the unusual colours of these objects are the result of *an additional component* of hot dust which may not be associated with the torus (Mor, Netzer & Elitzur, 2009). Dust is expected to sublimate at temperatures $\sim$1500 K (Barvainis 1987; Laor & Draine 1993). Therefore, if the emission is in the form of a black body this will peak at a wavelength of 1.93μm, or at 2.21μm at the median redshift of the sample (z=0.143$\pm$0.009), corresponding to the K_S-band. While a significant proportion of the PG quasars (29%) and

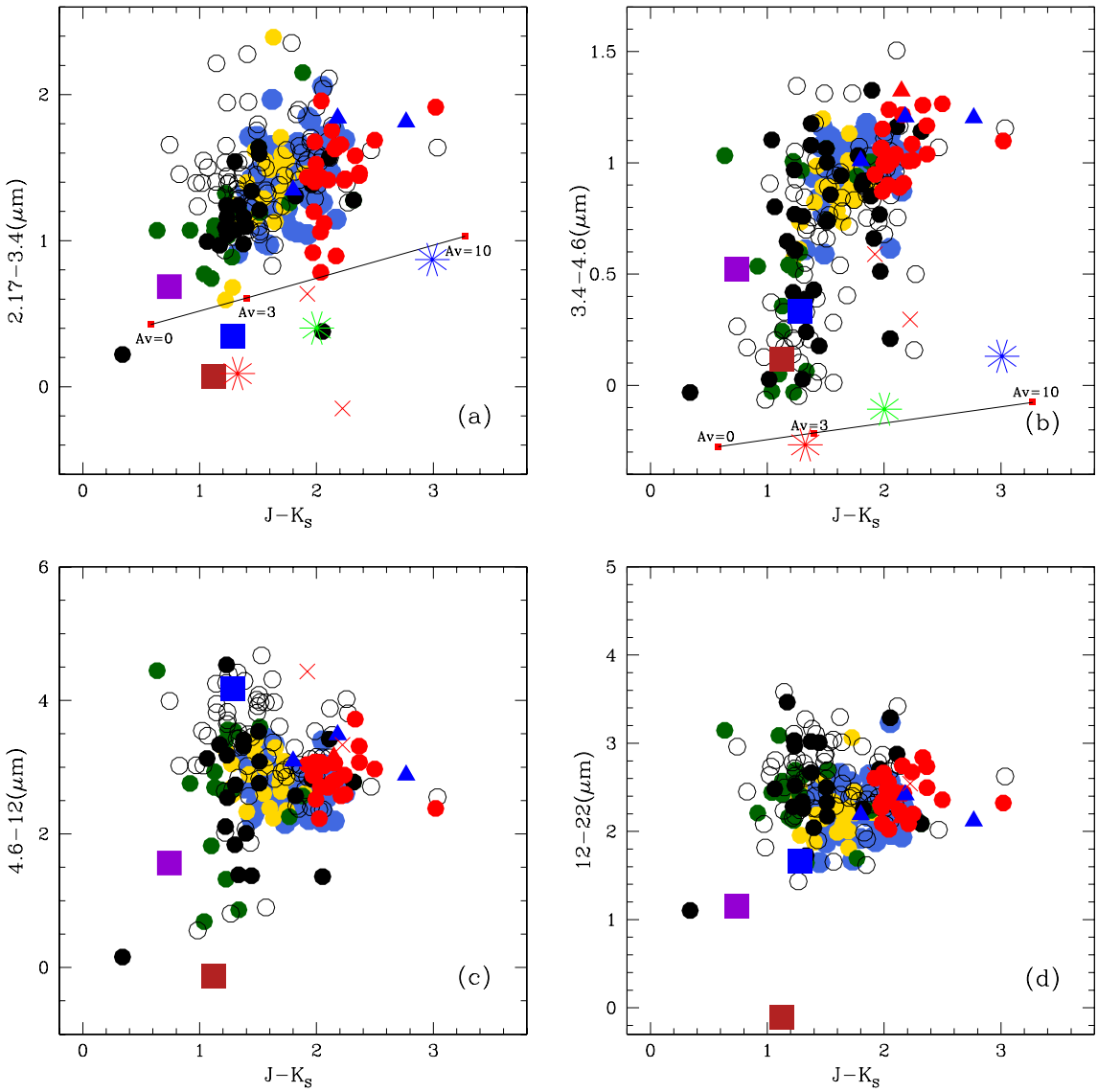

Figure 5.1: Colour-colour diagrams plotting (a) 2.17-3.4μm, (b) 3.4-4.6μm, (c) 4.6-12μm and (d) 12-22μm against J-K$_S$$\mu$m for all the samples. The red 2MASS AGN are represented by red circles, PG quasars by blue circles, the unobscured type 1 AGN population are represented in gold, 2Jy sample in black, the 3CRR sample in green and the 12 μ Seyfert galaxies are represented by unfilled circles. J1131+16 is represented by a red triangle, and III Zw 77, Tololo 0109-383 and ESO 138 G1 are represented by blue triangles. The HII composite objects in the 2MASS sample are represented by red crosses. The template elliptical galaxy is represented by a red square, Sbc galaxy by a blue square, accretion disk emission by a violet square, and the 1200K, 1500K and 1800K black-body emitters are represented by blue, green and black asterisks respectively. In addition I plot a reddening line on plots (a) and (b) to demonstrate how reddening can effect the near- to mid-IR colours of the AGN.

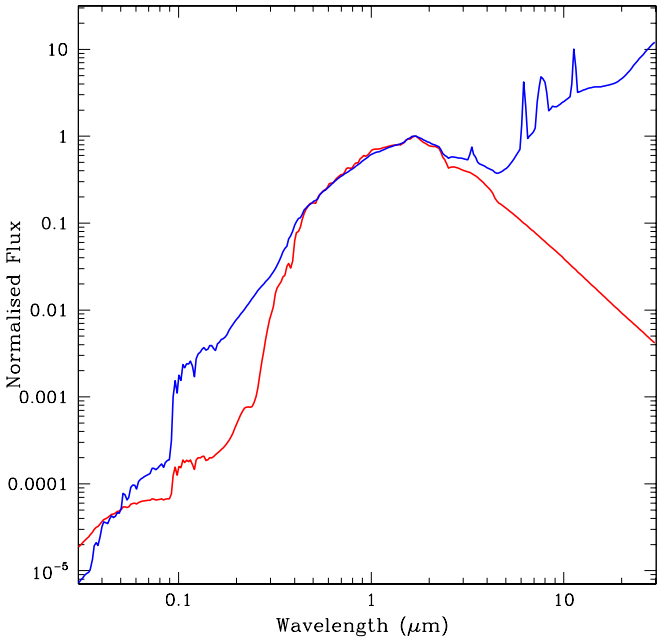

Figure 5.2: The normalised elliptical (red line) and Sbc type spiral (blue line) galaxy SED templates taken from Assef et al. (2010). Note the dominant emission of the spiral galaxy at longer wavelengths when compared to the elliptical galaxy. This is due to dust emission from star formation regions in the host galaxies.

Table 5.2: The median near- to mid-IR colours of all the samples across the 2MASS and WISE bands. Medians for the PG quasar and unobscured type 1 AGN samples have been presented for both the full samples, and redshift limited samples (z<0.2). The uncertainties are the standard errors on the medians.

Sample	K_S-W1 (2.17-3.4μm)	W1-W2 (3.4-4.6μm)	W2-W3 (4.6-12μm)	W3-W4 (12-22μm)
2MASS AGN	1.44±0.09	1.04±0.04	2.92±0.08	2.44±0.12
PG	1.43±0.03	0.97±0.01	2.69±0.04	2.27±0.04
Unobscured Type 1	1.40±0.08	0.85±0.03	2.84±0.07	2.21±0.03
12 Micron	1.45±0.03	0.75±0.04	3.22±0.08	2.55±0.04
2Jy	1.19±0.07	0.76±0.08	2.80±0.21	2.49±0.11
3CRR	1.09±0.08	0.57±0.10	2.73±0.23	2.43±0.09

unobscured type 1 AGN (43%) also have blue 2.17-3.4μm colours, their J-K_S colours are also blue when compared to the 2MASS AGN. This suggests that, rather than these PG quasars and unobscured type 1 AGN also having an additional component of hot dust emission, it is more likely that their SEDs are intrinsically bluer than other AGN.

3.4-4.6μm, 4.6-12μm and 12-22μm, Figures 5.1(b)-(d). Once again, at these wavelengths, when compared to most of the radio-quiet AGN, the 2MASS AGN have a comparable *range* of colours. However, in the 3.4-4.6μm colours, there are 5 2MASS objects (21% out of the 24 $z < 0.2$ 2MASS objects with available WISE magnitudes) with redder colours (3.4-4.6μm > 1.2) when compared to both the rest of the 2MASS sample, and the type I comparison samples. All of these 6 2MASS objects are type 2 AGN. This suggests that AGN orientation and/or high levels of dust extinction due to the torus may have a significant role in determining the near- to mid-IR colours of AGN at these wavelengths. The fact that these type 2 objects showing red 3.4-4.6μm colours are not redder in J-K_S — as would be expected from the reddening line — may be due to significant contamination from the stellar populations of host galaxies at near-IR wavelengths. This is discussed further in § 5.2.1.

Overall, the comparisons with the PG quasars and unobscured type 1 AGN suggest that the combination of moderate/high levels of dust extinction, and host galaxy emission play a crucial role in determining the near- to mid-IR colours of the 2MASS AGN.

Comparison with other AGN samples

2.17-3.4μm, Figure 5.1(a). When compared to the radio-loud AGN, the 2MASS objects are clearly redder in this colour. This is reflected in Table 5.2: the median 2.17-

3.4μm colour is comparable to all the radio-quiet samples, whereas the radio-loud samples have much bluer ($>2\sigma$) median colours. This is likely due to the greater contribution from the host galaxies of the radio-loud AGN in these bands, because most of the radio galaxies are NLRGs, or WLRGs. Indeed, the colours of the template quiescent galaxies are significantly bluer than the AGN presented in Figure 5.1(a). Therefore, the more dominant the emission from the host galaxy, the bluer the near- to mid-IR colours will become.

3.4-4.6μm, Figure 5.1(b). When compared to the radio-loud AGN, and a significant fraction of the 12μ Seyfert galaxies, the 2MASS AGN are redder in colour in this plot. Again, this is likely due to the greater contribution of the host galaxies of the radio-loud AGN in these bands. Once more this is supported by the colours of the template quiescent galaxies.

4.6-12μm, Figure 5.1(c). Overall, the majority of all the comparison samples are comparable to the 2MASS AGN in this colour. This is reflected in the medians presented in Table 5.2. It is likely that at these wavelengths the AGN dominate over their host galaxies. However, there is a small fraction of radio-loud and 12μ Seyfert galaxies which still have large contributions from their host galaxies. The elliptical galaxy template shows a particularly blue 4.6-12μm colour, supporting this argument.

The most significant difference in these colours (4.6-12μm) is between the 12μ Seyfert galaxies and the rest of the samples. The 12μ Seyfert galaxies appear to have significantly stronger 12μm band fluxes than the other samples. This is possibly because they were selected using the 12μm IRAS band (see Chapter 2): IRAS was less sensitive than WISE at mid-IR wavelengths, and therefore these IRAS-selected AGN may have stronger 12μm fluxes when compared to other AGN, and hence redder 4.6-12μm colours. The emission in the 12μm band is possibly due to emission from dust heated by young stars (emission of this type is expected at longer wavelengths in galaxies where young stars are present; Law, Gordon & Misselt 2011). This is supported by the similarity to the colour of the template Sbc galaxy, that shows a much redder 4.6-12μm colour when compared to the AGN populations, and that of the elliptical galaxy, thus suggesting that these AGN reside in a late-type galaxy. Such dust emission could dominate over the continua of highly obscured (type 2) AGN, as well as LINERs. Alternatively, the sample could be biased towards objects that are stronger at 12μm than the other samples, because of reddening, or a specific dust distribution in the torus.

12-22μm, Figure 5.1(d). The trends seen in this colour space are similar to those above, however there is less evidence for host galaxy flux contribution. Some of the 12μ Seyfert galaxies still appear redder than the rest of the samples, as reflected in the

Table 5.3: The median near- to mid-IR colours of all the AGN types across the 2MASS and WISE bands. Again, the uncertainties are the standard errors on the medians. Note that the types 'Broad Line' and 'Narrow Line' refer to the broad and narrow line objects in the *comparison* samples, whereas 'BL 2MASS' and 'NL 2MASS' refer to the broad and narrow line objects in the 2MASS sample.

Type	J-K_S (1.25-2.17μm)	K_S-W1 (2.17-3.4μm)	W1-W2 (3.4-4.6μm)	W2-W3 (4.6-12μm)	W3-W4 (12-22μm)
Broad Line	1.73±0.02	1.46±0.02	0.97±0.01	2.78±0.03	2.35±0.02
Narrow Line	1.47±0.07	1.39±0.05	0.86±0.06	3.27±0.10	2.69±0.05
LINER	1.42±0.12	1.24±0.18	0.30±0.07	3.70±0.29	2.26±0.14
WLRG	1.30±0.11	1.07±0.09	0.33±0.07	1.92±0.23	2.23±0.15
BL 2MASS	2.05±0.07	1.42±0.08	1.01±0.02	2.84±0.06	2.34±0.04
NL 2MASS	2.28±0.12	1.64±0.07	1.22±0.03	3.00±0.13	2.57±0.08

medians presented in Table 5.2, where the median colour of the 12μ Seyfert galaxies is redder overall. In these cases it is likely that the emission detected in the 22μm band is a combination of flux from dust heated by the AGN, and emission from the host galaxy.

5.2.1 AGN type

Can the trends described above be explained in terms of AGN orientation effects? The orientation of an AGN may have a significant affect on its colours. If viewed face on, any emission from the host galaxy (either from stars or from dust in the ISM) may be outshone by the AGN if its luminosity is high enough. But, as the inclination of the AGN becomes more edge on, emission from the host galaxy will play a key role in determining the colours of the AGN, because the AGN continuum will be obscured by high levels of dust extinction from the torus ($>$ A_V 10).

In this section I plot the same data as in Figures 5.1(a)-(d), however I divide the samples into their spectral types, which, according to the unified schemes, are related to the orientation of the torus relative to the line of sight. In addition, I present the median colour values of the AGN types in Table 5.3. All broad-line objects are plotted in blue, narrow-line objects in red, LINERs/HII region type in green and WLRGs in yellow. Also, I have circled the 2MASS AGN in the plots for clarity.

2.17-3.4μm, Figure 5.3(a). From Figure 5.3(a) it is clear that, overall, ignoring the 2MASS objects, the narrow-line, weak-line and LINER objects are bluer in both their 1.25-2.17μm and 2.17-3.4μm colours when compared to the broad-line objects. This is reflected in their median colour values presented in Table 5.3, and can be explained by

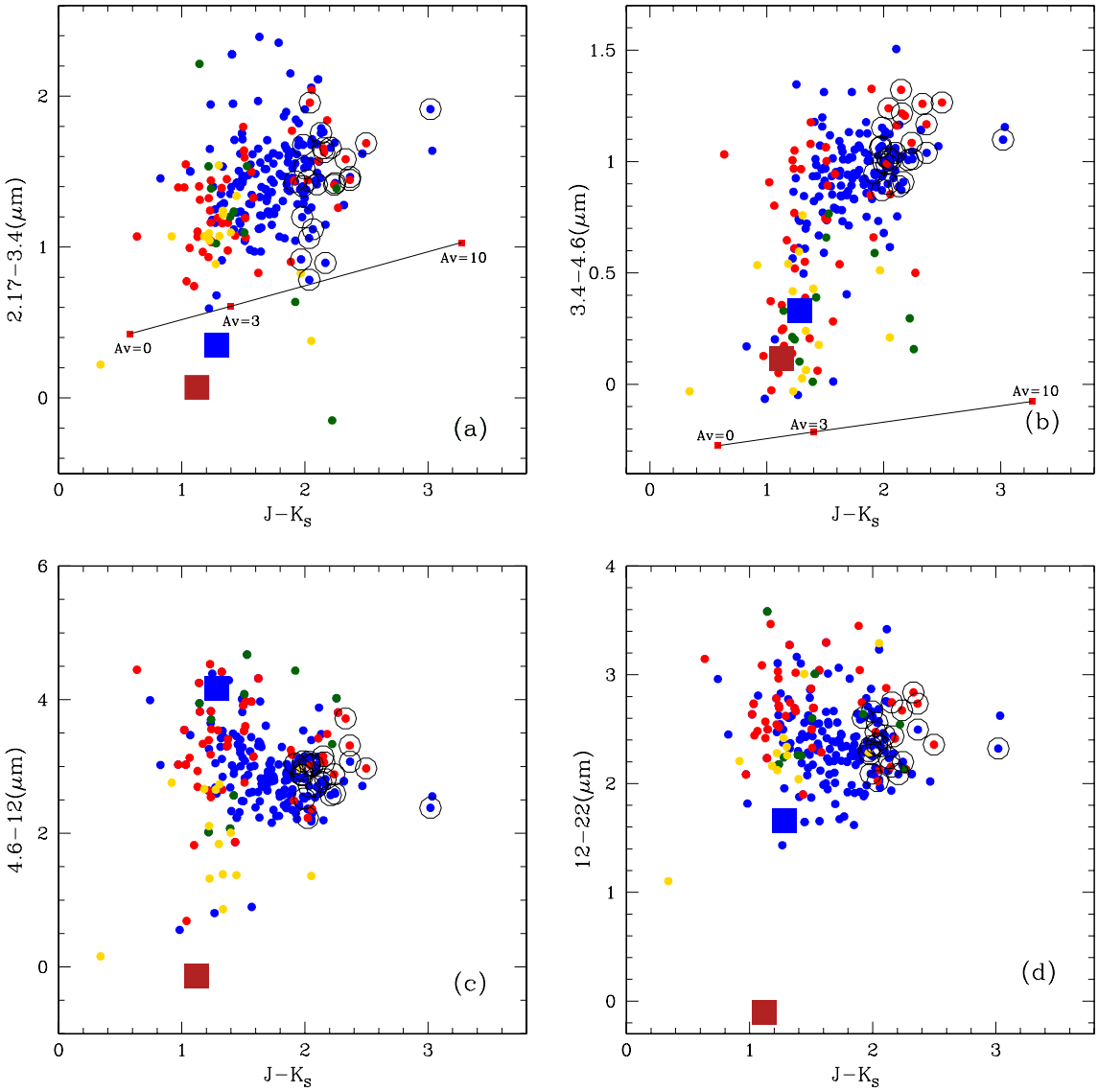

Figure 5.3: Presented here are similar colour-colour plots to Figures 5.1(a)-(d), however the samples are divided by AGN type. All broad-line objects are plotted in blue, narrow-line objects in red, LINERs/HII region type in green and WLRGs are plotted in yellow. The template elliptical galaxy is represented by a red square and Sbc galaxy by a blue square. In addition, I have circled the 2MASS AGN on the plots to determine whether type plays a significant role in the colours of these objects as well.

the contamination of emission from the host galaxies in the shorter wavelength bands: the host galaxy emission is more important at these wavelengths in narrow-line objects than in broad-line objects. This is supported by the colours of the template quiescent galaxies in Figure 5.3(a), which also have bluer 2.17-3.4μm colours when compared to the broad-line AGN.

The narrow-line 2MASS objects however have significantly redder 2.17-3.4μm colours when compared to the majority of AGN, including many of the type 2 objects from the comparison samples, this is also reflected in the mid-IR colours of the AGN types in Table 5.3. It is likely that the red colours of the narrow-line objects in the 2MASS sample are the result of high levels of dust extinction (> 10 A_V), which have a noticeable effect on the emission from the AGN at all wavelengths. As mentioned previously, the fact that there is a little difference between the J-K_S colours of the 2MASS narrow-line and broad-line objects may be the result of more dominant host galaxy emission in the narrow-line objects at the shorter wavelengths (otherwise the J-K_S and other mid-IR colours of the 2MASS narrow-line objects would be much redder than the 2MASS broad-line objects). This is modelled in Chapter 6.

3.4-4.6μm, Figure 5.3(b). In a similar manner to what is observed in Figure 5.3(a), it is clear from Figure 5.3(b) that overall the narrow-line, weak-line and LINER objects are bluer than the broad-line objects. Once again, this can be explained by contamination from the host galaxies at shorter wavelengths. Also as observed in Figure 5.3(a), the 2MASS objects whose optical spectra are consistent with the properties of narrow-line AGN appear to have redder 3.4-4.6μm colours than their broad-line counterparts.

4.6-12μm, Figure 5.3(c). In 4.6-12μm colour space, both the narrow-line and LINER type objects appear redder than the broad-line objects, again supporting the view that torus obscuration is important in producing the red near-IR colours of these objects. I note that from Figure 5.1(c) most of narrow-line and LINER objects are drawn from the 12μ Seyfert galaxy sample. This, along with the 4.6-12μm colour indicated by the template Sbc galaxy suggests that it is likely the red 4.6-12μm colours of these objects are due to high levels of extinction (possibly due to the torus) coupled with emission from starburst heated dust in the host galaxy.

Conversely, the weak-line objects appear bluer in this colour space. In WLRGs the activity of the central AGN is low, either due to low accretion leading to a low-luminosity AGN, or the AGN having recently switched off (Tadhunter et al., 1998), thus the AGN does not illuminate the surrounding toroidal dust. Alternatively, the torus does may not actually exist in WLRGs (Hardcastle, Evans & Croston, 2007), resulting in very little dust emission in these objects. Therefore the flux is dominated by the host

elliptical galaxy. Again the narrow-line 2MASS objects are redder than their broad-line counterparts.

12-22μm, Figure 5.3(d). Like in 4.6-12μm colour space, both the narrow-line and LINER type objects of the comparison samples are redder than the broad-line objects in 12-22μm colour space. In addition, the weak-line objects are comparable with the broad-line objects in this colour space. However in the case of the 2MASS AGN, unlike at other wavelengths, the narrow-line and broad-line 2MASS objects have a comparable range of 12-22μm colours. This highlights the fact that both host galaxy emission, and dust extinction, are less important than AGN illumination at these wavelengths in the 2MASS AGN.

5.2.2 Summary

The trends seen in Figures 5.1(a)-(d) and 5.3(a)-(d) for the 2MASS AGN suggest that there are two main processes which result in their red near-IR colours: combined moderate/high levels of dust extinction with host galaxy contamination, and emission from an additional hot dust component.

In the cases where the red near-IR colours are due to dust extinction, the mid-IR colours of the narrow-line objects are consistently redder than the broad-line objects. This suggests that the narrow-line objects are subject to higher levels of extinction (probably by the torus) when compared to the broad-line objects, and that the emission from the AGN is extinguished such that the host galaxy can provide sufficient emission, such that the near-IR colours do not deviate greatly from those of the broad-line objects.

44% of the broad-line 2MASS AGN have blue 2.17-3.4μm colours when compared to the rest of the 2MASS AGN, despite their red J-K_S colours. This is consistent with there being an additional component of hot dust dominating at K_S-band wavelengths in these objects.

5.2.3 J1131+16 and the other FHIL objects

Following on from Chapter 3, it is also interesting to consider the behaviour of J1131+16 and the other FHIL objects on the colour-colour plots. Generally, the FHIL objects are similar to the reddest objects of the 2MASS sample in the 2.17-3.4μm, 4.6-12μm and 12-22μm vs. 1.25-2.17μm colour plots. However, in 3.4-4.6μm colour space J1131+16 is the reddest 2MASS object. Also, I note Tololo 0109-383 and ESO-138-G1 show very red colours in 3.4-4.6μm colour space when compared to other AGN. Therefore, it is possible

that there is a substantial amount of dust that is emitting at a temperature that peaks in the 4.6μm band, and the associated ISM has physical conditions which also allows for the emission of FHILs in these objects.

Assuming this material behaves as a black body, at the redshift of J1131+16 I calculate a black-body temperature of $\sim$740 K, that corresponds to a distance range of $4.4 < r < 7.9$ pc following the arguments in $\oint$ 3.5.4 in Chapter 3. This radius range is consistent with the radii computed using the ionization parameter and luminosity determined in Chapter 3; it is also consistent with observational estimates of the size of the torus in nearby AGN, based on IR interferometry (e.g. Haschick et al. 1994; Chou et al. 2007; Tristram et al. 2007a), suggesting that this material is possibly part of the torus. Also, this dust component must outshine any dust on a smaller scale that might be responsible for obscuring the broad line AGN in this object.

5.3 Mid-IR-optical luminosity correlations

Previous studies (e.g. Dicken et al. 2009; LaMassa et al. 2010) have demonstrated that the mid-IR continuum luminosity correlates strongly with the AGN power. The thermal emission from warm dust radiating in the mid-IR is readily explained by models of AGN heating of the toroidal dust (Pier & Krolik 1992,1993; Granato & Danese 1994; Nenkova et al. 2002, 2008a,b). This is most naturally understood if the mid- to far-IR emission is primarily powered by the AGN. However, I note that other sources of emission, such as starbursts, may contribute significantly in the less luminous AGN.

In addition to the mid- to far-IR emission, optical emission lines are also a good indicator of AGN power, in particular the [OIII]λ5007 emission line from the NLR (Tadhunter et al., 1998) which is photoionised by the AGN itself. However, there are uncertainties relating to the degree of dust extinction in the NLR which will affect the observed [OIII] emission. The mid-IR emission on the other hand is notably less affected (LaMassa et al., 2010). Using a combination of AGN power indicators, we may be able to identify whether an AGN is subject to higher levels of dust extinction when compared to other AGN. Alternatively, this may enable us to identify objects with unusually strong emission at longer wavelengths.

In Figures 5.4(a)-(e), I plot $\log_{10}$ L_{IR} (W/Hz) against $\log_{10}$ $L_{[OIII]}$ for the red 2MASS AGN and the comparison samples, with the IR thermal emission plotted for (a) 2.17μm, (b) 3.4μm, (c) 4.6μm, (d) 12μm and (e) 22μm bands. Note that I also indicate the 2MASS objects with blue (<1.3) 2.17-3.4μm colours with black crosses.

It is clear that, for the majority of the comparison samples, the mid-IR luminosities are strongly correlated with $L_{[OIII]}$, supporting the argument that the mid-IR emission from AGN is intrinsically linked to the AGN power (LaMassa et al., 2010). However, overall, the 2MASS sample objects appear to fall above the correlation, which either indicates that the NLRs of these objects are moderately reddened, or that the mid-IR emitting dust in the 2MASS objects has an unusually high covering factor when compared to the NLR. It is interesting to note that, at similar [OIII] luminosities, the 2MASS AGN with 2.17-3.4μm < 1.3 have fainter mid-IR luminosities when compared to the rest of the 2MASS AGN at similar luminosities. However, they are comparable to those of the comparison samples. I discuss the behaviour of these objects further in $\oint$ 5.3.4. In addition, I note that J1131+16, falls below the rest of the 2MASS objects with similar [OIII] luminosity on all of these correlations.

5.3.1 Dust extinction

In Chapter 4, I established that, overall, the red 2MASS AGN are moderately reddened when compared to samples of 'typical' AGN. Assuming that the same levels of reddening also apply to the [OIII] emission, moderate reddening of the NLR will have a noticeable effect on the correlation between an AGN's [OIII] luminosity, and its mid-IR thermal emission at longer wavelengths: the thermal emission will appear 'enhanced' when compared to the [OIII] emission; adjusting the [OIII] emission for dust extinction will correct this.

If the 2MASS AGN fall above the correlations in figures 5.4(a)-(e) because of dust extinction of the [OIII] emission, then following a correction for this extinction, we would expect the 2MASS objects to fall on the main correlation determined by the PG quasars and unobscured type 1 AGN. In Figures 5.5(a)&(b), where possible, I have corrected the [OIII] luminosities for dust extinction in the NLRs (violet circles; see Chapter 4). For the 2MASS objects which can be corrected for dust extinction, I connect these objects with their uncorrected estimates with a straight line. I have also included a line showing how an extinction of $A_V = 3$ can effect the [OIII] luminosity for clarity. Note that the mid-IR emission has not been corrected for dust extinction. I only plot the mid-IR luminosities for the longer wavelength (12μm and 22μm) bands. This is to negate any effects of dust extinction on the mid-IR luminosities.

It is clear from Figures 5.5(a)&(b) that dust extinction in the NLR can have a major effect on where the 2MASS objects fall on the mid-IR correlation plots. After correction, many objects appear similar to the samples of 'typical' AGN, suggesting that the NLRs

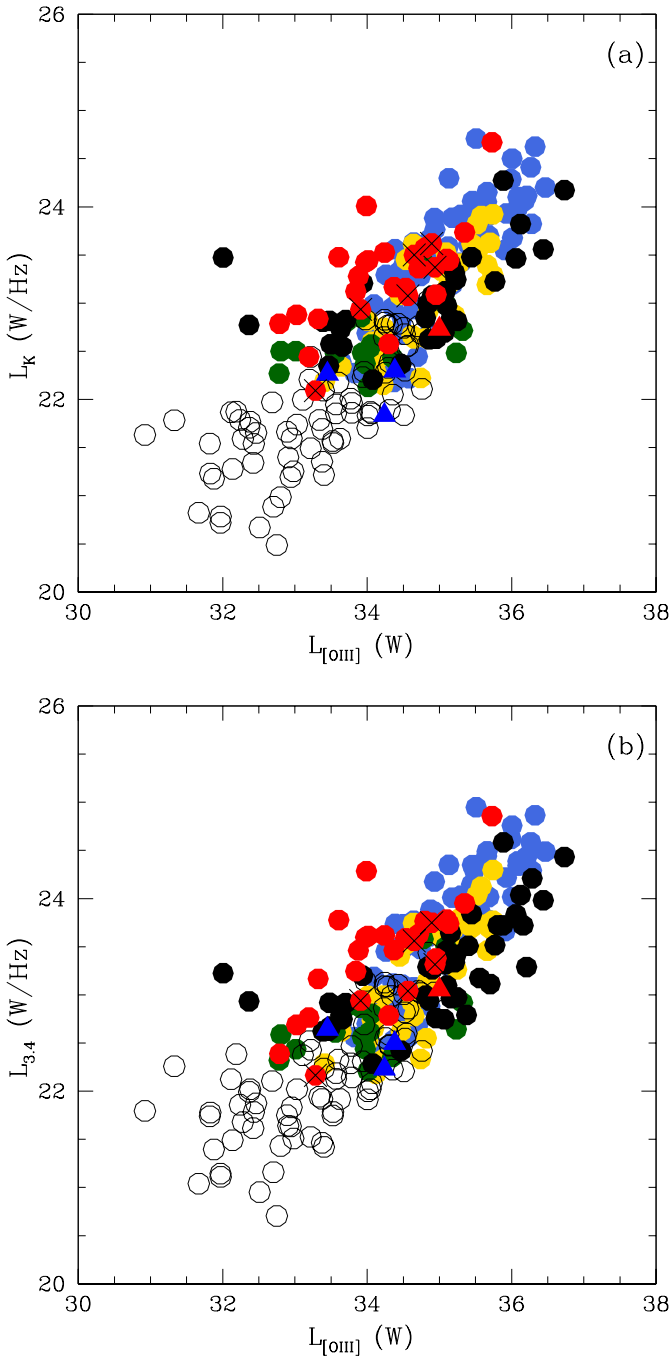

Figure 5.4: Luminosity correlation plots of (a) $L_{2.17\mu m}$, (b) $L_{3.4\mu m}$, (c) $L_{4.6\mu m}$, (d) $L_{12\mu m}$ and (e) $L_{22\mu m}$ plotted against $L_{[OIII]}$ for all the samples. The red 2MASS AGN are represented by red circles, PG quasars by blue circles, the unobscured type 1 AGN population are represented in gold, 2Jy sample in black, the 3CRR sample in green and the 12 μ Seyfert galaxies are represented by unfilled circles. The 2MASS objects with blue (<1.3) 2.17-3.4μm colours are highlighted with black crosses. J1131+16 is represented by a red triangle, and III Zw 77, Tololo 0109-383 and ESO 138 G1 are represented by blue triangles. CONTINUED ON NEXT PAGE.

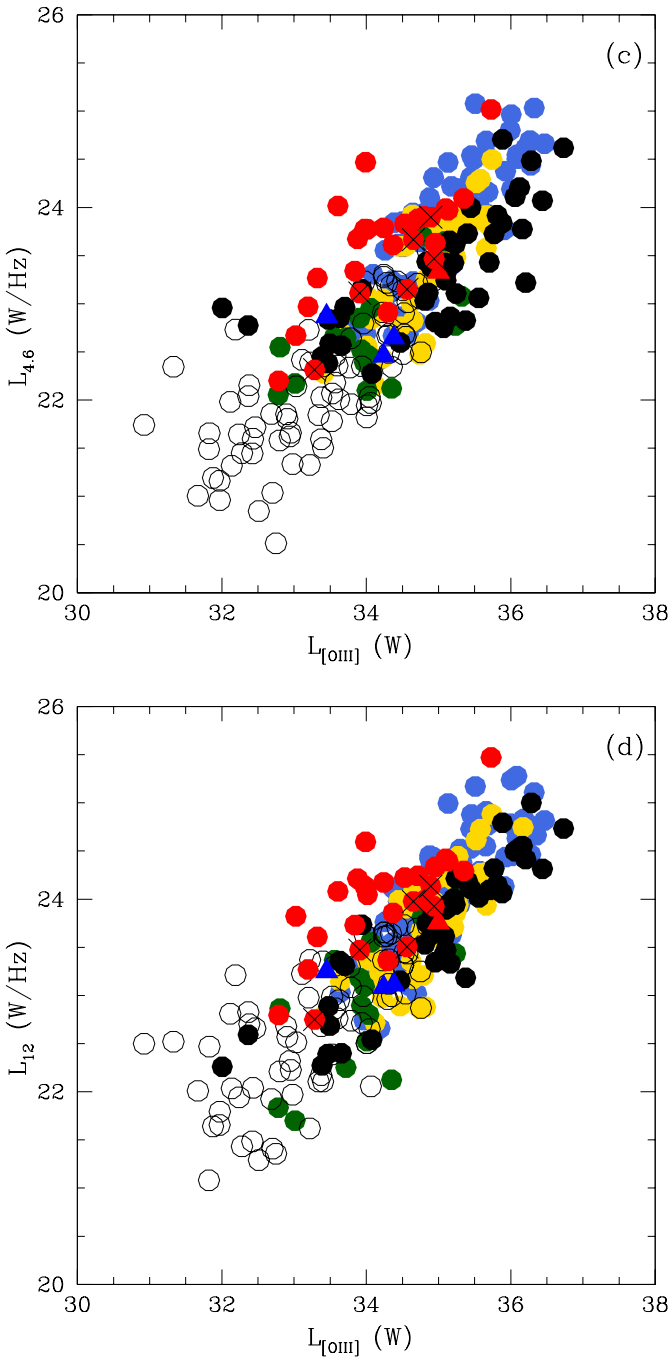

Figure 5.4: CONTINUED ON NEXT PAGE.

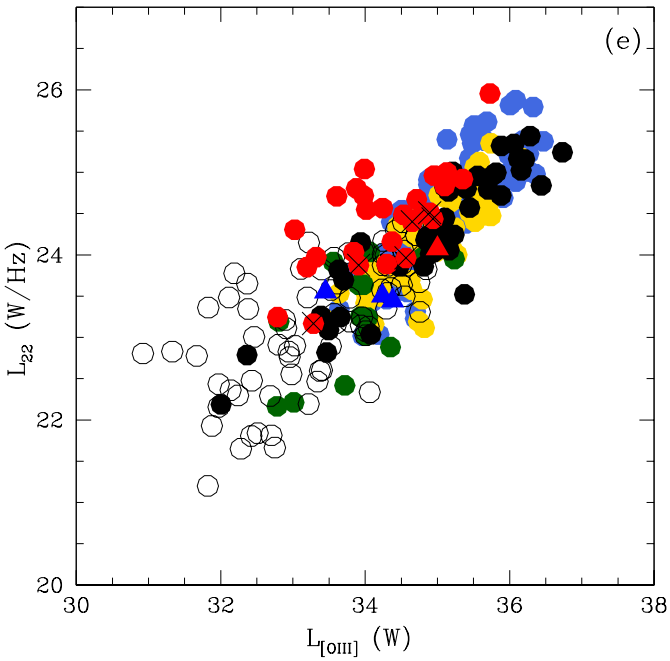

Figure 5.4

(and therefore possibly the BLRs) of these objects are highly reddened. The objects which shift from a high mid-IR luminosity to [OIII] luminosity ratio to a ratio, which is comparable to that of the comparison AGN are J0306-05, J0400+05, J0409+07, J1057-13, J1158-30, J1212-14 and J1407+42. However, I note that some of these objects appear to be over-corrected. This is likely to be due to inaccurate NLR reddening estimates.

However, J0435-06 and J1127+24 still fall well above the correlations, even after being corrected for dust extinction. Also, J2124-17, an object with an optical continuum that resembles a typical UV/optical selected type 1 AGN, and does not show any evidence for dust extinction in its optical spectrum (it has a combined Balmer decrement of 2.15±1.15, which is in agreement with Case B recombination), falls well above the correlation. This suggests that the properties of the entire red 2MASS AGN population cannot be explained by extinction alone. It is possible that a relatively large covering factor for the torus dust, that is emitting radiation at all temperatures and at mid-IR wavelengths, could also result in the red J-K_S colours.

5.3.2 Orientation

In § 5.2.1, I showed that AGN type plays an important role in the near- to mid-IR colours. In particular, I demonstrated that the narrow-line AGN are redder at longer

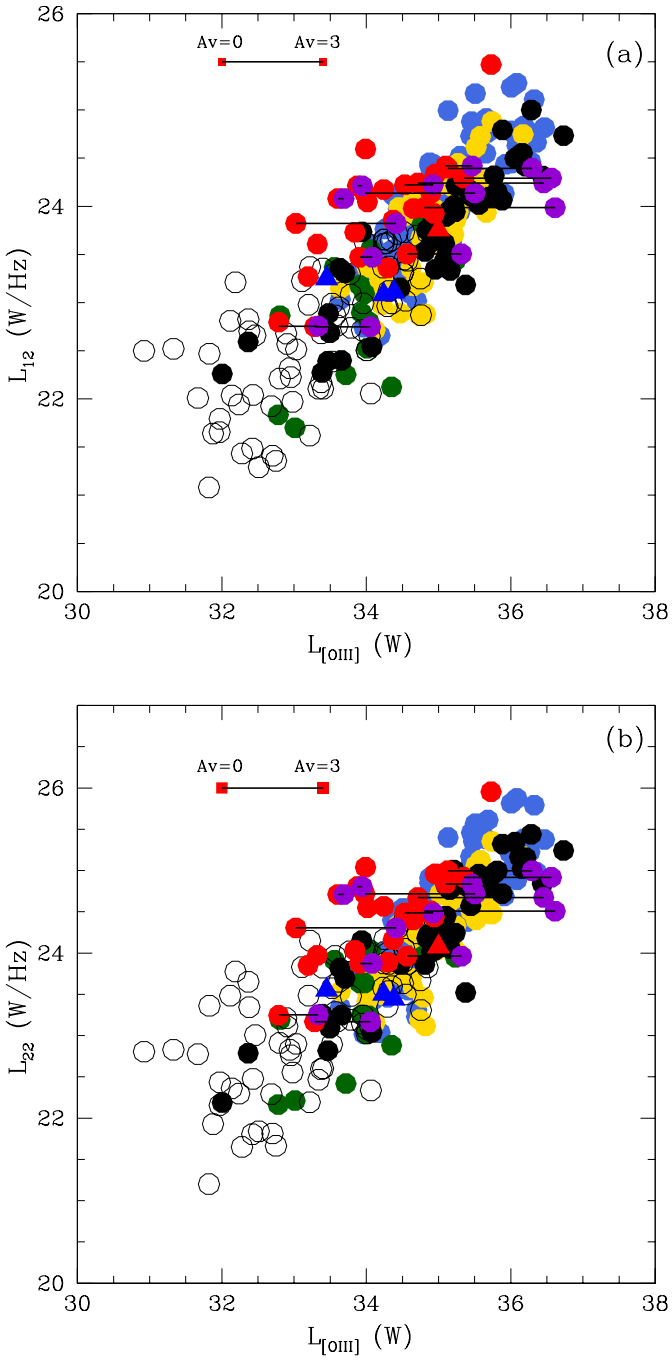

Figure 5.5: The same plots as Figures 5.4(d)&(e), however where possible the [OIII] luminosities have been corrected for dust extinction in the NLRs (violet circles). Objects where I present both the corrected and uncorrected estimates have been connected with a straight line. In addition I plot a reddening line on the plots to further demonstrate how reddening can effect the near- to mid-IR colours of the AGN.

wavelengths when compared to the broad-line AGN. To determine whether the AGN type has a significant effect on the luminosity correlations for the 2MASS sample, I divide all of the samples into their spectral types.

From Figures 5.6(a)&(b) it is clear that, overall, the broad-line objects are more luminous in both their [OIII] and mid-IR luminosities than the other AGN types. In addition, the LINERs and WLRGs fall at the low luminosity end as expected. More interestingly, the AGN that show enhanced mid-IR luminosities relative to the [OIII] luminosities are dominated by narrow-line and LINER type objects. These include J0221+13, J0306-05 and J1001+41 from the 2MASS sample. Assuming that the [OIII] luminosities are a good indicator of AGN power for unreddened AGN, this highlights the probability that the narrow-line/composite objects are subject to higher levels of NLR extinction when compared to broad-line objects. These levels of extinction are likely to have an impact on the strength of the [OIII] emission, leading to lower [OIII] luminosities.

However, there remain broad-line objects in the 2MASS sample which fall well above the correlation, suggesting that, either dust extinction is also important in the broad-line objects, or there may be a higher dust covering factor in these objects when compared to other broad-line AGN. The 2MASS broad-line objects which deviate significantly from the correlation are J0435-06, J0447-16, J1040+59 and J2124-17[1]. The latter objects are investigated further in § 5.3.3.

5.3.3 Covering factors

In § 5.3.1 I showed that, although dust extinction may be sufficient to explain the red colours in most of the 2MASS AGN, other 2MASS AGN may require a relatively large covering factor for the torus dust in order to explain the near-IR colours. In addition, I have shown that there is a sub-sample of 2MASS AGN with unusual blue 2.17-3.4μm colours when compared to the other 2MASS AGN, suggesting that the covering factor of dust radiating at close to the sublimation temperature is unusually large (see § 5.2) in these objects. Also, there is some overlap in J-K_S colours between the red 2MASS AGN and the comparison samples (see Figure 2.1 in Chapter 2) which include unreddened type 1 objects. If dust extinction alone cannot explain the red colours, then we need to consider whether a high dust covering factor could produce these colours.

If the red near-IR colours of the 2MASS sample are the result of an unusually high

[1]Unfortunately it was not possible to obtain separate NLR extinction estimates using the Balmer emission lines for these objects.

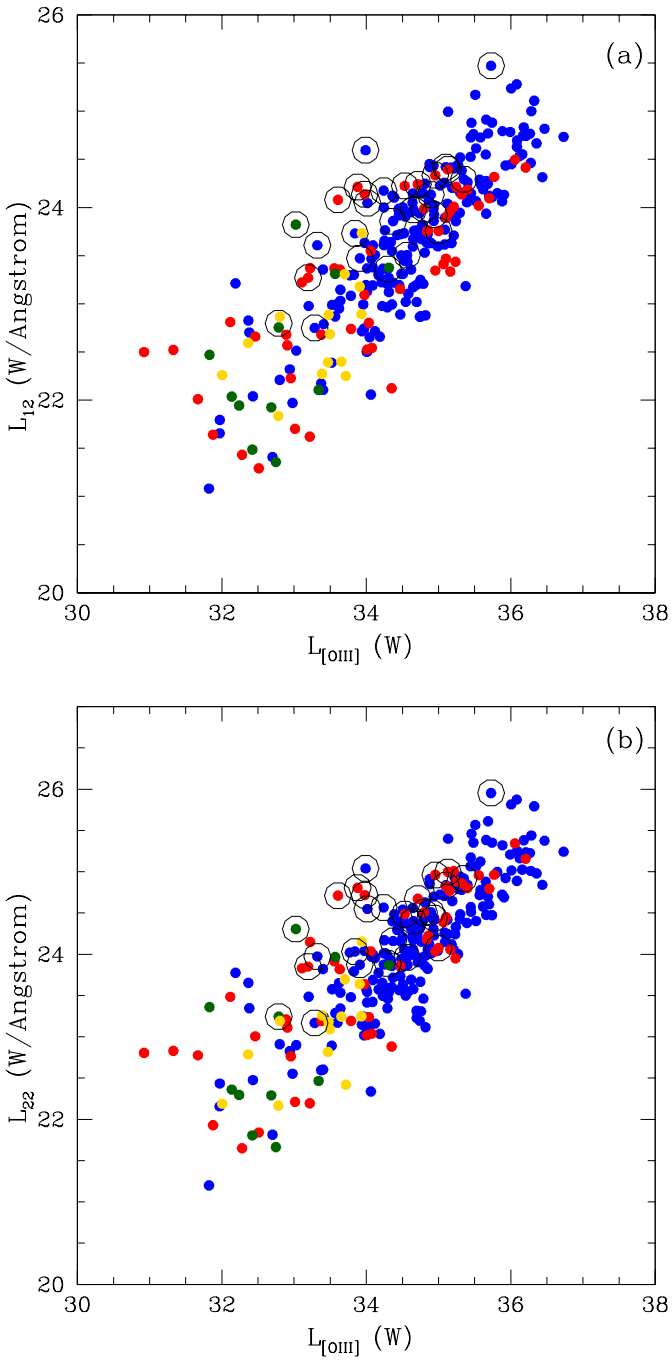

Figure 5.6: Luminosity correlation plots of (a) $L_{12\mu m}$ and (b) $L_{22\mu m}$ plotted against $L_{[OIII]}$ for all AGN types. All broad-line objects are plotted in blue, narrow-line objects in red, LINERs/HII region type in green and WLRGs are plotted in yellow. In addition, I have circled the 2MASS AGN on the plots.

dust covering factor of the torus dust that is radiating at mid-IR wavelengths, then there may be a trend on the mid-IR correlation plots, such that objects with redder J-K_S colours fall above objects with bluer J-K_S colours. In Figures 5.7(a)&(b) I group all the objects in the samples (2MASS and the comparison samples) into different ranges of near-IR colours. In addition, I plot the best fit lines for the red (1.97 < J-K_S), green (1.5 < J-K_S < 1.97) and blue (J-K_S < 1.5) populations to help illustrate any differences between the samples in the colour divisions. Note that I only use mid-IR emission from the 12 and 22μm bands. Once again, this is to negate any effects that dust extinction and host galaxy emission may have on the mid-IR emission.

From Figures 5.7(a)&(b) it is clear that, overall, for objects with similar [OIII] luminosities, the redder the near-IR J-K_S colours are, the higher the mid-IR luminosities become. This is emphasised by the best fit lines, where the line representing the trend of the red AGN is presented in red, the line representing the intermediate colour AGN is presented in green, and the line representing the bluer AGN is presented in blue. The line parameters are outlined in Table 5.4.

In Table 5.4 I first present the values of the slopes I have fitted to the data points plotted in Figures 5.7(a)&(b) (the bisector of a linear least squares fit of x on y, and y on x). Next I present the mean bisector slope values for 5000 bootstrap trials, along with the uncertainty in the slopes. The slopes for the best fit lines are all consistent within 2σ of each other. In the next column of Table 5.4 I present the intercepts of the best fit lines. I note that the intercepts of the lines differ significantly when comparing the AGN with J-K_S > 1.97 to the other AGN. Note that, although the intercept is not independent of the slope, the slopes are not significantly different for the three lines.

In addition, I present the coefficient of determination, R^2, the percentage of the total variation in the y-values that is explained by the regression equation, derived from regression statistics for each slope in Table 5.4, based on the least squares fits to the data. The R^2 values indicate that almost two thirds of the variation in the data sets can by explained by the relationship derived from the least squares fits, which indicates that the mid-IR luminosities and the [OIII] luminosities are indeed strongly correlated (LaMassa et al. 2010).

If the objects with large mid-IR luminosities are the result of a high covering factor of toroidal dust that is emitting radiation at all temperatures, then I must establish whether this is energetically feasible. Dicken et al. (2009) investigated whether it is energetically feasible for the mid-IR dust to be predominately heated by AGN in the 2Jy and 3CRR samples. Dicken et al. (2009) assumed a simple model in which the mid-IR continuum and [OIII] emission lines are produced by AGN illumination of structures with covering

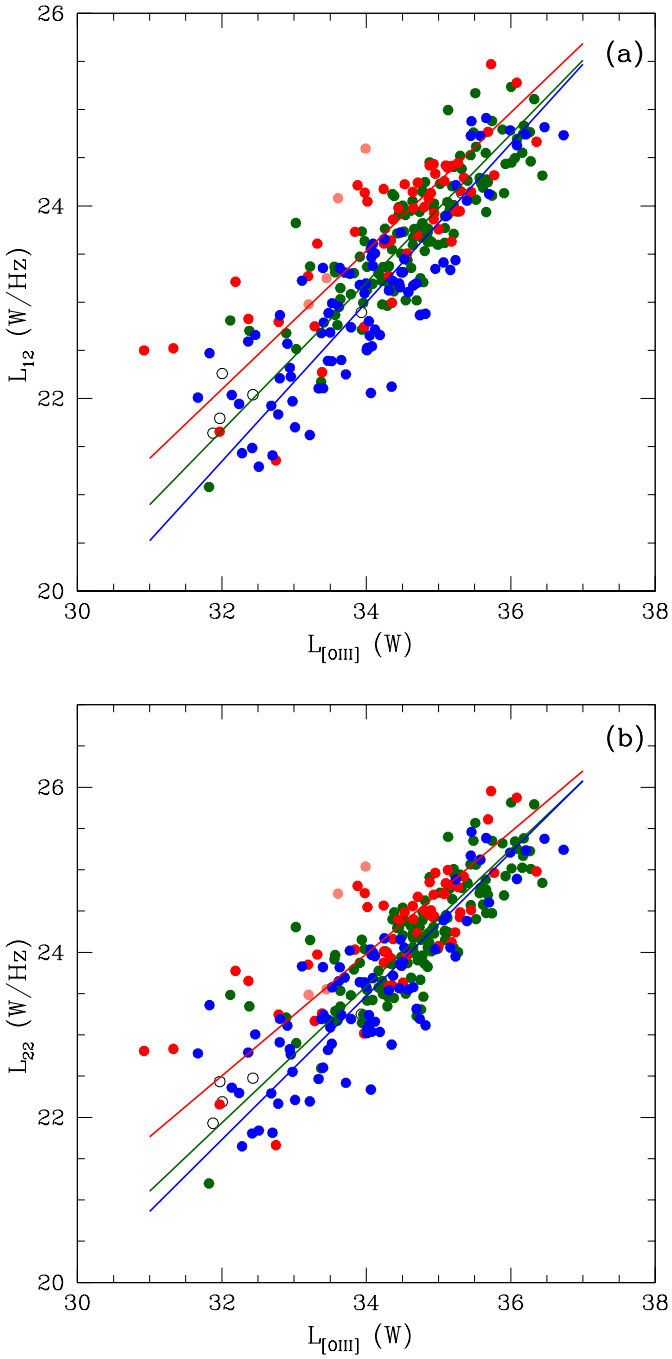

Figure 5.7: The same plots as Figures 5.4(a)&(b), however all the objects in the samples have been grouped into near-IR colours where objects with J-K_S > 2.5 are represented by salmon coloured circles, objects with 1.97[a] < J-K_S < 2.5 are represented by red circles, objects with 1.5 < J-K_S < 1.97 are represented by green circles, objects with 1.0 < J-K_S < 1.5 are represented by blue circles and objects with J-K_S < 1.0 are represented by open circles. The best fit lines are also plotted for the sample divisions. The line parameters are outlined in Table 5.4. [a]This is the lowest J-K_S colour found in the 2MASS sample.

Table 5.4: Correlation slopes determined from linear least square fits of x on y, and y on x to the data, and from bootstrap analysis. The subscripts '12' and '22' refer to the 12μm and 22μm luminosity correlations respectively.

Line	Bisector	Bootstrap	Intercept	R^2
Red_{12}	0.72	0.79±0.04	-0.88	0.63
Int_{12}	0.77	0.84±0.03	-2.95	0.70
$Blue_{12}$	0.83	0.82±0.04	-5.04	0.68
Red_{22}	0.74	0.78±0.05	-1.14	0.60
Int_{22}	0.83	0.81±0.03	-4.57	0.66
$Blue_{22}$	0.87	0.80±0.05	-6.10	0.64

factors C_{mir} and C_{nlr} respectively, where C_{mir} is the total covering factor for all the dust that radiates between 2 and 30μm (assuming that the SED at these wavelengths can be approximated by a single power law). In addition, no assumptions were made about the radial distribution of dust. Based on this model, Dicken et al. (2009) found that the covering factor of the mid-IR emitting dust is consistent with what is expected for a torus.

To test whether it is feasible that both the red near-IR colours, and the high mid-IR luminosities relative to the [OIII] luminosities in the 2MASS sample, can be explained by high torus dust covering factors, I assume the same model outlined in Dicken et al. (2009). However, rather than use the Spitzer M-FIR of 24μm fluxes, I use the luminosities measured in the mid-IR WISE bands of 12μm and 22μm. Therefore, the work carried out to determine a model for the AGN illumination is identical to that carried out in Dicken et al. (2009) until the spectral index (γ; assuming $F_\nu \propto \nu^\gamma$) is calculated:

$$\gamma = \frac{log(L_{12}/L_{22})}{log(22/12)}. \tag{5.1}$$

For the combined samples I find a median mid-IR colour of $L_{12\mu m}/L_{22\mu m} = 0.364 \pm 0.008$, leading to $\gamma_{median} \approx -1.67 \pm 0.04$. Therefore the mid-IR monochromatic luminosities can be related to the AGN bolometric luminosities by:

$$L_{mir} = 1 \times 10^9 L_{bol} C_{mir} \nu^{-1.67}. \tag{5.2}$$

By substituting equation (1) from Dicken et al. (2009) into equation 5.2 I find:

$$L_{(12\mu m)} = 7.6 \times 10^{-13} L_{[\mathrm{OIII}]} \frac{C_{mir}}{C_{nlr}} \tag{5.3}$$

Table 5.5: Median C_{mir}/C_{nlr} covering factor ratios for the samples. Note that the standard errors are not presented because as the scatter in the R values for the samples are high, the resulting standard errors often exceed the median value.

Sample	R_{12}	R_{22}
2MASS AGN	46.1	43.6
PG Quasars	16.2	15.6
Unobscured Type 1	30.6	25.3
12 Micron	25.0	21.9
2Jy	9.12	10.8
3CRR	10.3	8.75

and

$$L_{(22\mu m)} = 2.1 \times 10^{-12} L_{[\mathrm{OIII}]} \frac{C_{mir}}{C_{nlr}}. \tag{5.4}$$

In Figures 5.8(a)&(b) I have plotted L_{MIR} against $L_{[OIII]}$ correlations, along with predictions from the above calculations for ranges of C_{mir}/C_{nlr} covering factor ratios (labelled as R on the figures) and, in addition, the 2MASS objects have been indicated by red circles.

The majority of the 2MASS AGN on Figures 5.8(a)&(b) have covering factor ratios ($R=C_{mir}/C_{nlr}$) in the region $12.5 < R < 100$, and in general, the covering factor ratios for the 2MASS AGN are higher than those of the comparison samples. This is reflected in the median R values presented in Table 5.5. There are however a significant number of objects with $R > 100$ (41% of the 2MASS population), which are discussed later in this section.

Assuming that the NLR has a covering factor in the range $0.02 < C_{nlr} < 0.08$ (Netzer & Laor, 1993), I estimate a mid-IR dust covering factor in the range $0.25 < C_{mir} < 8$ for these 2MASS objects, where 16% exceed $C_{mir}=1$ assuming $C_{nlr}=0.02$, and 84% exceed $C_{mir}=1$ assuming $C_{nlr}=0.08$. Although a large C_{mir} is feasible assuming that it is related to the dusty torus, it obviously cannot exceed a value of 1, but the higher ($C_{mir} > 1$) covering factors may be misleading. Indeed, if I assume the lower NLR covering factor limit only, the mid-IR covering factor range becomes $0.25 < C_{mir} < 1.5$. Thus the mid-IR luminosities of most of the objects can be explained in terms of AGN illumination of the circumnuclear torus, especially if the covering factor for the NLR is relatively low in these objects. As described in Chapter 4, a relatively large covering factor for the torus dust could result in red J-K_S colours.

However, when considering the outliers (objects where the C_{mir}/C_{nlr} covering factor

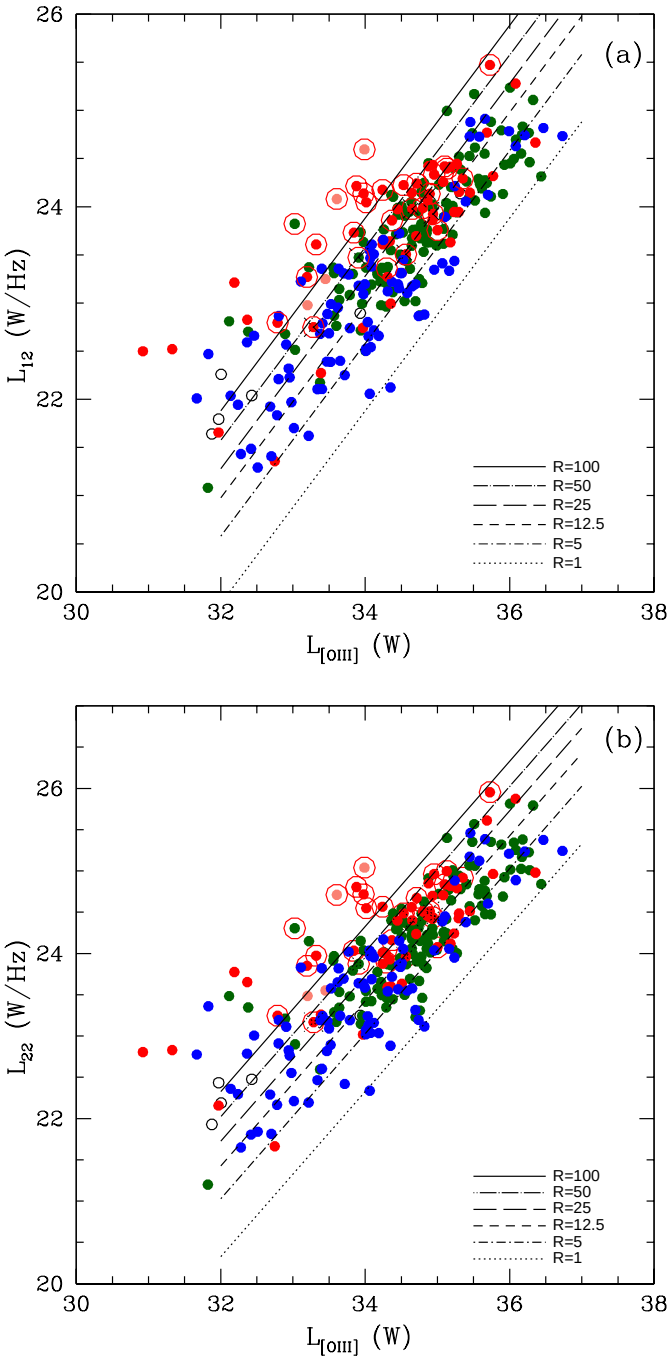

Figure 5.8: Same plots as Figures 5.7(a)&(b), however here I highlight the 2MASS AGN (red circles) and include the predictions for the ranges of C_{mir}/C_{nlr} covering factor ratios (labelled as R).

ratios are greater than 100), the covering factors become unfeasible unless the NLR covering factor is *extremely* low ($C_{nlr} < 0.01$). Following the same assumptions for the NLR covering factor as above, I find a lower limit on the mid-IR dust covering factor to be $C_{mir} > 2$. This suggests that the objects which show the greatest mid-IR luminosity 'excess' cannot simply be explained in terms of an unusually high covering factor alone. As demonstrated in Figures 5.5(a)-(b), moderate amounts of dust extinction can significantly increase the [OIII] luminosity, therefore these objects would require a lower C_{mir}/C_{nlr} covering factor ratio. In objects where an accurate extinction estimate cannot be estimated, I would recommend using the IR emission line [OIV]λ25.9μm. By using [OIV], an IR emission line that indicates the AGN power but is not affected strongly by dust extinction, Dicken et al. (2013) show that emission from optical [OIII] scatters significantly when plotted against [OIV].

But, as described in § 5.3.1, even after correcting some of the 2MASS objects for dust extinction, objects such as J0435-07 and J1127+24 still have a mid-IR luminosities 'excess'. For these objects, assuming that the model and assumptions are correct, the calculated C_{mir} range can only be feasible if the NLR covering factor is unusually low. Physically, this suggests that the AGN could be obscured as seen by the NLR clouds, possibly by the torus. Alternatively, the number of NLR clouds could simply be low in these objects. Since the torus is likely to be on a much smaller scale (<50 pc) than the NLR (up to 1kpc), another possibility is that the AGN has only recently switched on, or increased significantly in brightness: due to light travel time effects the information about the increase in AGN brightness has reached the torus, but not the bulk of the NLR.

In Chapter 4, I found that the Balmer decrements for the type 1 2MASS AGN J0435-06, J1338-04 and J2124-17, did not show any evidence for moderate levels of dust extinction. In addition, their optical continua resembled typical UV/optical selected type 1 AGN. In this section, both J0435-06 and J2124-17 have been identified as objects that have unusually high covering factors for the torus dust, in the sense that they have higher mid-IR luminosities when compared with AGN with similar [OIII] luminosities. However, J1338-04 appears to have a mid-IR luminosity comparable to typical UV/optical selected type 1 AGN.

Overall, the analysis of the colour trends seen on the correlation plots (see Figures 5.7(a)&(b)), combined with the feasibility calculations, suggest that it is possible that the near-IR colours for some of the 2MASS AGN are the result of emission from torus dust, with an unusually high covering factor.

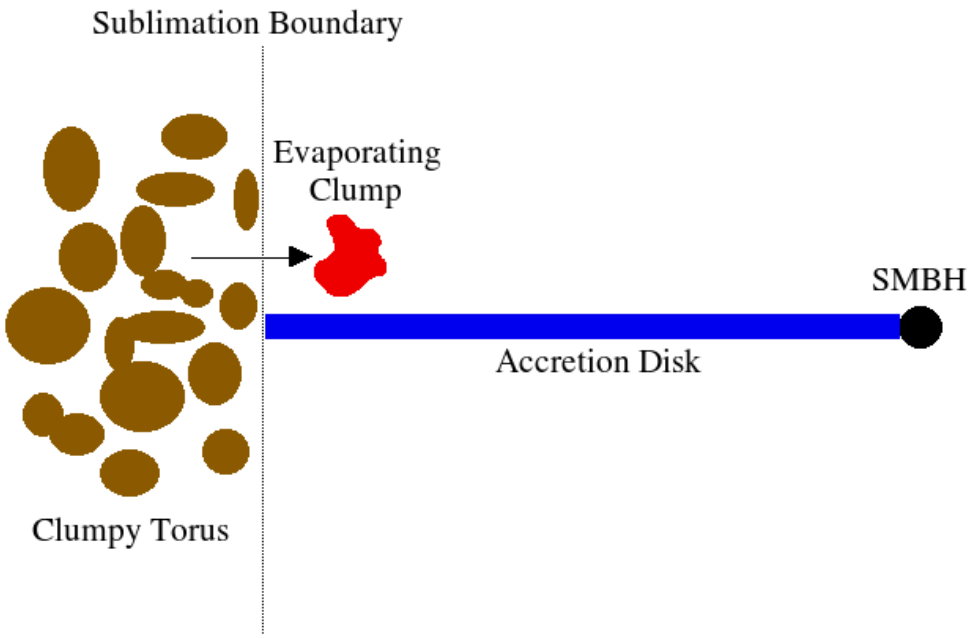

Figure 5.9: Schematic illustrating the scenario described in this section.

5.3.4 Blue 2.17-3.4μm objects

In § 5.2 I identified 6 red 2MASS AGN with blue (< 1.3) 2.17-3.4μm colours. While these objects are blue in the 2.17-3.4μm colour space, they are indistinguishable from the rest of the 2MASS AGN at other wavelengths. From their position on the correlations (see Figures 5.4(a)-(e)), it is clear that, at similar [OIII] luminosities, these objects have comparable mid-IR luminosities to the PG quasars and unobscured type 1 AGN. This is reflected in their estimated C_{mir}/C_{nlr} covering factor ratios (see § 5.3.3): the median ratio, R, of these objects is 32. Therefore the covering factors of the dust emitting at longer wavelengths is not unusual in these objects.

The source of emission in the K_S bands in these objects is possibly a clump of dust, that may have been removed or 'broken off' from the torus, and has moved within the boundary of the sublimation temperature of the SMBH. This clump is heated to higher (post sublimation) temperatures, and evaporates at a rate that allows us to observe the emission from this clump. The 'evaporation lifetime' of the clumps may determine the probability of observing such a phenomenon over the lifetime of the AGN. In addition, the emission will likely fade as the clump continues to evaporate. In the case of the 6 2MASS objects with blue 2.17-3.4μm colours, the emission is strong and is therefore

evident in the broadband near- to mid-IR colours, implying that the clump has recently moved within the boundary of the sublimation temperature of the SMBH. It is likely such an object could only be viewed at an orientation that allows for the observation of the emission from the BLR; this is supported by the fact that all 6 of these objects are type 1 AGN, as illustrated in Figure 5.9. In Chapter 6 I test whether such an emitter is feasible when explaining the near- to mid-IR colours of these AGN.

5.3.5 J1131+16 and the other FHIL objects

In contrast to the rest of the 2MASS AGN, J1131+16 falls towards the bottom of the mid-IR luminosity correlations. The same is true for the FHIL objects III Zw 77 and ESO 138–G1. However, Tololo 0109-383 falls within the luminosity range of the 2MASS objects. This could be due to low levels of extinction in the NLRs of these objects which lead to higher observed [OIII] luminosities, lowering the mid-IR luminosity to [OIII] ratio. Alternatively, the covering factor of the torus dust could be lower than expected in these objects.

From Figures 5.8(a)-(b), I find that the covering factor ratio, R, is relatively low for J1131+16: on the L_{12} correlation I find a ratio of R = 7.52, and on the L_{22} correlation I find a ratio of R = 5.66. If the NLR emission is radiated by the same structure that radiates the mid-IR emission (as expected for J1131+16, see Rose et al. 2011), then a relatively low ratio is expected. Thus this evidence supports the interpretation outlined in Chapter 3.

5.4 SEDs

So far, much of the work I have presented in this chapter has concentrated on the narrow wavelength ranges provided by the 2MASS and WISE bands. While this approach has revealed some interesting results (e.g. objects with blue 2.17-3.4μm colours), the full SEDs of the red 2MASS AGN may give more detailed information which might help to explain some of the trends visible on the colour-colour plots.

In Figures 5.10(a)-(c) I present the median SEDs of all the samples over a wavelength range $1.25 < \lambda < 22$ μm: (a) presents the median SED of the entire sample, (b) presents the median SED over a redshift range $0 < z < 0.1$, and (c) presents the SED over the redshift range $0.1 < z < 0.2$. All the SEDs are normalised to their 12μm-band fluxes. The 12μm-band fluxes have been chosen because 12μm is a long enough wavelength such that any direct flux from the AGN accretion disks and stars in the host galaxies is

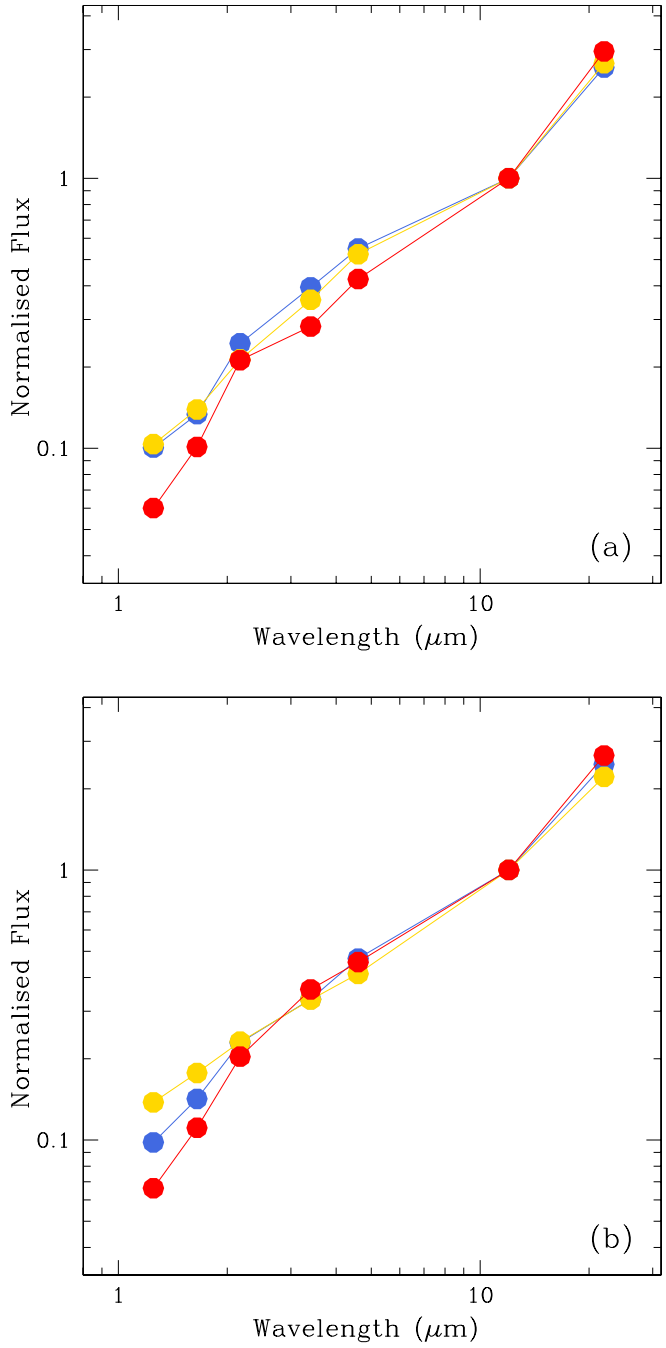

Figure 5.10: The near- to mid-IR median spectral energy distributions plotted against wavelength (μm) of (a) all the samples, (b) objects in the redshift range of $0 < z < 0.1$, and (c) objects in the redshift range of $0.1 < z < 0.2$, all normalised to the flux of the 12μm band. Note the flux is plotted as F_ν. The red 2MASS AGN are represented by red circles, PG quasars by blue circles and the unobscured type 1 AGN population are represented in gold. CONTINUED ON NEXT PAGE

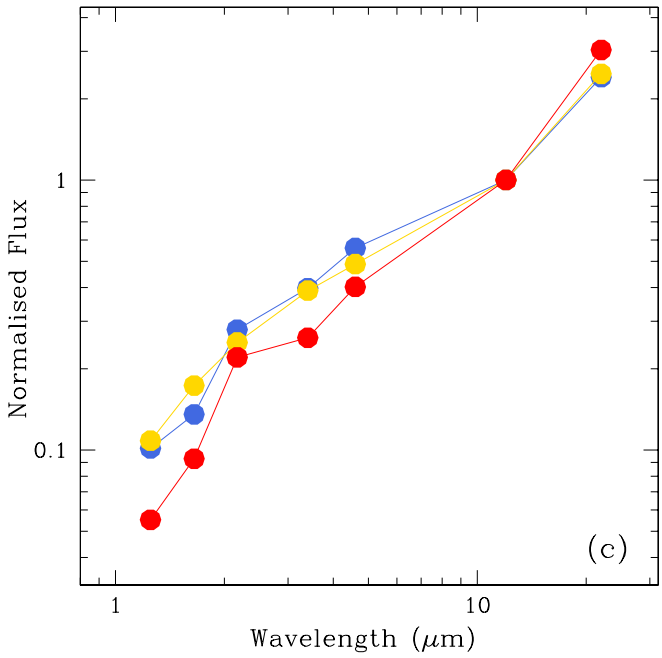

Figure 5.10

negligible, and short enough such that there is a minimal contribution from any possible star formation in the host galaxy. However, there is a caveat when normalising to the 12μm band. It is possible that there could be a strong presence of the 9.7μm silicate absorption feature in this band, caused by Si-O bond stretching (Rieke & Low., 1975). At a sufficient redshift, it is possible that this feature could be shifted well within the WISE 12μm band. This absorption may be strong enough to lower the overall 12μm band flux, and therefore normalising by this band will lead to high normalised fluxes observed in the other bands.

Note that I do not present the median SEDs for the 12μ Seyfert galaxy, 2Jy and 3CRR samples, this is because these samples contain both type 1 and type 2 objects. Therefore there would be no clear-cut comparison.

From Figures 5.10 (a)-(c), it is clear that the 2MASS sample has one of the reddest overall SEDs, because there is less normalised flux at shorter wavelengths ($\lambda < 4.6\mu$m) when compared to the unobscured type 1 AGN. This supports the view that the majority of the 2MASS AGN are moderately reddened because the flux will be extinguished at shorter wavelengths.

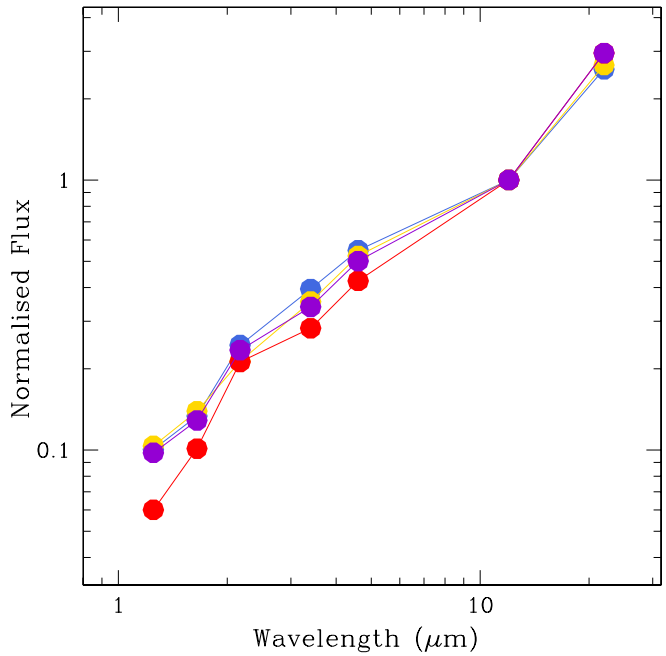

Figure 5.11: Same as Figure 5.10(a), however the median SED of the 2MASS AGN has been corrected for an extinction of A_V=2 magnitudes (violet).

Reddening

If the observed differences in the SEDs between the 2MASS and comparison samples are down to moderate/high levels of dust extinction, then it should be possible to reproduce the SEDs of the comparison samples by correcting the 2MASS SED for dust extinction. In Figure 5.11, I correct the 2MASS sample for A_V=2 magnitudes of extinction (represented in violet). This clearly shows that, after correcting the median 2MASS SED for moderate dust extinction, it is comparable to that of the PG quasars and unobscured type 1 AGN. This supports the idea that a significant proportion of the 2MASS AGN are red at near-IR wavelengths as a result of dust extinction. However, I note that while many of the 2MASS AGN show evidence for reddening in their optical spectra, there are other objects which show no such evidence, and appear similar to traditional UV/optical selected AGN (e.g. J0435-06, J1338-04 and J2124-17). This implies that this explanation cannot be used for all the 2MASS AGN.

5.4.1 Individual SEDs

In the previous section I stated that the red colours of the 2MASS-selected AGN cannot be described by reddening alone. Therefore, it is likely that much could be learnt from

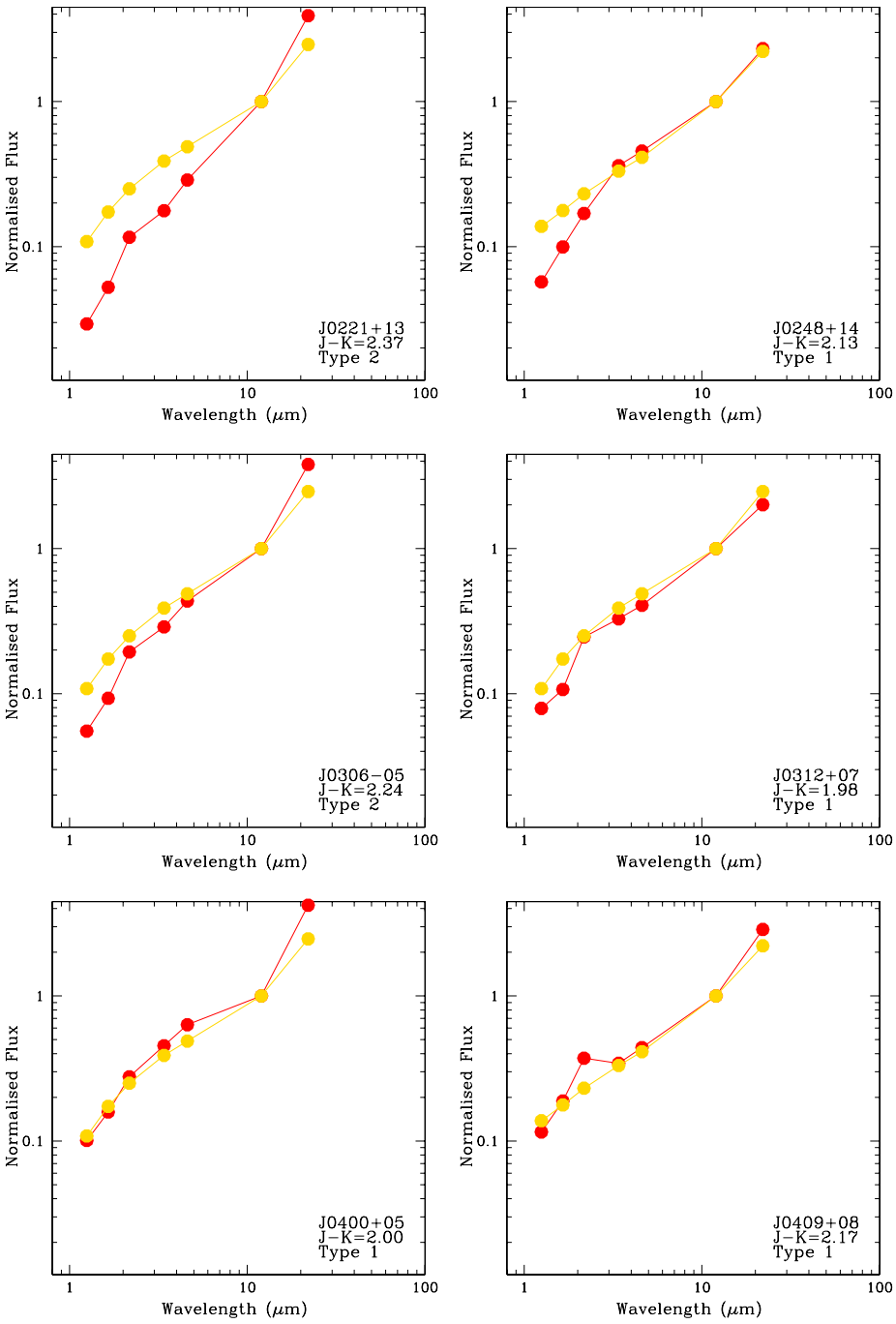

Figure 5.12: The individual SEDs of the 2MASS sample (red) plotted alongside the unobscured type 1 AGN median SED (gold). Note that the redshift ranges used to determine the median SED of the unobscured type 1 AGN coincides with the redshift of the individual 2MASS object. In addition, the flux is plotted as F_ν. Details for the individual objects are given in the bottom right hand corners of each plot. CONTINUED ON THE NEXT PAGE.

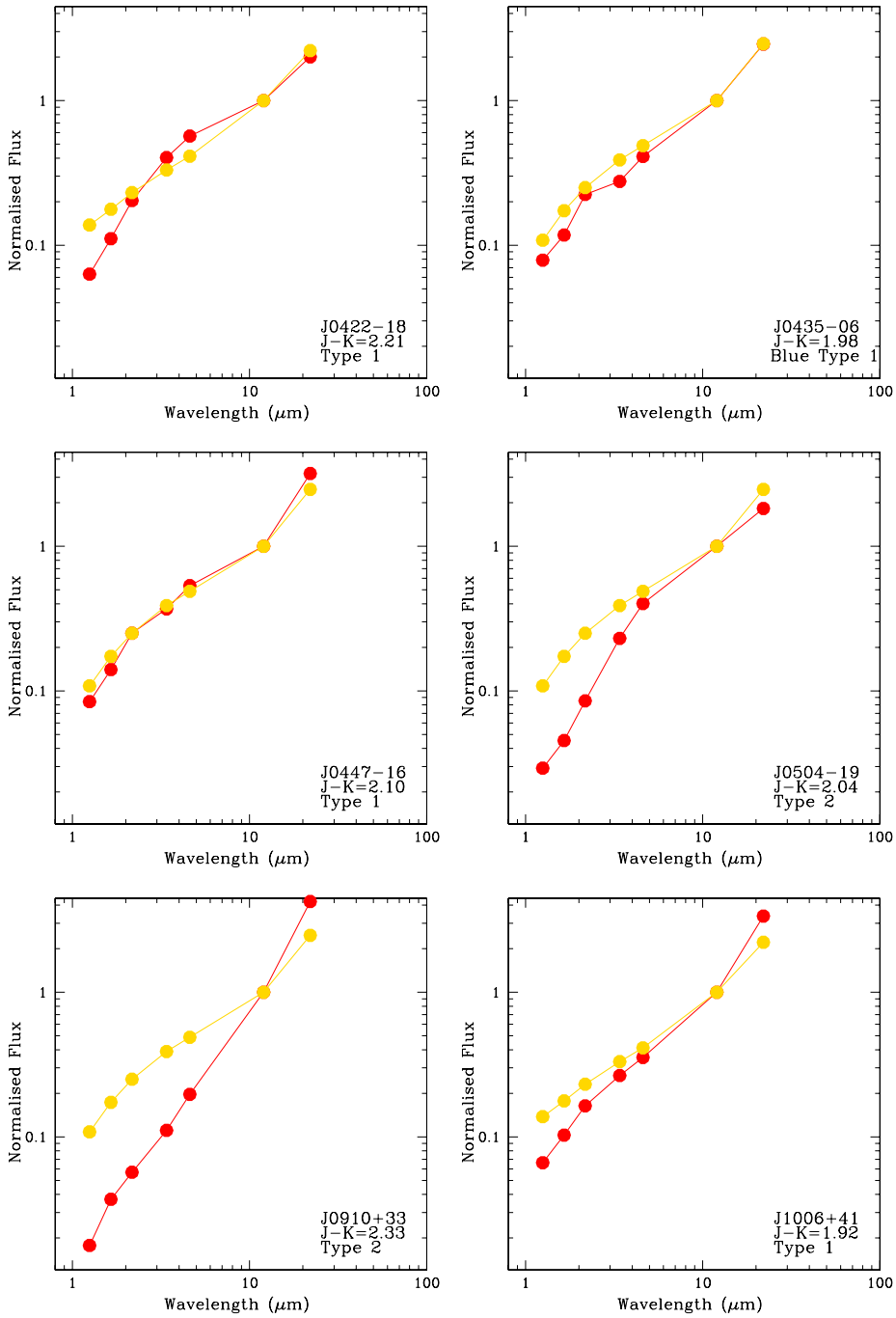
Normalised Flux
Wavelength (μm)
J0422−18
J−K=2.21
Type 1
J0435−06
J−K=1.98
Blue Type 1
J0447−16
J−K=2.10
Type 1
J0504−19
J−K=2.04
Type 2
J0910+33
J−K=2.33
Type 2
J1006+41
J−K=1.92
Type 1

Figure 5.12

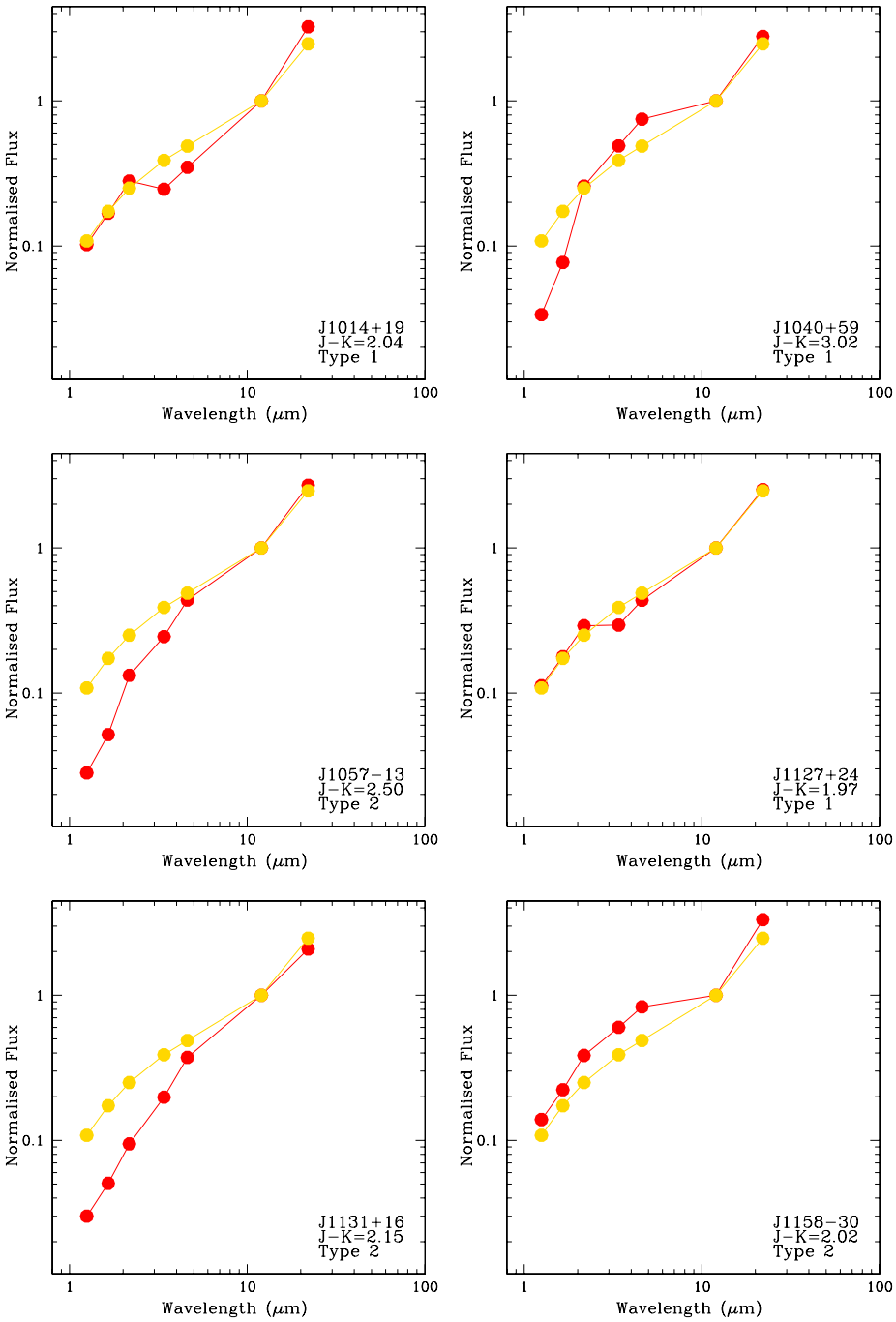
Normalised Flux
Wavelength (μm)
J1014+19
J−K=2.04
Type 1
J1040+59
J−K=3.02
Type 1
J1057−13
J−K=2.50
Type 2
J1127+24
J−K=1.97
Type 1
J1131+16
J−K=2.15
Type 2
J1158−30
J−K=2.02
Type 2

Figure 5.12

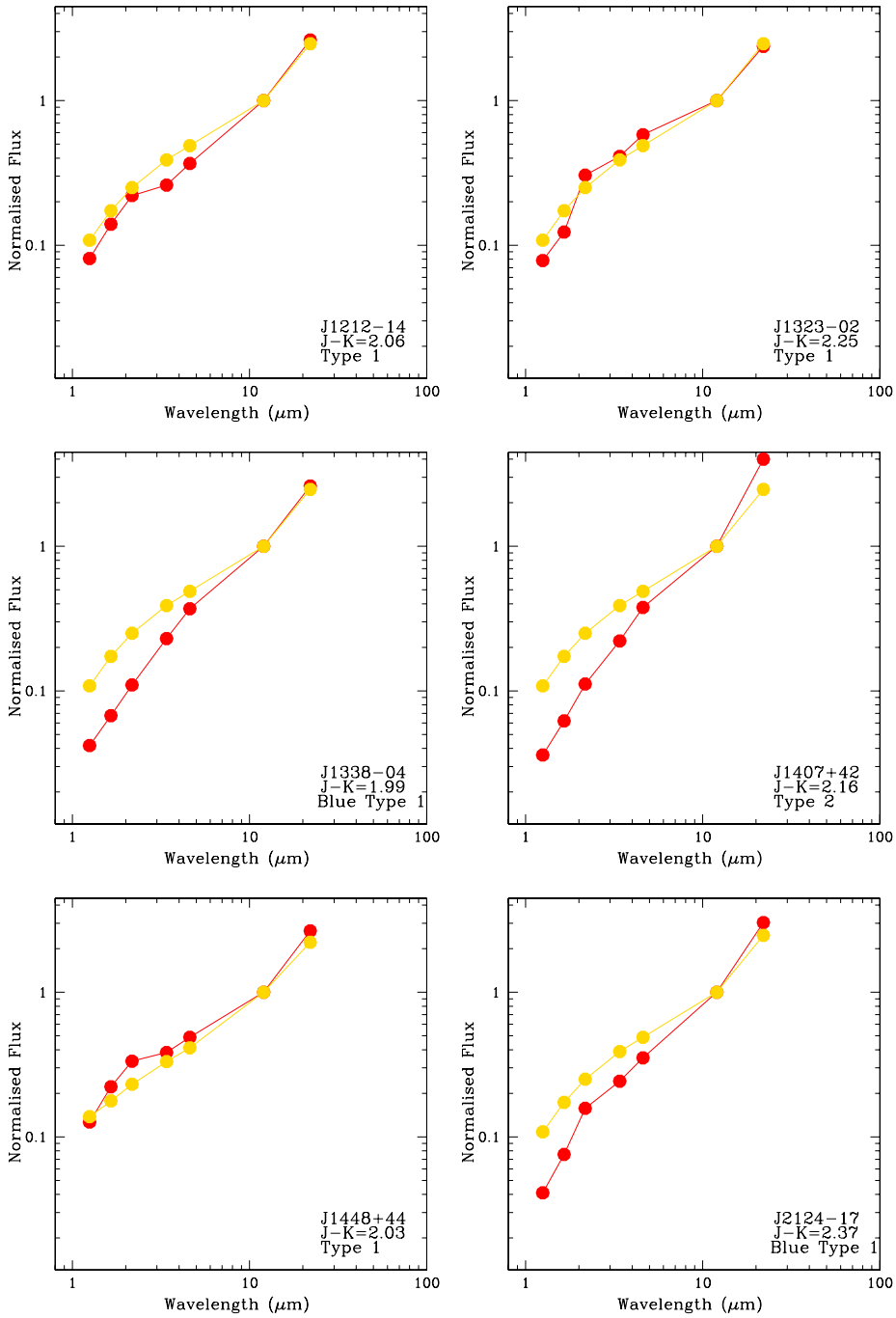
Normalised Flux
Wavelength (μm)
J1212−14
J−K=2.06
Type 1
J1323−02
J−K=2.25
Type 1
J1338−04
J−K=1.99
Blue Type 1
J1407+42
J−K=2.16
Type 2
J1448+44
J−K=2.03
Type 1
J2124−17
J−K=2.37
Blue Type 1

Figure 5.12

the red 2MASS AGN if their near- to mid-IR SEDs were studied individually. In Figure 5.12, I present the normalised SEDs of each object in the 2MASS sample. Note that the redshift ranges used to determine the median SED of the unobscured type 1 AGN coincides with the redshift of the individual 2MASS object i.e. for example, J0221+13 is a type 2 AGN at a redshift of z = 0.140, therefore it is compared to the median unobscured type 1 AGN SED whose objects were in the redshift range of $0.1 < z < 0.2$.

The SEDs vary remarkably from object to object. However, by analysing the shapes of the SEDs of these objects, I can broadly classify them into four types as follows.

- **Reddening.** Many of the normalised SEDs of the 2MASS objects have short wavelength fluxes that are low when compared to the comparison type 1 SEDs, with the SEDs diverging most strongly at the shortest wavelengths. The levels to which the fluxes have been extinguished vary from object to object. This likely reflects the different levels of dust extinction in these AGN. Indeed, the type 2 objects show the greatest levels of extinction, as expected from obscuration by the torus. The objects which can be categorised in this way include J0248+14, J0422-18, J0504-19, J0910+33, J1006+41, J1131+16, J1338-04 and J1407+42. However, I do not find a clear trend between the level of dust extinction measured from the Balmer lines in the optical spectrum and the shape of the individual SEDs. This suggests that other factors, such as the torus covering factor, hot dust emission, and hot galaxy emission, are also important when determining the shape of the SED.

- **'K-Hump'.** Some objects do not show any strong evidence for reddening, but instead show enhanced emission in the K_S-band when compared to the comparison SEDs. These objects include J0409+08, J0435-06, J1014+19, J1127+24, J1212-14, J1323-02 and J1448+44. Apart from J1323-02, these objects correspond to the type 1 objects identified as having relatively blue 2.17-3.4μm colours in § 5.3.4. Given that it is clear that there is enhanced emission in the K_S-band for the SED of J1323-02, I conclude that there is a similar process occuring in this object compared to the objects with blue (<1.3) 2.17-3.4μm colours.

- **Reddening plus inflection.** Other objects show a combination of the effects described above, i.e. extinguished short wavelength fluxes combined with enhanced emission in the K_S-band. However, I note that in these cases the enhanced emission

is not as pronounced as in the 'K-Hump' objects: the 'hump' appears as more of an inflection. This could possibly be due to lower levels of emission detected from the hot dust in these objects due to moderate/high levels of dust extinction. The objects whose SEDs show this trend are J0221+13, J0306-05, J0312+07, J1057-13 and J2124-17.

- **Typical type 1 AGN.** For the object J0447-16, there is no significant difference between its near- to mid-IR SED, and the comparison type 1 SEDs, apart from at the shortest near-IR wavelengths. This is unusual because in Chapter 4 I report substantial reddening for this object.

Note that the SEDs of J0400+05, J1040+59 and J1158-30 cannot be easily classified into any of these categories. It is likely that there is strong silicate absorption in the 12μm bands of these objects, and therefore the lower wavelength normalised fluxes appear to be higher than those of the comparison SEDs (see $\oint$ 5.4).

Both J1338-04 and J2124-17 show no evidence for dust extinction at optical wavelengths, yet their near- to mid-IR SEDs appear redder than the other 2MASS type 1 AGN. While the mid-IR luminosity of J2124-17 presented in $\oint$ 5.3 was consistent with an object that has an unusually high covering factor for the torus dust, J1338-04 shows no such evidence. It is likely that there is no straight-forward interpretation for the SEDs of both of these objects, and further investigation is needed in order to explain their interesting properties.

Even though there is no sufficient evidence for reddening of the NLR of J1131+16, the SED shape for the J1131+16 is consistent with that of a reddened AGN. This suggests that the accretion disk and the SMBH is obscured by the torus, whilst the NLR is relatively unaffected by dust extinction. Therefore, I believe that the J-K_S colour of J1131+16 is red because it is a 'genuine' type 2 AGN, and the NLR emission is radiated by the same structure that radiates the mid-IR emission which has an electron density $n_e > 10^5$ cm^{-3}, which allows for the emission of strong FHILs.

So far, I have shown that the 2MASS AGN sample is heterogeneous, and that there may be a need for more than one explanation its red near-IR colours. While for many of the 2MASS AGN their is strong evidence that dust extinction produces the red near-IR colours, there is evidence that in other objects there is a strong component of hot dust ($\sim$ 1500K) whose emission peaks in the K_S-band, resulting in the red near-IR colours. Therefore, in the next chapter, I investigate the feasibility of these explanations.

5.5 Summary

In this chapter I have presented an analysis of the near- to mid-IR 2MASS and WISE data of the 2MASS and comparison samples. The aim was to investigate the nature of the near-IR J-K_S colours of the 2MASS sample. Based on the results of this chapter, there are four possible explanations for the red near-IR colours of the 2MASS objects.

- As indicated by the results in Chapter 4, moderate levels of dust extinction are sufficient to explain the red near-IR colours of many of the type 1 2MASS objects.
- The colour-colour plots indicate that the colours of the type 2 AGN in the 2MASS sample are possibly the result of a combination of large levels of dust extinction, along with host galaxy contamination.
- The work in ∮ 5.3.3 shows that it is feasible that the red near-IR colours of some of the 2MASS objects, in particular those which cannot be explained by reddening, such as J0435-07 and J1127+24, are the result of unusually high covering factors of the torus dust, which is radiating at mid-IR wavelengths.
- In ∮ 5.2 I identified 6 red 2MASS AGN with blue 2.17-3.4μm colours (2.17-3.4μm < 1.3): J0409+08, J0435-06, J1014+19, J1127+24, J1212-14, and J1448+44. The combination of red J-K_S colours and blue 2.17-3.4μm colours cannot be easily explained in terms of reddening effects or host galaxy contamination. It is possible that the colours of these objects are the result of a component of hot dusty emission whose SED peaks in the K_S-band.
- In ∮ 5.4.1 I presented the SEDs of the 2MASS sample. The shape of SEDs of individual red 2MASS AGN support many of the findings outlined above. However, I also identified a set of objects which show evidence for a combination of reddening, and enhanced hot dust emission.
- Overall, I have shown that for one of the three objects that is 'blue' at optical wavelengths (J0435-06), but 'red' in its near- to mid-IR colours, it is possible that its red near- to mid-IR colour is the result of emission from dust, rather than the result of moderate levels of reddening. However, further data is needed for J1338-04 and J2124-17 before any meaningful conclusion can be made in regards to the nature of the red near-IR colours of these objects.

In Chapter 6 I investigate the feasibility of these explanations by modelling the near- to mid-IR colours of the 2MASS AGN, varying the levels of dust extinction, relative

covering factors of the torus and any additional hot dust, as well as the degree of host galaxy contamination.

Chapter 6

Modelling the near- to mid-IR colours of the red, 2MASS-selected AGN in the local Universe

6.1 Introduction

From the *combined* analysis of the optical spectra and near- to mid-IR photometry of the 2MASS AGN, I have found that there are several possible explanations for their red J-K_S colours: moderate levels of dust extinction; high levels of dust extinction coupled with host galaxy emission (i.e. 'genuine' type 2 AGN); an unusually high covering factor for the torus; and a possible additional component of emission radiating at a temperature which coincides with the K_S band; or a combination of these effects.

Table 6.1 presents a truth table which indicates whether the Balmer decrements measured from the optical spectra, or any aspect of the near- to mid-IR photometry (e.g. blue 2.17-3.4μm colours), provide evidence for a particular explanation of the red J-K_S colours for each object in the 2MASS sample. In addition, I indicate whether any of the 2MASS objects are type 2 AGN. This is important because it may support the argument that some of these AGN have red J-K_S colours because they are obscured by the torus. Note that, for the cases where it was not possible to separate the broad and narrow line contributions to the Balmer decrement, I indicate whether the total Balmer decrement (combined broad and narrow line emission) suggests that moderate levels of dust extinction could be responsible for the red J-K_S colours.

It is clear from Table 6.1 that the sample of 2MASS AGN is heterogeneous, in the sense that the reason for the red J-K_S varies from object to object. From the combined

analysis presented in Chapters 4 and 5, 32% of the sample show evidence which is consistent with moderate levels of dust extinction, 32% show evidence for high levels of dust extinction coupled with host galaxy emission, 28% have a possible additional component of hot dust emission radiating in the K_S band, and 8% cannot be readily explained[1].

In this chapter, I model the near- to mid-IR colours of the 2MASS AGN in order to test the feasibility of the main explanations outlined above. I do this by first reproducing the observed properties of the unobscured type 1 AGN. This is achieved by finding the typical parameters for the different components which contribute to the continua of the objects. Then, I vary these parameters to test whether it is possible to reproduce the red colours observed for the 2MASS AGN, given the possible explanations outlined above.

6.2 Model parameters

In order to investigate whether moderate/high levels of reddening, or high covering factors for the torus dust emitting at all temperatures, are responsible for the differences between the near- to mid-IR colours of the 2MASS AGN, I need to produce a model in which these components can be varied. The results can then be compared to the colours of the 2MASS AGN.

In this section, I describe how the components for the model are calculated, and give details of how they can be varied.

6.2.1 Accretion disk

One of the primary components of the continuum SED model is the accretion disk of the AGN. As well as providing the bulk of the emission at shorter wavelengths, it can be used to estimate the bolometric flux of the AGN. For the model I assume that the flux emitted by the accretion disk ($f(\nu)_A$) is proportional to the frequency (ν) of the emission raised to the power of a third ($f(\nu)_A \propto \nu^{1/3}$). This spectral shape is consistent with the theoretical predictions of Shakura & Sunyaev (1973), and confirmed observationally by Kishimoto et al. (2008), who isolated the disk emission spectrum by using optical and near-IR polarimetry of AGN, and found that the accretion disks of their sample objects were all consistent with the shape $\nu^{1/3}$, where the weighted mean of the slopes is 0.44±0.11.

[1]Note that I do not include the LINERs, J0411-01 and J1001+41, or the objects with redshifts z > 0.2, J1307+23 and 1637+25, in these statistics.

Table 6.1: Truth table presenting the incidences where the observational evidence supports the deductions made throughout the thesis. The evidence from the optical spectra ('Bal Dec'), and the near- to mid-IR photometry ('Colours') has been separated by vertical lines. 'NLR', 'BLR' and 'Total' indicate whether the Balmer decrements provides evidence for reddening in the object. Note that for the 'Type 2' column, the spectral type is confirmed by the optical spectra, however the evidence supporting the argument that their red J-K_S colours are due to their type is presented in Chapter 5. 'Cf' indicates whether there is sufficient evidence to support the view that the red J-K_S colour of the object is due to an unusually high covering factor for the torus. 'Ext.' indicates whether the analysis of the luminosity plots, or SEDs, presented in Chapter 5 suggests whether these objects are reddened. 'K-Hump' indicates whether the object has blue 2.17-3.4μm (< 1.3) colours. 'Ext.+Infl' shows whether the SED of the object supports the idea that the object has red J-K_S colours due to a combination of reddening and dust emission from an additional hot dust component. Y=True, N=False and P=Possible evidence for a BLR.

Object	Bal Dec				Colours			
ID	NLR	BLR	Total	Type 2	Cf	Ext.	K-Hump	Ext.+Infl
J0221+13	N	N	N	Y	N	Y	N	Y
J0248+14	N	N	Y	N	N	Y	N	N
J0306-05	Y	N	N	Y	N	Y	N	Y
J0312+07	N	N	Y	N	N	Y	N	Y
J0400+05	Y	Y	Y	N	N	N	N	N
J0409+07	Y	N	N	N	N	Y	Y	N
J0422-18	N	N	Y	N	N	Y	N	N
J0435-06	N	N	N	N	Y	N	Y	N
J0447-16	N	N	Y	N	Y	N	N	N
J0504-19	N	Y	N	Y	N	Y	N	N
J0910+33	N	N	N	Y	N	Y	N	N
J1006+41	N	N	Y	P	N	Y	N	N
J1014+19	N	N	Y	N	N	N	Y	N
J1040+59	N	N	Y	P	N	N	N	N
J1057-13	Y	N	N	Y	N	Y	N	Y
J1127+24	N	Y	Y	N	Y	N	Y	N
J1131+16	N[a]	N	N	P	N	Y	N	N
J1158-30	Y	N	N	Y	N	N	N	N
J1212-14	Y	Y	Y	N	N	Y	Y	N
J1321+13[b]	Y	N	N	Y	-	-	-	-
J1323-02	N	N	Y	N	N	N	Y	N
J1338-04	N	N	N	N	N	Y	N	N
J1407+42	Y	N	N	Y	N	Y	N	N
J1448+44	N	N	Y	N	N	N	Y	N
J2124-17	N	N	N	N	Y	N	N	Y

[a] The Hα emission of this object is likely to be enhanced by collisional excitation. See Chapter 3 for full description.

[b] This object was not detected by WISE because it was too faint.

In what follows, the bolometric flux of the AGN is estimated from the flux in the accretion disk by integrating the total flux of the accretion disk from 0.3 μm to 30μm[2]. This is important when determining the covering factors of the torus material, and host galaxy contributions to the SEDs of the AGN. The parameters which vary the accretion disk component are described in ∮ 6.2.5.

6.2.2 Torus emission

The second main source of emission in the model is the torus dust (see Chapter 5). The torus dust consists of two components: the exponential cut-off of a black-body curve at short wavelengths corresponding to the hottest dust at the sublimation temperature of the dust grains, and a power-law component at longer wavelengths than the peak of black-body curve of the sublimation dust. The black-body component is described by Equation 6.1:

$$f(\nu)_B = \frac{2h\nu^3}{c^2}\frac{1}{e^{h\nu/kT}-1}, \tag{6.1}$$

where h is the Planck constant, c is the speed of light, k is the Boltzmann constant and T is the sublimation temperature of the dust. The shape of the power-law component is based on the shape of the median SED of the PG quasars from the K_S-band to the 22μm band. I find that this component of the dust emission has a spectral index of α_D = -0.83±0.07, based on the photometric measurements from the K_S-band to the 22μm WISE band. This spectral index is consistent with other estimates such as those of Simpson & Rawlings (2000) for radio-loud quasars, and Franceschini et al. (2005) for unreddened type 1 AGN. I assume that the median SED of the PG quasars has negligible host galaxy contamination and zero dust extinction, and that all dust is heated by the AGN. The parameters which affect the torus emission component are described in the following sections.

Covering factor

One of the crucial components of determining the flux contribution of the torus dust is its covering factor (Mor, Netzer & Elitzur, 2009): higher covering factors will result in a greater proportional contribution to the SED of emission from the torus dust, and therefore redder near-IR colours, given that the emission from the torus dominates at

[2]Note that this carries a caveat in the sense that I assume that the flux from the accretion disk is described by $f(\nu)_A \propto \nu^{1/3}$ at all wavelengths.

near- to mid-IR wavelengths. This is important because, as outlined in Chapters 4 and 5, some of the red 2MASS AGN show very little evidence for dust extinction (e.g. J2124-17).

Equation 6.2 describes how the covering factor of the torus dust is determined in the model:

$$C_D = \frac{1}{F_{BOL}} \int_{peak}^{30\mu m} f(\nu)_D d\nu, \tag{6.2}$$

where the bolometric flux, F_{BOL}, is calculated to be the total integrated flux of the accretion disk from 0.3 μm to 30 μm (see $\oint$ 6.2.1), and *peak* refers to the peak of the black-body component of the hottest dust, which varies with the grain sublimation temperature (see below). In general, there are no issues with assuming that the emission from the torus dust begins at this wavelength because any flux emitted at lower wavelengths is minimal when compared to the total emission. I chose 30μm as the upper limiting torus emission wavelength in order to be consistent with the work of Dicken et al. (2009; and therefore the work in Chapter 5), and also to minimise the issue of including the far-IR emission from cool dust heated by stars or the AGN.

In the model, I vary the relative covering factor of the torus material in order to attempt to reproduce the colours of the objects.

Sublimation temperature

One of the key properties that will have an affect on the near-IR colours of AGN is the sublimation temperature of the torus dust grains. Lower sublimation temperatures will result in redder J-K_S colours when compared to higher sublimation temperatures. This is because black bodies at lower temperatures peak at longer wavelengths, as illustrated in Figure 6.1. Note that, although theoretical studies find sublimation temperatures for graphite/silicate dust grains in the range of 1500-1800 K (Salpeter 1977; Huffman 1977), observational studies of type 1 AGN find a lower of range temperatures: 1200-1500 K (Barvainis 1987; Rodríguez-Ardila & Mazzalay 2006). Therefore, in the model I vary the sublimation temperature of the hot dust over the range 1200-1800 K to investigate its effect on the colours of the AGN.

6.2.3 An additional hot dust component

When reproducing the colours of a sample of 26 broad-line AGN, Mor, Netzer & Elitzur (2009) found that, as well as the emission from the torus dust that is radiating at a

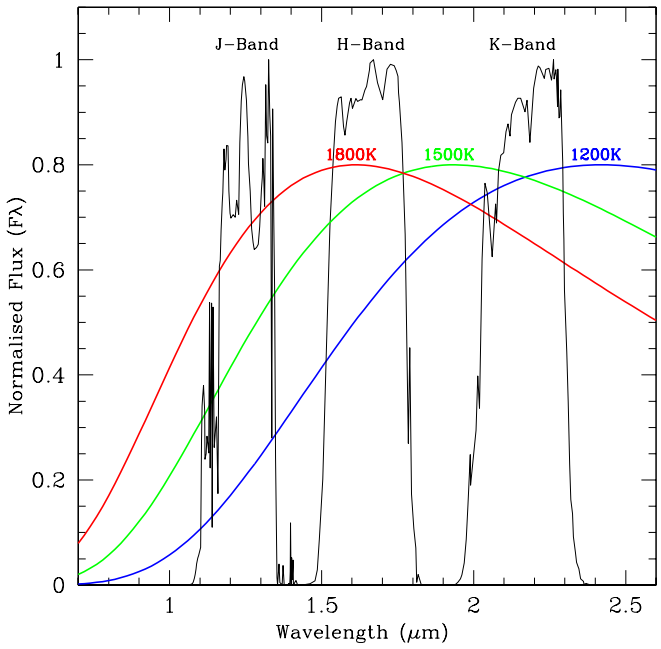

Figure 6.1: Normalised black-body curves plotted with the spectral responses of the filters used for the 2MASS survey. The black-body curve is presented for three temperatures: 1200 K (blue), 1500 K (green) and 1800 K (red).

range of temperatures below the sublimation temperature, they required an addition black-body component whose emission peaks at the sublimation temperature of dust grains[3]. This component can potentially explain the relatively blue 2.17-3.4μm colours seen for some of the type 1 AGN in the 2MASS sample. In the sample of Mor, Netzer & Elitzur (2009) only $\sim$35% of the AGN show the blue colours (2.17-3.4μm < 1.3), however, in general they find that the spectra of all their objects were better fit when this black-body component was included in their models.

Therefore, in order to represent this additional hot dust component a black-body emitter, initially modelled using a standard black-body curve (see Equation 6.1, integrated over all frequencies), is included in the model. The additional black-body component is scaled by increasing the covering factor of this component (C_B) relative to the bolometric flux derived from the accretion disk of the AGN. In all cases I assume that this component radiates at a temperature that is greater than, or equal to, the sublimation temperature that has been assumed for the torus component.

[3]Mor, Netzer & Elitzur (2009) believe that this component is likely to consist of graphite grains, because additional silicate grains in their model would overestimate the mid-IR silicate emission features in their spectra.

6.2.4 Host galaxy

In addition to emission from the accretion disk and torus dust, emission from the host galaxy is important when determining the colours of an AGN. To model the emission from the host galaxy, I use the galaxy SED templates of Assef et al. (2010). These templates represent the SEDs of both an elliptical galaxy and a late-type spiral galaxy (Sbc) over the wavelength range: 0.3 to 30 μm; they were derived from extensive multi-wavelength observations of the NDWFS Boötes field and the AGES spectroscopic survey. The SEDs of these templates are presented in Figure 5.2 in Chapter 5. For this component, I assume that there is no dust extinction.

6.2.5 Other variables

In this section I describe the variables which can affect all the components of the model.

Reddening

One of the the most important parameter that affects the flux contribution of both the accretion disk and torus to the SED is the level of dust extinction. As described in Chapters 4 and 5, moderate levels of dust extinction may be sufficient to produce the observed red near-IR colours of most of the 2MASS AGN. In addition, rather than moderately extinguished AGN, it is possible that some of these objects are 'genuine' type 2 objects in which the torus completely extinguishes the broad-line AGN at shorter wavelengths.

To redden the modelled AGN, I use the extinction law described by the work of Indebetouw et al. (2005). This extinction law is only valid up to 8μm, however in this chapter I only need to model the effect of dust extinction up to and including the 4.6μm WISE band.

As well as being applied to the accretion disk component of the model, the torus dust component will also be reddened in the models.

Redshift

Redshift is also important when determining the near-IR colours of AGN, because an AGN's observed optical/near-IR continuum colours will change significantly with redshift for a given intrinsic AGN SED. An important feature of the SED of an AGN is found at near-IR wavelengths: the point of inflection. The point of inflection marks the boundary between the wavelength regions in which the accretion disk and thermal dust emission

dominate (Neugebauer et al. 1987; Saunders et al. 1989). The J-K_S colour becomes bluer with redshift due to the accretion disk component of emission moving into the near-IR spectral region (Cutri et al., 2002). Therefore, redshift is included as a parameter in the model. The redshift will affect the importance of the accretion disk, torus dust and host galaxy components. I assume that the host galaxy and AGN components are in the same frame of reference i.e. there is no offset between the redshifts of the separate components.

6.2.6 Flux contributions to the bands

It is also important to take into account the effects of the bandwidths and spectral responses of the filters used for the 2MASS and WISE surveys. To account for these effects, I determine the overall flux contribution in each filter normalised to the integrated filter response:

$$F_{Band} = \frac{\int_{\nu_a}^{\nu_b}(f(\nu)_A + f(\nu)_D + f(\nu)_B + f(\nu)_H) \cdot R(\nu)d\nu}{\int_{\nu_a}^{\nu_b} R(\nu)d\nu}, \tag{6.3}$$

where $f(\nu)_A$, $f(\nu)_D$, $f(\nu)_B$ and $f(\nu)_H$ are the flux contributions of the accretion disk, torus material, black-body component and host galaxies respectively over the frequency range (ν_a to ν_b), and $R(\nu)$ is the spectral response of the filter. The spectral responses for the 2MASS filters are taken from Cohen, Wheaton & Megeath (2003), and those for the WISE bands are taken from Wright et al. (2010). Once the flux in each band has been determined, the colours are calculated as follows:

$$A - B = 2.5log_{10}\left[\frac{F_B}{F_A} \cdot \frac{Z_A}{Z_B}\right], \tag{6.4}$$

where A and B are the magnitudes in each band, F_A and F_B are the fluxes in each respective band, and Z_A and Z_B are the zero-point fluxes presented in Table 2.4.

A schematic figure, plotting the components of the model, is presented in Figure 6.2. It is clear from this figure that the different components of the model will be dominant at different positions on the SED of the AGN. Note that the relative contributions of each SED component have been arbitrarily chosen such that they can be illustrated on the figure.

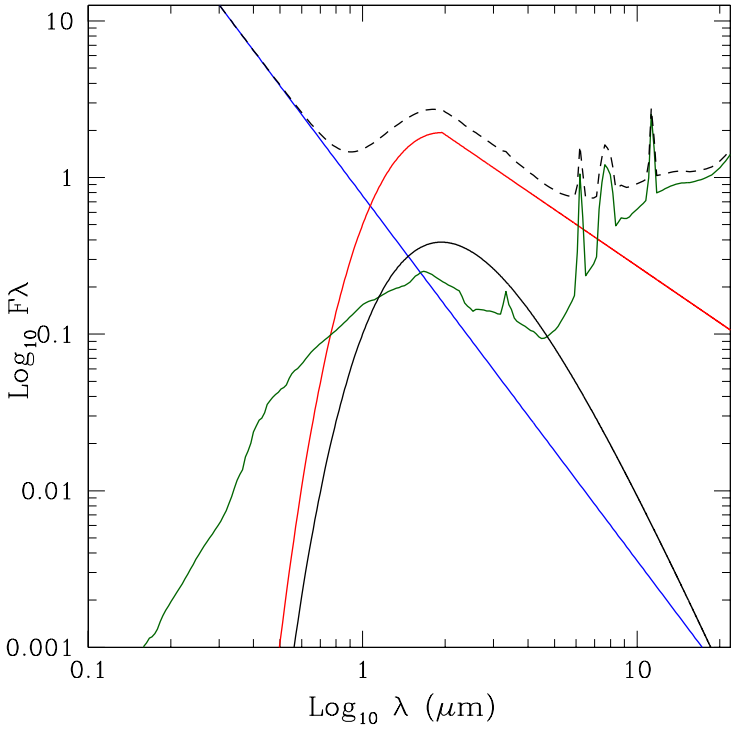

Figure 6.2: Schematic diagram plotting the components of the model. I plot the flux, (F_λ), against wavelength (λ) for the accretion disk (blue), torus component radiating at all temperatures below the sublimation temperature, (assumed to be 1500 K; red), the hot black-body component radiating at a temperature of 1500 K (black) and spiral host galaxy (green) components. In addition, I plot the combined SED (which sums all the components) above the components (dashed line). Note that I have only presented the spiral host galaxy template as an example, and the relative contributions of each component of the flux have been arbitrarily chosen such that they can be illustrated on the figure.

6.3 Model fits

Presented in this section are the results of the modelling of the 2MASS AGN near- to mid-IR colours. Note that I begin by only varying one parameter in each section. This is to determine the feasibility of the explanations for the red colours of the 2MASS AGN outlined in Chapters 4 and 5.

6.3.1 Covering factor

There are a few objects in the 2MASS sample that, according to the results presented in Chapters 4 and 5, have near-IR colours which cannot be explained by moderate/high levels of dust extinction. Instead of dust extinction, it is possible that the near-IR colours of the 2MASS AGN are the result of unusually high covering factors of the torus dust (C_D), that is radiating at all temperatures below the dust sublimation temperature. In Chapter 5 I showed that, in terms of their mid-IR luminosities, some 2MASS AGN have high ratios of mid-IR to NLR covering factors. These high ratios could be the result of a high covering factor for the torus.

In this section, I use the model to show how varying the covering factor impacts on the near- to mid-IR colours of AGN. The results are presented in Figures 6.3 and 6.4. Note that I model the AGN at redshifts of 0, 0.1 and 0.2, as well as assuming three different sublimation temperatures for the dust grains: 1200 K, 1500 K and 1800 K. It must be stated that there will be degeneracies when reproducing the near- to mid-IR colours of the AGN when varying both the redshift and sublimation temperature, because both will have significant effects on the observed wavelength position of the point of inflection. Initially I assume there is no extinction, no host galaxy contribution and no emission from an additional hot dust component. As well as reproducing the colours for the 2MASS AGN, it is my aim to reproduce the colours of the unobscured type 1 comparison AGN in this section, so that I can define a standard set of parameters that reproduce the typical colours of the unobscured AGN component. This can then be used to help model the red 2MASS AGN.

It is clear from Figures 6.3 and 6.4 that the colours of the majority of the comparison type 1 AGN can be explained by a combination of sublimation temperature and covering factor alone. The parameters required for the models to reproduce the median colours of the comparison samples are given in Table 6.2. When compared to the work outlined in $\oint$ 5.3.3, the torus covering factors required by the model to reproduce the median colours of the PG quasars and unobscured type 1 AGN, are within the ranges indicated

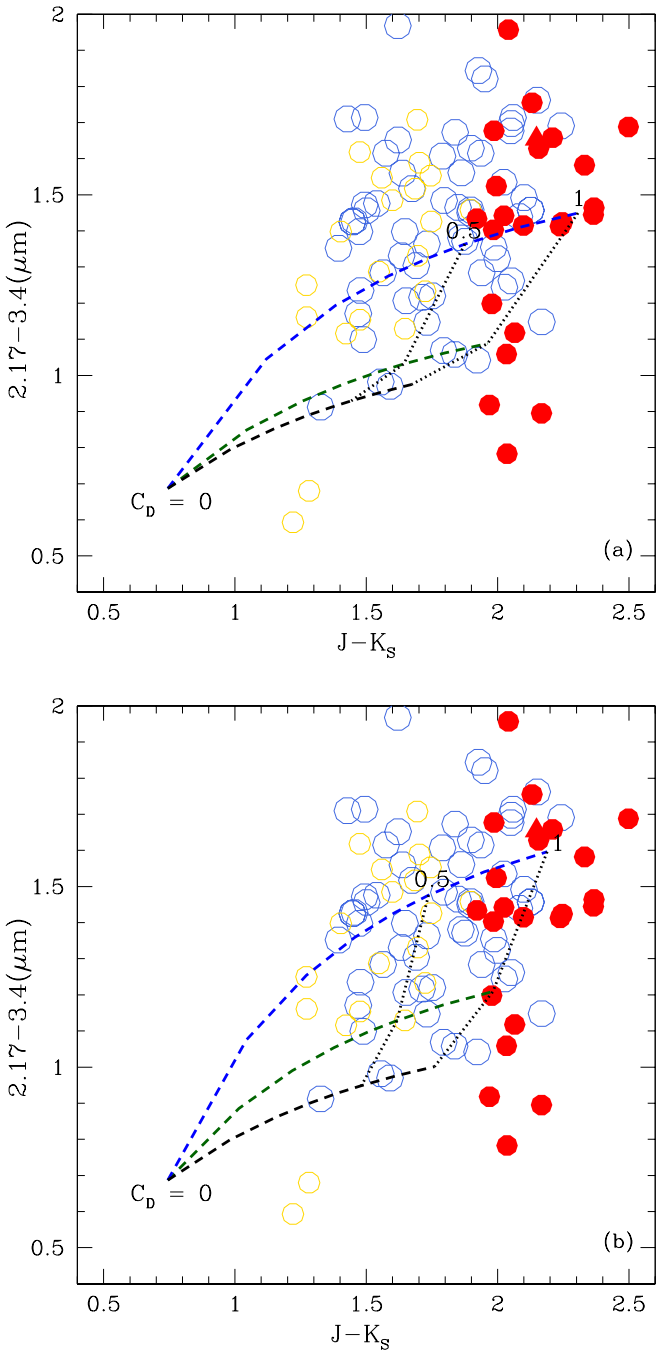

Figure 6.3: 2.17-3.4μm versus J-K$_S$ model results, varying the covering factor of the torus over the range $0 < C_D < 1$. For each model, covering factors of 0.2 and 1 for each temperature model are joined by a dotted line. Plot (a) shows the model results at a redshift of z = 0, (b) gives z = 0.1, and (c) gives z = 0.2. The red 2MASS AGN are represented by red circles, PG quasars by open blue circles and the unobscured type 1 AGN population are represented by open gold circles. The sublimation temperatures of the dust grains are modelled as 1200 K (blue), 1500 K (green) and 1800 K (black).

CONTINUED ON NEXT PAGE

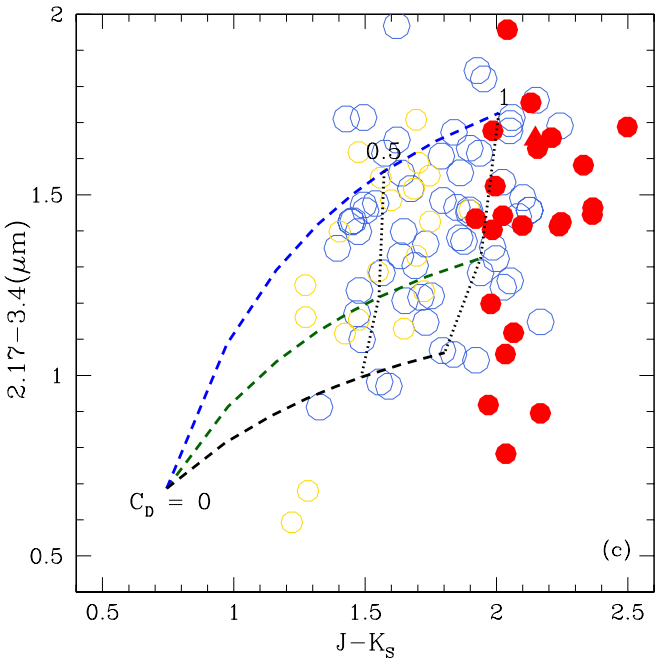

Figure 6.3: CONTINUED

in § 5.3.3: $0.1 < C_{mir} < 1$[4]. In addition, despite the potentially large uncertainties associated with calculating the covering factors using F_{BOL} (see § 6.3.1), the results are consistent with the opening angles typically estimated for the torus (45 to 60 degrees e.g. Tadhunter & Tsvetanov 1989).

Lower sublimation temperatures lead to redder mid-IR colours when compared to higher temperatures. Therefore by modelling a lower temperature than 1200 K the colours of the comparison AGN, which are not covered by the current models, can easily be reproduced. In addition, *I used the median slope of the SED of the PG quasars to describe the torus emission at all temperatures. This slope does not describe the torus emission of* **all** *the comparison AGN, therefore, in future work, the slope could be a variable as well.*

Now considering the 2MASS AGN, it appears that the colours of the type 1 2MASS AGN, which do not show evidence for an additional component of dust emission, can be modelled by increasing the covering factor of the torus alone. The redshifts, torus covering factors and dust grain sublimation temperatures required to produce an AGN

[4]The majority of the mid-IR luminosities of these AGN could be described with NLR and mid-IR covering factor ratios, R, between R = 5 and R = 25. Given the assumed ranges of the NLR covering factor ($0.02 < C_{nlr} < 0.08$; Netzer & Laor 1993), this leads to a lower limit for the torus covering factor of 0.1, and an upper limit of 1.

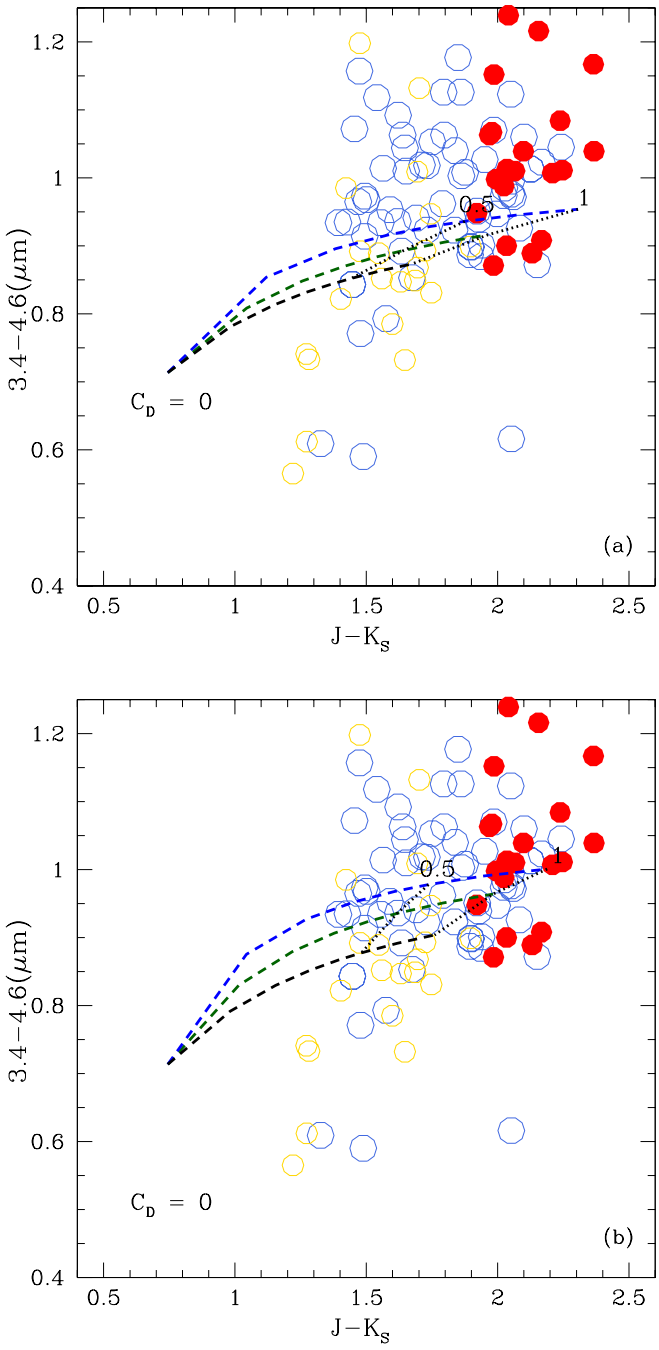

Figure 6.4: 3.4-4.6μm versus J-K$_S$ model results, varying the covering factor of the torus over the range $0 < C_D < 1$. Plot (a) shows the model results at a redshift of z = 0, (b) gives z = 0.1, and (c) gives z = 0.2. All the components of these plots are described in the caption of Figure 6.3. CONTINUED ON NEXT PAGE

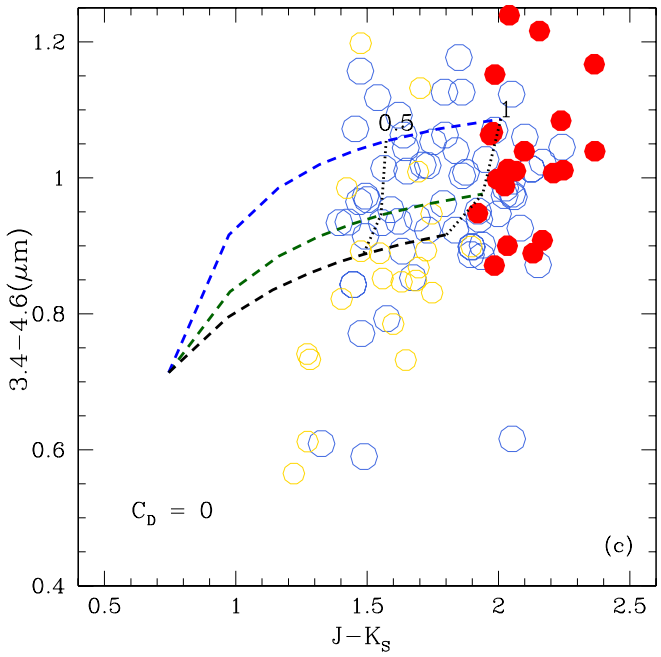

Figure 6.4: CONTINUED

Table 6.2: Model results showing the combination of redshift, torus covering factor and dust grain sublimation temperature needed to produce an AGN with the median J-K$_S$ colours of the comparison AGN, within one error bar, and an AGN with J-K$_S$ > 2.0. Note that I do not present results where a torus covering factor greater than 1 was required to produce the required J-K$_S$ colours.

Model	PG	Unobscured Type 1	J-K$_S$ > 2.0
z(1200K)			
0	0.43±0.02	0.31±0.02	0.62
0.1	0.55±0.03	0.40±0.03	0.76
0.2	0.72±0.05	0.53±0.08	0.99
z(1500K)			
0	0.68±0.03	0.46±0.04	-
0.1	0.70±0.04	0.48±0.03	-
0.2	0.77±0.05	0.55±0.04	-
z(1800K)			
0	-	0.78±0.08	-
0.1	1.0±0.1	0.67±0.06	-
0.2	0.97±0.04	0.65±0.05	-

with J-$K_S > 2.0$, are presented in Table 6.2. The torus covering factor needed to produce an AGN with J-$K_S > 2.0$ is clearly greater than that required to reproduce the J-K_S colours of the comparison type 1 AGN.

In § 5.3.3, I showed that covering factors of $0.25 < C_{mir} < 1$ are required to produce the observed mid-IR luminosities at the [OIII] luminosities of the red 2MASS AGN. The torus covering factors outlined in Table 6.2 are within the ranges indicated in Chapter 5, supporting the view that the red J-K_S colours of some of the 2MASS AGN are the result of unusually high torus covering factors. This is interesting because it demonstrates that, for a significant fraction of the type 1 AGN, it is plausible that their red colours can be the result of high covering factors for the torus. However, simply increasing the torus covering factor is not by itself sufficient to explain the red near- to mid-IR colours of the *entire* sample.

In the following sections I investigate how varying other parameters affects the colours of AGN. Note that I only use models based on a redshift of z = 0.1, which is within the uncertainties of the median redshift of the redshift limited comparison samples (0.10±0.01 and 0.08±0.05 for the PG quasars and unobscured type 1 AGN respectively), and standard torus covering factors of 0.48, 0.64 and 0.84, which give a reasonable approximation of the colours of 'typical' unobscured AGN with dust sublimation temperatures of 1200K, 1500K and 1800K respectively.

6.3.2 Moderate reddening

In this section I explore how varying the levels of dust extinction can affect the near- to mid-IR colours of AGN. I first investigate the impact of moderate extinction levels. Then I compare the levels of extinction required in the models to those found observationally.

From the work in Chapters 4 and 5, there is strong evidence that the majority of the red colours of the 2MASS AGN are the result of moderate levels of dust extinction. In Figure 6.5, I model AGN assuming the three different sublimation temperatures as before. I then redden these AGN up to an extinction of $A_V = 4$ to determine how feasible it is to produce the red colours of the 2MASS AGN by dust extinction alone, assuming a typical torus covering factor of 0.5.

Figure 6.5 shows that, like in § 6.3.1, the colours of the type 1 2MASS AGN, which do not show evidence for an additional component of emission, can be modelled by moderate levels of extinction alone ($A_V \sim 2$). This highlights a possible degeneracy in the models when producing some of the colours of the 2MASS AGN. In addition, I have tested an alternate extinction law, presented in Nishiyama et al. (2009), in order

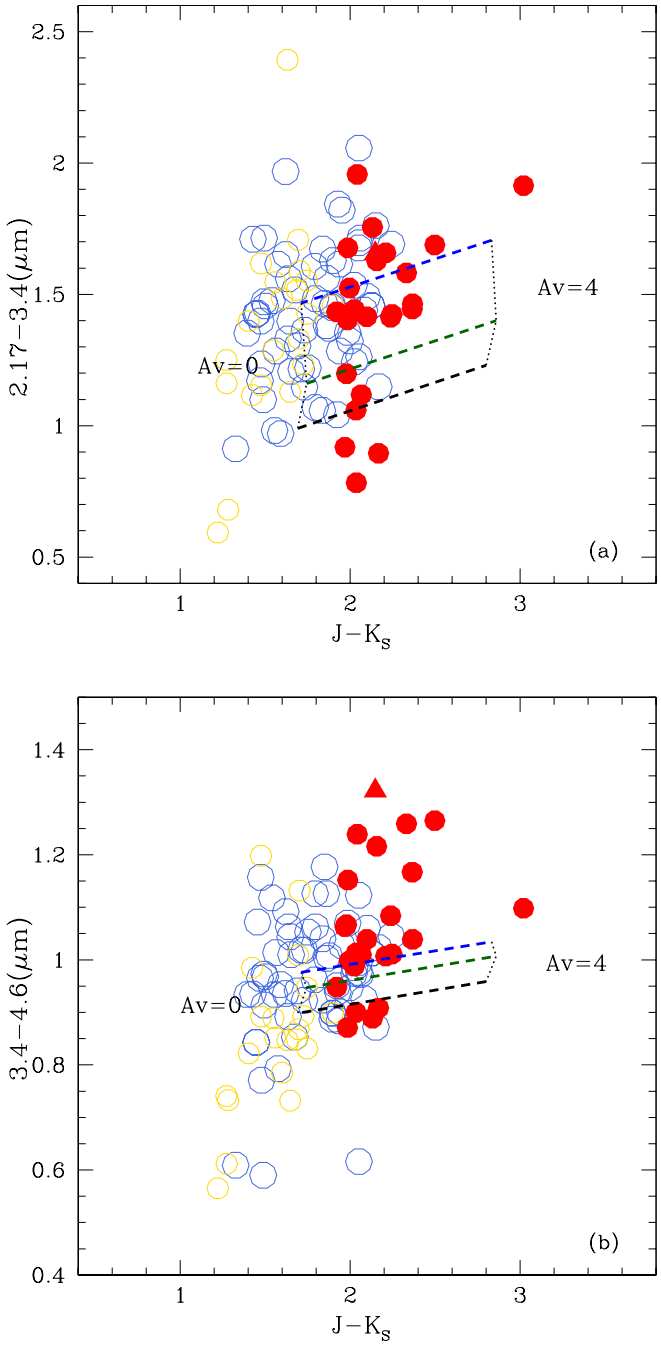

Figure 6.5: (a) the 2.17-3.4μm versus J-K$_S$, and (b) 3.4-4.6μm versus J-K$_S$ model results varying the levels of dust extinction. The red 2MASS AGN are represented by red circles, PG quasars by open blue circles and the unobscured type 1 AGN population are represented by open gold circles. The sublimation temperature of the dust grains are modelled as 1200 K (blue), 1500 K (green) and 1800 K (black). In addition, a line is plotted joining the model results at extinctions of $A_V = 0$ and 4 (labelled dotted lines).

to check how important the assumed law is when determining the colours of the 2MASS AGN with this model. I have found that, at least for the wavelength range used in this model, a different extinction law has very little affect on the colours determined by the model. Nevertheless, I have shown that moderate levels of reddening can indeed produce the red J-K_S colours of the 2MASS AGN, supporting the results based on the Balmer decrements presented in Chapter 4. However, additional modelling is required for the type 2 2MASS AGN, and type 1 AGN with blue 2.17-3.4μm colours.

Comparing the models to the observational results

In Chapter 4, I measured the Balmer Decrements of the 2MASS sample in order to determine the levels of extinction in these objects. The results suggested that the J-K_S colours of the majority of the 2MASS AGN can be explained by moderate levels of reddening. In this section, I test whether the model for the mid-IR continuum gives similar levels of extinction to those derived from the Balmer decrements in Chapter 4. Note that there is a caveat with this approach, in the sense that this technique is likely to underestimate the AGN extinction in objects with significant host galaxy contamination. For the observational data, I only use the Balmer decrements for objects where broad Balmer emission is detected. Where possible I use the separated BLR Balmer decrement. However, in cases where I could not separate the narrow and broad emission, I use the total Balmer decrement. I model an AGN with a covering factor of 0.48, at a redshift of 0.1, assuming a sublimation temperature for the grains is 1500 K. The J-K_S colour of this default AGN is 1.60. The results are presented in Table 6.3 and illustrated in Figure 6.6.

From the results presented in Table 6.3, it appears that the model has successfully matched 6 of the objects' extinction estimates (within 3 σ) from the observational data. The extinctions in 3 of the objects were underestimated, most likely because there may be host galaxy contamination in these objects. And the extinction in the other 5 objects were overestimated, probably because there is a higher covering factor of torus dust in these objects. In fact, two of the latter objects are those with bluer 2.17-3.4μm colours. These results highlight the probability that some of these objects require more than one component in the model to describe their red colours. However, it should be noted that the extinctions calculated using the model (with the exception of the object J1040+59) are all relatively moderate. This scatter described here are illustrated on Figure 6.6 in the sense that the points fall both well above and below the one to one relationship between the extinction estimates.

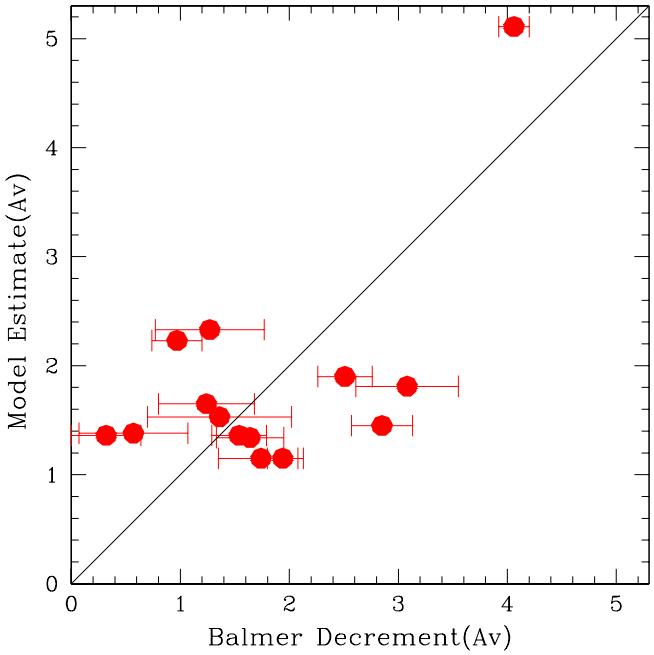

Figure 6.6: Extinction estimates based on those derived from the model compared to those estimated from the Balmer decrements. In addition, I have plotted a line showing a one to one relationship between the extinction estimates based on the model results, and those estimated from the Balmer decrements.

Table 6.3: Extinction comparisons between the results based on the Balmer decrements, and those derived from the model. The A_V^{BAL} column gives the extinction estimates determined from the Balmer decrements presented in Chapter 4. The A_V^{MOD} column gives the extinctions needed in order for the models to produce the J-K_S colour of each object.

Object	A_V^{BAL}	A_V^{MOD}
J0248+14	2.51 ± 0.25	1.90±0.02
J0312+07	1.54 ± 0.25	1.36±0.02
J0400+05	2.85 ± 0.28	1.45±0.01
J0422-18	0.97 ± 0.23	2.23±0.01
J0435-06	0.32 ± 0.32	1.36±0.01
J0447-16	3.08 ± 0.47	1.81±0.02
J1006+41	1.94 ± 0.14	1.15±0.02
J1014+19	1.74 ± 0.39	1.15±0.02
J1040+59	4.06 ± 0.14	5.11±0.02
J1127+24	1.64 ± 0.31	1.34±0.02
J1212-14	1.24 ± 0.44	1.65±0.02
J1323-02	1.27 ± 0.50	2.33±0.02
J1338-04	0.57 ± 0.50	1.38±0.01
J1448+44	1.36 ± 0.66	1.53±0.01

6.3.3 High reddening with host galaxy emission

In Chapter 5, I noted that, while the J-K_S colours of the type 2 2MASS AGN are not significantly redder to those of the type 1 2MASS AGN, their 3.4-4.6μm colours are redder. I hypothesised that this is likely the result of a combination of high levels of dust extinction due to the torus, and stellar emission from the host galaxy. I now test whether this is feasible using the model.

In Figure 6.7, I plot the model results for a highly reddened AGN that is contaminated by stellar emission from the host galaxy. The flux contribution of the host galaxy required to reproduce the J-K_S, 2.17-3.4μm and 3.4-4.6μm colours is in the range 70-92% of the total flux in the J-band. Note that I only use the elliptical galaxy template in the model. This is because the differences in the colours computed with different host galaxy models is negligible at these wavelengths. I model an AGN at a redshift of z = 0.1, with a dust sublimation of 1200 K, and a torus covering factor of 0.5.

It is clear from Figure 6.7 that the colours of the type 2 2MASS AGN can be explained by the combination of high levels of AGN reddening plus some host galaxy contamination. However, there are inconsistencies between the required combinations of dust extinction

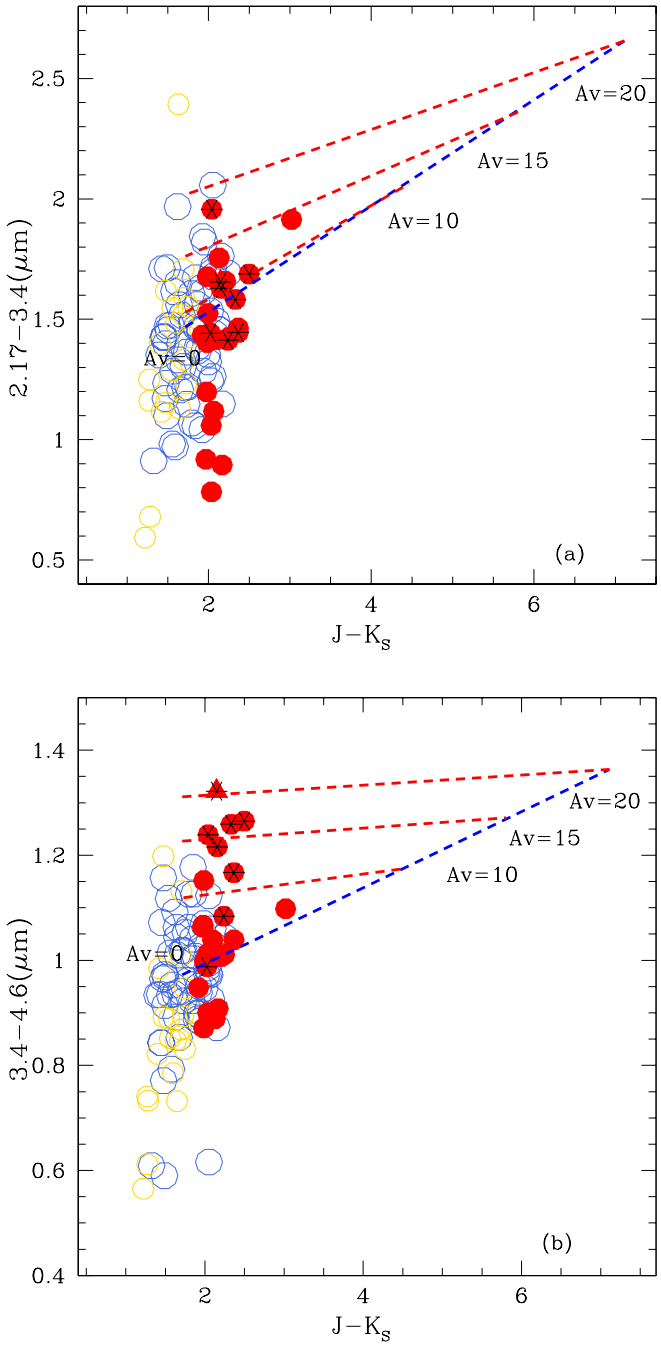

Figure 6.7: (a) the 2.17-3.4μm versus J-K$_S$, and (b) 3.4-4.6μm versus J-K$_S$ model results for high levels of dust extinction coupled with host galaxy emission. I include the host galaxy in the model after I have reddened the AGN by an extinction of A_V = 10, 15 and 20. The red 2MASS AGN are represented by red circles, PG quasars by open blue circles and the unobscured type 1 AGN population are represented by open gold circles. The dashed red line is for the model using the elliptical host galaxy, where the host galaxy contribution to the J-band is increasing from the right to the left in J-K$_S$ colours.

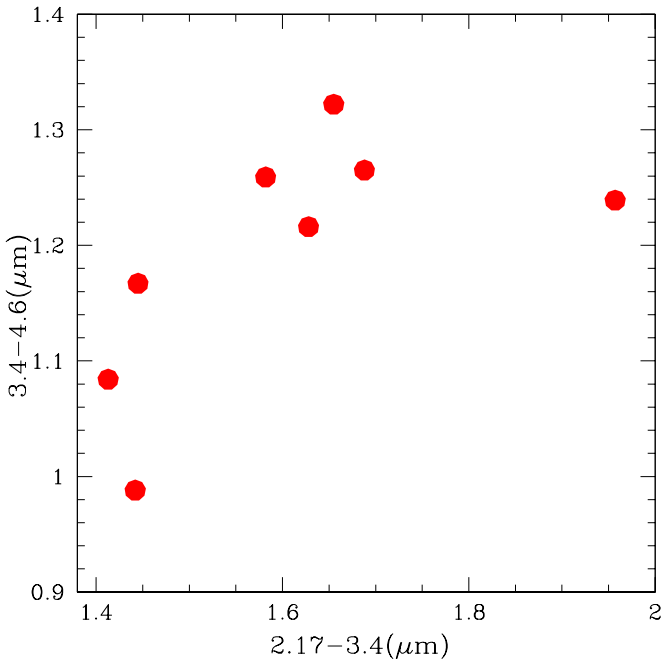

Figure 6.8: The 3.4-4.6μm colours of the type 2 2MASS AGN plotted against the 2.17-3.4μm colours. Note the lack of clear correlation between the two colours.

and host galaxy emission when reproducing both the 2.17-3.4μm and 3.4-4.6μm colours of the AGN. This is because there is considerable scatter in the 2.17-3.4 colours i.e. there is little correlation between the 2.17-3.4μm and 3.4-4.6μm colours of the type 2 objects. Evidence for this scatter is clear from the SEDs of individual 2MASS AGN (see Chapter 5): some of the SEDs of the type 2 AGN appear to be a composite of a highly reddened AGN, with an additional, weak, hot dust component. This scatter is illustrated in Figure 6.8.

Overall, it is likely that the near- to mid-IR colours of the type 2 2MASS AGN are the result of a combination of large levels of dust extinction due to the torus, and host galaxy contamination. However, at present, the model is not complex enough to describe the scatter in the 2.17-3.4μm and 3.4-4.6μm colours of these objects.

6.3.4 Additional hot dust component

On the 2.17-3.4μm colour-colour plots in Chapter 5 I identified 6 type 1 2MASS AGN with unusually blue (<1.3) 2.17-3.4μm colours. I also identified an additional object (J1323-02) whose near- to mid-IR SED indicates the presence of this additional emission. The combination of the red J-K_S and blue 2.17-3.4μm colours cannot be easily explained

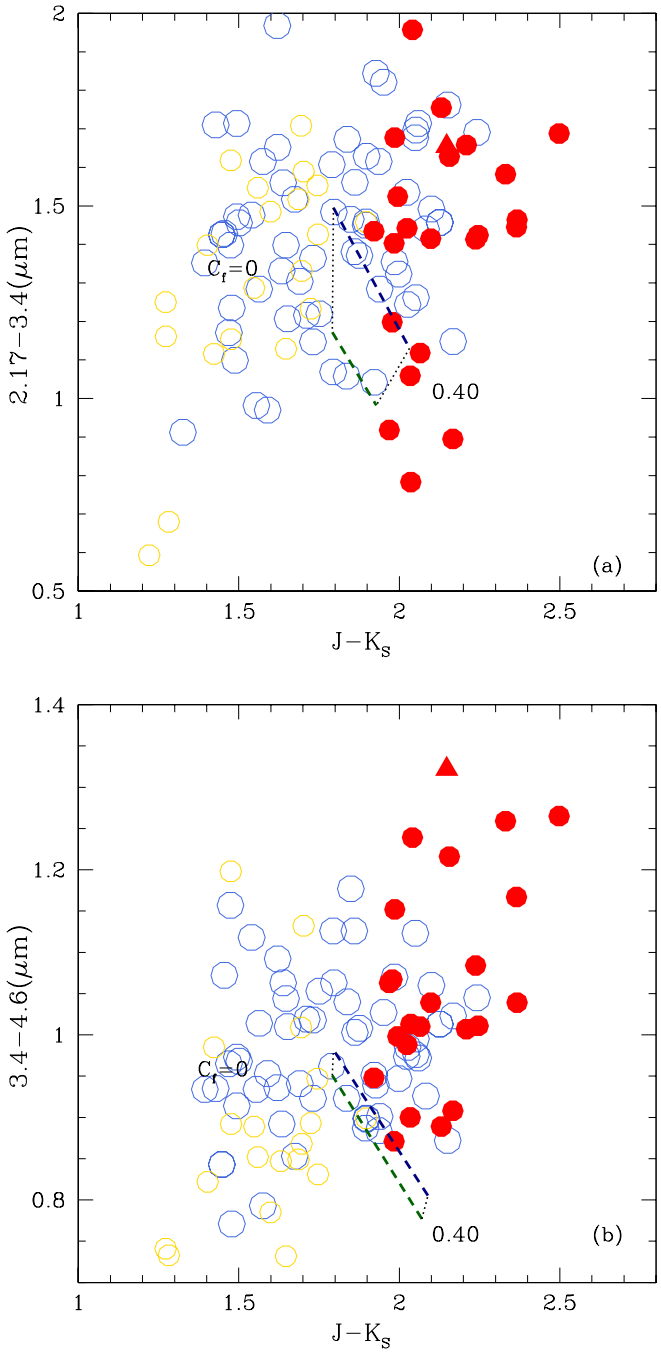

Figure 6.9: (a) the 2.17-3.4μm versus J-K$_S$, and (b) 3.4-4.6μm versus J-K$_S$ model results including an additional black-body emitter. The red 2MASS AGN are represented by red circles, PG quasars by open blue circles and the unobscured type 1 AGN population are represented by open gold circles. The sublimation temperatures of the dust grains are modelled as 1200 K (blue) and 1500 K (green). In addition, dotted lines are plotted joining the model results with hot black-body emitter covering factors of 0 and 0.4 (labelled dotted lines).

in terms of reddening effects, or host galaxy contamination in these objects. However, these colours are consistent with there being an additional component of emission, which is radiating at a temperature that coincides with the K_S band. This is supported by the shapes of the individual SEDs presented in ∮ 5.4.1.

To attempt to explain this trend, I have added an additional black-body emitter to the models. To do this I model AGN at a redshift of z = 0.1, with zero host galaxy contribution, which have torus covering factors of 0.55 and 0.6, for sublimation temperatures of 1200 K and 1500 K respectively. These covering factors are chosen such that their colours represent the median colour of the PG quasars. I model the additional black-body emitter to have a temperature of 1600 K, in order to ensure that it is hotter than the inner wall of the modelled torus. I vary the covering factor of the emitter (C_{BB}) from a covering factor of 0, up to a covering factor of 0.4, so as not to exceed a total covering factor of 1 for the combined torus and additional black-body emission. The emitter is modelled as an optically thick black body. Note that I do not model a torus with a sublimation temperature of 1800 K. This is because the bulk of the emission of the hotter black-body emitter will be shifted into the J-band.

It is clear from Figure 6.9(a) that this additional component struggles to reproduce the bluest 2.17-3.4μm colours of the 2MASS AGN. In addition, the model overestimates the flux contribution at longer wavelengths: in Figure 6.9(b) the resulting 3.4-4.6μm colours are bluer than observed. This is possibly because, at longer wavelengths (or at lower frequencies), the combination of emission from the torus and black-body emitter over-predicts the fluxes in both the 3.4μm and 4.6μm bands.

However, while an optically thick black body may contribute too much flux at longer wavelengths, an optically thin dust emitter, whose peak coincides with the K_S-band may not. To test this, I model an AGN with the same parameters as used in Figures 6.9(a)&(b), however, rather than modelling the additional component as an optically thick black body, I model it as an optically thin clump of dust using the modified black-body law appropriate for optically thin dust emission:

$$f(\nu)_B = \frac{2h\nu^{3+\beta}}{c^2}\frac{1}{e^{h\nu/kT}-1}, \tag{6.5}$$

where all the parameters, with the exception of β, are outlined in ∮ 6.2.2. β is the spectral index of the dust emissivity law, and varies between a value of 1 and 2 for typical ISM dust grains (Draine, 2006). In Figure 6.10 I compare an optically thick black-body curve to modified black-body curves with β values of 1 and 2, which is the range indicated for β discussed in (Draine, 2006). It is clear that in optically thin cases

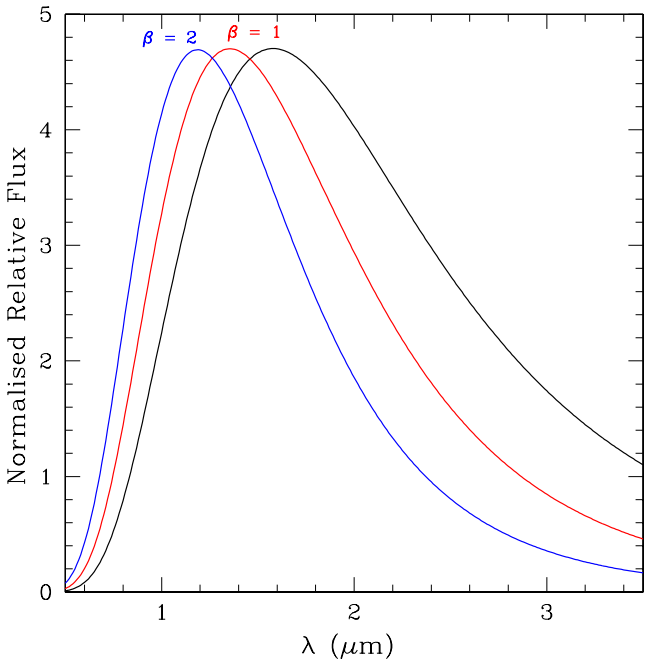

Figure 6.10: The optically thick and optically thin black-body curves. The flux is plotted as F_λ. The optically thick curve is plotted in black, optically thin curve with a spectral index of β=1 is plotted in red, and the optically thin curve with a spectral index of β=2 is plotted in blue. Note that the black bodies are all modelled with a temperature of 1500K.

there is less emission at longer wavelengths when compared to optically thick cases; the wavelength of the peak of the black-body curves also change. In addition, higher spectral indices result in less flux emitted at longer wavelengths. Therefore, it is conceivable that an optically thin black-body emitter could produce the observed colours of the 2MASS AGN with blue 2.17-3.4μm colours.

The model results including optically thin dust emission are shown in Figures 6.11(a) & (b). These models clearly do not overestimate the flux in the 3.4μm WISE band (see Figure 6.11(b)), while still reproducing the blue 2.17-3.4μm colours (see Figure 6.11(a)). In Figures 6.11(a) & (b) I present the results which model the optically thin emitter with a spectral index of β=1. Modelling the emitter with higher spectral indices also produced the required colours, however at spectral indices $\beta > 1.4$, while the 2.17-3.4μm and 3.4-4.6μm colours could be reproduced with higher covering factors for the component, the J-K_S became too blue (J-K_S < 1.6). This is to be expected because, as illustrated in Figure 6.10, modified black bodies with higher spectral indices will emit even less flux at longer wavelengths while maintaining similar levels of emission at shorter wavelengths.

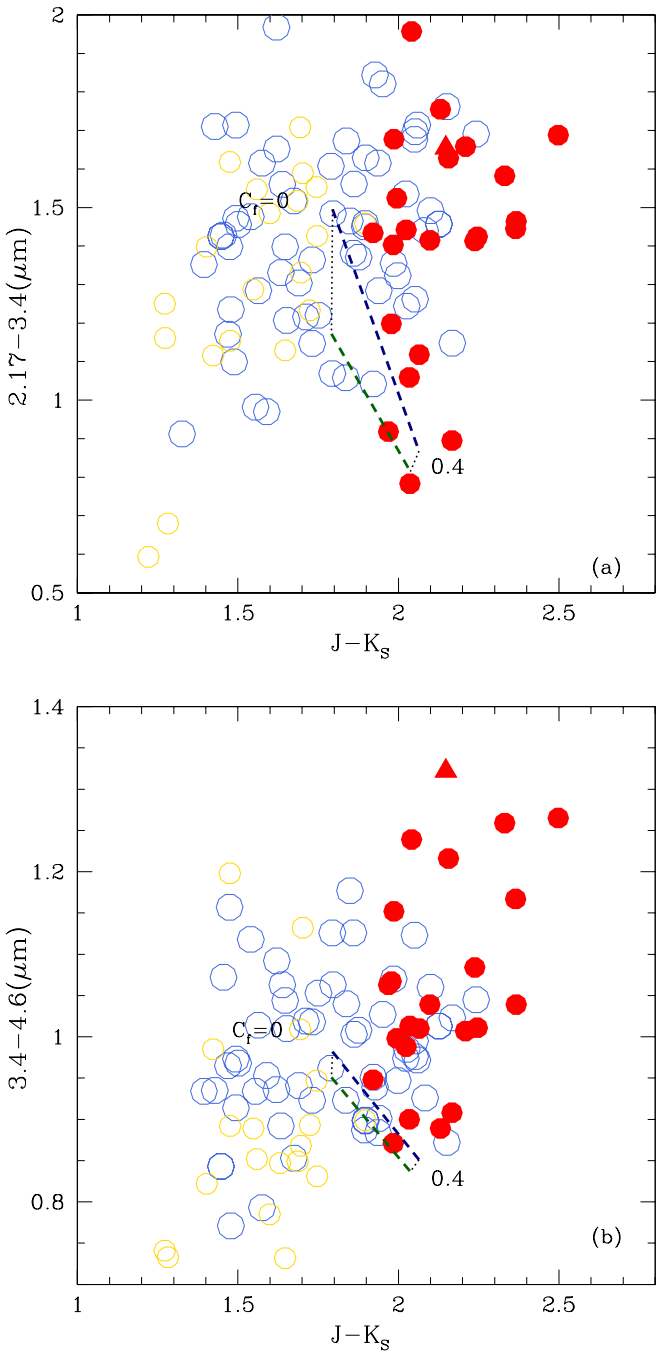

Figure 6.11: Similar plots to those of Figures 6.9(a)-(b), however the additional black-body emitter is modelled as an optically thin emitter with a spectral index of β=1. Note that a line is plotted joining the models results with black-body emitter covering factors of 0 and 0.4 (labelled dotted lines).

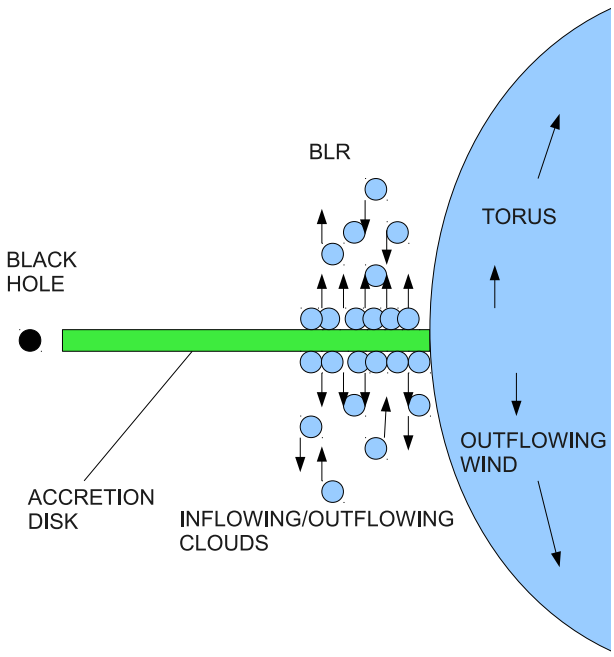

Figure 6.12: Figure 1 from Czerny & Hryniewicz (2011).

Therefore, I have shown that an additional component of hot dust emission is a feasible explanation for the observed colours of these AGN, as long as it is optically thin.

The fact that this component needs to be optically thin in order to reproduce both the red J-K_S, and blue 2.17-3.4μm colours is interesting. This is because it implies that if a clump of dust has 'broken off' from the torus (see § 5.3.4), it would be a small cloud, and therefore its physical size and optical depth would be small. Alternatively, much of the dust in the cloud could have sublimated resulting in a small optical depth.

However, this additional hot dust emission need not originate from a clump of dust that has 'broken off' from the torus. Using reverberation techniques, Czerny & Hryniewicz (2011) placed constraints on the origin of the BLR in AGN. Their evidence suggests that a strong local dusty wind from the cooler outer parts of the accretion disk causes the BLR to form. As a dusty clump in the wind rises above the disk, it is exposed to the radiation from the central source, sublimating the dust, reducing the radiation pressure and causing the clump to fall back to the accretion disk. This allows for a mixture of both inflowing and outflowing dusty clouds, as illustrated in Figure 6.12. In this scenario it is conceivable that we are viewing the emission from sublimating clouds above the accretion disks that have unusually large covering factors, resulting in both the red J-K_S and blue 2.17-3.4μm colours.

Overall, the work presented on the 2MASS AGN with blue 2.17-3.4μm colours further

supports the growing evidence for additional emission at near- to mid-IR wavelengths (e.g. Mor, Netzer & Elitzur 2009; Czerny & Hryniewicz 2011), which is not clearly associated with the host galaxy or the torus. In addition, I find that this component of emission is likely to be optically thin, so as to ensure that the modelled emission at longer wavelengths is not overestimated when compared to the observational evidence.

6.4 Summary

This chapter has concerned the emission mechanisms which define the near- to mid-IR colours of the red 2MASS AGN. I have tested the four main hypotheses outlined in Chapters 4 and 5 by producing a model which considers the main components of an AGN, and calculates the near- to mid-IR colours. Remarkably, this model shows that all the hypotheses are plausible, meaning that the colours of the red 2MASS AGN the result of either (a) moderate levels of dust extinction; (b) unusually high covering factors of the torus; (c) high levels of dust extinction (possibly due to the torus) coupled with host galaxy emission; (d) contain an additional source of optically thin hot dust emission; or (e) a combination of these effects.

In the final chapter I conclude the thesis, outlining how I have answered the questions put forward in Chapter 1. I also group the sample into the likely explanations for their near- to mid-IR colours. In addition, I summarise any future work required to further understand this 2MASS sample.

Chapter 7

Conclusions and future work

A key result of the 2MASS survey was the discovery of a population of luminous AGN that appear redder than their traditional optical/UV selected counterparts at IR wavelengths (J-K_S > 2.0). These red AGN are important because they represent a large fraction of the overall population of AGN in the local Universe (up to 60%; Glikman et al. 2007). Therefore, characterising this population is critical to our general understanding of active galaxies. To this end, this thesis has presented the results of optical spectroscopic observations of an RA-limited sample of 29 2MASS-selected AGN (J-K_S $\gtrsim$ 2.0) with a narrow range of redshifts: 0.09 < z < 0.28. In addition, this has been followed up with a photometric study of the near- to mid-IR continuum emission of the sample.

In this chapter I summarise the main conclusions in the thesis, incorporating both the detailed study of the object J1131+16, and the results for the full red 2MASS AGN. I then conclude the chapter with ideas for follow-up studies of the red 2MASS AGN.

7.1 Conclusions

From the analysis of red 2MASS AGN in previous studies, there appear to be two main models to explain the red near-IR colours of these objects: (a) they are young, dust enshrouded, transitional objects (Glikman et al. 2004, 2007, 2011, 2012; Shi et al. 2007; Georgakakis 2009; Urrutia et al. 2008, 2009, 2012), or (b) they are objects which are simply reddened by dust in the host galaxy/torus (Smith et al. 2002; Marble et al. 2003; Kuraszkiewicz et al. 2009a,b). The studies that support the first hypothesis used samples which extend up to relatively high redshifts (z $\gtrsim$ 0.2), included an optical colour selection criterion as well as a near-IR colour selection, and some of the studies required

that the objects had broad emission lines. These additional selection criteria were used because they favour more extreme objects that are likely to be genuinely young and dust enshrouded. However, from the results of my analysis of the sample of low redshift red 2MASS-selected AGN presented in this thesis, I find no evidence to support this view, based on the [OIII] outflow properties, the incidence of NLS1, and the distribution of Eddington ratios.

Instead, I have found that much of the evidence provided by the optical spectra of red 2MASS-selected AGN supports the findings in other studies: the red near-IR colours of many of the objects are simply the result of moderate level of extinction by dust in the outer layers of the torus, or in the disk of the host galaxy. In addition, rather than being moderately extinguished AGN, I find that some of these objects are genuine type 2 objects, in which the torus completely extinguishes the broad-line AGN in the optical and shorter wavelength near-IR bands. The reddening hypothesis is supported by the Balmer decrements which provide evidence for significantly higher levels of reddening in the type 2 2MASS AGN population compared to samples of UV/optical selected AGN; it is also consistent with the near- to mid-IR colours measured for some of the type 1 objects in the sample. However, this is not the complete picture since, while some objects are moderately reddened at optical wavelengths (E(B-V) $\approx$ 1.4), others show relatively little (if any) evidence for reddening, and have optical continuum shapes that appear similar to UV/optical selected AGN.

Emission from hot dust (T $\sim$ 1500K) could also result in red near-IR colours. From my investigation of the near- to mid-IR colours of the sample, I find that there are two sources of dust emission which could contribute to the red near-IR colours of the red 2MASS-selected AGN: enhanced emission from circumnuclear dust in the torus due to an unusually high covering factor for the torus dust; and emission from an additional component of hot dust which is radiating at close to the sublimation temperature of the dust grains. A larger than average covering factor for the dust in the torus would increase the flux measured in the K_S-band relative to that of the J-band (likely dominated by accretion disk emission), thus producing the red J-K_S colours measured for objects in the 2MASS sample. The evidence supporting the idea that the red colours are a result of emission from the torus include the fact that some of the 2MASS objects, when comparing their [OIII]λ5007 emission to their mid-IR emission, require large circumnuclear dust covering factors to explain their [OIII]λ5007 to mid-IR flux ratios. This explanation was confirmed by my modelling the near- to mid-IR emission of the AGN which showed that higher covering factors for the circumnuclear dust do indeed result in redder J-K_S colours. However, it must be noted that moderate levels of dust

extinction can also reproduce this result and, based on the examination of their near- to mid-IR continuum colours, some objects may require both dust extinction and a larger than average covering factor for the dust in the torus (e.g. J0447-16 and J1127+24).

In addition, a significant fraction of 2MASS-selected objects (26%) have blue 2.17-3.4 μm colours when compared to the rest of the 2MASS-selected AGN, leading to the suggestion that there is an additional component of hot (T $\sim$ 1500K) dust emission which is radiating at a temperature that coincides with the K_S-band. Modelling this component revealed that it is likely to be an optically thin dust component, which is emitting at a temperature close to the sublimation temperature of the dust grains in the torus.

Overall, based on the evidence provided by both the optical spectra and near- to mid-IR continuum emission, I find that the red 2MASS-selected AGN are a heterogeneous population: no single mechanism can explain the properties of the full sample. The sample can be divided into the following four groups to explain their red near-IR colours[1].

- **Moderate levels of dust extinction in type 1 AGN:** J0248+14, J0312+07, J0400+05, J0422-18, J0447-16, J1006+41, J1040+59 and J1321+13.
- **High levels of dust reddening coupled with significant host galaxy emission i.e. 'genuine' type 2 AGN:** J0221+13, J0306-05, J0504-19, J0910+33, J1057-13, J1131+16 J1158-30, and J1407+42.
- **Emission from an additional component of hot, optically-thin dust:** J0409+07, J0435-06, J1014+19, J1127+24, J1212-14, J1323-02 and J1448+44.
- **Not readily explained by any of the interpretations given above:** J1338-04 and J2124-17.

However, based on the near- to mid-IR SEDs presented in Chapter 5, and the modelling in Chapter 6, there may be some overlap in these explanations i.e. the colours could be the result of moderate reddening coupled with a high torus covering factor (e.g. J0447-16 and J1127+24, see above).

In addition, the serendipitous discovery of the object J1131+16, an AGN which has the richest spectrum of FHILs yet reported for an AGN, provides a rare opportunity to investigate the physical conditions and kinematics of the region(s) emitting the FHILs. I find that the FHIL emitting region has a high electron density ($n_e > 10^6$ cm^{-3}) and

[1]Note that the two LINER/HII composite objects have not been categorised. This is because I have concentrated solely on the confirmed AGN in this thesis. See Chapter 4 for more details.

ionisation parameter, yet its kinematics are similar to those of the low ionisation emission line region detected in the same object. The deduced physical conditions lie between those of the BLR and the NLR of AGN, and the FHIL emitting regions must be situated relatively close to the illuminating SMBH. I find that the inner torus wall is the most likely location for the FHIL region, and that the unusual strength of the FHILs in this object is due to a specific viewing angle of the far wall of the torus, coupled with a lack of dust on larger scales that might otherwise obscure our view of the torus.

Overall, the results presented in this thesis provide strong evidence that the majority of the red 2MASS-selected AGN are intrinsically similar to typical UV/optical selected AGN, with little evidence that their observed colours are the result of an early evolutionary stage. The most of these AGN (64%) are obscured by moderate/large levels of dust which is located either in the extended dust structures of the host galaxies, or the circumnuclear torus. However, in a significant subset of objects, the red near-IR colours are the result of an additional component of optically thin emission which is heated close to the sublimation temperature of the dust grains in the torus (28%).

7.2 Outstanding questions and future work

The work presented in this thesis has clarified some important issues regarding the red 2MASS-selected AGN. However, there remain some outstanding questions about the red 2MASS AGN sample as a whole, as well as some of the individual objects in the sample. These are as follows.

- What is the location of the obscuring dust in the red 2MASS AGN? Does it originate in the host galaxy (e.g. large scale dust structures)? Or is it part of the torus?
- Can the red near-IR colours of the 2MASS-selected AGN be explained by dust reddening alone? Or does the reddening have to be coupled with unusually high torus covering factors, or enhanced emission from hot dust?
- How universal are the evaporating dust clumps in type 1 AGN?
- Is J0400+05 a black hole recoil candidate?

I believe that optical imaging, near-IR spectroscopy and improved SED modelling would help to tackle these questions. In the following sections, I describe the new observations/models that will be required.

7.2.1 Optical imaging

Deep optical imaging observations will aid in the understanding of the host galaxies of the 2MASS-selected AGN, and their large-scale environments. Below I outline how imaging can be used to increase our understanding of the red 2MASS AGN.

Host Galaxies. If the red AGN are indeed young, recently triggered objects, then the red 2MASS AGN are expected to have more morphological disruption than the UV/optical selected AGN. This is because morphological disturbances associated with galaxy mergers are expected to disperse over relaxation timescales (Barnes, 1988), implying that the young AGN would not have had enough time to lose their morphological irregularities. Using the scheme first used by Heckman et al. (1986) (and adopted by Ramos Almeida et al. 2011, Bessiere et al. 2012 and Ramos Almeida et al. 2012) to classify the level and nature of morphological disturbances (if any), I will compare the incidence of tidal disruption in red 2mass AGN to that of a comparison sample of type 2 AGN at similar redshifts[2]. In this way I will determine whether the red 2MASS AGN display more, or less, morphological disturbance in their host galaxies. Examples of morphological disturbance include features such as tidal tails, isophotal irregularities, double nuclei and bridges (Mihos, 1995) which are associated with interactions between the host galaxy and another galaxy. Such morphological features indicate that there may have been interactions with other galaxies in the recent past; such processes are often credited with the triggering of AGN (Sanders et al., 1988).

Finally, the detections of kpc-scale dust structures in the nuclear regions of the 2MASS AGN host galaxies could be used to investigate whether the moderate levels of dust extinction, implied by the optical spectra of some of these objects, could be caused by the large scale dust in the host galaxies, rather than in the torii surrounding the AGN.

In addition, the object J0400+05 is a possible black hole recoil candidate (see Chapter 4). When two SMBHs coalesce, they emit strong gravitational waves. The gravitational waves are emitted anisotropically during coalescence, removing linear momentum from the system (Bekenstein, 1973). Once the SMBHs coalesce, a single SMBH is formed, however, because of the loss of linear momentum the SMBH recoils. Certain configurations of coalescing black holes can lead to kick velocities up to several thousand km s^{-1} (Dain, Lousto & Zlochower, 2008). In terms of observational tests that involve op-

[2]Type 2 AGN are chosen because it is difficult to determine the morphologies for the host galaxies of type 1 AGN, given the bright AGN emission

tical imaging, two signatures associated with such a phenomenon come to mind. One signature is that accreting SMBHs that are recoiling should appear as quasars spatially off-set from the centres of the bulges of their host galaxies, provided that the direction of the kick is not orientated such that the AGN travels either directly towards/away from us. The other, is related to the fact that, because two SMBHs are required in order to produce a recoiling black hole, the host galaxy should show high surface brightness features characteristic of major mergers. Therefore, obtaining images of the host galaxy would confirm whether J0400+05 is indeed a black hole recoil candidate.

Galaxy environments. Another important aspect of the images is to quantify the large-scale environments of the red 2MASS AGN. This will enable us to determine how the various properties of these objects depend on the large-scale environments of their host galaxies, with implications for the AGN triggering process. An example of this is that, if cooling flows associated with massive hot X-ray haloes are responsible for triggering of activity in these objects, then one would expect to find the galaxies at the centres of clusters of galaxies. Indeed, using HST WFC3 observations, McDonald et al. (2013) detect a substantial reservoir of cold gas at the core of the Phoenix Cluster which hosts a quasar-like AGN, and find evidence that a cooling flow is responsible for this reservoir, instead of a merger of gas-rich galaxies.

7.2.2 Near-IR spectroscopy

Near-IR spectroscopy can both improve upon the results obtained from optical spectroscopy, and give further insights into the nature of these objects. The benefits of near-IR spectroscopy for the 2MASS AGN sample are discussed below.

The degree of dust extinction to the red AGN nuclei. In this thesis, the levels of extinction in the AGN have been determined using the optical Balmer emission lines: extinctions in the range $0 \leq \mathrm{E(B\text{-}V)} \leq 1.4$ have been determined. However, the caveats with estimating the extinction using Balmer decrements are (a) the flux of Hα may be boosted by collisional excitation in clouds with high electron densities (Rose et al., 2011), and (b) there are degeneracies with fitting the Hα emission line due to the blending with [NII] emission lines. Near-IR observations of the Paschen and Brackett series hydrogen lines are essential for improving on such studies, since they provide a wider wavelength baseline for the reddening determination, and are not subject to the fitting degeneracies that affect Hα. Therefore, the detection of broad Paα and Paβ would substantially im-

prove our ability to estimate the reddening by comparison with the optical Balmer line fluxes.

Are the SEDs of red quasars intrinsically different? As discussed earlier in the thesis, the red near-IR colours of the red 2MASS AGN population are not necessarily due to dust reddening effects. I have shown that it is possible that the near-IR SEDs are intrinsically red, due to an unusually large contribution from a hot dust component at longer near-IR wavelengths. By modelling the detailed, spectroscopic UV/optical/near-IR SEDs simultaneously I will be in a better position to determine whether the SEDs of the red 2MASS AGN can be reconciled with those of 'typical' UV/optical selected AGN reddened by various amounts of extinction.

Intrinsic AGN properties. In Chapter 4, I determined the SMBH masses of the red 2MASS AGN sample, and found that the masses are higher than those of the PG quasars and unobscured type 1 AGN of similar intrinsic power. This could be because either (a) the BLRs of the 2MASS AGN are affected by inaccurate extinction corrections, therefore the broad Balmer emission lines yield inaccurate results, or (b) the masses are genuinely higher. To distinguish between these possibilities, the broad line emission from the near-IR hydrogen lines can be used. Such lines are less affected by dust extinction and their profiles are easier to fit. Therefore, they can be used to estimate accurate virial black hole masses.

In Chapter 4 I noted that the BLR Balmer emission in J0400+05 is significantly blue shifted by -2870±160 km s^{-1} relative to the NLR emission. Such shifts in the BLR are predicted for the recoils ('kicks') that result from the merger of two black holes (Shields & Bonning, 2008). If this object is indeed a black hole recoil candidate, the blue shifted BLR emission will be observed at near-IR wavelengths in the Paschen line emission. Because emission is less affected by extinction at these wavelengths, I could gain a better insight into the nature of the SMBH of this object using near-IR emission lines.

7.2.3 Modelling

In Chapter 6, I developed a model for the purpose of reproducing the near- to mid-IR colours of the 2MASS AGN in order to test the explanations developed in the previous chapters. While this model confirmed the feasibility of the explanations in the sense that the red J-K_S colours of the *population* of 2MASS AGN could be reproduced, the

model could be substantially improved by fitting all the near- to mid-IR points of the individual AGN SEDs simultaneously, using a minimum χ^2 approach. This would have the advantage of being able to determine the relative proportions of the different components, such as the degree of reddening and dust covering factors, for *individual* objects. By improving the modelling in this way, it would be possible to determine the most likely cause of the red near-IR colours of objects for which the explanation based on the observational evidence is ambiguous (e.g. for objects such as J0447-16 and J1127+24).

Bibliography

Adams, T. F. 1977, ApJS, 33, 19

Alloin D., Bica, E., Bonatto, C., Prugniel, P., 1992, A&A, 226, 117

Antonucci, R. R. J., 1984, ApJ, 278, 499

Antonucci, R. R. J., Miller, J. S., 1985, ApJ, 297, 621

Antonucci, R. R. J. 1993, ARA&A, 31, 473

Appenzeller I., Östreicher, R., 1988, AJ, 95, 45

Appenzeller I., Wagner, S.J., 1991, A&A, 250, 57

Assef, R. J., Kochanek, C. S., Brodwin, M., Cool, R., Forman, W., Gonzalez, A. H., Hickox, R. C., Jones, C., Le Floc'h, E., Moustakas, J., Murray, S. S., Stern, D., 2010, ApJ, 713, 970

Baade, W., Minokowski, R., 1954, ApJ, 119, 206

Baldwin J., 1977, MNRAS, 178, 67

Baldwin J., Phillips M., Terlevich R. 1981, PASP, 93, 5

Balsara, D. S., Krolik, J. H., 1993, ApJ, 402, 109

Barnes, J. E., 1988, ApJ, 331, 699

Barvainis R. 1987, ApJ, 320, 537

Baum, S. A., Gallimore, J. F., O'Dea, C. P., Buchanan, Ca. L., Noel-Storr, J., Axon, D. J., Robinson, A., Elitzur, M., Dorn, M., Staudaher, S., 2010, ApJ, 710, 289

Bekenstein, J. D., 1973, ApJ, 183, 657

Bennett, A. S., 1962, MNRAS, 125, 75

Bessiere, P. S., Tadhunter, C. N., Ramos Almeida, C., Villar Martín, M., 2012, MNRAS, 426, 276

Bian W., Gu Q., Zhao Y., Chao L., Cui Q., 2006, MNRAS, 372, 876

Blandford, R. D., Rees, M. J., 1974, MNRAS, 169, 395

Blandford R. D., Znajek R. L., 1977, MNRAS, 179, 433

Bolton, J. G. 1948, Nature, 162, 141

Bolton, J. G. Stanley, G. J. 1948, Nature, 161, 312

Bolton, J. G. Stanley, G. J., Slee, O. B., 1949, Nature, 164, 101

Boroson T. A., Green R. F., 1992, ApJS, 80, 109

Bruzual G., Charlot S., 2003, MNRAS, 344, 1000

Burbidge, G. R. 1956, ApJ, 124, 416

Calzetti D., Armus L., Bohlin R. C., Kinney A. L., Koornneef J., Storchi-Bergmann Th., 2000, ApJ, 533, 682

Canalizo G., Wold M., Hiner K. D., Lazarova M., Lacy M., Aylor K., 2012, ApJ, 760, 38

Capetti, A., Buttiglione, S., Axon, D.J., Robinson, A., Celotti, A, Baldi, R.D., Chiaberge, M., Macchetto, F.D., Sparks, W.B., 2011, A&A, 527, 2

Chou, R. C. Y., Peck, A. B., Lim, J., Matsushita, S., Muller, S., Sawada-Satoh, S., Dinh-V-Trung, Boone, F., Henkel, C., 2007, ApJ, 670, 116

Cohen, M., Wheaton, Wm. A., Megeath, S. T. 2003, AJ, 126, 1090

Comastri, A., Setti, G., Zamorani, G., Hasinger, G., 1995, A&A, 296, 1

Condon, J. J. 1992, ARAA, 30, 575

Condon, J. J., Anderson, E., Broderick, J. J. 1995, AJ, 109, 2318

Condon, J. J., Yin, Q. F., Thuan, T. X., Boller, Th. 1998, AJ, 116, 2682

Cutri R.M., 1995, A&AS, 187, 7509

Cutri R. M., Nelson B. O., Kirkpatrick J.D., Huchra J.P., Smith, P. S., 2001, ASPC, 232, 78

Cutri, R. M., Nelson, B. O., Francis, P. J., Smith, P. S. 2002, PASP, 284, 127

Czerny, B., Hryniewicz, K., 2011, A&A, 525, 8

Dain S., Lousto C. O., Zlochower Y., 2008, PhRvD, 78, 4039

Di Matteo, T., Springel, V., Hernquist, L. 2005, Nature, 433, 604

Dicken, D., Tadhunter, C., Morganti, R., Buchanan, C., Oosterloo, T., Axon, D., 2008, ApJ, 678, 712

Dicken D., Tadhunter, C., Axon, D., Morganti, R., Inskip, K. J., Holt, J., González Delgado, R., Groves, B., 2009, ApJ, 694, 268

Dicken, D., Tadhunter, C., Axon, D., Robinson, A., Morganti, R., Kharb, P., 2010, ApJ, 722, 1333

Dicken, D., Tadhunter, C., Rose, M., et al. 2013 (in prep)

Dickson, R., Tadhunter, C., Shaw, M., Clark, N., Morganti, R., 1995, MNRAS, 273, 29

Draine, B. T., 2006, ApJ, 636, 1114

Draper, A. R., Ballantyne, D. R., 2012, ApJ, 751, 72

Dunlop, J. S., McLure, R. J., Kukula, M. J., Baum, S. A., O'Dea, C. P., Hughes, D. H., 2003, MNRAS, 340, 1095

Edge, D. O., Shakeshaft, J. R., McAdam, W. B., Baldwin, J. E., Archer, S., 1959, MmRAS, 68, 37

Elitzur M., 2008, NewAR, 52, 274

Elvis M., Wilkes, B.J., McDowell, J.C., Green, R.F., Bechtold, J, Willner, S. P., Oey, M. S., Polomski, E, Cutri, R., 1994, ApJS, 95, 1

Elvis M., Journal of Physics: Conference Series 372 (2012) 012032

Fabian, A. C., Barcons, X., 1992, ARAA, 30, 429

Fanaroff, B. L., Riley, J. M., 1974, MNRAS, 167, 31

Fasano G., Franceschini A., 1987, MNRAS, 225, 155

Fath, E. A. 1909, Lick Obs. Bull., 5, 71

Ferguson, J. W., Korista, K. T., Ferland, G. J., 1997, ApJs, 110, 287

Ferland, G. J., Korista, K. T., Verner, D. A., Ferguson, J. W., Kingdon, J. B., Verner, E. M., 1998, PASP, 110, 761

Ferrarese, F., Merritt, D., 2000, ApJ, 539, 9

Ferruit, P., Wilson, A. S., Mulchaey, J. 2000, ApJS, 128, 139

Flaherty K. M., Pipher J. L., Megeath S. T., Winston E. M., Gutermuth R. A., Muzerolle J., Allen L. E., Fazio G. G., 2007, ApJ, 663, 1069

Fosbury R.A., Sansom A.E., 1983, MNRAS, 204, 1231

Franceschini, Alberto; Manners, James; Polletta, Maria del Carmen; Lonsdale, Carol; Gonzalez-Solares, Eduardo; Surace, Jason; Shupe, Dave; Fang, Fan; Xu, C. Kevin; Farrah, Duncan; Berta, Stefano; Rodighiero, Giulia; Perez-Fournon, Ismael; Hatziminaoglou, Evanthia; Smith, Harding E.; Siana, Brian; Rowan-Robinson, Michael; Nandra, Kirpal; Babbedge, Tom; Vaccari, Mattia; Oliver, Seb; Wilkes, Belinda; Owen, Frazer; Padgett, Deborah; Frayer, Dave; Jarrett, Tom; Masci, Frank; Stacey, Gordon; Almaini, Omar; McMahon, Richard; Johnson, Olivia; Lawrence, Andrew; Willott, Chris., 2005, AJ, 129, 2074

Francis P.J., Whiting M.T., Webster R.L., 1999, PASA, 17, 56

Gallimore, J. F., Yzaguirre, A., Jakoboski, J., Stevenosky, M. J., Axon, D. J., Baum, S. A., Buchanan, C. L., Elitzur, M., Elvis, M., O'Dea, C. P., Robinson, A, 2010, ApJS, 187, 172

Garcia-Lorenzo, B., Holt, J., 2001, Maps of the standard arc-lamps for the WHT ISIS-Blue arm, Calibration manual 125, Isaac Newton Group, La Palma

Gaskell C. M., Ferland G. J., 1984, PASP, 96, 393

Georgakakis, A., Clements, D. L., Bendo, G., Rowan-Robinson, M., Nandra, K., Brotherton, M. S., 2009, MNRAS, 394, 533

Giacconi, R., Gursky, H., Paolini, F., Rossi, B. 1962. Phys. Rev. Lett. 9: 439-43

Ginzburg, V. L., Syrovatskii, S. I., 1965, ARA&A, 3, 297

Glikman E., Gregg M. D., Lacy, M., Helfand D. J., Becker R. H., White R. L., 2004, ApJ, 607, 60

Glikman E., Helfand D. J., White R. L., Becker R. H., Gregg M. D., Lacy, M., 2007, ApJ, 667, 673

Glikman E., 2011, PoS(Bash11)009

Glikman, E., Urrutia, T., Lacy, M., Djorgovski, S. G., Mahabal, As., Myers, A. D., Ross, N. P., Petitjean, P., Ge, J., Schneider, D. P., York, D. G., 2012, ApJ, 757, 51

Goodrich R.W., 1989, ApJ, 342, 224

Granato, G. L., Danese, L. 1994, MNRAS, 268, 235

Greene J.E., Ho L.C., 2004, ApJ, 610, 722

Greene J.E., Ho L. C., 2005, ApJ, 630, 122

Greenstein, J. L. Schmidt, M. 1964, ApJ, 140, 1

Grevesse, N., Anders, E. 1989, Cosmic Abundances of Matter, AIP Conference Proceedings 183, p. 1, Ed. C. J. Waddington, (New York: AIP)

Grevesse, N., Noels, A. 1993 in Origin & Evolution of the Elements, ed. N. Prantzos, E. Vangioni-Flam, & M. Casse p. 15 (Cambridge: Cambridge Univ. Press)

Gu, M. F., Ai, Y. L., 2011, A&A, 534, 59

Hao, C. N., Xia, X. Y., Mao, S., Wu, H., Deng, Z. G., 2005, ApJ, 625, 78

Hardcastle, M. J., Evans, D. A., Croston, J. H., 2007, MNRAS, 376, 1849

Haschick A.D., Baan, W.A., Peng, E.W., 1994, ApJ, 437, 35

Hazard, C., Mackey, M. B. Shimmins, A. J. 1963, Nature, 197, 1037

Heckman, T. M. 1978, PASP, 90, 241

Heckman T. M., 1980, A&A, 87, 152

Heckman, T. M., Smith, E. P., Baum, S. A., van Breugel, W. J. M., Miley, G. K., Illingworth, G. D., Bothun, G. D., Balick, B., 1986, ApJ, 311, 526

Heckman T. M., Kauffmann G., Brinchmann J., Charlot S., Tremonti C., White S. D. M., 2004, ApJ, 613, 109

Hewett, P. C., Foltz, C. B., Chaffee, F. H., 1995, AJ, 109, 1498

Hey, J. S., Parsons, S. J. Phillips, J. W. 1946, Nature, 158, 234

Hill, G. J., Goodrich, R. W., Depoy, D. L., 1996, ApJ, 462, 163

Ho, L. C., Filippenko, A. V., Sargent, W. L. W. 1993, ApJ, 417, 63

Ho, L. C., 1999, AdSpR, 23, 813

Holt, J., Garcia-Lorenzo, B., 2001, Maps of the standard arc-lamps for the WHT ISIS-Red arm, Calibration manual 126, Isaac Newton Group, La Palma

Holt J., Tadhunter C. N., González Delgado R. M., Inskip K. J., Rodriguez Zaurin J., Emonts B. H. C., Morganti R., Wills K. A., 2007, MNRAS, 381, 611

Holt J., Tadhunter C. N., Morganti R., 2008, MNRAS, 387, 639

Hopkins, P. F., Hernquist, L., Cox, T. J., Di Matteo, T., Martini, P., Robertson, B., Springel, V., 2005, ApJ, 630, 705

Hopkins P. F., Hernquist L., Cox T. J., Di Matteo T., Robertson B., Springel V., 2006, ApJS, 163, 1

Howarth I. D., 1983, MNRAS, 203, 301

Howarth I. D., Murray J., Mills D., Berry D. S., 2004, Starlink User Note 50.24 (Swindon: PPARC), http://www.starlink.rl.ac.uk/star/docs/sun50.htx/sun50.html

Huffman, D. R. 1977, Adv. Phys., 26, 129

Hutchings, J.P., Maddox, N., Cutri, R.M., Nelson, B.O., 2003, AJ, 126, 63

Ivezić, Ž., et al. 2002, AJ, 124, 2364

Ilovaisky, S. A, Lequeux, J., 1972, A&A, 20, 347

Indebetouw, R., Mathis, J. S., Babler, B. L., Meade, M. R., Watson, C., Whitney, B. A., Wolff, M. J., Wolfire, M. G., Cohen, M., Bania, T. M., Benjamin, R. A., Clemens, D. P., Dickey, J. M., Jackson, J. M., Kobulnicky, H. A., Marston, A. P., Mercer, E. P., Stauffer, J. R., Stolovy, S. R., Churchwell, E., 2005, ApJ, 619, 931

Jansky, K. G. 1932, Proc. IRE, 20, 1920

Jansky, K. G. 1935, Proc. IRE, 21, 1158

Jin C., Ward M., Done C., Gelbord J., 2012, MNRAS, 420, 1825

Jin C., Ward M., Done C., 2012, MNRAS, 422, 3268

Jin C., Ward M., Done C., 2012, MNRAS, 425, 907

Kaler J.B., 1976, ApJS, 31, 517

Kennicutt, R. C. 1978, Ph.D thesis, University of Washington, Seattle, Washington

Kewley L. J., Groves, B., Kauffmann, G., Heckman, T., 2006, MNRAS, 372, 961

Khachikian, E. Y., Weedman, D. W. 1974, ApJ, 192, 581

Kim D. -C., Sanders, D. B., 1998, ApJS, 119,

Kishimoto, M., Antonucci, R., Blaes, O., Lawrence, A., Boisson, C., Albrecht, M., Leipski, C., 2008, JPhCS, 131, 2039

Komossa S., Zhou, H., Lu, H., 2008, ApJ, 678, 81

Komossa S., et al., 2009, ApJ, 701, 105

Korista K.T., Ferland G. J., 1989, ApJ, 343, 678

Koski, A. T., 1978, ApJ, 223, 56

Kovačević J., Popović, L.Č., Dimitrijević M.S., 2010, MSAIS, 15, 176

Kuraszkiewicz J., Wilkes B. J., Schmidt G., Ghosh H., Smith P. S., Cutri R., Hines D., Huff E. M., McDowell J. C., Nelson B., 2009, ApJ, 692, 1143

Kuraszkiewicz J., Wilkes B. J., Schmidt G., Smith P. S., Cutri R., Czerny B., 2009, ApJ, 692, 1180

Laing, R. A., Riley, J. M., Longair, M. S., 1983, MNRAS, 204, 151

LaMassa S, M., Heckman T, M., Ptak A., Martins L., Wild V., Sonnentrucker P., 2010, ApJ, 720, 786

Laor A., Draine B. T., 1993, ApJ, 402, 441

Law K., Gordon K. D., Misselt K. A., 2011, ApJ, 738, 124

Lawrence A., Elvis M., 1982, ApJ, 256, 410

Low F.J, Cutri R. M., Huchra J.p., Kleinmann S. G., 1988, ApJ, 327, 41

Malkan, M. A., Gorjian, V., Tam, R., 1998, ApJS, 117, 25

Manchado, A., Fuentes, F. J., Prada, F., Ballesteros, E., Barreto, M., Carranza, J. M., Escudero, I., Fragoso-Lopez, A. B., Joven-Alvarez, E., Manescau, A., Pi, M., Rodriguez-Ramos, L. F., Sosa, N. A., 1998, SPIE, 3354, 448

Marble A. R., Hines . C., Schmidt G. D., Smith P. S., Surace J. A., Armus L., Cutri R. M., Nelson B. O., 2003, ApJ, 590, 707

Marconi, A., Risaliti, G., Gilli, R., Hunt, L., Maiolino, R., Salvati, M. 2004, MNRAS, 351, 169

Markarian, B. E. 1967, Astrofizika, 3, 55

Markarian, B. E., Lipovetskii, V. A., Stepanian, D. A. 1981, Astrofizika, 17, 619

Mathur, S. 2000, MNRAS, 314, 17

Matthews, T. A., Sandage, A. R. 1963, ApJ, 138, 30

McDonald, M., Benson, B., Veilleux, S., Bautz, M. W., Reichardt, C. L., 2013, ApJ, 765, 37

McLure, R. J., Dunlop, J. S., 2001, MNRAS, 327, 199

McLure, R. J., Dunlop, J. S., 2004, MNRAS, 352, 1390

Meinel A.B., et al. 1975, Catalogue of Emission Lines in Astrophysical Objects, Optical Sciences Center (Univ. of Arizona)

Mihos J. C., 1995, ApJ, 438, 75

Mor R., Netzer H., Elitzur M., 2009, ApJ, 705, 298

Mullaney J.R., Ward M.J., 2008, MNRAS, 385, 53

Mullaney J.R., Ward, M. J., Done, C., Ferland, G. J., Schurch, N., 2009, MNRAS, 394, 16

Murayama T., Taniguchi. Y, 1998, ApJ, 497, 9

Mushotzky, R., 2004, ASSL, 308, 53

Nagao T., Taniguchi, Y, Murayama, T., 2000, AJ, 119, 2605

Nagao T., Murayama, T, Taniguchi, Y., 2001, ApJ, 549, 155

Nagao, T., Murayama, T., Shioya, Y., Taniguchi, Y., 2003, AJ, 125, 1729

Narayanan, D., Cox, T. J., Robertson, B., Davé, R., Di Matteo, T., Hernquist, L., Hopkins, P., Kulesa, C., Walker, C. K., 2006, ApJ, 642, 107

Nelson C. H., Whittle M., 1995, ApJS, 99, 67

Nenkova, M., Ivezić, Ž., Elitzur, M., 2002, ApJ, 570, 9

Nenkova, M., Sirocky, M. M., Ivezić, Ž., Elitzur, M., 2008, ApJ, 685, 147

Nenkova, M., Sirocky, M. M., Nikutta, R,. Ivezić, Ž., Elitzur, M., 2008, ApJ, 685, 160

Netzer H., Laor A., 1993, ApJ, 404, 51

Neugebauer, G., Green, R. F., Matthews, K., Schmidt, M., Soifer, B. T., Bennett, J., 1987, ApJS, 63, 615

Nipoti, C., Blundell, K. M., Binney, J., 2005, MNRAS, 361, 633

Nishiyama S., Nagata T., Tamura M., Kandori R., Hatano H., Sato S., Sugitani K., 2008, 680, 1174

Nishiyama, S., M. Tamura, H. Hatano, and et al 2009, ApJ, 696, 1407

Nussbaumer H., Osterbrock D.E., 1970, ApJ, 161, 811

Nussbaumer H., Storey P.J, 1982, A&A, 1131, 21

Oke J.B., Sargent W.L.W., 1968, ApJ, 151, 807

Osterbrock D.E., 1978, Phys. Scr., 17, 285

Osterbrock, D.E., 1981, ApJ, 249, 462

Osterbrock D.E., Pogge R., 1985, ApJ, 297, 166

Osterbrock, D. E., Fulbright, J. P., Martel, A. R., Keane, M. J., Trager, S. C., Basri, G., 1996, PASP, 108, 277

Osterbrock D.E., Ferland G.J., 2006, Astrophysics of Gaseous Nebulae and Active Galactic Nuclei, 2nd edition, University Science Books, USA

Paglione, T.A.D., Timothy A. D., Jackson, J.M., Bolatto, A.D., Heyer, M.H., 1998, ApJ, 493, 680

Peacock J.A., 1983, MNRAS, 202, 615

Penston M.V., Fosbury R.A.E., 1978, MNRAS, 185, 479

Penston M.V., Fosbury, R. A. E., Boksenberg, A., Ward, M. J., Wilson, A. S., 1984, MNRAS, 208, 347

Peterson, B. M., 1997, 'An Iintroduction to Active Galactic Nuclei', Cambridge University Press

Pier E. A., Krolik J. H. 1992, ApJ, 401, 99

Pier E. A., Krolik J. H. 1993, ApJ, 418, 673

Pier, E.A., Voit, G.M., 1995, ApJ, 450, 628

Pooley, G. G. 1969, MNRAS, 144, 10

Pounds, K. A., Done, C., Osborne, J. P. 1995, MNRAS, 277, 5

Ramos Almeida, C., Tadhunter, C. N., Inskip, K. J., Morganti, R., Holt, J., Dicken, D., 2011, MNRAS, 410, 1550

Ramos Almeida, C., Bessiere, P. S., Tadhunter, C. N., Pérez-González, P. G., Barro, G., Inskip, K. J., Morganti, R., Holt, J., Dicken, D., 2012, MNRAS, 419, 687

Reber, G. 1944, ApJ, 100, 279

Rees, M. J., 1984, ARA&A, 22, 471

Richards, G. T., Fan, X., Newberg, H. J., Strauss, M. A., Vanden B., Daniel E., Schneider, D. P., Yanny, B., Boucher, A., Burles, S., Frieman, J. A., Gunn, J. E., Hall, P. B., Ivezić, Ž., Kent, S., Loveday, J., Lupton, R. H., Rockosi, C. M., Schlegel, D. J., Stoughton, C., SubbaRao, M., York, D. G., 2002, AJ, 123, 2945

Rieke G. H., Low F. J., 1975, ApJ, 199, 13

Rieke, G. 1978, ApJ, 226, 550

Risaliti, G., Elvis, M., Nicastro, F., 2002, ApJ, 571, 234

Risaliti, G., Elvis, M., Fabbiano, G., Baldi, A., Zezas, A, 2005, ApJ, 623, 93

Robinson, A., Binette, L., Fosbury, R. A. E., Tadhunter, C. N., 1987, MNRAS, 227, 97

Robinson T. G., Tadhunter C. N., Axon D. J., Robinson A., 2000, MNRAS, 317, 922

Roche, P. F., Aitken, D. K., Smith, C. H., 1991, MNRAS, 252, 282

Rodríguez-Ardila, A., Mazzalay, X., 2006, MNRAS, 367, L57

Rodríguez Zaurín J., Tadhunter C. N., González Delgado R. M. 2009, MNRAS, 400, 1139

Rodríguez Zaurín, J., Tadhunter, C. N., Rose, M., Holt, J., 2013, MNRAS, 432, 138

Rose M., Tadhunter C. N., Holt, J., Ramos Almeida, C., Littlefair, S. P., 2011, MNRAS, 414, 3360

Rose, M., Tadhunter, C. N., Holt, J., Rodríguez Zaurín, J., 2013a, MNRAS, 432, 2150

Rose, M., Tadhunter, C. N., Holt, J., Dicken, D., 2013b, (in prep)

Rowan-Robinson M., 1977, ApJ, 213, 635

Rush, B., Malkan, M. A., Spinoglio, L., 1993, ApJS, 89, 1

Salpeter, E. E. 1977, ARA&A, 15, 267

Sanders, D. B., Soifer, B. T., Elias, J. H., Madore, B. F., Matthews, K., Neugebauer, G., Scoville, N. Z., 1988, ApJ, 325, 74

Sarzi M., Falcón-Barroso J., Davies R. L., Bacon R., Bureau M., Cappellari M., de Zeeuw P. T., Emsellem E., Fathi K., Krajnović D., Kuntschner H., McDermid R. M., Peletier R. F., 2006, MNRAS, 366, 1151

Sanders, R., Baldwin, J. E., Rawlings, S., Warner, P. J., Miller, L., 1989, MNRAS, 238, 777

Scheuer, P. A. G., 1974, MNRAS, 166, 513

Schinnerer E., Eckart A., Tacconi L. J., 1999, ApJL, 524, 5

Schinnerer E., Eckart A., Tacconi L. J., Genzel R., Downes D., 2000, ApJ, 533, 850

Schlegel D. J., Finkbeiner D. P., Davis M., 1998, ApJ, 500, 525

Schmidt, M. 1963, Nature, 197, 1040

Schmidt M., Green R. F., 1983, ApJ, 269, 352

Seaton M. J., 1979, MNRAS, 187, 73

Seyfert, C. K., 1943, ApJ, 97, 28

Shakura, N. I., Sunyaev, R. A., 1973, A&A, 24, 337

Shanks, T., Georgantopoulos, I., Stewart, G. C., Pounds, K. A., Boyle, B. J., Griffiths, R. E., 1991, Nature, 353, 315

Shi Y., Ogle P., Rieke G. H., Antonucci R., Hines D. C., Smith P. S., Low F. J., Bouwman J., Willmer C., 2007, ApJ, 669, 841

Shields, J. C. 1992, ApJ, 399, 27

Shields, J. C. 1999, PASP, 111, 661

Shields G. A., Bonning E. W. 2008, ApJ, 682, 758

Siegel, W., et al., 1998, At.Data Nucl. Data tables 68, 303

Silk, J., Rees, M. J., 1998, A&A, 331, 1

Simpson C., Rawlings S., 2000, MNRAS, 317, 1023

Skrutskie, M. F., Cutri, R. M., Stiening, R., Weinberg, M. D., Schneider, S., Carpenter, J. M., Beichman, C., Capps, R., Chester, T., Elias, J., Huchra, J., Liebert, J., Lonsdale, C., Monet, D. G., Price, S., Seitzer, P., Jarrett, T., Kirkpatrick, J. D., Gizis, J. E., Howard, E., Evans, T., Fowler, J., Fullmer, L., Hurt, R., Light, R., Kopan, E. L., Marsh, K. A., McCallon, H. L., Tam, R., Van Dyk, S., Wheelock, S., 2006, AJ, 131, 1163

Smith, M. G. 1975, ApJ, 202, 591

Smith, M. G., Aguirre, C., Zemelman, M. 1976, ApJS, 32, 217

Smith P. S., Schmidt G. D., Hines D. C., Cutri R. M., Nelson B. O., 2002, ApJ, 569, 23

Smith N., Silverman, J.M., Chornock, R, Filippenko, A.V., Wang, X, Li, W, Ganeshalingam, M, Foley, Ryan J., Rex, J, Steele, T.N., 2009, ApJ, 695, 1334

Spergel, D. N., Verde, L., Peiris, H. V., Komatsu, E., Nolta, M. R., Bennett, C. L., Halpern, M., Hinshaw, G., Jarosik, N., Kogut, A., Limon, M., Meyer, S. S., Page, L., Tucker, G. S., Weiland, J. L., Wollack, E., Wright, E. L., 2003, ApJS, 148, 175

Spinrad, H., Djorgovski, S., Marr, J., Aguilar, L. 1985, PASP, 97, 932

Stein, W. A., Odell, S. L., Strittmatter, P. A., 1976, ARA&A, 14, 173

Tadhunter, C. N., Tsvetanov, Zl., 1989, Nature, 341, 422

Tadhunter, C. N., Morganti, R., di Serego-Alighieri, S., Fosbury, R. A. E., Danziger, I. J., 1993, MNRAS, 263, 999

Tadhunter, C. N., Morganti, R., Robinson, A., Dickson, R., Villar-Martin, M., Fosbury, R. A. E., 1998, MNRAS, 298, 1035

Tadhunter C., Robinson T. G., González Delgado R. M., Wills K., Morganti R., 2005, MNRAS, 356, 480

Tadhunter, C. N., Ramos Almeida, C., Morganti, R., Holt, J., Rose, M., Dicken, D., Inskip, K., 2012, MNRAS, 427, 1603

Terlevich, R., Melnick, J., 1985, MNRAS, 213, 841

Torres, D. F., Anchordoqui, L. A., 2004, RPPh, 67, 1663

Tran H. D., Cohen, M.H., Ogle, P. M., Goodrich, R.W., di Serego Alighieri, S., 1998, ApJ, 500, 660

Tristram, K. R. W.. Meisenheimer, K., Jaffe, W., Cotton, W. D., 2007a, IAUS, 238, 93

Tristram, K. R. W., Meisenheimer, K., Jaffe, W., Schartmann, M., Rix, H.-W., Leinert, Ch., Morel, S., Wittkowski, M., Röttgering, H., Perrin, G., Lopez, B., Raban, D., Cotton, W. D., Graser, U., Paresce, F., Henning, Th., 2007b, A&A, 474, 837

Trump J. R., Hall P. B., Reichard T. A., et al. 2006, ApJS, 165, 1

Urrutia T., Lacy M., Becker R. H., 2008, ApJ, 674, 80

Urrutia T., Becker R. H., White R. L., Glikman E., Lacy M., Hodge J., Gregg M. D., 2009, ApJ, 698, 1095

Urrutia, T., Lacy, M., Spoon, H., Glikman, E., Petric, A., Schulz, B., 2012, ApJ, 757, 125

Urry, C. M., Padovani, P., 1995, PASP, 107, 803

Véron-Cetty M.-P., Véron P., Gonçalves A. C., 2001, A&A, 372, 730

Voit, G. M., Weymann, R. J., Korista, K. T., 1993, ApJ, 413, 95

Wall, J. V., Peacock, J. A., 1985, MNRAS, 216, 173

Webster, R. L., Francis, P. J., Peterson, B. A., Drinkwater, M. J., Masci, F. J., 1995, Nature, 375, 469

Weedman D. W., 1971, ApJ, 167, 23

Weymann R. J., Morris S. L., Foltz C. B., Hewett P. C., 1991, ApJ, 373, 23

White, R. L., Becker, R. H., Gregg, M. D., Laurent-Muehleisen, S. A., Brotherton, M. S., Impey, C. D., Petry, C. E., Foltz, C. B., Chaffee, F. H., Richards, G. T., Oegerle, W. R., Helfand, D. J., McMahon, R. G., Cabanela, J. E., 2000, ApJS, 126, 133

Whiting, M. T., Webster, R. L., Francis, P. J., 2001, MNRAS, 323, 718

Whittle M., 1985, MNRAS, 213, 1

Wilkes B. J., Schmidt G. D., Cutri R. M., Ghosh H., Hines D. C., Nelson B., Smith P. S., 2002, ApJ, 564, 65

Wilson, A. S., Colbert, E. J. M, 1995, ApJ, 438, 62

Wisotzki, L., Koehler, T., Groote, D., Reimers, D., 1996, A&AS, 115, 227

Wright, E. L., 2010, AJ, 140, 1868

Zakamska, N. L., Strauss, M. A., Krolik, J. H., Collinge, M. J., Hall, P. B., Hao, L., Heckman, T. M., Ivezić, Ž., Richards, G. T., Schlegel, D. J., Schneider, D. P., Strateva, I., Vanden B., D. E., Anderson, S. F., Brinkmann, J., 2003, AJ, 126, 2144

Zakamska N. L., Strauss, M. A., Heckman, T. M., Ivezić, Ž., Krolik, J. H., 2004, AJ, 128, 1002

Zhou H., Wang T., Yuan W., Lu H., Dong X., Wang J., Lu Y., 2006, ApJS, 166, 128